

**Quasi-Static Fracture Behaviour of AISI
304L and CA6NM**

A Thesis submitted in partial fulfilment for the Degree
of Doctor of Philosophy

Olivia Angel

May 2023

Abstract

Nuclear transport packages are required to transport radioactive material for a variation of reasons such as the transport of new fuel to reactor sites. Depending on the type of nuclear transport package, AISI 304L is used for various components such as internal/external shock absorbers and outer containment structures. Literature regarding CA6NM suggests that the material provides the mechanical properties to be used for thick wall castings for nuclear transport packages. The aim of this thesis was to obtain data characterising the plasticity and fracture behaviour of two grades of stainless steel, AISI 304L and CA6NM when subjected to a range of multiaxial loading.

Nuclear transport packages must pass a series of testing standards regulated by the IAEA before they can be licenced for use. The main motivating factor in this study was to acquire data regarding the failure of AISI 304L and CA6NM, by producing a fracture locus which could be utilised to assist structural integrity assessments for the design of nuclear transport packages.

The experimental testing programme had 4 main phases of testing, a total of 200 tests were performed at ambient temperature under quasi-static conditions on test specimens having 15 different geometries. The methodology used DIC in parallel with FE analysis, to find the equivalent fracture strain, average stress triaxiality and average Lode angle parameter over the load history.

Initially, the fracture initiation point was assumed to be at the location of the maximum plastic equivalent strain of the FE analysis. However, fracture initiation at the critical location of the geometries designed to provide pure shear data, occurred at the point of maximum tensile stress. This led to an investigation to extract data from a central node located in the shear region or alternatively averaging the whole of the failure zone of the specimen. Various fracture loci were constructed at the moment of failure but using the different methods for extracting the data. From this a strain-based criterion for AISI 304L and CA6NM was produced. Analytical expressions of the fracture envelope for each method can be utilised for practical relevance, regarding nuclear transport packages depending on the failure model. Methods developed in this thesis can be used for other materials and can aid future experiments investigating plasticity and fracture behaviour for factors such as a range of strain rates and temperatures.

Acknowledgments

I would like to express my gratitude to my supervisor team. Dr. Glynn Rothwell and Dr. Russell English have continuously gone out of their way to help me and have always made time to have discussions and review regarding my work, for that I would like to say thank you. I would like to thank Dr. Ariyan Ashkanfar for his review and comments on my paper and helping me grow academically with discussions regarding my work. I also extend my appreciation to Dr. James Ren, those discussions regarding material science have been invaluable. The support from all of my supervisory team whether it be discussions or motivation has helped me finish this thesis.

I would like to recognise that this research was supported by NTS (Nuclear Transport Solutions), I appreciate that opportunity to study research that I have thoroughly found interesting and challenging. I would like to thank Dr. Andrew Cummings at NTS, for his continuous guidance and discussion throughout my research.

I would like to make a special thanks to all my family and my friends who have given me unconditional love and encouragement throughout this period. I would like to give a special thanks to my mother, who taught me nothing is impossible, the word itself says "I'm possible"!

Lastly, I would like to acknowledge myself, throughout this PhD there has been many challenges, some completely out of my control. However, I have turned up each day moving slowly closer to the completion of this thesis. Every week of my PhD I have chosen an inspirational quote, I would like to end my acknowledgments with one of my favourites that I feel sums up my journey in these last years.

"A person who never made a mistake never tried anything new" - Albert Einstein.

Peer Reviewed Publications

O. Angel, G. Rothwell, and R. English

“Numerical simulations of Quasi-Static Fracture Behaviour of AISI 316 for Nuclear Transport Packages”. Journal of Physics: Conference Series, 2198(2022) 012022, doi:10.1088/1742-6596/2198/1/012022.

O. Angel, G. Rothwell, R. English, J. Ren, and A. Cummings

“Effect of Post Processing of Digital Image Correlation on Obtaining Accurate True Stress-Strain Data for AISI 304L”. Nuclear Engineering and Technology, <https://doi.org/10.1016/j.net.2022.03.038>.

Table of Contents

Abstract.....	ii
Acknowledgments.....	iii
Peer Reviewed Publications.....	iv
Table of Contents.....	v
Nomenclature.....	viii
List of Figures.....	x
List of Tables.....	xvii
1 Introduction.....	1
1.1 Background.....	1
1.2 Project Aim.....	5
1.3 Project Objectives.....	5
1.4 Structure of Thesis.....	6
2 Background and Literature Review.....	7
2.1 Introduction.....	7
2.2 Aims and Objectives.....	7
2.3 Material Properties.....	8
2.3.1 Austenitic Stainless Steel 304L.....	8
2.3.2 Martensitic stainless steel CA6NM.....	9
2.4 Ductile Fracture.....	10
2.4.1 Microscopic Analysis of Ductile Fracture.....	13
2.4.2 Ductile Fracture – A Historical Perspective.....	14
2.5 Stress State.....	29
2.5.1 Decomposition of the Stress Tensor.....	30
2.5.2 Lode Angle.....	32
2.6 Fracture Locus.....	36
2.6.1 Fracture Experiments.....	38
2.7 Summary.....	51
2.8 Research Gap.....	52
3 Digital Image Correlation.....	53
3.1 Introduction.....	53
3.2 Aims and Objectives.....	56
3.3 Basic Principles of Digital Image Correlation.....	56
3.4 DIC Correlation Criteria.....	58

TABLE OF CONTENTS

3.4.1	DIC Set up and Definitions.....	60
3.5	Main Processes for Digital Image Correlation.....	62
3.6	Preliminary Design of DIC Measurements.....	64
3.6.1	Lens Selection and Extension Tubes.....	65
3.6.2	Stereo Angle Selection.....	67
3.6.3	Specimen Pattern.....	68
3.6.4	Lighting Conditions.....	75
3.6.5	Calibration.....	78
3.7	Post Processing.....	79
3.8	DIC Errors.....	81
3.9	Summary.....	83
4	Experimental Methodology.....	85
4.1	Introduction.....	85
4.2	Aims and Objectives.....	85
4.3	Experimental Testing Programme.....	86
4.4	Methodology between DIC and FE analysis.....	88
4.5	Experiment Set Up.....	90
4.6	Summary.....	95
5	Results and Discussion.....	96
5.1	Introduction.....	96
5.2	Aims and Objectives.....	96
5.3	Material Data.....	97
5.3.1	Introduction.....	97
5.3.2	Methodology.....	98
5.3.3	Experimental Test.....	99
5.3.4	Specimen.....	99
5.3.5	Results and Discussion.....	100
5.3.6	Extraction of DIC Data.....	100
5.3.7	Finite Element Model.....	103
5.3.8	True Stress-Strain Curve.....	104
5.3.9	Conclusion.....	107
5.4	Anisotropy of AISI 304L.....	110
5.5	High and Low Stress Triaxiality.....	112
5.5.1	Introduction.....	112
5.5.2	Experiments and Results.....	113

TABLE OF CONTENTS

5.5.3	Summary of Low and High Stress Triaxiality	128
5.5.4	Conclusion	146
5.6	Negative Stress Triaxiality	148
5.6.1	Introduction.....	148
5.6.2	Experiments	149
5.6.3	FE Analysis.....	149
5.6.4	Results and Discussion	151
5.6.5	Conclusion	162
5.7	Summary	163
6	Conclusion and Recommendations for Further Work.....	164
6.1	Conclusion.....	164
6.2	Contributions to Knowledge and Novel Techniques Developed.....	167
6.2.1	Contributions to Knowledge	167
6.2.2	Novel Techniques Developed.....	167
6.3	Recommendations for Further Work.....	168
	References.....	169
	Appendix.....	186
	Appendix A - Fracture Locus for a Range of Materials.....	186
	Appendix B - Design of DIC Measurement.....	189
	Appendix C – Speckle Pattern Test.....	192
	Appendix D – Engineering Drawings	196
	Appendix E - Manufacture Conformity and Inspection Report.....	211
	Appendix F – Summary of DIC Measurements.....	216
	Appendix G – Recording Procedures for DIC	217
	Appendix H – Yield Stress and Plastic Strain.....	220
	Appendix I – High and Low Stress Triaxiality Force Displacement Curves.....	221
	Appendix J – Python Scripts	225
	Appendix J-1 - Script to obtain the Lode angle parameter in Abaqus for each frame ...	225
	Appendix J-2 - Script to obtain the PEEQ of selected nodes/elements for the last frame	227
	Appendix J-3 - Script to obtain the average Stress Triaxiality and Lode angle parameter for selected nodes/elements	228
	Appendix J-4 - Additional Script to obtain Element volume for selected elements for the last frame -	230
	Appendix K – High Stress Triaxiality Range of Locations	231
	Appendix L – Negative Stress Triaxiality Force Displacement Curves	232

Nomenclature

a/b	Unknown Parameters for Change in Intensity
a_f	Fracture Radius
a_o	Initial Radius
a	Cross-Sectional Area
A_o	Initial Cross-Sectional Area
A_5	Elongation
$b_o/c_o/d_o$	Constants
D	Damage
D_{1-5}	Constants
D/H	Initial Diameter to Initial Height Ratio
E	Young's Modulus
ε	Strain
$\bar{\varepsilon}$	Equivalent Strain
ε_e	Engineering Strain
$\bar{\varepsilon}_f$	Equivalent Fracture Strain
$\bar{\varepsilon}_{f0}$	Reference Equivalent Fracture Strain
ε_t	True strain
$\dot{\varepsilon}$	Strain Rate
$f_{1,2,3}(\sigma_{ij})$	Equivalent Stress at the Onset of Failure
F	Force
F_i	Greyscale Intensity for Reference Subset
G_i	Greyscale Intensity for Deformed Subset
I	Identity Tensor
I_1	First Invariant of the Stress Tensor
I_2	Second Invariant of the Stress Tensor
I_3	Third Invariant of the Stress Tensor

NOMENCLATURE

J_2	Second Deviatoric Stress Invariant
J_3	Third Deviatoric Stress Invariant
l	Gauge Length
l_0	Initial Gauge Length
L	Lode Parameter
η	Stress Triaxiality
η_{avg}	Average Stress Triaxiality
r/X	Normalised Third Invariant
R	Radius
R_σ, R_2, R_3	Demarcation Values of Stress Triaxiality
R_m	Tensile Strength
$(R_{p(0,2)}) / (R_{p(1,0)})$	Yield Point
$s_{ij} / s_{11}, s_{22}, s_{33}$	Deviatoric Stresses
S	Deviatoric Stress Tensor
T	Homologous Temperature
τ	Maximum Shear Stress
u_f	Displacement to Fracture
$\mu_p(p)$	Pressure Dependence
$\mu_\theta(\theta)$	Lode angle dependence
θ	Lode Angle
$\bar{\theta}$	Lode angle Parameter
$\bar{\theta}_{avg}$	Average Lode angle Parameter
σ	Stress
$\bar{\sigma}$	von Mises Equivalent Stress
σ_e	Engineering Stress
σ_H	Hydrostatic/Mean Stress
σ_N	Normal Stress
$\sigma_{11}, \sigma_{22}, \sigma_{33}$	Principal Stresses
ζ	Normalized Third Stress Invariant

List of Figures

Figure 1.1. Example of Tests for Type B Packages, after U.S. Department of Energy [7].	1
Figure 1.2. LWTC Concept, after S.Porter et al. [10].	2
Figure 1.3. CA6NM Stress-Strain Curves for Various Strain Rates at Room Temperature, after Ove Arup & Partners [21].	4
Figure 2.1. CA6NM Stress-Strain Curves for a Range of Temperatures, Data Provided By Lucideon [37].	10
Figure 2.2. Typical Stress-Strain Curve for a Ductile Material.	11
Figure 2.3. Schematic of Nucleation, Growth, and Coalescence of Voids in Ductile Metals, adopted from Gatea et al. [50].	14
Figure 2.4. Bridgman's Diagram of Necking in a Round Bar Specimen, adaptation from Bai [58].	15
Figure 2.5. a) Long Cylindrical Void Extended in the Direction of its axis, b) Spherical Void in a Remote Simple Tension Strain Rate Field, adopted from Rice and Tracey [61].	16
Figure 2.6. a) Plane Strain Specimen b) Axisymmetric Specimen c) Failure Locus for Axisymmetric and Plane Strain Specimens, adopted from Hancock and Brown [69].	18
Figure 2.7. Failure Locus Constructed showing Three Distinct Regions for Low, Intermediate and High Stress Triaxialities, adopted from Bao and Wierzbicki [12].	22
Figure 2.8. Fracture Surface in the 3D Space of the Plastic Strain Plane and the Hydrostatic Stress, adopted from Xue and Wierzbicki [82].	23
Figure 2.9. 3D Asymmetric Fracture Locus, adopted from Bai and Wierzbicki [84].	24
Figure 2.10. Ductile Fracture Timeline.	28
Figure 2.11. Summary of Stress States for Various Loading Conditions, adaptation from Mohr [51].	29
Figure 2.12. Stress State Diagram.	30
Figure 2.13. Dependence of Stress State on Void Evolution, adaptation from Mohr [99].	31
Figure 2.14. Mohr's Circle to Demonstrate Lode Parameter, adaptation from Mohr [99].	33
Figure 2.15. Three Types of Coordinate System in the Space of Principal Stresses, adaptation from Xue [72].	34
Figure 2.16. Fractured Tensile Specimens a) Smooth, b) R = 12mm and c) R = 4mm, adopted from Bao and Wierzbicki [12].	39

LIST OF FIGURES

Figure 2.17. a) 1045 Steel Round Bar Specimens with Different Notches, b) Flat-grooved Plane Strain Specimen, adopted from Bai et al. [58].	39
Figure 2.18. Geometry of the Tensile Specimen and Notches: a) C-notch, b) V-notch, c) U-notch, adopted from Kiran and Khandelwal [111].	40
Figure 2.19. Fracture Locus for a Range of Materials on the Space of the Equivalent Plastic Strain against Stress Triaxiality[12][58][107].	41
Figure 2.20. a) Plate with Hole Specimen after Failure, adopted from Bao and Wierzbicki [12], b) Plate with Hole Specimen FE contour, adopted from Bao [112].	42
Figure 2.21. Pure Shear Specimen, a) Undeformed Specimen, b) Fractured Specimen, adopted from Bao and Wierzbicki [12].	43
Figure 2.22. Lindholm Type Tubular Design Torsion Specimen, adopted from Gao et al. [13].	43
Figure 2.23. Pure Shear Specimen, a) Undeformed Specimen, b) Fractured Specimen, adopted from Bao and Wierzbicki [12].	44
Figure 2.24. Shear-dominated Specimens, adopted from Qian et al. [113].	44
Figure 2.25. Butterfly Specimen, adopted from Bai [102].	45
Figure 2.26. Butterfly Specimen fitted in a Universal Biaxial Testing Device (UBTD) with an inclination angle of 10° with respect to the loading axis, adopted from Bai [102].	45
Figure 2.27. Principal Strain at the Surface of a Butterfly Specimen Measured using DIC and FE analysis, adopted from Dunand and Mohr [107].	46
Figure 2.28. Upsetting Test showing Shear Decohesion, adopted from Bao [79].	47
Figure 2.29. Upsetting Tests and Relative SEM Fractography: (a) Cylindrical Upsetting with $H/D = 2$ (b) Cylindrical Upsetting with $H/D = 1$ (c) Flanged Upsetting (d) Tapered Upsetting, adopted from H. Li et al. [120].	48
Figure 2.30. Upsetting Specimen's Before and showing the Barrel Effect of the Deformed Specimens, adopted from Bai [102].	49
Figure 2.31. New Configuration of Compression Specimen showing Shear Fracture, adopted from Bao and Wierzbicki [12].	50
Figure 3.1. Using DIC for Airbag Testing in the Automotive Industry, adopted from Trillion [130].	54
Figure 3.2. Using DIC for Femur–Implant Construct Under Load, adopted from Rankin et al. [131].	54
Figure 3.3. Using DIC for Structural Health Monitoring of Bridges, adopted from Nonis et al. [132].	54

LIST OF FIGURES

Figure 3.4. Magnitude of Measurement Uncertainty for Cylindrical Shell during Buckling Test, adopted from Gardner et al. [133].	54
Figure 3.5. Comparison of Load-Displacement Curve, adopted from Quach et al. [140].	55
Figure 3.6. a) Typical Specimen Pattern b) Pixels of Pattern c) Histogram of Pattern.	57
Figure 3.7. Subset Displacement during Deformation, adopted from LePage [144].	57
Figure 3.8. Deformation of Subset Before and After.	58
Figure 3.9 Diagram showing 2D Test Rig Set Up and Stereo Rig DIC Set Up.	61
Figure 3.10. Flow Diagram displaying the Main Processes of DIC.	63
Figure 3.11. Dantec 3D Image Correlation System Q-400 and Istra4D Software Set Up.	64
Figure 3.12. Lens and Extension Tube Provided in DIC Package.	65
Figure 3.13. a) 50mm Lens + 10 mm Extension Tube, b) 50mm Lens + 5 mm Extension Tube c) 16mm Lens d) 16 Lens + 5 mm Extension Tube.	66
Figure 3.14. Aperture Example [156].	66
Figure 3.15. Depth of Field Example a) Image when using F2.8, b) Image when using F16.	67
Figure 3.16. Graph showing the amount of Grid Points Depending on the Stereo Angle.	67
Figure 3.17. Resolution of Camera.	68
Figure 3.18. Diagram showing a) Aliased and b) Unaliased Speckle Images, adopted from Reu [163].	69
Figure 3.19. Plate with Hole Specimen using Painted and Printed Speckle Pattern [173].	71
Figure 3.20. Paint Failure before the Specimen Fractures on a Tensile Test.	72
Figure 3.21. DIC set up for Speckled Pattern Tests.	72
Figure 3.22. A range of Subset Sizes for the Same Speckle Pattern.	74
Figure 3.23. Influence of the Subset Size on the Contour Statistical Error Radius.	75
Figure 3.24. The Exposure Triangle [177].	76
Figure 3.25. Different types of lights set ups for a variety of lighting conditions.	77
Figure 3.26. Image of Calibration Target in Different Orientations.	78
Figure 3.27. Major Strain before Failure of Tensile Test with a range of a) Local Regression Filters and b) Grid Reduction.	80
Figure 3.28. Diagram showing Different Types of Errors during the Different Processes of DIC.	81
Figure 4.1. Range of Geometries for Experimental Programme.	87
Figure 4.2. Methodology Flow Chart.	89
Figure 4.3. Levelling of Test Rig and Centralising Cameras.	90
Figure 4.4. Experimental Test Set-Up - Example for T2 6mm Notched Bar.	91

Figure 4.5. Recording Procedure Explained.	92
Figure 4.6. Testing Machine and DIC Software Schematic.	93
Figure 4.7. Specimen Spray Booth.	94
Figure 4.8. The Process of Speckling a Sample.....	95
Figure 5.1. Tensile Specimen Dimensions.	99
Figure 5.2. a) Force-Crosshead Displacement Graph using Machine Data b) Fracture Initiation of Tensile and Failure of Specimen.	100
Figure 5.3. a) Contour of Displacement in Y-direction b) Measured True Strain in Y Direction against Distance Along the Vertical Line.	101
Figure 5.4. Contour Plot of Horizontal Line used to find the Instantaneous Cross-Sectional Area Until failure a) Line CD at Step 0 b) Line CD at Step 269.	102
Figure 5.5. Contour Plot showing different Gauge Parameters.	102
Figure 5.6. FE Model of a Tensile Specimen.	103
Figure 5.7. a) True Stress-Strain Curves b) Force Displacement Curves for a Range of Subsets.	104
Figure 5.8. Matched Force Displacement Curves.....	105
Figure 5.9. Contours of True Y strain for DIC image and FE model at the Onset of Failure.	106
Figure 5.10. a) True Stress-Strain Curves b) Force Displacement Curves for a Range of Filtering.....	107
Figure 5.11. Final True Stress-Strain Data for AISI 304L.	108
Figure 5.12. a) Force Displacement Curves for CA6NM b) True Stress-Strain Data for CA6NM.....	109
Figure 5.13. Rolling Directions of Tensile Specimens.	110
Figure 5.14. Force Displacement Curves for a Range of Rolling Directions.	111
Figure 5.15. True Stress-Strain Curves for a Range of Rolling Directions.	111
Figure 5.16. High and Low Stress Triaxiality Specimens.	112
Figure 5.17. 4mm Notched Bar (T3) DIC Contour for True Tangential Strain Y, a) AISI 304L, b) CA6NM.	113
Figure 5.18. Smooth Bar (SB) a) Loading and Boundary Conditions b) Three Different Meshes c) Equivalent Plastic Strain for the Different Meshes.	114
Figure 5.19. 4mm Notched Bar (T3) Force Displacement Curves a) AISI 304L, b) CA6NM, c) AISI 304L Elastic Region.....	115
Figure 5.20. Fracatograph for a Range of Tensile Specimens.	117

LIST OF FIGURES

Figure 5.21. Experimental Test Set-Up for Plate with Hole (PH) Specimen.	118
Figure 5.22. Plate with Hole (PH) Specimen DIC Contour for True Tangential Strain Y a) AISI 304L, b) CA6NM.....	119
Figure 5.23. a) Loading and Boundary Conditions of Plate with Hole (PH) b) FE Plastic Equivalent Strain Contour Example c) Mesh density of FE model.....	120
Figure 5.24. Plate with Hole (PH) Force Displacement Curves a) AISI 304L, b) CA6NM.	120
Figure 5.25. Experimental Test Set-Up for Shear and Tension (ST) Specimen.....	121
Figure 5.26. Shear and Tension (ST) Specimen DIC Contour for True Tangential Strain Y a) AISI 304L, b) CA6NM.	122
Figure 5.27. a) Loading and Boundary Conditions of Shear and Tension (ST), b) Mesh Density for the Failure Region.	123
Figure 5.28. Shear and Tension (ST) Specimen Force Displacement Curves a) AISI 304L, b) CA6NM.....	123
Figure 5.29. Experimental DIC Set Up for Butterfly Specimens.	124
Figure 5.30. AISI 304L Butterfly Specimen DIC Contours for True Tangential Strain Y. ..	125
Figure 5.31. CA6NM Butterfly Specimen DIC Contours for True Tangential Strain Y.....	126
Figure 5.32. Loading and Boundary Conditions of Butterfly Specimen (BU0/45/90).....	127
Figure 5.33. Butterfly Specimen BU90 Force Displacement Curves a) AISI 304L, b) CA6NM.	127
Figure 5.34. Plastic Equivalent Strain Contours showing Critical Locations.....	128
Figure 5.35. An example showing how the equivalent fracture strain, average stress triaxiality and the average Lode angle parameter is obtained a) Contour plot of the displacement for AISI 304L T3 at failure, b) Graph showing how the data was extracted.	129
Figure 5.36. AISI 304L Plate with Hole at Failure.....	130
Figure 5.37. AISI 304L PH a) FE Contour Y-True Strain b) DIC Contour Y-True Strain... ..	131
Figure 5.38. Fracture Loci for High and Low Stress Triaxiality Region and Lode Angle Parameter as a function of Stress Triaxiality for both AISI 304L and CA6NM.	132
Figure 5.39. Evolution of Stress Triaxiality for Tensile Tests, a) Results from AISI 304L b) Results from AL2024-T35, adopted from Bao and Wierzbicki [12].	133
Figure 5.40. The Onset of Failure for AISI 304L BU90 a) FE Equivalent Plastic Strain Contour b) DIC Image c) FE Lode angle Parameter Contour d) FE Stress Triaxiality Parameter Contour.	134
Figure 5.41. The Onset of Failure for AISI 304L BU90 FE Equivalent Plastic Strain Contour, a) Fine Mesh used in Study b) Coarser Mesh.	135

LIST OF FIGURES

Figure 5.42. Plastic Equivalent Strain Contour of CA6NM ST, showing the Range of Locations Depending on the Fracture Locus.	137
Figure 5.43. Method 2 - Fracture Loci for High and Low Stress Triaxiality Region and Lode angle Parameter as a function of Stress Triaxiality for both AISI 304L and CA6NM.....	138
Figure 5.44. An Example using an FE Model for AISI 304L BU0 to Show the Spatial Averaging Method.	140
Figure 5.45. Flow Chart Showing the Process of Accounting for the Element Volume for Axisymmetric Models.....	141
Figure 5.46. Method 3 - Fracture Loci for High and Low Stress Triaxiality and Lode angle Parameter as a function of Stress Triaxiality for both AISI 304L and CA6NM.	142
Figure 5.47. Fracture Loci for Various Methods for High and Low Stress Triaxiality for CA6NM.....	144
Figure 5.48. Fracture Loci for Various Methods for High and Low Stress Triaxiality for AISI 304L.	145
Figure 5.49. Negative Stress Triaxiality Specimens.....	148
Figure 5.50. Notched Compression Specimen Experimental Set Up.	149
Figure 5.51. Loading and Boundary Conditions for Compression Specimens.....	150
Figure 5.52. Comparison of Force Displacement Curves for a Range of Coefficient of Friction.	151
Figure 5.53. Accumulation of Paint on a Compression Specimen.	152
Figure 5.54. Deformed Compression Specimens at Various Loads Compared to an Undeformed Specimen.....	152
Figure 5.55. A Range of Options in Order to Observe the Centre of the Specimen.....	152
Figure 5.56. a) 480KN Compression Specimen b) 500KN Compression Specimen c) Magnification 20x - 500KN Right Side.....	153
Figure 5.57. CA6NM NC1 No failure Observed a) Left Side b) Right Side.....	154
Figure 5.58. a) AISI 304L NC3 b) CA6NM NC3 Compression Specimen.	154
Figure 5.59. CN2 Compression Specimen Force Displacement Curves a) AISI 304L, b) CA6NM.....	155
Figure 5.60. Plastic Equivalent Strain Contour of CA6NM NC3, showing the Range of Locations.....	156
Figure 5.61. AISI 304L NC3 at Failure a) FE Model Displacement Contour b) DIC Displacement Contour c) Deformed Specimen.	157

LIST OF FIGURES

Figure 5.62. Evolution of Stress Triaxiality and Lode Angle Parameter showing the Range of Locations for CA6NM NC3.....	158
Figure 5.63. Plastic Equivalent Strain Contours for Compression Specimens showing Critical Locations.....	160
Figure 5.64. Fracture Loci for Negative Stress Triaxiality Region and Lode angle Parameter as a Function of Stress Triaxiality.....	161

List of Tables

Table 1.1. A Range of Package Types with their Relative Materials to Transport [4][5]	1
Table 2.1. Summary of Definitions of Lode angle [101].....	33
Table 2.2. Summary of Critical Locations used from Various Researchers.....	37
Table 3.1. Summary of Various Correlation Criterion [148][149][146].	59
Table 3.2. Camera Specification –VCXU- 50M.....	64
Table 3.3. A Range of Speckle Patterns.	73
Table 3.4. Range of Lighting Conditions.....	76
Table 4.1 Phases of Testing Programme.....	86
Table 5.1 Chemical Composition of AISI 304L and CA6NM.	99
Table 5.2. Failure Strains using a Range Gauge Parameters.	103
Table 5.3. Failure Measurement Comparisons.	106
Table 5.4. Material Properties used in the Simulation for CA6NM and AISI 304L.	109
Table 5.5. Tabulated data for AISI 304L and CA6NM for Equivalent Fracture Strain, Stress Triaxiality and the Lode Angle Parameter.....	133
Table 5.6. Method 2 - Tabulated data for AISI 304L and CA6NM for Equivalent Fracture Strain, Stress Triaxiality and the Lode Angle Parameter.....	139
Table 5.7. Method 3 - Tabulated data for AISI 304L and CA6NM for Equivalent Fracture Strain, Stress Triaxiality and the Lode Angle Parameter.....	143
Table 5.8. Analytical Expressions for Various Methods for AISI 304L and CA6NM.	146
Table 5.9. Compression Specimens Characterisation of Failure	154

1 Introduction

1.1 Background

Nuclear energy was discovered when scientists started exploring the nature of the atom. Currently, nuclear energy provides approximately 10% of the world's electricity from around 450 power reactors [1]. Nuclear power generation does not directly produce CO₂ or pollution to contribute to climate change, however, if fossil fuels are used for the mining and refining of uranium ores or during construction of the nuclear power plant, then there is an associated carbon footprint. The main environmental concern related to nuclear power is radioactive waste [2]. Radioactive waste is defined by the International Atomic Energy Agency (also known as the IAEA) as “*any material that contains or is contaminated by radionuclides at concentrations, or radioactivity levels greater than the exempted quantities established by the competent authorities and for which no use is foreseen*” [3].

Transport of radioactive material can be required for many reasons including, transport of new fuel to reactor sites and the transport of irradiated material from the reactor to the reprocessing plant. Due to this, nuclear transport packages must facilitate the range of transport modes, whilst ensuring they are able to withstand and respond to any serious accidents as well as preventing any radiation leaks [1]. Types of nuclear packages vary depending on the radioactive capacity and material transport requirements as shown in Table 1.1.

Table 1.1. A Range of Package Types with their Relative Materials to Transport [4][5]

Package Type	Radioactive designed capacity	Materials to Transport
Exempted package	Small quantities of radioactive material	Radiopharmaceuticals
Industrial package	Low specific activity (LSA) materials	Low-level radioactive wastes and uranium ore
Type A package	Limited radioactivity	Fresh nuclear fuel and uranium hexafluoride
Type B package	Larger amounts of radioactive material	Spent fuel, high-level waste, and mixed oxide fuel
Type C package	Radioactive material beyond a definite threshold	Mixed oxide and fuel plutonium

For different types of packages there are a range of rigorous post design safety tests, which must be passed to demonstrate its ability to withstand normal and accidental conditions. Testing standards are regulated by the IAEA before nuclear transport packages can be licenced for use [1][2]. The IAEA establish requirements, that must be satisfied to ensure safety and to protect people, property, and the environment from harmful effects of ionising radiation during the transport of radioactive material globally and set the standards across international borders [4]. Based upon the standards developed by the IAEA, the office for nuclear regulation (ONR) regulates safety and security during transport of radioactive material across the UK [6].

For example, for a type B package, the tests for demonstrating ability to withstand accident conditions of transport are composed of mechanical, thermal and water immersion tests. The mechanical tests typically consist of three different drop tests, for the first test a package is dropped onto a target (as shown in Figure 1.1a). During the second drop the specimen falls onto a bar rigidly mounted perpendicularly on the target (as shown in Figure 1.1b). Lastly, the package is subjected to a dynamic crush test by dropping a 500kg mass from 9m onto the package. This is then followed by thermal tests, which expose the package to a thermal environment of minimum average flame emissivity coefficient of 0.9, and an average temperature of at least 800°C. This is to ensure the package is fully engulfed, providing a heat flux simulating a hydrocarbon fuel–air fire. Finally, the package is immersed under a head of water of at least 15m for a period of time. The packages are assessed on their ability to withstand the cumulative effects of the series of tests discussed for maximum damage [4].

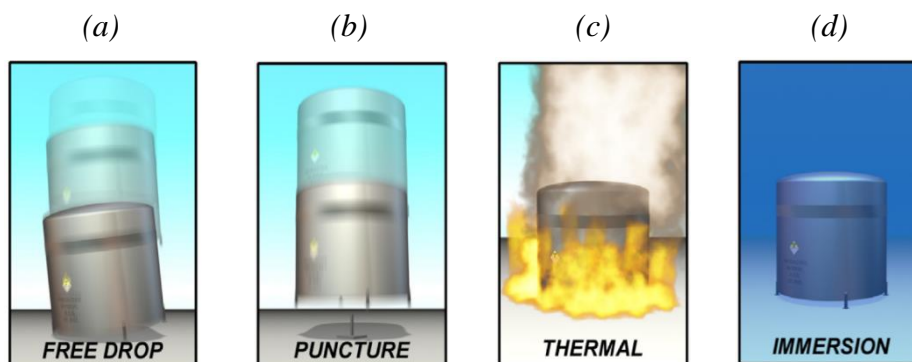


Figure 1.1. Example of Tests for Type B Packages, after U.S. Department of Energy [7].

Breach of the outer shielding during the series of drop tests may lead to the failure of the package during the thermal tests, by offering a route for oxygen ingress, encouraging the prolonged and undesirable burning of internal materials such as wood. AISI 304L is a ductile material, meaning that it has the ability to deform and absorb energy, which makes it an optimal material to use for impact of a nuclear transport package. Current nuclear transport packages use AISI 304L stainless steel depending on the type of package for the internal and external shock absorbers, as well as being used for thin-walled transport packages. CA6NM is a cast martensitic stainless steel, which has wide applications in which mechanical behaviour, corrosion and erosion resistance are of significance. CA6NM is used for large castings but has not been used to produce nuclear transport packages. An investigation into CA6NM [8] found it to be capable of satisfying the IAEA brittle fracture criterion and that the material was low cost compared to forged materials. CA6NM provides the essential mechanical properties for thick wall castings for nuclear transport packages [9], however, there is limited data on ductile failure in complex stress-states.

For example, a large waste transport container (LWTC) design concept [10] which was developed by Nuclear Transport Solutions (NTS) is shown in Figure 1.2. The upstand material for the top loading was AISI 304L. Whereas, CA6NM was chosen for the body/lid material [11].

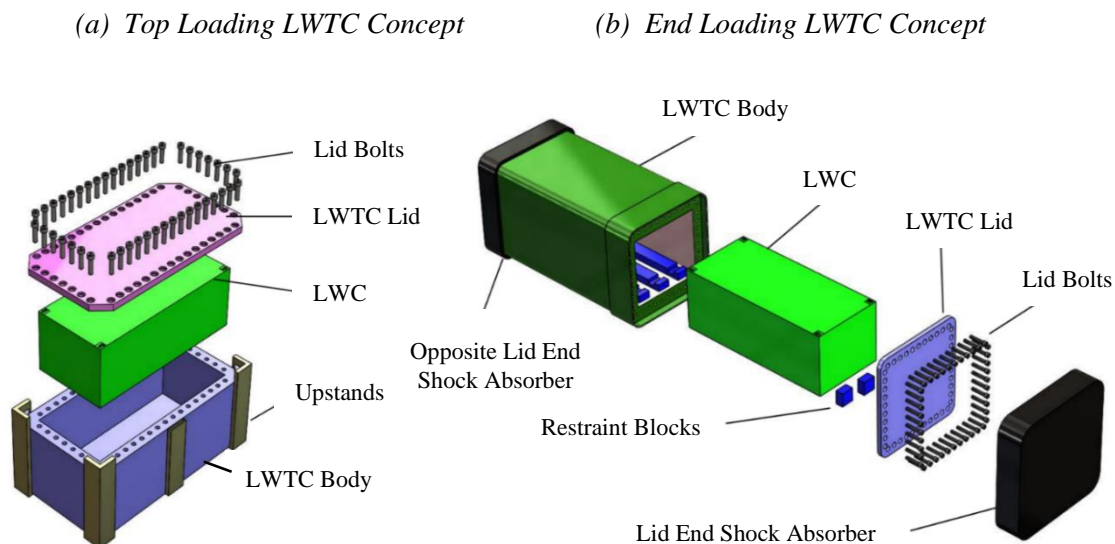


Figure 1.2. LWTC Concept, after S.Porter et al. [10].

This PhD investigates two materials, stainless steel AISI 304L and CA6NM. To further understand the capacity of energy absorption of the materials is of importance with regard to

package design in the case of impact. Data characterising failure of a material is necessary to satisfy structural failure design criteria. Failure of a material depends on factors such as loading conditions (tension, compression, and shear), temperature, strain rate and ductility of the material.

Ductility of the material is critical, as in accidental conditions during impact, the material must absorb enough energy to avoid failure. Stress triaxiality is one of the most important factors that defines stress state and controls the initiation of ductile fracture, however, it does not always accurately predict ductile fracture for specimens with complicated geometry and loading conditions [12]. Alongside stress triaxiality, Lode angle parameter can be used to give a complete description of the stress state of a material [13][14]. One of the methods associated with analysing the overall ductility of materials in terms of fracture strain, is to develop a fracture locus of the material [15]. The data produced by a fracture locus can be utilised to predict safety thresholds for the design of nuclear transport packages subjected to various loadings. Strain rate is the change in strain of a material with respect to time, it is an important parameter during experimental testing. Mechanical properties of metals can be directly affected by the speed of the test, and are thus strain rate sensitive [16]. For scenarios such as crash events, strain rate can be used to describe a materials response with different impact applications. This can be split into two types of testing: quasi-static and impact testing. Quasi-static tests are defined when loads are applied at slow rates (up to 10^{-1} s^{-1}), at which inertial effects are assumed as negligible. Whereas, impact testing can be used for a large range of applications in which a material is subjected to accidental drops, collisions and shock loading [17]. Many researchers [17][18][19][20] have investigated how materials are effected by a range of strain rates, using both quasi-static and impact testing to characterise strain rate sensitive materials. Jin et al. [17] investigated the mechanical characterisation of AISI 304L when subjected to a range of strain rates from 10^{-3} to 2580 s^{-1} , the study found when observing the tensile stress-strain response the AISI 304L exhibits strain rate dependence. In 1993, Ove Arup and Partners [21] performed a feasibility study to provide information regarding the mechanical properties of CA6NM, by conducting a series of dynamic tensile tests. The tests were carried out in three regimes, for both room temperature and -40° :

1. Quasi-static rates - up to 10^{-1} s^{-1}
2. Intermediate rates - 10^{-1} to 10^3 s^{-1}
3. Impact rates - above 10^3 s^{-1}

The study found CA6NM became harder with the increase in strain rate. The highest rate sensitivity was shown by the yield stress, which increased from 600-800 MPa as the strain rate increased from 10^{-2} to 10^3 s^{-1} . This occurred for all tensile tests performed at room temperature and at -40° . The stress-strain curves, as shown in Figure 1.3, steadily increased at strain rates up to 100 s^{-1} . At higher strain rates, CA6NM began to display a transition from a smooth stress-strain curve to an “upper/lower yield” stress type of curve. Limitations of testing equipment for this project, mean that the research presented in this thesis is solely focused on quasi-static testing.

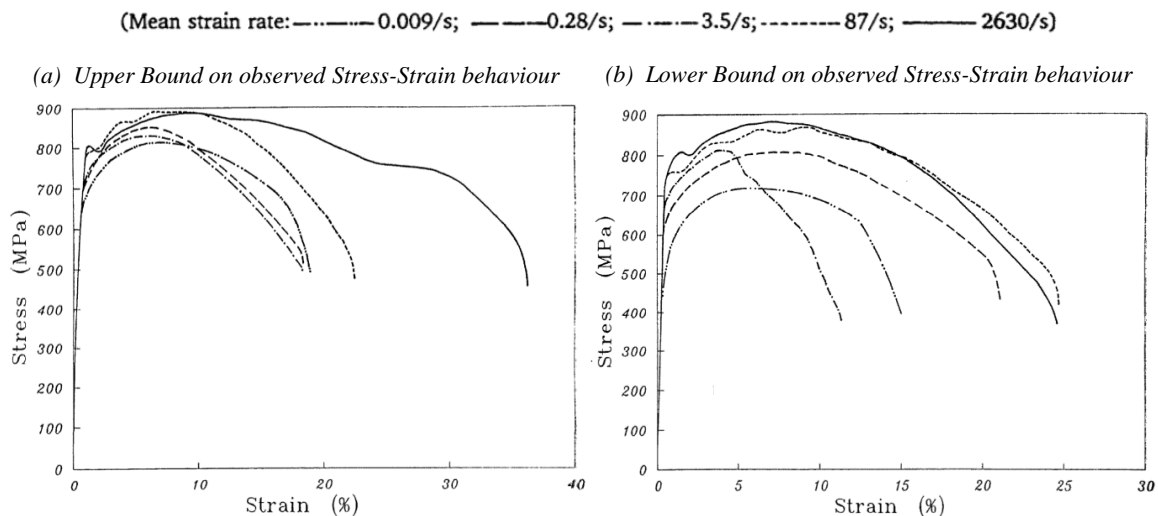


Figure 1.3. CA6NM Stress-Strain Curves for Various Strain Rates at Room Temperature, after Ove Arup & Partners [21].

Finite element (FE) models are utilised for demonstrating the performance of nuclear transport packages. Current FE models accurately reproduce elastic material response and also calculate the materials behaviour in the plastic regime up to the ultimate tensile strength (UTS). The UTS is the maximum stress that a material can withstand while being stretched or pulled before failing or breaking. Standard tensile testing of a material, to produce an elastic-plastic material model (typically used in industry) is insufficient to predict the stress-strain response beyond UTS. Therefore, the accuracy of the multi-axial plasticity response beyond UTS is unknown. Digital image correlation (also known as DIC) is the application of non-intrusive, non-contact methods which can be used to evaluate displacements and strains across a range of materials. Traditional methods of strain measurement cannot be employed because they provide average values, rather than the fracture process zone values necessary, for accurate prediction of failure using FE techniques. This project uses both DIC and FE analysis in parallel as a direct and efficient approach for identifying material parameters during testing.

1.2 Project Aim

The aim of the thesis is to characterise the plasticity and fracture behaviour of two grades of stainless steel, AISI 304L and CA6NM. The outcome is the construction of a fracture locus with regard to stress triaxiality and Lode angle parameter space beyond UTS, at ambient temperature under quasi-static conditions. Analysing and assessing the fracture behaviour of these materials for a range of multiaxial loading conditions contributes material data, aiding the design of nuclear transport packages.

1.3 Project Objectives

1. Investigate literature regarding the materials AISI 304L, CA6NM and ductile fracture.
2. Develop test methodology and a multiaxial loading design program of specimens, which produces different stress triaxialities.
3. Carry out experimental tests of the AISI 304L and CA6NM until failure, whilst using DIC and FE analysis in parallel.
4. Evaluate experimental data and FE analysis to construct a fracture locus for both materials. Proposing safety failure limits for various loading conditions.

1.4 Structure of Thesis

The thesis consists of six chapters. In **Chapter 1**, the motivation for the thesis is introduced and the aim and objectives required are presented.

The background and literature review are included in **Chapter 2**. Material properties of CA6NM and AISI 304L are discussed and fracture behaviour of ductile materials are reviewed. A methodical summary of ductile fracture history highlights the basis of ductile fracture, which is a product of researchers such as Bridgman, McClintock, Rice and Tracey. These researchers introduced a simple exponential expression for the evolution of the equivalent strain with stress triaxiality which is the basis of what is presently known as a fracture locus. Fracture loci are of importance, as they show the overall ductility of a material during multiaxial loading conditions in terms of fracture strain. This chapter provides a fracture locus constructed from various materials and geometries from previous researchers.

DIC is used alongside experiments to obtain accurate strain data throughout testing until failure. The core principles and processes of DIC are reviewed in **Chapter 3**, including the standard of preliminary requirements to achieve the optimum experimental set up, by investigating parameters such as equipment selection and what makes a suitable speckle surface. Potential DIC errors are evaluated and summarised.

The fracture locus constructed in **Chapter 2**, provided indications of which geometries were necessary to provide a data point in the desired region, this led to the final designs for the 15 specimens. The experimental procedure is given in **Chapter 4**. The methodology between using both FE analysis and DIC to produce a fracture locus is detailed, followed by the thesis experimental testing programme. The process of obtaining material data for both AISI 304L and CA6NM was developed, which provided the material data for all FE analysis. Anisotropy of AISI 304L was investigated. Experiments were performed for different geometries under a variation of stress states. Various fracture loci were constructed at the moment of failure but using the different methods for extracting the data. From this a strain-based criterion for AISI 304L and CA6NM was produced.

Finally, in **Chapter 5** the thesis main results are discussed and recommendations for future study are given.

2 Background and Literature Review

2.1 Introduction

This chapter is divided into four main sections. Firstly, the material properties of CA6NM and AISI 304L were reviewed. Concepts of ductile fracture, including ductile fracture history are presented and a summary of stress states of a material is provided. Lastly, fracture loci were investigated and a fracture locus of various geometries from previous researchers were constructed. This fracture locus provides indications on the geometries necessary to obtain data for each region of a fracture locus.

2.2 Aims and Objectives

- Review material properties of CA6NM and AISI 304L, to further understand how these materials can be used with regard to nuclear transport packages.
- Provide detailed literature review on ductile fracture and its history.
- Discuss the fundamentals of the stress state, regarding stress triaxiality and Lode angle parameter.
- Review and discuss what is a fracture locus and the fracture experiments required for each region.

2.3 Material Properties

Stainless steels are alloys of iron and carbon containing more than 10.5% chromium. Classification of stainless steels varies with the chemical composition, it is typically divided down into five main categories: austenitic, ferritic, martensitic, duplex and precipitation hardening [22]. Stainless steels are ideal materials for the manufacture regarding the outer layer of nuclear transport packages, due to their combination of strength and long-term integrity. During the design phase, the durability, thermal and mechanical characteristics needed to be considered when determining the materials for the manufacture of nuclear transport packages. As well as the materials suitability for the necessary fabrication or manufacturing [23].

Current nuclear transport packages use AISI 304L stainless steel depending on the type of package for the internal and external shock absorbers, as well as being used for thin-walled transport packages. CA6NM is used for large castings but has not been used to produce nuclear transport packages. An investigation into CA6NM [8] found it to be capable of satisfying the IAEA brittle fracture criterion and that the material was low cost compared to forged materials. CA6NM provides the essential mechanical properties for thick wall castings for nuclear transport packages [9], however, there is limited data on ductile failure in complex stress-states.

2.3.1 *Austenitic Stainless Steel 304L*

AISI 304L is an austenitic stainless steel which is used throughout engineering applications due to its material properties [21][22]. AISI 304L is a ductile material, meaning that it has the ability to deform, which may lead to fracture depending on the applied force [26]. Nuclear transport packages, use AISI 304L due to its capacity to accept large amount of deformation without fracture, making the material ideal to withstand and respond to any serious accidents.

The material AISI 304L is versatile, has high strength, good welding and forming characteristics as well as a lower carbon content. AISI 304L has a lower carbon amount compared to AISI 304 [27]. Carbon is normally considered as an undesirable impurity in most austenitic steels, although it stabilises the austenitic structure, a lower carbon content minimises any harmful carbide precipitation due to welding [28]. Intergranular corrosion is a key issue when welding austenitic stainless steels. Carbides reduce the chromium concentration in the austenite adjacent to the grain boundaries, generating the conditions for intergranular corrosion.

Carbide precipitation forms more rapidly in steels with higher carbon concentrations. Thus, the lower carbon content allows for the AISI 304L to be able to sustain severe corrosion environments [29][30].

2.3.2 *Martensitic stainless steel CA6NM*

The initial experiments on CA6NM started in 1959. The development of CA6NM took George Fisher steel foundry approximately 5 years, after the materials strength/impact behaviour was accidentally discovered [31].

CA6NM is a cast martensitic stainless steel. This particular material has wide applications in which mechanical behaviour, corrosion and erosion resistance are of significance. Such as, structures which are submerged in water like hydro turbine runners and ship blades [32][33]. The formation of martensite includes quenching austenite in steel to room temperature, to avoid the formation of pro-eutectoid ferrite, pearlite, and bainite [31]. This process is referred to as a diffusionless, shear transformation as deformation causes a change in the shape, consisting of a large shear and a volume expansion [34]. CA6NM has a combination of advantageous material characteristics, such as strength, ductility and hardness improved weldability and corrosion resistance as discussed in existing literature [35][36][31].

Temperature conditions can alter ductile material's behaviour, as part of meeting the IAEA regulations, the materials used must be able to absorb impact when subject to range of temperatures. Nuclear Transport Solutions (NTS) have performed a range of tensile testing for the material CA6NM, at a range of temperatures in order to obtain mechanical property data, as shown in Figure 2.1. When the temperature of ductile material is reduced, so is its ability to absorb energy. The stress-strain curves in Figure 2.1 show the tensile tests performed at -40°, had the highest ultimate tensile strength (UTS).

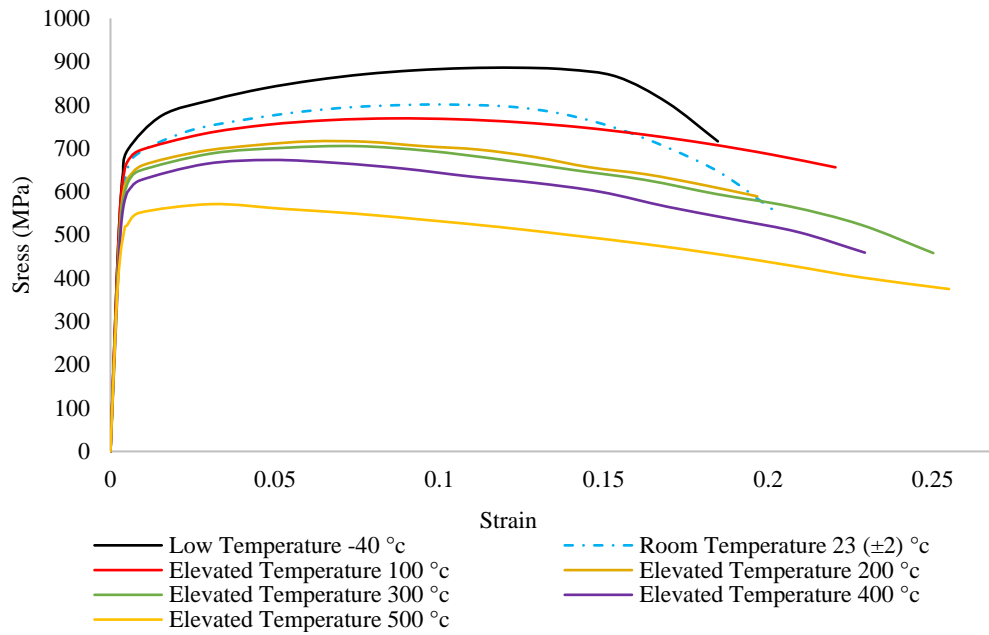


Figure 2.1. CA6NM Stress–Strain Curves for a Range of Temperatures, Data Provided By Lucideon [37].

2.4 Ductile Fracture

Fracture is caused by disconnection of atomic or molecular bonds, and is defined as the separation of a material into two or more parts [38], it is dependent on parameters such as stress state, the rate of application of stress and temperature. Fracture of material can be characterised by ductile fracture and brittle fracture. Brittle materials such as concrete and ceramics, fail after very small or without any plastic deformation. Whereas, failure of ductile materials such as aluminium, copper and steel will typically only occur after large plastic deformation [39].

As nuclear transport packages must be able to withstand normal and accidental conditions, it is critical that the materials typically used are ductile. Ductility is the capacity of a material to deform, which may lead to fracture depending on the applied force. Energy absorption is a valuable characteristic of ductile materials, and fracture ductility means these materials have good formability [26]. Ductile fracture takes place in a material after plastic deformation, it is typically composed of three mechanisms involving nucleation, growth and coalescence of voids until final fracture [40]. Ductile fracture has a significant role in engineering disciplines

due to the optimisation of technological processes in safety evaluations. Thus, the realistic modelling of inelastic behaviour and failure processes of ductile metals is critical [41].

Uniaxial tensile tests are used to determine a materials characteristics by observing the materials response when subjected to a load. This is divided into elastic and plastic regions, as shown in Figure 2.2.

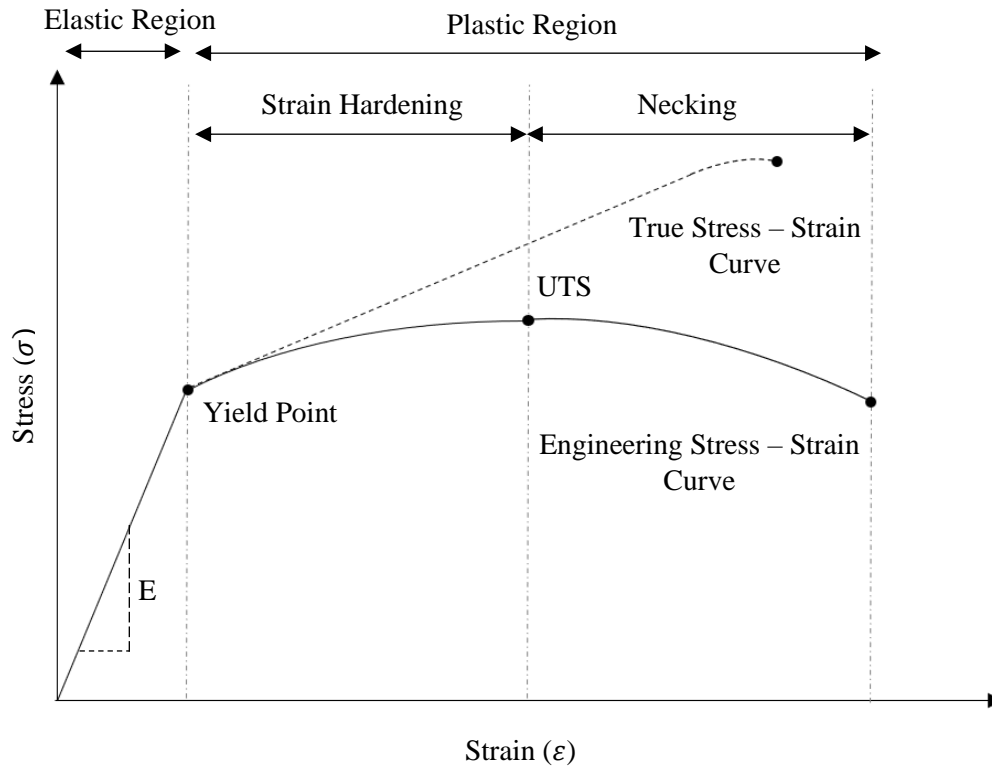


Figure 2.2. Typical Stress-Strain Curve for a Ductile Material.

A material yield point indicates the limit of the elastic region and the start of the plastic region. When the material response is within the elastic region and has not surpassed the material yield point, if the load is removed the material reverts to its original shape without permanent deformation.

Within the linear elasticity regime, Hooke's law states that the stress is proportional to the strain. This is represented by Young's Modulus, which is a property used to describe the stiffness or elasticity of a material. Young's Modulus is defined as the ratio of stress to strain in the material (as shown in Equation 1).

$$\sigma = E\varepsilon \rightarrow E = \frac{\sigma}{\varepsilon} \quad (1)$$

When a material is subjected to load and surpasses its yield point, strain hardening (also known as work hardening) takes place, during this stage the material plastically deforms up to its UTS. Ultimately, the specimen will then start necking until fracture occurs [42].

A general engineering stress-strain curve (also known as nominal stress-strain curve) for a ductile material is shown in Figure 2.2. Engineering strain ε_e is defined as the change in the gauge length Δl , relative to the initial gauge length l_0 , as shown by Equation 2.

$$\varepsilon_e = \frac{l - l_0}{l_0} = \frac{\Delta l}{l_0} \quad (2)$$

Engineering stress σ_e is defined as the force F divided by the initial cross-sectional area A_0 as described by Equation 3.

$$\sigma_e = \frac{F}{A_0} \quad (3)$$

True stress-strain curves can be used as a direct measure of a materials response in the plastic region. True strain ε_t can be calculated using Equation 4,

$$\varepsilon_t = \int_{l_0}^l \frac{\Delta l}{l} = \ln\left(\frac{l}{l_0}\right) = \ln(1 + \varepsilon_e) \quad (4)$$

where Δl is the change in length and l is the instantaneous length. True stress σ_t is related to engineering stress, assuming material volume conservation. True stress is found by dividing the force F by the current cross-sectional area A , as shown by Equation 5.

$$\sigma_t = \frac{F}{A} = \sigma_e(1 + \varepsilon_e) \quad (5)$$

Generally, Equations 4 and 5 can be used to derive the true stress-strain curve from the engineering curve, up to UTS when necking of the specimen begins. Beyond the necking region, strain is non-uniform along the gauge length.

2.4.1 *Microscopic Analysis of Ductile Fracture*

Microstructural aspects of ductile fracture are of importance as only on a microscopic scale can the characteristics of ductile deformation and fracture behaviour be understood. Length scales for processes and materials are generally classified as nanoscale (< 100 nm), microscale (100 nm to 100 μm) and mesoscale (> 100 μm) [43].

Voids are present in all engineered and natural materials; the void volume is described as the absence of material. Voids have broad functionalities to the materials containing them [44]. However, the voids found in ductile metals such as AISI 304L and CA6NM and are not advantageous. Internal voids may be found after casting depending on the metal forming process, there are many studies that focus on modelling the closure of these metallurgical defects, this has been studied for a range of aspects such as; hot metal forming [45], theoretical and laboratory modelling [46] and studying void closure during plastic deformation [47]. Voids coalescence consists of the transition from a plastic deformation to the stable growth of small internal voids, it's the most common fracture initiation mechanism in ductile materials [48].

2.4.1.1 *Stages of the Fracture Process*

Ductile fracture takes place in a material after plastic deformation, it is typically composed of three mechanisms involving nucleation, growth and coalescence of voids until final fracture (as shown in Figure 2.3) [40].

The process starts at Stage A, where voids initiate at the materials inclusions, which are often small undissolved carbides [49][50]. During Stage B, void nucleation starts as the material is subjected to tensile loading conditions. At stage B-C, the material starts to plastically deform in which primary voids (also known as existing voids) evolve and new voids nucleate. Coalescence occurs by elongation of the voids and the bridges of material between the voids [38]. This then leads to the formation of a primary band of localisation at the mesoscale, as there is an increase in porosity and a reduction in macroscopic strain hardening. During Stage D, the material within this primary band of localisation undergoes accelerated void growth and nucleation. Due to the fact the porosity and the number of voids has rapidly increased, the mechanical fields around existing voids start to interact. Once the deformation begins to localise in Stage E, the secondary bands of localisation at the microscale are produced and the final coalescence phase sets in. For the final Stage F, the primary void coalescence leads to the

decohesion of voids, thus the formation of cracks through internal necking or void sheet fracture until final failure of the material [51][52].

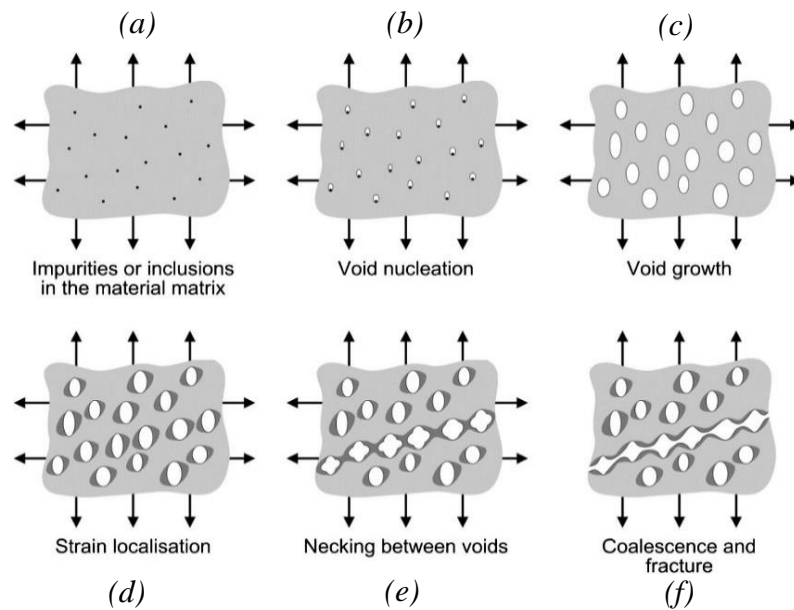


Figure 2.3. Schematic of Nucleation, Growth, and Coalescence of Voids in Ductile Metals, adopted from Gatea et al. [50].

However, most literature of ductile failure is based upon tensile loading conditions, as the voids become elongated whilst being pulled apart. There is limited information on the ductile fracture of a material when subjected to compression loading. The majority of failure criteria proposed for ductile fracture in metals is constructed upon the growth of void volume. In which the void volume increases relative to the tensile hydrostatic stress applied [53]. When ductile metals are subjected to compression the opposite deformation processes may occur, initiating closure of strain-induced defects under large hydrostatic pressure [54].

Understanding void nucleation and growth under dynamic loading is fundamental to understand damage initiation and evolution in ductile metals. This knowledge is incorporated into failure criteria which are theoretical approaches, which alone are limited use to design analysts, however, with the combination of experimental techniques and simulation methods developed this information on based on void nucleation and growth theories can be used practically.

2.4.2 Ductile Fracture – A Historical Perspective

The concept of uncoupled models was introduced by Freudenthal [55] in 1950. Freudenthal proposed a total plastic criterion using uncoupled fracture indicators to predict ductile fracture. Uncoupled models estimate the fracture initiation by using the damage parameter D , however the damage parameter does not feed back into the elastic-plastic behaviour of the material [56].

In 1952, Bridgman [57] was the first to assess the stress distribution for necking in round bar specimens with different notches. Bridgman composed a book of experimental data for over 20 different steels, recording over 350 tests. The findings concluded that fracture ductility is dependent on hydrostatic pressure. From this Bridgman derived a dimensionless parameter known as stress triaxiality as shown in Equation 6, this formula characterises stress triaxiality for this type of geometry. The equation physically describes the fracture initiation site when observing the middle of the necked cross-section shown on Figure 2.4. The local radius of the curvature of the neck for the specimen is R , and the radius of the necking cross-section is a . Equivalent strain at the fracture initiation site can be determined using Equation 7, where a_o is the original radius and a_f is the fracture radius.

$$\eta = \frac{1}{3} + \ln\left(1 + \frac{a}{1R}\right) \quad (6)$$

$$\bar{\epsilon}_f = 2\ln\left(\frac{a_o}{a_f}\right) \quad (7)$$

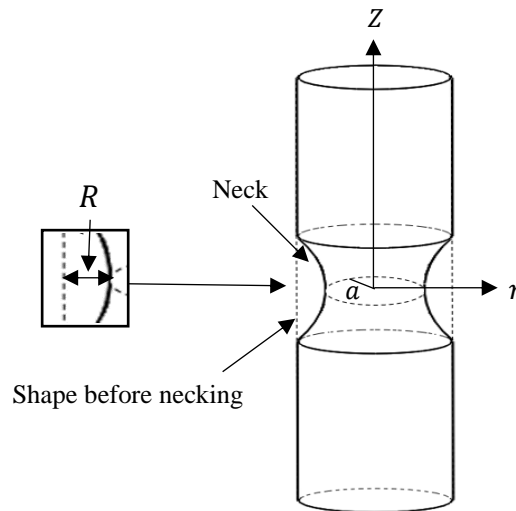


Figure 2.4. Bridgman's Diagram of Necking in a Round Bar Specimen, adaptation from Bai [58].

Following the work of Freudenthal, many other criteria were founded, such as Datsko's criterion [59] in 1966, which is based on equivalent plastic strain. A study conducted in 1968

by McClintock [60] found that ductile fracture of metals, is strongly dependent of hydrostatic stress when studying growth of long cylindrical voids (as shown in Figure 2.5a). McClintock [60] failure theory analysis was developed for the expansion of a long circular cylindrical cavity in a non-hardening material, pulled in the direction of its axis while subjected to transverse tensile stresses. From this research McClintock developed a criterion for ductile fracture by the growth of cylindrical holes. In 1969, Rice and Tracey [61] primarily focused on spherical voids (as shown in Figure 2.5b), it was concluded with the finding of the long cylindrical voids from McClintock, that the growth rates are dependent on hydrostatic stress and exponentially proportional to stress triaxiality.

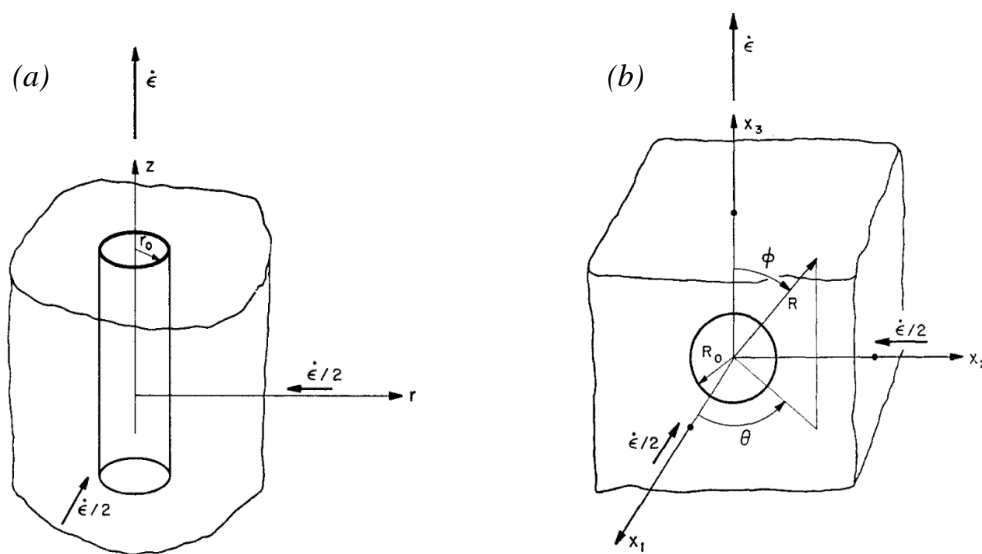


Figure 2.5. a) Long Cylindrical Void Extended in the Direction of its axis, b) Spherical Void in a Remote Simple Tension Strain Rate Field, adopted from Rice and Tracey [61].

Researchers Hancock and Mackenzie [62] conducted a series of tensile tests on pre-notched round tensile steel specimens in 1975. Hancock and Mackenzie, focused on the mechanisms of ductile failure in high strength steels, subjected to multi-axial stress states. Metallographic studies were used to compare the size, shape and orientation of the voids which caused failure initiation. They established ductility of high strength steels are dependent on stress triaxiality, which aligns with McClintock's model of ductile failure.

Following the approach of Rice and Tracey, in 1977 Gurson created a model using spherical voids, and based the void growth mechanics on axisymmetric stress states for the derivation of yield function. However, Gurson's original model only considers the growth of pre-existing

voids, without assuming any propagative mechanisms. Research by Tvergaard and Needleman suggested mathematical descriptions of the void nucleation and coalescence to overcome this limitation as discussed in existing literature [63][35],[36]. This then led to the Gurson–Tvergaard–Needleman (GTN) damage model as the final modified model [66]. In the GTN model, only the void nucleation and void growth are simulated and is assumed that coalescence occurs when a critical void volume fraction has been reached. The GTN model is a useful tool in analysing the formability of anisotropic sheet metals, as discussed by Kami et al [66].

In 1980, Wilkens et al. [67] used a cumulative stain damage criterion to predict the initiation and propagation of fracture in ductile materials. The model was applied to a 2D and 3D FE model in which the phenomena of void growth and coalescence was applied. The cumulative stain damage criterion assumes, fracture is the product of the strain damage history to the material. This criterion follows McClintock’s theory of damage history as strain damage is presumed to be affected by hydrostatic tension and asymmetric strain.

Two criteria of ductile fracture strain were presented by the research conducted by Oyane et al. [68] in 1980. A criterion of fracture for a triaxial state of stress is suggested and then is later modified, as the first equation as shown in Equation 8 assumed that fracture occurs when the volumetric strain reaches a certain value. In order to predict the failure strain more accurately a weighting factor d_0 is used as shown by Equation 9, as Oyane et al. [68] found that stress states at larger strains have a greater effect on fracture. Where, $b_0/c_0/d_0$ are constants, $\bar{\epsilon}_f$ is the equivalent fracture strain and $\bar{\sigma}$ is von Mises equivalent stress. The research concluded that the final criteria initially produced needed further work to include a complete equation of nucleation, growth and coalescence of voids.

$$\int_0^{\bar{\epsilon}_f} \left(1 + \frac{1}{b_0} \frac{\sigma_H}{\bar{\sigma}}\right) d\bar{\epsilon}_f = c_0 \quad (8)$$

$$\int_0^{\bar{\epsilon}_f} \left(1 + \frac{1}{b_0} \frac{\sigma_H}{\bar{\sigma}}\right) \bar{\epsilon}_f^{d_0} d\bar{\epsilon}_f = c_0 \quad (9)$$

Research conducted by Hancock and Brown [69] in 1983 on the effect of strain and stress state in ductile fracture, is shown by the fracture locus in Figure 2.6c. They found that ductility was determined by the stress state, and not the strain state. This was found when comparing

experimental data with the FE analysis of plane strain specimens and notched axisymmetric specimens.

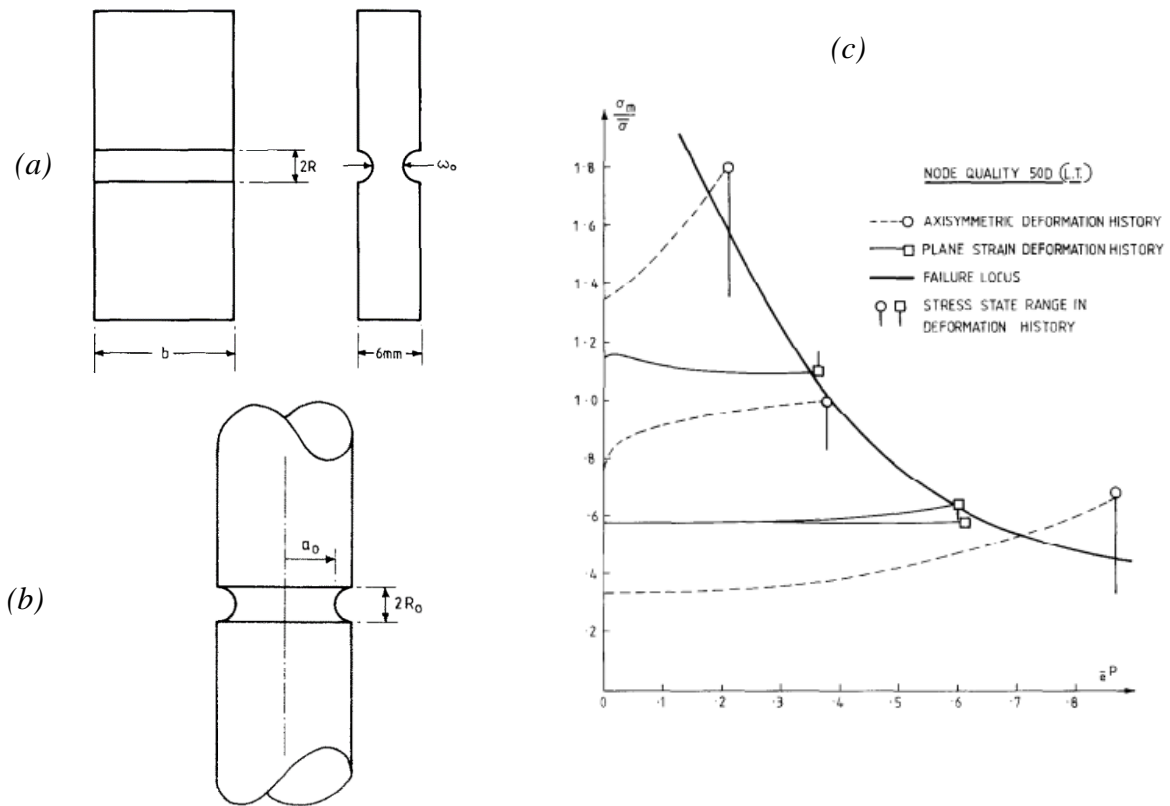


Figure 2.6. a) Plane Strain Specimen b) Axisymmetric Specimen c) Failure Locus for Axisymmetric and Plane Strain Specimens, adopted from Hancock and Brown [69].

In 1985, Johnson and Cook [70] pioneered work in failure mechanics by researching fracture characteristics of a range of materials. Johnson and Cook implemented experiments such as;

- Torsion tests over a range of strain rates
- Hopkinson bar tests over a range of temperatures
- Quasi-static tensile tests with various notch geometries

These tests led to the fracture model known presently as J-C criteria, which expresses the strain to fracture as a function of the strain rate, temperature and pressure. The fracture model is defined for the damage to an element as shown in Equation 10.

$$D = \sum \frac{\Delta\varepsilon}{\bar{\varepsilon}_f} \quad (10)$$

Where $\Delta\varepsilon$ is the increment of equivalent plastic strain which occurs during an integration cycle and $\bar{\varepsilon}_f$ is the equivalent fracture strain, under the conditions of strain rate, temperature, pressure and equivalent stress. Fracture occurs when $D = 1$. The general expression for equivalent fracture strain is shown in Equation 11.

$$\bar{\varepsilon}_f = [D_1 + D_2 e^{D_3 \eta}][1 + D_4 \ln \dot{\varepsilon}][1 + D_5 T] \quad (11)$$

Where the dimensionless strain rate is $\dot{\varepsilon}$ and the homologous temperature is T . The five constants are $D_1 - D_5$, the first set of brackets follows the work presented by Hancock and Mackenzie [62], in which the strain to fracture decreases as the hydrostatic stress σ_H increases. The three constants $D_1 - D_3$, are found when graphing the fracture strain against the hydrostatic stresses, which is then adjusted to correspond to a strain rate of $\dot{\varepsilon} = 1.0$. The strain rate constant, D_4 is obtained from the data of when looking at the effects of strain rate and temperature on the strain to fracture. Finally, the temperature constant, D_5 , is also obtained from the data of effects of strain rate and temperature on the strain to fracture. J-C criteria can accurately predict the flow stress of materials at a certain temperature and a high strain rate, but each parameter in the model is an independent variable, which makes this method have an increased computational complexity, therefore it cannot describe the coupling effects of temperature, strain rate and strain hardening on the flow stress.

Following Bridgman's research stress triaxiality η has since been defined as the ratio between hydrostatic and von Mises Stress $\bar{\sigma}$, as shown in Equation 12.

$$\eta = \frac{\sigma_H}{\bar{\sigma}} = \frac{\sigma_{11} + \sigma_{22} + \sigma_{33}}{3\bar{\sigma}} \quad (12)$$

Continuum damage mechanics (CDM) was introduced in 1958 by Kachanov [71], who investigated the creep of metals. CDM considers various damaging processes in materials and structures at a macroscale continuum level. Kachanov stated that damage can be quantified in many different ways. Kachanov's book; "*Introduction to continuum damage mechanics*" describes damage variables as a surface density of intersections of micro cracks and cavities [72][73]. In 1985, the concept of coupled models was introduced by Lemaitre's continuous damage mechanics (CDM) model [74]. Coupled models depend on a damage variable D for all

material parameters. Lemaitre's CDM model was developed on a thermodynamic and effective stress concept and is well known for including both isotropic hardening and damage.

In 1990 Kao et al. [75] studied the influence of superimposed hydrostatic pressure on tensile fracture of 1045 spheroidized steel. Fractographic features shown that matrix hardening influenced the void nucleation under applied pressure, as the tensile hydrostatic stress from necking is reduced by pressure.

Damage indicator was first implied by Fischer et al. [76], during 1995. The damage indicator was produced to define the onset of fracture. This was derived on the basis of a simplified micromechanical model considering a single pore in a plastic material under a homogeneous load stress field. The results of this study are restricted to regions in a material with low local stress gradients. This theory has been developed and is presently known as the incremental damage accumulation rule as shown in Equation 13, which is used to define the onset of fracture and helps to capture nonlinear strain paths. It is postulated that fracture initiates when $D = 1$,

The function D is a measure of ductility, where $D = 1$ is at the point of fracture [77].

$$D = \int_0^{\bar{\epsilon}} \frac{d\bar{\epsilon}}{\hat{\epsilon}(\eta, \bar{\theta})} \quad (13)$$

The rule shown in Equation 13 assumes for a given increment of the equivalent strain, $d\bar{\epsilon}$ contributes to the damage accumulation, depending on the current value of the normalised function $\hat{\epsilon}$. As fracture initiates when $D = 1$, the corresponding equivalent strain becomes the equivalent fracture strain [77]. The Lode angle parameter is shown in Equation 14, where ζ is the normalized third stress invariant,

$$\bar{\theta} = 1 - \frac{2}{\pi} \arccos \zeta, \quad -1 \leq \bar{\theta} \leq 1 \quad (14)$$

Mirza et al. [78] performed notched tensile tests for materials such as; pure iron, mild steel and aluminium alloy BS1474, over a wide range of strain-rates in 1996. The results confirmed the ductility of all three materials was found to be strongly dependent on the level of stress triaxiality in the specimen.

Fracture mechanics is based upon failure due to the growth of a pre-existing crack, whereas an alternative method is to assume that a solid is initially crack-free. During 2003, Bao [79] conducted experimental, numerical and analytical research with regard to ductile crack formation for uncracked bodies. The effects of specimen size, anisotropy and stress and strain ratios, were investigated. From this it was determined that stress triaxiality and the equivalent strain are the two most important parameters governing ductile crack formation while other parameters were found to be of secondary importance.

Bao's extensive experimental program included developing a fracture locus of A12024-T351, for a range of stress states including tensile, compressive, shear and combined loading conditions. The experimental tests provided the total force-displacement relationship. Parallel numerical simulations were required to determine the individual components of stress and strain tensors and their histories.

Bao discovered that the fracture locus consists of three distinct branches: low, intermediate and high stress triaxialities (as shown in Figure 2.7) and cannot be described by one smooth monotonic function as suggested by researchers [80][70]. Micro mechanism observations validated the presence of the three distinct branches proposed by Bao. Ductile materials in the high stress triaxiality region, displayed the common "void nucleation, growth, and linkage mechanism". However, a different micro mechanism of "shear fracture" was observed in the negative stress triaxiality range. A combination of those two mechanisms occurs in the intermediate stress triaxiality range, which is known as the transition range.

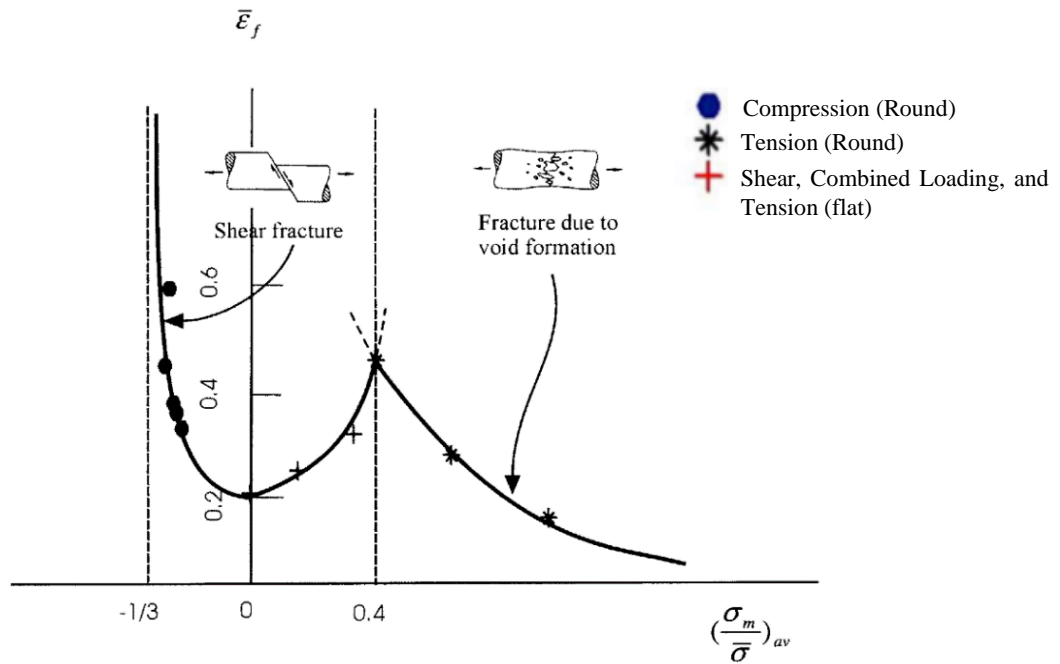


Figure 2.7. Failure Locus Constructed showing Three Distinct Regions for Low, Intermediate and High Stress Triaxialities, adopted from Bao and Wierzbicki [12].

Fracture loci are specific for a given material. In 2004 Bao and Wierzbicki [12] presented a methodology for constructing a fracture locus for A12024-T351, by comparing experimental results with FE simulations. The approach was developed as a general methodology for constructing a fracture locus for any ductile material. Further investigations of negative stress triaxiality were conducted by Bao and Wierzbicki by performing upsetting tests. During an upsetting test, short cylinders of materials are compressed between flat platens. The results of the upsetting tests, alongside the hydrostatic pressure research on fracture produced by Bridgman [57], Bao and Wierzbicki found there is a critical value of stress triaxiality of $-1/3$, below which it is assumed fracture never occurs.

Following the work of researchers Gurson, McClintock, Wilkins et al, Johnson and Cook and Rice and Tracey, in 2006 Xue [81] conducted research to establish cumulative damage as a criterion to predict the onset of fracture. Xue constructed a damage plasticity model for ductile fracture which incorporates pressure dependence, the Lode angle effect and a power law damage rule. Experimental results shown fracture initiation in uncracked ductile specimens were sensitive to the hydrostatic pressure and dependent on the Lode angle. This research was later influenced by Wierzbicki leading to the failure model currently known as the Xue–Wierzbicki fracture criterion [82]. For the Xue–Wierzbicki fracture criterion the damage rate

is calculated through a cylindrical decomposition, which was implemented under the fundamental hypothesis proposed by Xue [81] that “*the damaging process is self-similar on any deviatorically proportional loading path at any given pressure*”. The cylindrical decomposition employs the pressure, the Lode angle, the plastic strain to determine the damage rate. The fracture envelope can be equally characterised in the space of plastic strain and the hydrostatic stress, as shown in Figure 2.8.

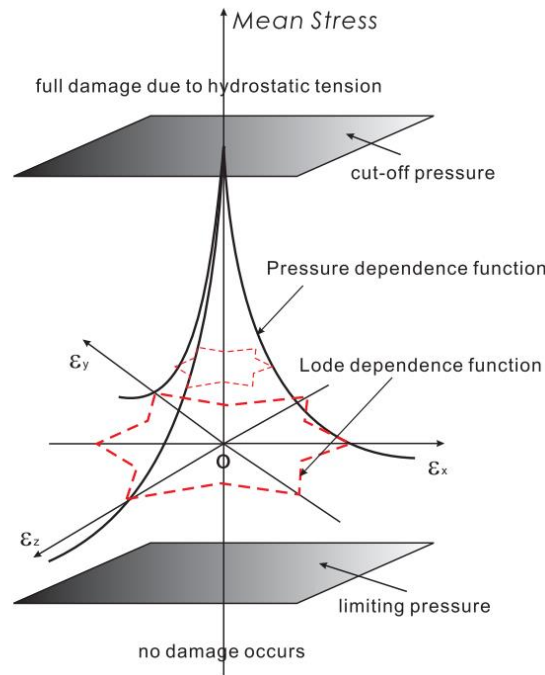


Figure 2.8. Fracture Surface in the 3D Space of the Plastic Strain Plane and the Hydrostatic Stress, adopted from Xue and Wierzbicki [82].

It is assumed the pressure sensitivity and the Lode angle dependence on the fracture strain are independent of each other. Merging the pressure sensitivity and the Lode dependence function by multiplication, the fracture envelope is assumed to take the form as shown in Equation 15.

$$\bar{\epsilon}_f = \bar{\epsilon}_{f0} \mu_p(p) \mu_\theta(\theta) \quad (15)$$

Where $\bar{\epsilon}_{f0}$ is a reference fracture strain indicated by zero mean stress tension, $\mu_p(p)$ characterises the pressure dependence and $\mu_\theta(\theta)$ describes the Lode angle dependence.

In 2007, to investigate the onset of fracture Mohr and Henn developed a new experimental technique for metals at low and intermediate stress triaxialities. Mohr and Henn [83] designed a butterfly specimen, the geometry of this specimen was designed so that cracks are most likely

to initiate within the specimen centre. During experiments the butterfly specimen was adjusted by changing the biaxial loading angle and applying a range of stress states to the same geometry.

Experiments on metals by Bai and Wierzbicki [84] in 2008 concluded that both the pressure effect and the influence of the Lode angle parameter should be included in the description of the material. From this the 2D fracture locus was developed to a 3D asymmetric fracture locus, in the space of equivalent fracture strain, stress triaxiality and the Lode angle parameter (as shown in Figure 2.9). However, it was found that some materials show no obvious effect of hydrostatic pressure and/or Lode angle parameter dependence on metal plasticity. Two methods of calibration of the fracture locus were used in their research. One is based on classical round and flat specimens in uniaxial tests, and the other method followed Mohr and Henn by using a butterfly specimen under biaxial testing.

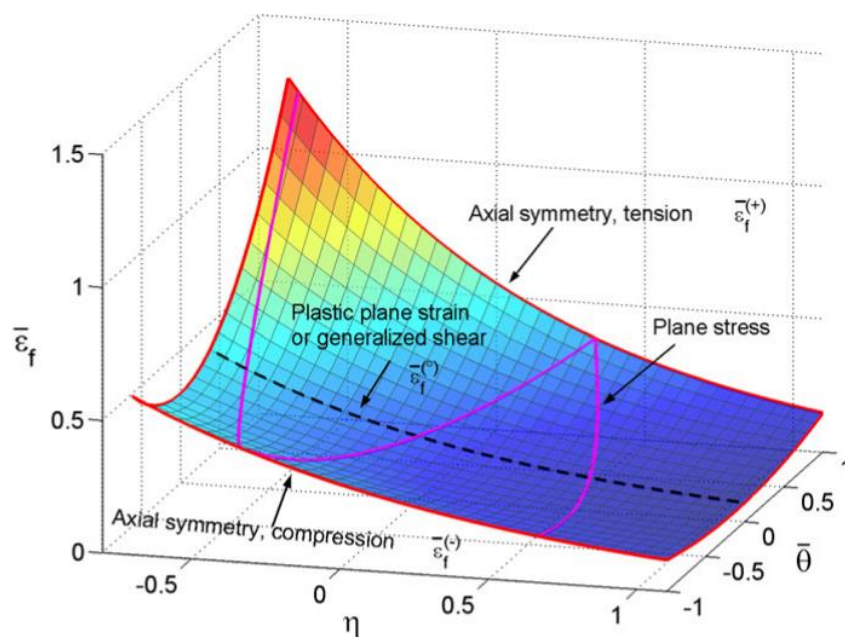


Figure 2.9. 3D Asymmetric Fracture Locus, adopted from Bai and Wierzbicki [84].

Nahshon and Hutchinson [85] stated that the Gurson Model predicts no damage change with strain under zero mean stress, except when voids are nucleated. Due to this Gurson's model excludes the prospect of shear localisation and fracture under conditions of low triaxiality, unless voids are nucleated. Nahshon and Hutchinson extended the Gurson's damage model by

incorporating a parameter, which characterises damage growth under low stress triaxiality conditions.

In 2010, an experimental programme on deformation and failure behaviour of ductile metals was proposed by Driemeier et al. [41]. This methodology can be used as an effective tool to investigate effects of the stress intensity, stress triaxiality and Lode angle parameter [86].

The study by Stoughton and Yoon [87] in 2011, was motivated to provide an efficient method for the analysis of necking and fracture limits for sheet metals. When investigating the relation between necking and fracture, Stoughton and Yoon revised a large range of fracture data provided by Wierzbicki [88] in 2005. Wierzbicki's research concluded that the maximum shear stress (MSS) fracture criterion shown accurate correlation with experimental data, meaning fracture is not strongly related to a specimen geometry, but fracture occurs when a critical stress is achieved. Stoughton and Yoon suggested a new approach to develop a complete description of metal forming limits including both necking and fracture. Stoughton and Yoon's criteria is based on the MSS fracture criterion, combined with the stress-based forming limit curve for necking.

Following the study by Stoughton and Yoon, in 2012 Khan and Liu [89] also investigated the deformation and failure behaviour of the same aluminium alloy. Khan and Liu conducted biaxial compression tests in order to establish a universal, accurate and efficient fracture phenomenological fracture criterion. Khan and Liu's empirical ductile fracture criterion is known as MSV fracture criterion, it is based on the relationship between hydrostatic pressure and magnitude of stress vector. Results were compared to MSS criterion extended by Stoughton and Yoon, J2 fracture criterion and the Xue–Wierzbicki fracture criterion. It was concluded that the MSV criterion was more accurate at predicting ductile fracture. One of the main findings in the research was that the biaxial compression tests, contradicted the critical cut-off value of stress triaxiality proposed by Bao and Wierzbicki [90] of $-1/3$. As the specimens fractured up to the stress triaxiality of -0.495 , suggesting that the cut-off value is not constant but depends on the stress state.

During 2018, Brünig et al. [91] conducted a series of shear compression experiments with biaxial loaded specimens for aluminium alloys at room temperature and under quasi-static loading. The evolution of strain fields was evaluated in parallel with FE simulations and DIC

in critical regions of the specimens where damage and failure occur. The research by Brüning discussed the cut-off value of stress triaxiality. By using the data presented from the study and the experimental results of Khan and Liu [89] and Bao and Wierzbicki [90], a function as shown in Equation 16 was suggested for the cut-off value of stress triaxiality for aluminium alloys at room temperature, under quasi-static loading.

$$\eta_{cut} = -0.6 + 0.27L \quad 0 \leq L \leq 1 \quad (16)$$

Where L is the Lode parameter, which is discussed further in Section 2.5.2.

The prediction of fracture initiation of metal materials at various stress states for nuclear waste storage was studied by Zhihui Li et al. [92] in 2019. They stated the main issues in nuclear waste storage and other engineering applications is providing realistic information on the fracture mechanism, as well as fracture criterions accuracy in assessing the safety factor against fracture initiation. Dominant factors of fracture mechanisms i.e., quasi-cleavage fracture, shear fracture with and without void are all distinctive. Therefore, research was conducted as a single criterion was not found to be able to capture all features of fracture initiation under different stress states. Zhihui Li et al. [92] recommended a new fracture criterion using various functions to predict fracture initiation of different mechanisms, as shown in the form of Equations 17-19. The value of equivalent stress corresponding to the onset of fracture initiation respectively is $f_{1,2,3}(\sigma_{ij})$. To predict the initiation of the quasi-cleavage fracture and normal fracture with void Equation 17 was used.

$$f_1(\sigma_{ij}) = \sigma_1 + b_1(\sigma_2 + \sigma_3) \quad R_\sigma \geq R_2 \quad (17)$$

Where, b_1 is the influence coefficient and R_2 is the value between normal fracture with void and shear fracture with void. The function relating to shear fracture with void is given by Equation 18.

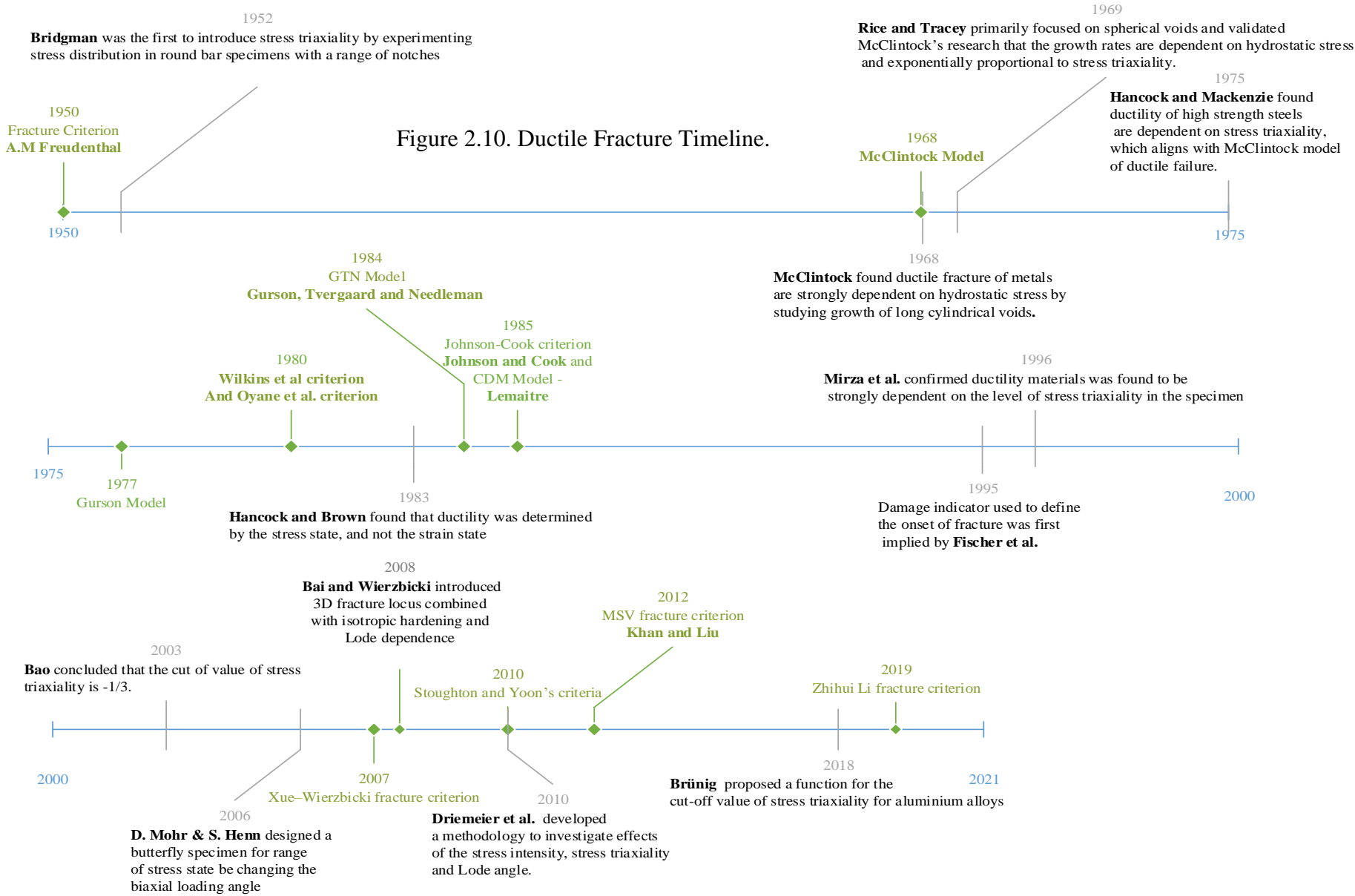
$$f_2(\sigma_{ij}) = \tau_{max} + b_2(R_\sigma - R_3) \quad R_3 \leq R_\sigma < R_2 \quad (18)$$

In which b_2 is the influence of stress state on shear fracture with void for different materials and R_3 is the boundary value between shear fracture with void and shear fracture without void. Lastly, the fracture function for predicting the shear fracture without void is described only by the maximal shear stress, as shown in Equation 19.

$$c_3 = \tau_{max} = f_3(\sigma_{ij}) \quad R_\sigma < R_3 \quad (19)$$

It was concluded by Zhihui Li et al. [92] that the proposed fracture criterion is recommended to evaluate the fracture initiation of metal structures in nuclear waste storage and other engineering applications.

In conclusion, the fundamentals of ductile fracture are continuously being extended by incorporating innovative knowledge. Ductile fracture history is summarised as a timeline in Figure 2.10. Failure criterions have been developed since 1950's to predict damage evolution up to final fracture and have become important to the progress and utilisation of material deformation. Research for ductile materials failure criteria is continuous, as the development and application of material strength is of interest across engineering disciplines, as discussed in existing literature [93][94][95][96][97].



2.5 Stress State

Stress state of a material is dependent on the loading conditions (tension, compression, and shear) and is characterised by the stress triaxiality and the Lode angle parameter. Stress triaxiality as shown previously in Equation 12 is one of the most important factors that defines stress state and controls the initiation of ductile fracture [12]. However, stress triaxiality alone does not always accurately predict ductile fracture for specimens with complicated geometry and loading conditions [12]. Alongside stress triaxiality, Lode angle parameter (as shown in Equation 14) can be used to give a complete description of the stress state of a material [13][14]. The stress states for a fracture locus consists of three distinctive regions. The negative stress triaxiality region is typically obtained from compression tests, there is a cut-off value of the stress triaxiality equal to $-1/3$, below this it is assumed fracture never occurs [90]. However, it was discussed previously in Section 2.4.2 that there is a contradiction in literature, as the cut-off value of the stress triaxiality equal to $-1/3$, is researched throughout literature it will still be considered throughout this thesis. Low stress triaxiality region relates to shear, combined loading, and tension (flat plates) and high stress triaxiality region is characteristically determined by tensile tests (round bars) [12] as summarised in Figure 2.11.

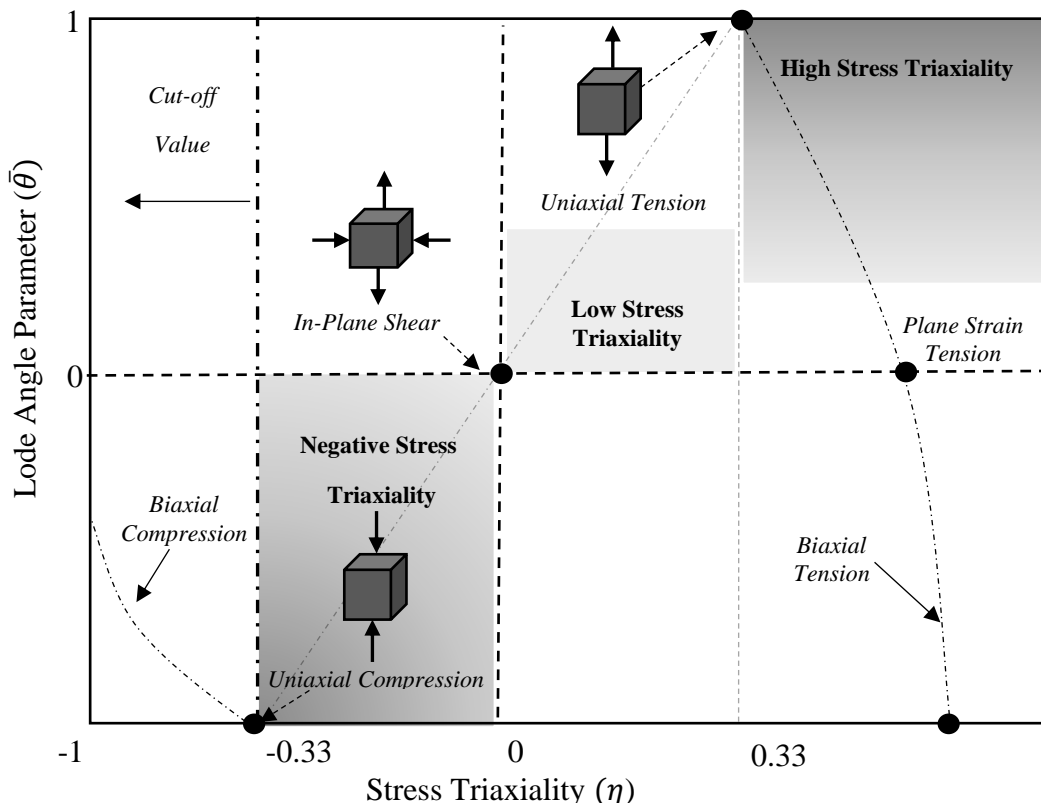


Figure 2.11. Summary of Stress States for Various Loading Conditions, adaptation from Mohr [51].

2.5.1 *Decomposition of the Stress Tensor*

The first process in understanding the fundamentals of the stress state is decomposition of the stress tensor. As long as the stress tensor is symmetric at a given point, the normal stress components on the three principal planes are called principal stresses and is expressed by, $\sigma_{11}, \sigma_{22}, \sigma_{33}$ [98]. The stress state diagram is displayed in Figure 2.12 and the stress tensor is shown in Equation 20, as the sum of hydrostatic stress (also known as mean stress) and the deviatoric stresses.

$$|\sigma| = \sigma_H + s_{ij} \tag{20}$$

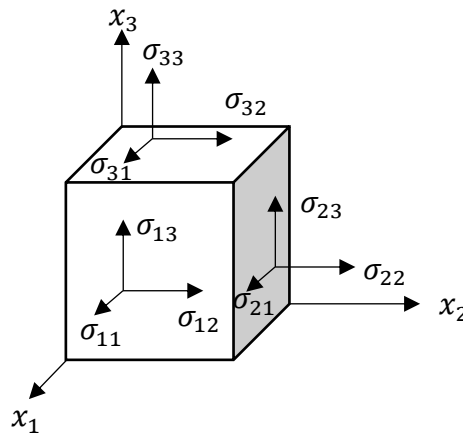


Figure 2.12. Stress State Diagram.

Figure 2.13 displays the dependence of stress state on void evolution. The size of the yield surface affecting the void growth is dependent on the hydrostatic stress, while the deviatoric stress controls voids shape and is characterised by Lode parameter [84].

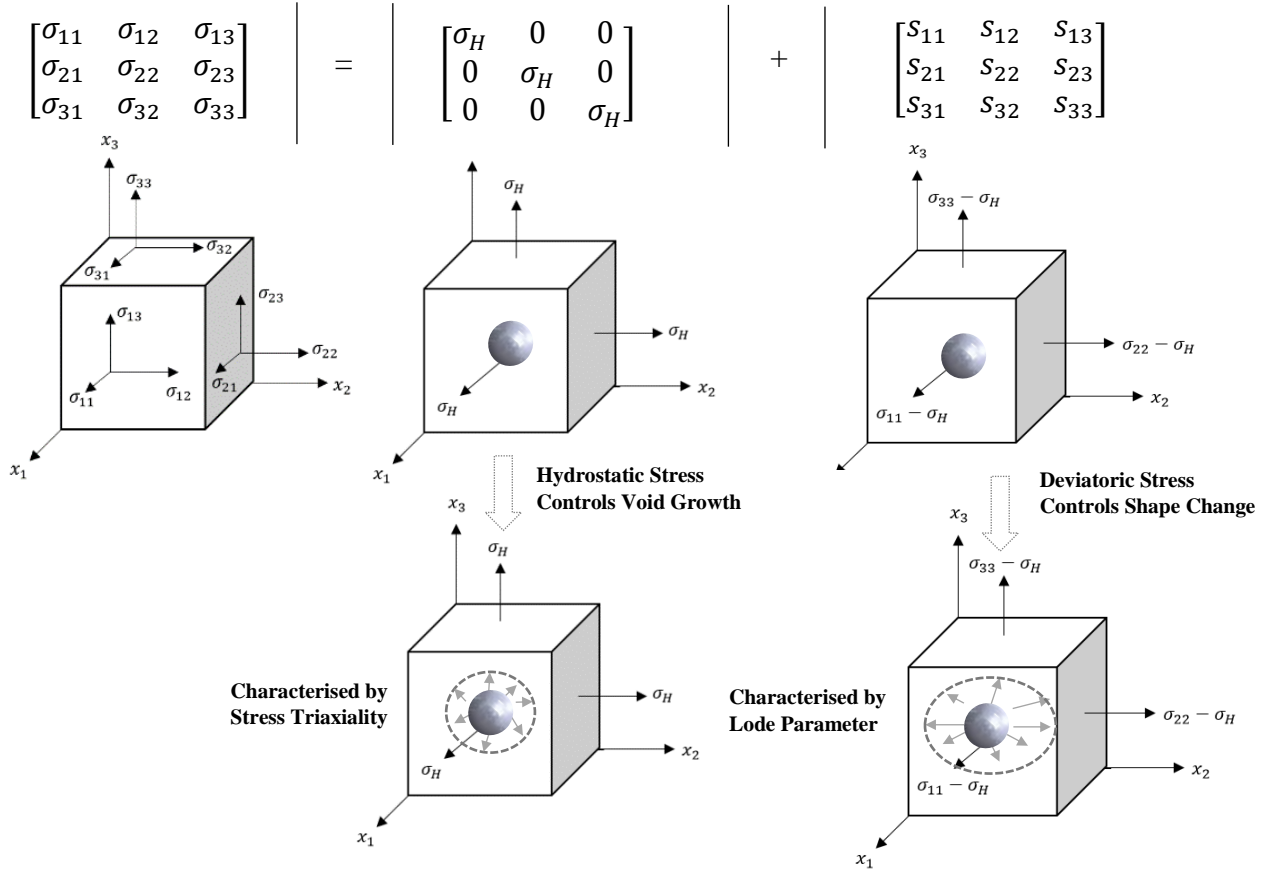


Figure 2.13. Dependence of Stress State on Void Evolution, adaptation from Mohr [99].

Hydrostatic part of the stress tensor is the average stress as shown in Equation 21, and deviatoric part as shown in Equation 22 which describes the differences among stresses.

$$\sigma_H = \frac{\sigma_{11} + \sigma_{22} + \sigma_{33}}{3} = \frac{1}{3} I_1 \quad (21)$$

$$\begin{bmatrix} S_{11} & S_{12} & S_{13} \\ S_{21} & S_{22} & S_{23} \\ S_{31} & S_{32} & S_{33} \end{bmatrix} = \begin{bmatrix} \sigma_{11} - \sigma_H & \sigma_{12} & \sigma_{13} \\ \sigma_{21} & \sigma_{22} - \sigma_H & \sigma_{23} \\ \sigma_{31} & \sigma_{32} & \sigma_{33} - \sigma_H \end{bmatrix} \quad (22)$$

The first, second, and third invariant of the stress tensor, I_1 , I_2 and I_3 are defined in the following equations,

$$I_1 = \sigma_{11} + \sigma_{22} + \sigma_{33} \quad (23)$$

$$I_2 = \begin{vmatrix} \sigma_{11} & \sigma_{12} \\ \sigma_{21} & \sigma_{22} \end{vmatrix} + \begin{vmatrix} \sigma_{22} & \sigma_{23} \\ \sigma_{32} & \sigma_{33} \end{vmatrix} + \begin{vmatrix} \sigma_{11} & \sigma_{13} \\ \sigma_{31} & \sigma_{33} \end{vmatrix} \quad (24)$$

$$I_3 = \det(\sigma) \quad (25)$$

The main invariants used for describing the three principal stresses for stress state, are I_1 , the first invariant of the stress tensor shown in Equation 23 and the roots of the polynomial are the three principal deviatoric stresses s_1, s_2 , and s_3 , which are used to express the second and third deviatoric stress invariants J_2 and J_3 as shown below in Equations 26, 27.

$$J_2 = \frac{1}{2}(s_1^2 + s_2^2 + s_3^2) \quad (26)$$

$$J_3 = s_1 s_2 s_3 \quad (27)$$

Industrial applications use von Mises stress to determine the yield of ductile materials when subjected to a loading condition. The equation for von Mises is shown in Equation 28,

$$\bar{\sigma} = \sqrt{\frac{1}{2} [(\sigma_{11} - \sigma_{22})^2 + (\sigma_{22} - \sigma_{33})^2 + (\sigma_{33} - \sigma_{11})^2]} \quad (28)$$

The deviatoric stress tensor is shown in Equation 29, where $|I|$ is known as the identity tensor,

$$|S| = |\sigma| - \sigma_H |I| \quad (29)$$

The third invariant r characterises the position of the second principal stress σ_{22} with reference to the maximum and minimum principal stresses [100]. The normalised third invariant ζ can also be related to the Lode angle θ ,

$$r = \left[\frac{27}{2} (\sigma_{11} - \sigma_H)(\sigma_{22} - \sigma_H)(\sigma_{33} - \sigma_H) \right]^{\frac{1}{3}} \quad (30)$$

$$\therefore \zeta = \cos(3\theta) = \left(\frac{r}{\bar{\sigma}} \right)^3 = \frac{3\sqrt{3}}{2} \frac{J_3}{J_2^{\frac{3}{2}}}, \quad 0 \leq \theta \leq \pi/3 \quad (31)$$

2.5.2 Lode Angle

Introduced by Walter Lode in 1925, Lode parameter is used alongside stress triaxiality in describing a material's stress state. However, there are many different definitions of Lode parameter in ductile fracture literature, this is summarised in Table 2.1.

Table 2.1. Summary of Definitions of Lode angle [101].

Name	Definition	Range	Reference
Lode Parameter	$L = \frac{2\sigma_{22} - \sigma_{11} - \sigma_{33}}{\sigma_{11} - \sigma_{33}}$	$-1 \leq L \leq 1$	Lode, 1926
Lode Angle	$\cos(3\theta) = \frac{3\sqrt{3} J_3}{2 J_2^{\frac{3}{2}}}$	$0 \leq \theta \leq \pi/3$	
Normalised Third Invariant	$X = \frac{27 J_3}{2 \bar{\sigma}^3}$	$-1 \leq X \leq 1$	Wierzbicki et al, 2005
Normalised Lode Angle/ Lode Angle Parameter	$\bar{\theta} = 1 - \frac{2}{\pi} \arccos \zeta$	$-1 \leq \bar{\theta} \leq 1$	Bai and Wierzbicki,2008

To further understand the terms shown in Table 2.1, this section explains Lode parameter by using stress invariants and Lode angle parameter as a vector in the stress space. Lode parameter is defined by Equation 34 in terms of the principal stresses for when, $\sigma_{11} \geq \sigma_{22} \geq \sigma_{33}$. Mohr's circle shown in Figure 2.14, shows the Lode parameter as the position of the intermediate principal stresses. This is determined using the maximum shear stress τ , and the normal stress on plane of maximum shear σ_N , as shown by Equations 32 and 33 respectively.

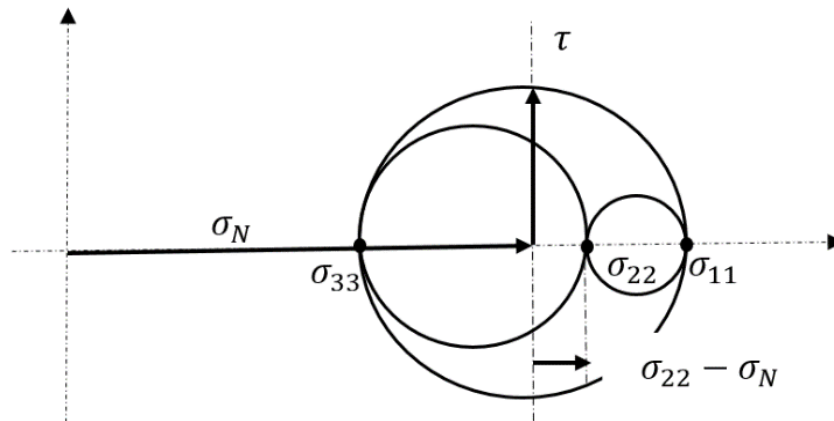


Figure 2.14. Mohr's Circle to Demonstrate Lode Parameter, adaptation from Mohr [99].

$$\tau = \frac{\sigma_{11} - \sigma_{33}}{2} \tag{32}$$

$$\sigma_N = \frac{\sigma_{11} + \sigma_{33}}{2} \tag{33}$$

$$L = \frac{\sigma_{22} - \sigma_N}{\tau} = \frac{2\sigma_{22} - \sigma_{11} - \sigma_{33}}{\sigma_{11} - \sigma_{33}}, \quad -1 \leq L \leq 1, \quad (34)$$

Whereas, the Lode angle θ , shown in Equation 35 can be defined in the stress space shown in Figure 2.15, as the smallest angle between the line of pure shear and projection of the stress tensor on the deviatoric plane [86].

$$\cos(3\theta) = \frac{3\sqrt{3}}{2} \frac{J_3}{J_2^{3/2}}, \quad 0 \leq \theta \leq \frac{\pi}{3} \quad (35)$$

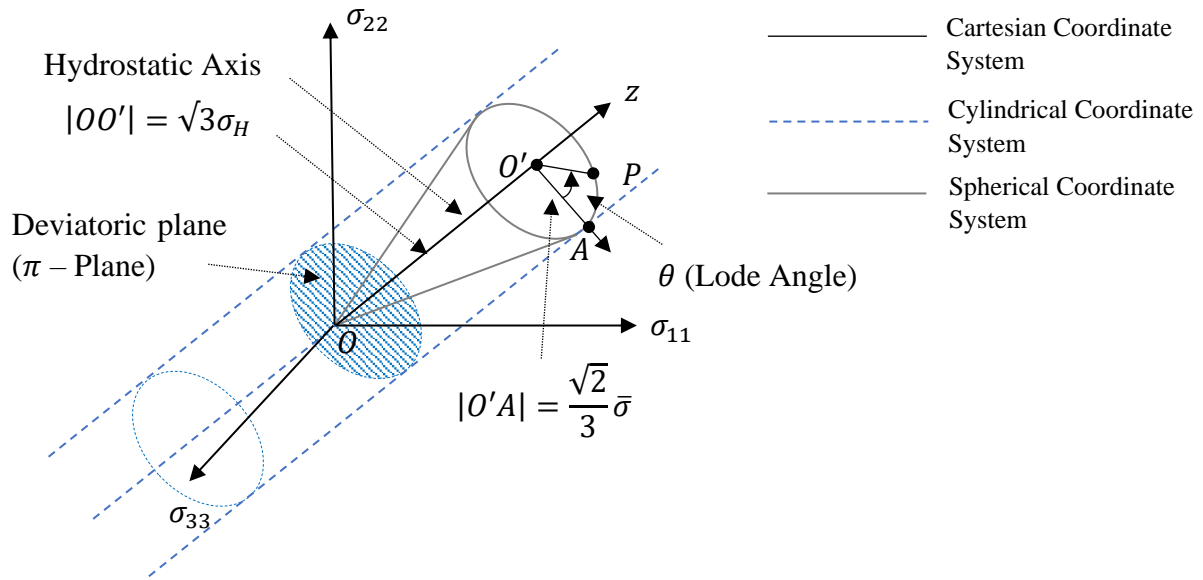


Figure 2.15. Three Types of Coordinate System in the Space of Principal Stresses, adaptation from Xue [72].

The principal stresses can be geometrically characterised by a vector in the 3D space as shown in Figure 2.15, where the principal stresses are taken as the Cartesian coordinates. The Cartesian principal space is reinterpreted in a cylindrical coordinate system, aligned with the hydrostatic axis on the same origin. The Lode angle in the cylindrical system is defined on the deviatoric plane. The z axis in the cylindrical system is the triad axis, where $\sigma_{11} = \sigma_{22} = \sigma_{33}$ [72][102].

Where point A intersects between all three coordinate systems, where point P is on the deviatoric plane, where the maximum from point P will be $\frac{\pi}{3}$. The principal stress vector of \vec{OA}

represents the stress state. This is composed of two component vectors, $\overrightarrow{OO'}$ and $\overrightarrow{O'A}$, where $\overrightarrow{OO'}$ is perpendicular to the deviatoric plane and $\overrightarrow{O'A}$ is in the deviatoric plane. The vector $\overrightarrow{OO'}$ characterises the hydrostatic pressure and the vector $\overrightarrow{O'A}$ represents the deviatoric term. The magnitude of these component vectors is related to hydrostatic pressure and the von Mises equivalent stress, as shown on the diagram in Figure 2.15 and in Equation 36 [72].

$$|O'P| = \frac{\sqrt{2}}{3} \bar{\sigma}, \text{ and } |OA'| = \sqrt{3} \sigma_H \quad (36)$$

The Lode angle as shown in Equation 35, is also related to the third invariant, it can be normalised by to give the Lode angle parameter, as shown in Equation 37 [102].

$$\bar{\theta} = 1 - \frac{6\theta}{\pi} = 1 - \frac{2}{\pi} \arccos \zeta, \quad -1 \leq \bar{\theta} \leq 1 \quad (37)$$

The loading conditions of each material in this thesis is characterised by the defined parameters stress triaxiality and Lode angle parameter ($\eta, \bar{\theta}$).

2.6 Fracture Locus

Understanding how materials behave under different loading conditions is important when assessing failure of the material. The equivalent strain to fracture (otherwise known as fracture strain) is a useful property as it can be used to characterise a materials fracture ductility. The fracture strain of a material is dependent on the stress state at which plastic deformation is accumulated [103]. Materials perform differently when subjected to tension and compression loading. In order to satisfy structural design criteria, data characterising how the material performs under a range of loading conditions is required. One of the methods associated with analysing the overall ductility of metals in terms of fracture strain, is to develop a fracture locus of a material [15].

A fracture locus also known as a limiting fracture curve, consists of three distinctive regions. The negative stress triaxiality region is typically obtained from compression tests, there is a cut-off value of the stress triaxiality equal to $-1/3$, below this fracture is assumed to never occur [90]. Low stress triaxiality region relates to shear, combined loading, and tension (flat plates) and high stress triaxiality region is characteristically determined by tensile tests (round bars) [12]. The development of a 2D and 3D fracture locus was previously discussed in Section 2.4.2. In summary, a 2D fracture locus displays the relation between equivalent strain to fracture and average stress triaxiality over the load history [104]. Whereas a 3D fracture locus represents the material in the space of equivalent fracture strain, stress triaxiality and the Lode angle parameter.

Bao and Wierzbicki provided a general methodology used in constructing the fracture locus for any ductile material [12]. This calibration procedure of the fracture locus has since been adopted by researchers [104][105]. To construct a fracture locus of material, a series of tests need to be performed with a range of specimens and loading conditions. The method requires experimental tests and FE analysis to be performed in parallel, to define the location of fracture initiation and also the displacement to fracture (u_f). The initial steps are to conduct a tensile test to measure the materials engineering stress-strain response and inputting true stress-strain data into the FE analysis. Subsequently, experimental tests of a geometry can be conducted to obtain force–displacement responses, whilst executing corresponding FE analysis. From this it is possible to calculate the evolution of the equivalent strain and the stress triaxiality at the

fracture location for a test. This determines the fracture strain and the average stress triaxiality for the test conducted. The final step is adding the data to the fracture locus and repeating for various geometries and stress states [12][104]. The fracture location is known as the critical location hereinafter, a table summarising previous researchers critical location with its relevant material and geometry is shown in Table 2.2

Table 2.2. Summary of Critical Locations used from Various Researchers.

Name of Specimen	Researcher	Material	Critical Location
Smooth Round Bar and Notched Round Bar Specimens	<i>Bao and Wierzbicki</i> [12]	2024-T351 Aluminium alloy	At the equatorial area and the centre.
	<i>Bai et al.</i> [58]	1045 steel round	Assumed to be the centre of the specimen.
	<i>Chang-Sik Oh et al.</i> [106]	API X65 steel	Centre of the minimum section in the specimen.
	<i>Dunand and Mohr</i> [107]	TRIP780 sheets	Centre of the gage area.
Plate with Hole	<i>Bao and Wierzbicki</i> [12]	2024-T351 Aluminium alloy	Fracture initiated at the middle of the circumferential surface of the hole perpendicular to the loading during the present experiments on plates with circular holes.
Various Tensile Specimens	<i>Dunand and Mohr</i> [107]	TRIP780 sheets	The location of the onset of fracture coincides with the location of the highest equivalent plastic strain within the specimen at the instant of onset of fracture.
Various Tensile and Shear Specimens	<i>Sung-Ju Park et al.</i> [94]	EH36 grade steel	The element with the highest equivalent plastic strain. In notched tension specimens, the critical element is located at the centre of the gauge, while in central-hole specimen it is located on the hole boundary. In the shear specimen, the critical element is slightly off the centre of the gauge section.

Flat plates (<i>Pure shear and combined shear and tension</i>)	<i>Bao and Wierzbicki</i> [12]	2024-T351 Aluminium alloy	Bao and Wierzbicki could not find the exact location of fracture initiation for these tests.
Upsetting tests			Critical locations of the cylinders were found at the equatorial area.
New Compression Geometry			Fracture initiation also occurred at the equatorial area.
Butterfly Specimens	<i>Dunand and Mohr</i> [107]	TRIP780 sheets	Where the equivalent plastic strain reaches its maximum at the instant of onset of fracture.
Various Tensile and Shear Specimens	<i>Mohr and Marcadet</i> [51]	Two Dual-Phase (DP) steels and one TRIP-assisted steel	The location of the highest equivalent plastic strain within the gage section.
Tensile and Shear Specimens	<i>Maclean</i> [108]	DH-36 Navy steel	The element with the maximum equivalent plastic strain at the onset of fracture.

2.6.1 Fracture Experiments

There are a number of fracture experiments that have been recorded, detailing the dependence of equivalent strain, from a range of materials and utilising different models of ductile fracture criterion. The fracture locus constructed in Figure 2.19 displays a sufficient amount of data points available to evaluate the main deformation modes. In Appendix A there is a table which includes further information for each point. The experimental data obtained is divided into three distinctive regimes of stress triaxiality and their relative loading conditions.

2.6.1.1 High Stress Triaxiality

Tensile testing is a destructive test process, commonly utilised in engineering to obtain information for the tensile strength, yield strength and ductility of materials [109]. Tensile loading conditions can show the relationship between the formation of shear bands and the fracture of the material [110].

Bao and Wierzbicki [12] performed conventional tensile tests on smooth round specimens and for specimens with different circumferential notches, as shown in Figure 2.16. The study concluded fracture occurred due to void formation in tensile tests, on pre-notched specimens which is in the range of high stress triaxialities. For the experiments performed, fracture initiated at the centre of the bar, where the stress triaxiality and equivalent strain were the largest.

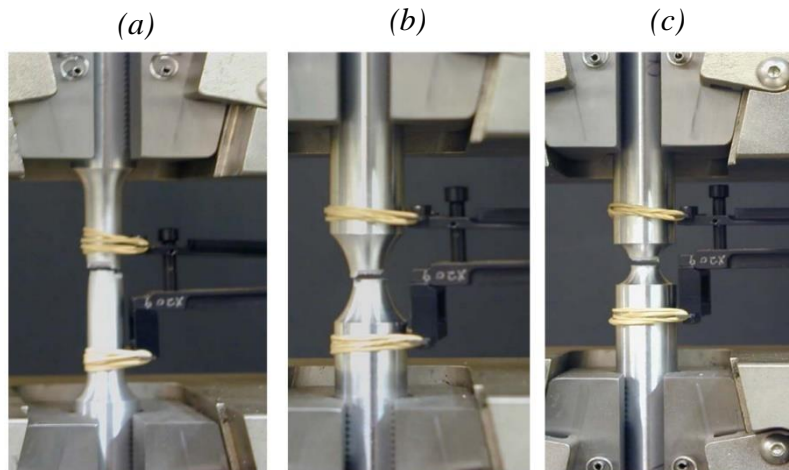


Figure 2.16. Fractured Tensile Specimens a) Smooth, b) $R = 12\text{mm}$ and c) $R = 4\text{mm}$, adopted from Bao and Wierzbicki [12].

Bai et al. [58] performed a series of fracture tests on notched round bars and flat-grooved specimens, as shown in Figure 2.17. Following Bridgman's analysis for inside the necking of a plane strain specimen (as shown in Figure 2.4 and by Equation 6), Bai et al. [58] derived a closed-form solution, for the stress triaxiality inside the notch of a flat-grooved plane strain specimen. The study found the range of stress triaxiality in round notched bars and flat-grooved specimens were similar, but the values of the Lode angle parameter were different.

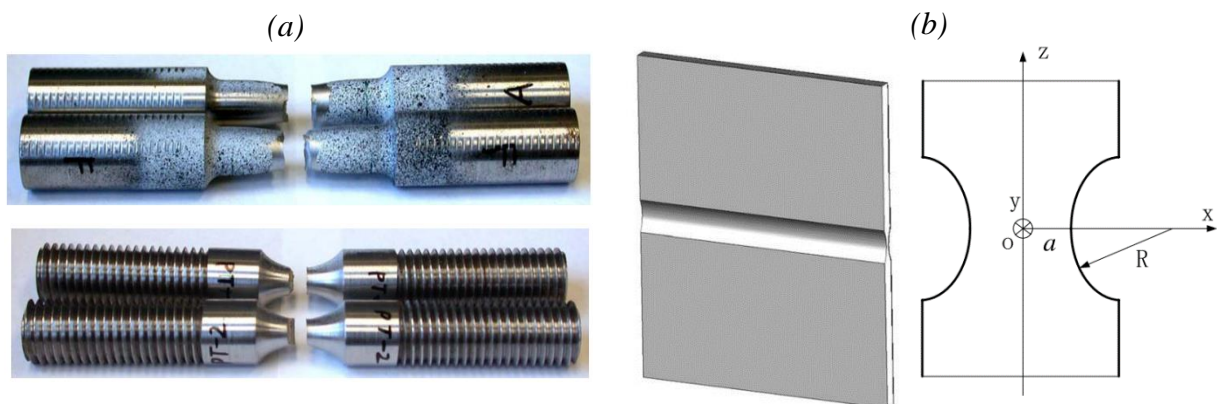


Figure 2.17. a) 1045 Steel Round Bar Specimens with Different Notches, b) Flat-grooved Plane Strain Specimen, adopted from Bai et al. [58].

Kiran and Khandelwal [111] conducted an experimental investigation for a variety of uniaxial tension tests on the notched tensile specimens (as shown in Figure 2.18), for ASTM A992 structural steel. The experimental study concluded that the ductility varies significantly with stress triaxiality. It was observed that the high triaxiality significantly reduces the ductility of steels. The practical implication of this result is that the structural components should be proportioned such that high triaxiality regions are eliminated from the final designs. The micromechanical analysis by Kiran and Khandelwal [15] observed that in the high triaxiality region the equivalent strain to fracture decreases with the increase in stress triaxiality.

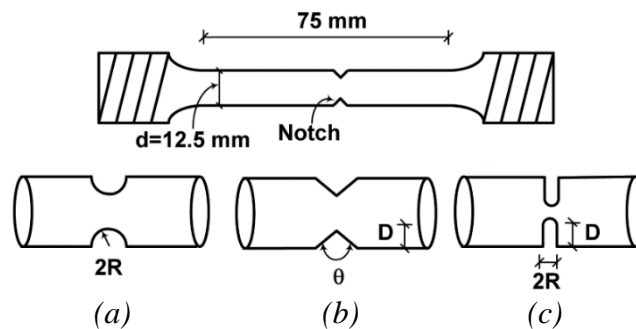


Figure 2.18. Geometry of the Tensile Specimen and Notches: a) C-notch, b) V-notch, c) U-notch, adopted from Kiran and Khandelwal [111].

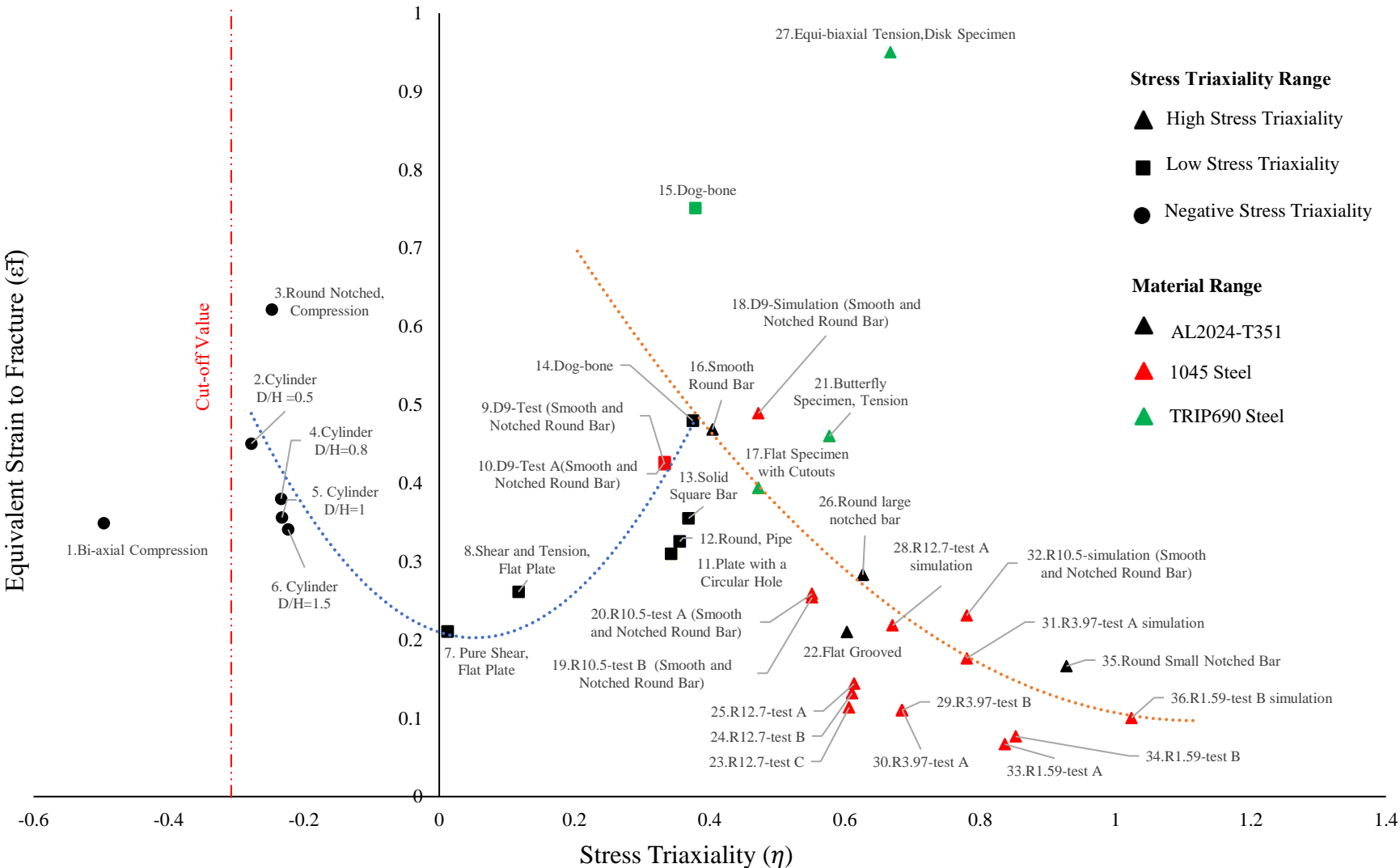


Figure 2.19. Fracture Locus for a Range of Materials on the Space of the Equivalent Plastic Strain against Stress Triaxiality[12][58][107].

2.6.1.2 Low Stress Triaxiality

To provide information of fracture ductility in the intermediate regime for a fracture locus, a variety of experimental tests can be performed using different loading conditions and geometries as summarised below:

- a) **Tensile Flat Plates:** Tensile plates, such as a flat rectangular plate with a circular hole (as shown in Figure 2.20a), can be used to obtain data in the low stress triaxiality region. Bao [112] performed an experimental and numerical study on flat rectangular plates with a circular hole subjected to tensile load, for different thicknesses and diameters of holes. The results concluded that the equivalent strain to fracture initiation, increased with the ratio of thickness to ligament until it reaches maximum and then decreases again.

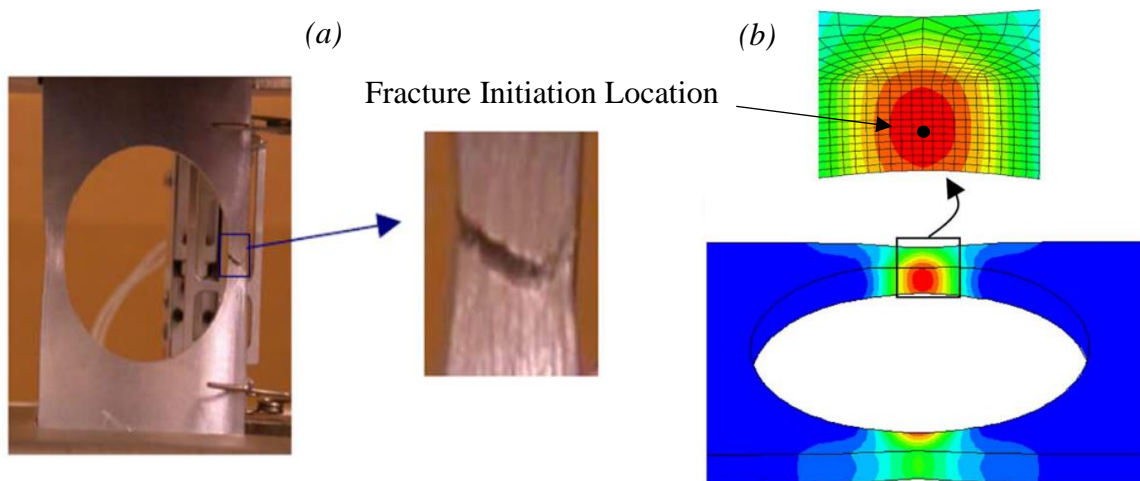


Figure 2.20. a) Plate with Hole Specimen after Failure, adopted from Bao and Wierzbicki [12], b) Plate with Hole Specimen FE contour, adopted from Bao [112].

- b) **Pure Shear:** During a uniaxial tensile test, the material increases in length and deforms perpendicular to the loading condition. However, pure shear is defined as the material deforming due to slippage along a plane parallel to the imposed stress. When constructing a fracture locus, pure shear experiments are used as the hydrostatic pressure is zero or very small compared to the equivalent stress at fracture locations [12]. Bao and Wierzbicki [12], introduced a novel geometry developed using the concept of a butterfly gauge section, as shown in Figure 2.21a. The fracture specimen shown in Figure 2.21b, displays the material failure under shear conditions.

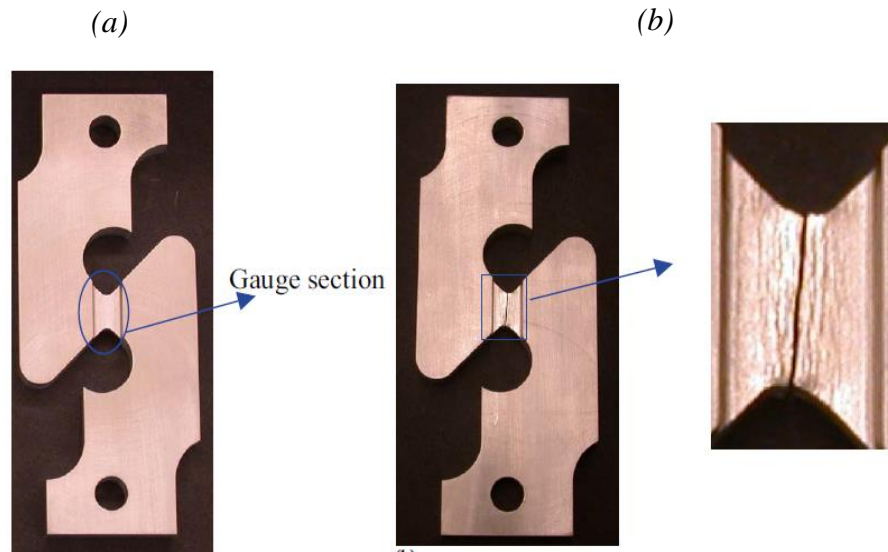


Figure 2.21. Pure Shear Specimen, a) Undeformed Specimen, b) Fractured Specimen, adopted from Bao and Wierzbicki [12].

- c) **Torsion:** Fracture tests performed by Gao et al. [13] implemented a “Lindholm type tubular” specimen design, as shown in Figure 2.22. A torsion experiment by Bai [102] was found to be on the bound limit, as torsion fracture is a pure shear condition.

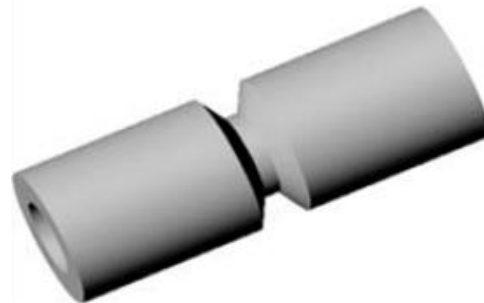


Figure 2.22. Lindholm Type Tubular Design Torsion Specimen, adopted from Gao et al. [13].

- d) **Combined Loading:** Specimens subjected to combined loading are developed with bespoke geometries, to provide information on crack formation in the range between pure shear and tensile tests. Bao and Wierzbicki [12], designed a geometry as shown in Figure 2.23a, so that the gauge section was under a combined shear and tension loading conditions, as shown by the fractured specimen in Figure 2.23b.

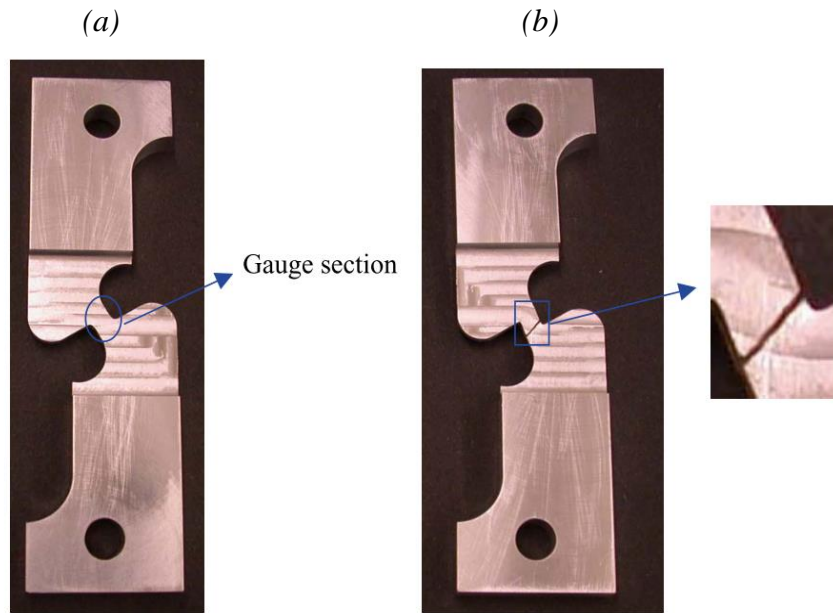


Figure 2.23. Pure Shear Specimen, a) Undeformed Specimen, b) Fractured Specimen, adopted from Bao and Wierzbicki [12].

Qian et al. [113] performed tests for three shear-dominated specimens as shown in Figure 2.24, the geometry in Figure 2.24a was designed symmetrically to reduce the effect of rotation on the shear stress state of an asymmetrical specimen.

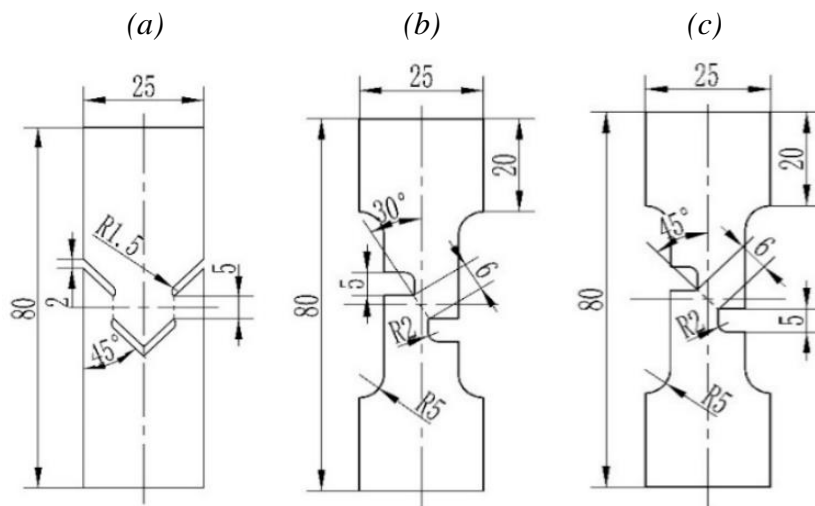


Figure 2.24. Shear-dominated Specimens, adopted from Qian et al. [113].

Bai [102] used material A710 steel to characterise fracture behaviour using a novel butterfly specimen design, as shown in Figure 2.25. The geometries of butterfly specimens are of

interest, as these specimens allow for the material to be tested for different loading cases using the same design [107][114]. The specimen gauge section involved two curvatures, to ensure strain is highly localised in the central region. Thus, dramatically decreasing crack formation at the boundaries. In order to hold the specimen securely the geometry has long shoulders, and to ensure the specimen stays rigid during the entire loading process, there is a difference of the thickness between the shoulder and gauge section.

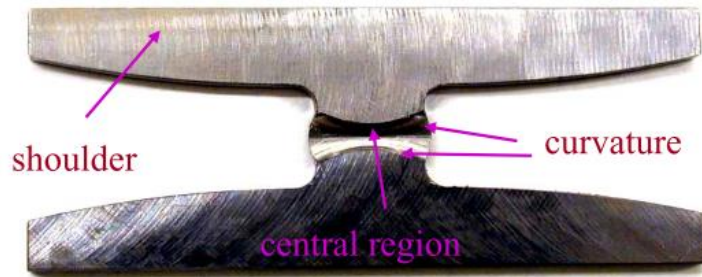


Figure 2.25. Butterfly Specimen, adopted from Bai [102].

Bai used a Universal Biaxial Testing Device (UBTD) as shown in Figure 2.26, where the specimens were loaded under different angles to obtain fracture properties for different stress states.

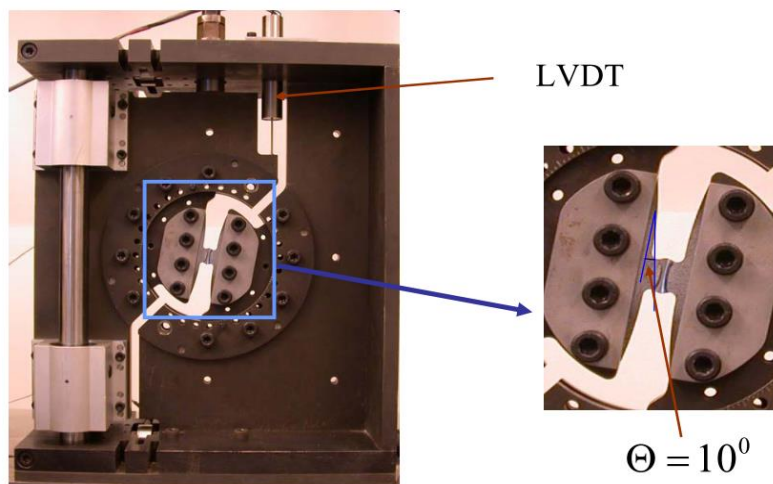


Figure 2.26. Butterfly Specimen fitted in a Universal Biaxial Testing Device (UBTD) with an inclination angle of 10° with respect to the loading axis, adopted from Bai [102].

The UBTD was originally used by Mohr and Doyoyo [115] to investigate the plasticity of aluminium honeycomb under multiaxial loading, since then it has been used in combination

with butterfly specimens to calibrate fracture properties of metals, as discussed in existing literature [116][117][114].

Dunand and Mohr [107] studied butterfly specimens for a range of loading angles. A location called the ‘critical element’ was found, where the equivalent plastic strain reaches its maximum at the instant of onset of fracture for each specimen. This study used DIC to measure the surface displacement and strain fields, using FE analysis to validate the results obtained. The contour plot in Figure 2.27, shows the principal strains at the surface of the specimen before failure is shown by using the DIC and FE analysis.

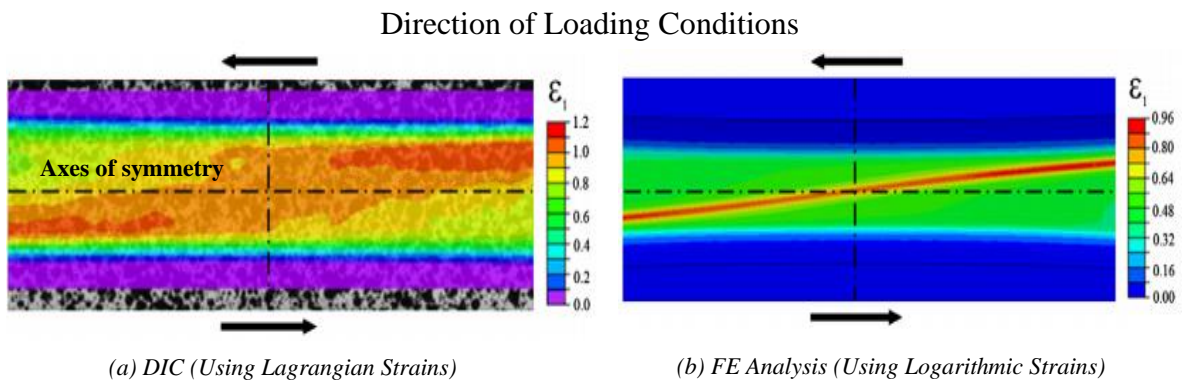


Figure 2.27. Principal Strain at the Surface of a Butterfly Specimen Measured using DIC and FE analysis, adopted from Dunand and Mohr [107].

2.6.1.3 Negative Stress Triaxiality

Negative stress triaxiality is generally associated with fracture under axial symmetric compression, where the Lode angle parameter is approximately -1. Investigations into the phenomenon of barrelling of solid cylinders, was mostly conducted to understand the mechanical manufacturing implementations. Industrial processes for metals that involve compressive hydrostatic stress state such as, rolling and forging, mean that researchers particularly investigate damage at negative triaxiality. Damage at small negative triaxiality is of significance, as research indicates shear damage exists at small negative triaxiality and most deformation in metal forming processes occur in the small negative triaxiality region [53][118]. Experiments for negative stress triaxiality typically have used conventional upsetting tests, which were introduced by Kudo and Aoi in 1967 [119]. During an upsetting test, short cylinders of materials are compressed between flat platens. Friction between specimens and the platens, generates barrelling of the specimen near the equator as the loading is applied [12]. The extrapolation method is when cylindrical specimens with a range of ratios of initial diameter to initial height (D/H) are subject to compression loading. By using the extrapolation method, it is possible to produce an approximate stress–strain curves for compression tests [90].

Bao conducted research on the matter of mechanisms dominating negative stress triaxiality. Fracture surfaces observed from SEM Fractography of Bao's upsetting tests are shown in Figure 2.28. The specimen fracture surface was relatively flat, and no clear dimples can be observed at the location of crack formation. Bao found no evidence presenting cracked particle and nucleated voids [90].

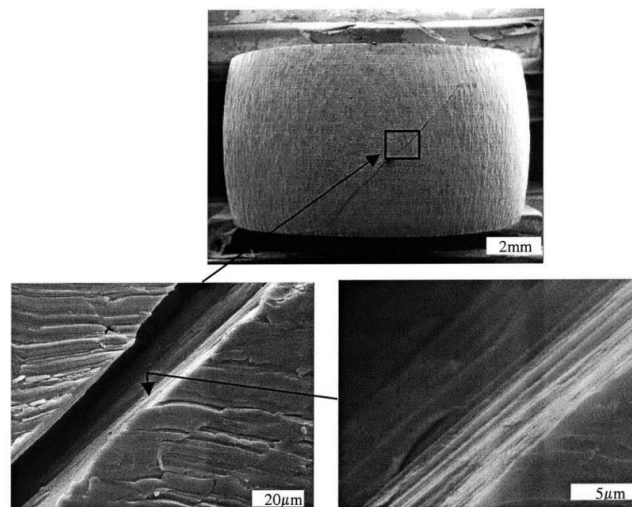


Figure 2.28. Upsetting Test showing Shear Decohesion, adopted from Bao [79].

H. Li et al. [120] observed smooth shear fractures at an angle of about 45° to the compression direction when performing upsetting tests. The programme of testing performed by H. Li et al [120]. included different sample geometries as well as different D/H ratios of cylinders for the upsetting tests such as; flanged and tapered upsetting specimens (as shown in Figure 2.29). Although, there are many elongated voids in the fracture surface along the shear fracture direction, the flanged upsetting specimen had a vertical fracture. This was also observed by Landre et al. [121] when performing upsetting experiments of AISI 1040 steel material. From this, it was suggested that hoop tensile stress and shear stress determined whether vertical or shear fracture occurs. For the tapered specimens, the failure was initiated at the equator of the sample and developed with a macroscopic shear fracture.

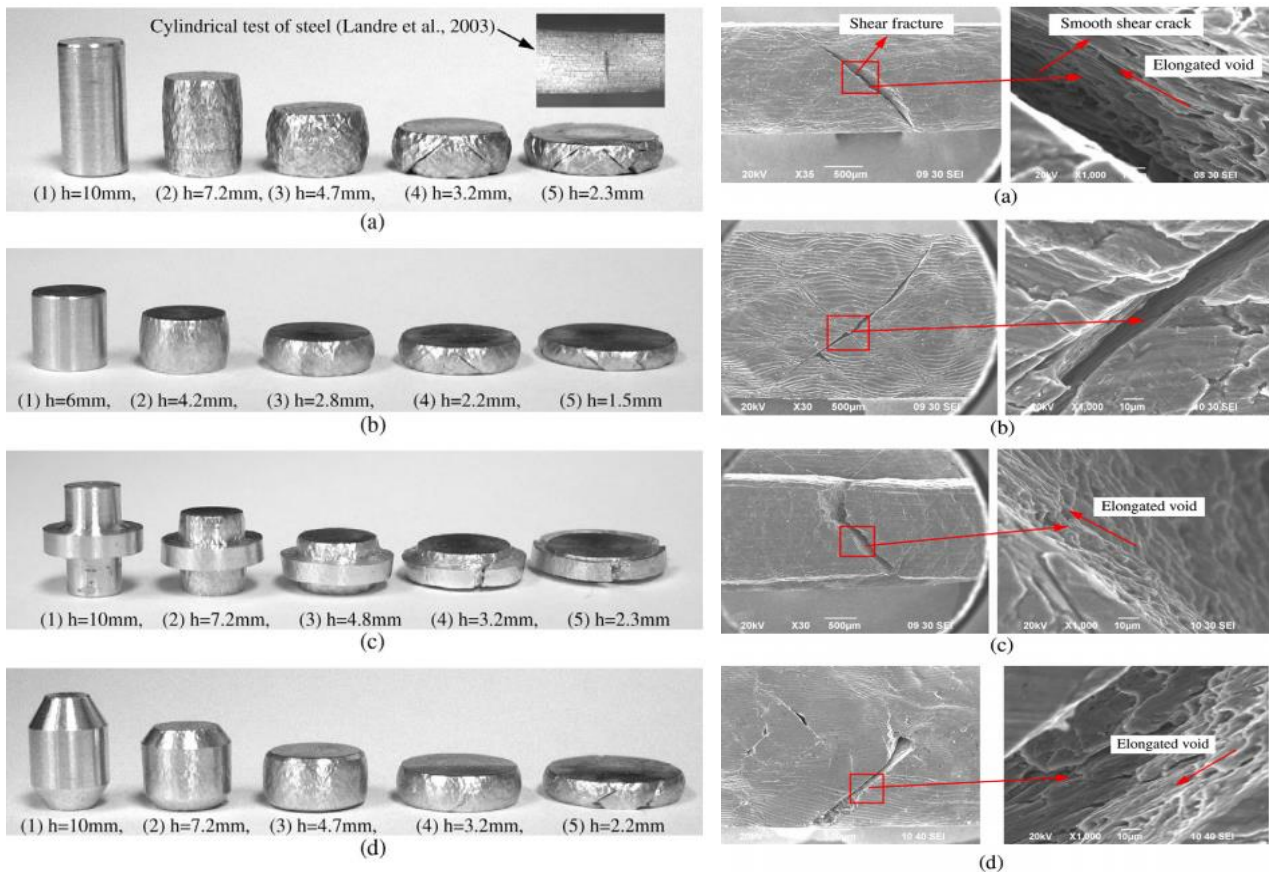


Figure 2.29. Upsetting Tests and Relative SEM Fractography: (a) Cylindrical Upsetting with $H/D = 2$ (b) Cylindrical Upsetting with $H/D = 1$ (c) Flanged Upsetting (d) Tapered Upsetting, adopted from H. Li et al. [120].

Bai [102] conducted a study of two groups of cylindrical specimens on 1045 steel with different aspect ratios. Cylinder specimens before test and after test are shown in Figure 2.30. DIC was used to measure the displacements between two compressive platens, thus, the speckle pattern

can be seen in Figure 2.30a. Whereas, Figure 2.30b demonstrates the barrel effect and that the specimen did not fail, as the tests observed no crack formation for this particular material. Whilst materials such as AISI 1040 and A12024-T351 show shear fracture, it is possible for some materials like the 1045 steel to show no sign of failure. Bai's [102] research found 1045 steel displays strong pressure dependence on the fracture strain. The fracture strain is small in tensile tests, but it increases to a large value in compressive tests. Therefore, to protect the testing machine, Bai's upsetting tests were stopped without observing fracture. If the upsetting tests carried on it is possible that the load is no longer applied to the specimen, but to the compression platens. This means that sometimes it is necessary to define compressive strength as specific deformations as a percentage of the specimen's original height [122].

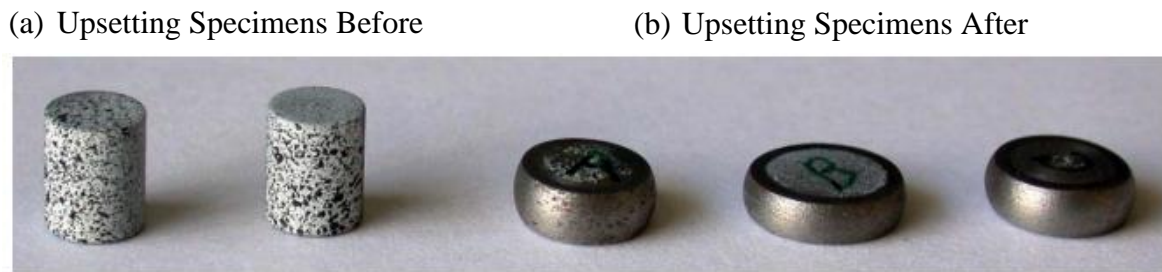


Figure 2.30. Upsetting Specimen's Before and showing the Barrel Effect of the Deformed Specimens, adopted from Bai [102].

Friction between specimens and compression platens generates barrelling causing fracture, however it can produce complications for FE simulations. Thus, following Bao and Wierzbicki's upsetting tests they decided to introduce a new compression specimen. The development of the new geometry led to a novel compression test, which removes the detrimental effect of friction with crack formation at the surface. The unique specimens were machined as large diameter round bars with a notched small gauge section in the middle, as shown in Figure 2.31. The specimen presented deformation localised in the gauge section and their experiments show that fracture initiation occurred at the equatorial area. Figure 2.31 shows no deformation in the shoulders of the specimen, confirming there was no horizontal force acting on the ends of the geometry caused by friction.

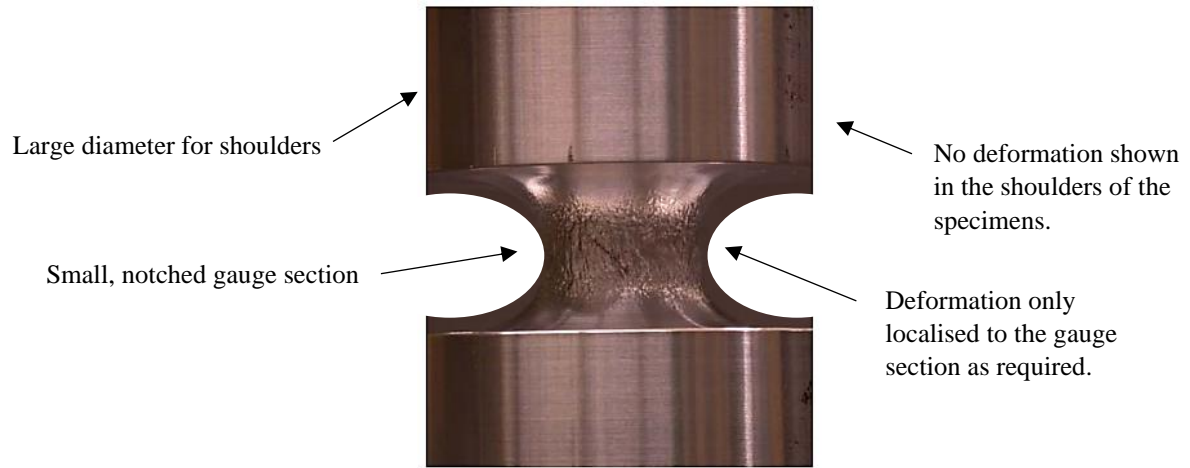


Figure 2.31. New Configuration of Compression Specimen showing Shear Fracture, adopted from Bao and Wierzbicki [12].

2.7 Summary

- AISI 304L stainless steel is presently used for nuclear transport packages, subject to the type of package for the internal and external shock absorbers, as well as being used for thin-walled transport packages. CA6NM has not yet been used to produce nuclear transport packages, however, the material provides the essential mechanical properties for thick wall castings for nuclear transport packages.
- The fundamentals of ductile fracture are continuously being extended by incorporating innovative knowledge on ductile fracture. This is shown by the evolving approaches, methodology and extensions of failure criteria. Literature regarding ductile fracture including its history has been summarised.
- Fundamentals of stress state, regarding stress triaxiality and Lode angle parameter and how they relate to a fracture locus have been discussed. A fracture locus was constructed using a variety of data points across three distinctive regimes of stress triaxiality and their relative loading conditions, for each region the geometries used by previous researchers were shown.
- There is restricted data for both AISI 304L and CA6NM with regard to a fracture locus, therefore there is currently a limitation to the literature present.
- Limitations in obtaining a fracture locus data for both AISI 304L and CA6NM.

2.8 Research Gap

Obtaining fracture data to construct a fracture locus can be done using FE analysis, to do this true stress strain data is needed. However, for a uniaxial tension experiment, true stress–strain data can only be extracted up to the onset of diffuse necking. Different strategies have been developed over the last decades to address this issue, can be divided into four groups: analytical corrections, inverse methods, experimental–numerical iterative approaches and direct methods. The analytical corrections for round bar specimens can be shown by Bridgman (1952) as previously discussed in Section 2.4.2. Analytical models use FE analysis as far as the stress-triaxiality approximation is concerned. Inverse methods use a reference stress-strain curve and iteratively adapt to reduce the divergence between the experimental data and FE analysis. Experimental–numerical iterative methods, iteratively change parameters which describe strain hardening in a detailed FE analysis of the tensile experiments, until there is a good agreement obtained with experimental measurements. A direct method uses instantaneous measured parameters, optical systems such as DIC can be used. DIC can produce data throughout testing, allowing for measurements such as true strain and instantaneous cross-sectional area up to failure to be extracted. As the direct method uses instantaneous measured parameters from the surface of the specimen, it is less time consuming compared to implementing the other methods discussed. Therefore, this thesis will further study the direct method using DIC.

Thus, following this background and literature review there will be a comprehensive independent study for DIC, which will review present research regarding the principles and processes of DIC. An investigation will be conducted into how DIC and FE can work together using the direct method to achieve modelling of ductile behaviour beyond the UTS point. This will allow for a methodology to be developed to obtain fracture data, which will enable a fracture locus to be created. Currently, there are no methodology found which uses DIC and FE to obtain data for fracture loci. The methodology developed from this will be able to be used for any ductile materials, not solely specific to CA6NM and AISI 304L.

3 Digital Image Correlation

3.1 Introduction

DIC is the application of non-contact methods, that utilises random patterns to compare sub-regions, obtaining a full-field of data during testing of structural components [123]. Strain gauges and extensometers provide a single dimension of strain or displacement. DIC has advantages compared to extensometers and strain gauges, as it is possible to assess more complex geometries due to it being a non-intrusive, non-contact method. A range of measurements can be provided from DIC, such as displacements and strains across the material, capturing various data from deformation testing up to failure.

Optical methods of stress analysis became a major research topic following the development of interferometry. Application for optical testing was created when Twyman and Green [124] used a modified Michelson interferometer to test optical components. Peters and Ranson [125] were among the first to introduce digital image techniques as they are currently known. They suggested the simplest approach for displacement measurements, is to correlate two speckle images mathematically in a similar process used for area correlation in pattern recognition. This method incorporates a system allowing the cross-correlation of a reference scene with a stored image. The utilisation of DIC was further established when Sutton et al. [126], [127] conducted experiments for the application of DIC methods. The researchers formed the basis of methods presently used for DIC. The experiments set up used a random speckled pattern and digital video acquisition to find parameters of interest for problems regarding rigid body dynamics. In recent studies, DIC is frequently used throughout experiments within failure mechanics. Researchers [96][102][107][128] have used DIC to obtain material failure data for a range of geometries and loading conditions.

DIC techniques are broadly used in a range of industries including Automotive (Shown in Figure 3.1), Biomechanics (Shown in Figure 3.2), Construction (Shown in Figure 3.3), and has also been used for the NASA Space Shuttle Program for buckling tests as displayed in Figure 3.4 [129].

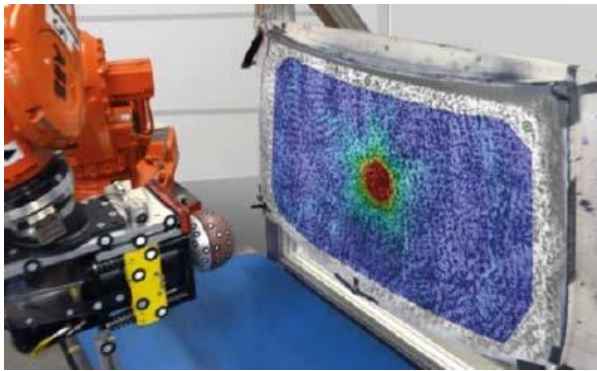


Figure 3.1. Using DIC for Airbag Testing in the Automotive Industry, adopted from Trillion [130].

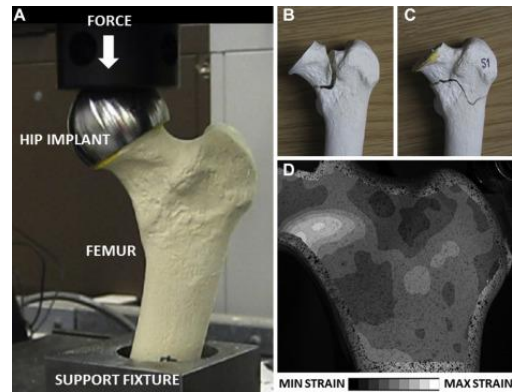


Figure 3.2. Using DIC for Femur–Implant Construct Under Load, adopted from Rankin et al. [131].

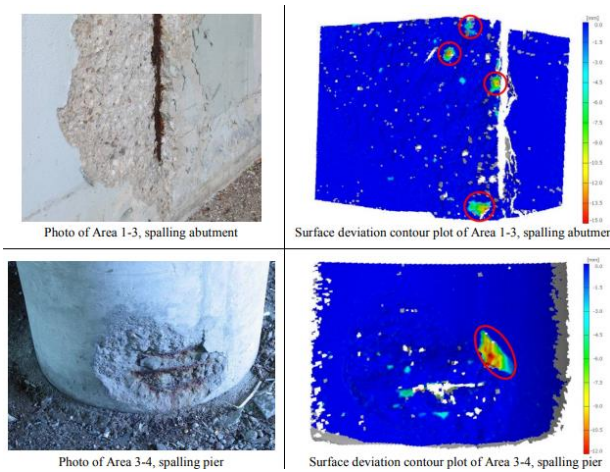


Figure 3.3. Using DIC for Structural Health Monitoring of Bridges, adopted from Nonis et al. [132].

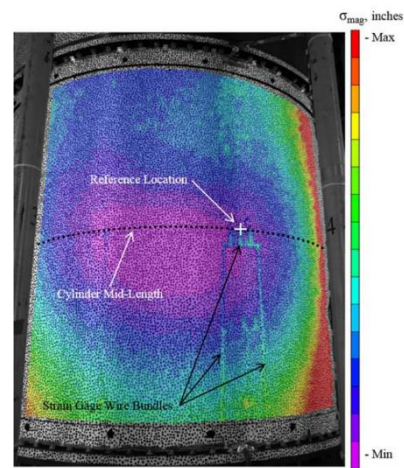


Figure 3.4. Magnitude of Measurement Uncertainty for Cylindrical Shell during Buckling Test, adopted from Gardner et al. [133].

In recent studies, DIC is used to obtain material failure data for a range of geometries and loading conditions, assessing a diverse range of materials, due to its simple and cost-effective results. This includes evolution and uniformity of strain in materials testing, crack tip and crack propagation investigations, identifying damage evolution and structural deformation, as discussed in existing literature [102][128][107][96][134].

The method of using optical measurement systems such as DIC in parallel with FE analysis for validating data, has been used by a series of researchers [107][135][136][137][138][139]. Utilising both DIC and FE analysis is a direct and efficient approach for identifying material parameters during testing [138]. For example, researchers have compared the measured strain evolutions from DIC and the calculated strains from the FE simulation, to find the results indistinguishable, meaning the determined material properties used for the FE analysis had substantial accuracy [113]. This is shown in Figure 3.5, which compares the force displacement curves of DIC and FE analysis of a tensile experiment, up to the onset of failure. This agreement between the force displacement curves of DIC and FE analysis was also demonstrated for in-plane shear testing and is not exclusive to tensile testing [140].

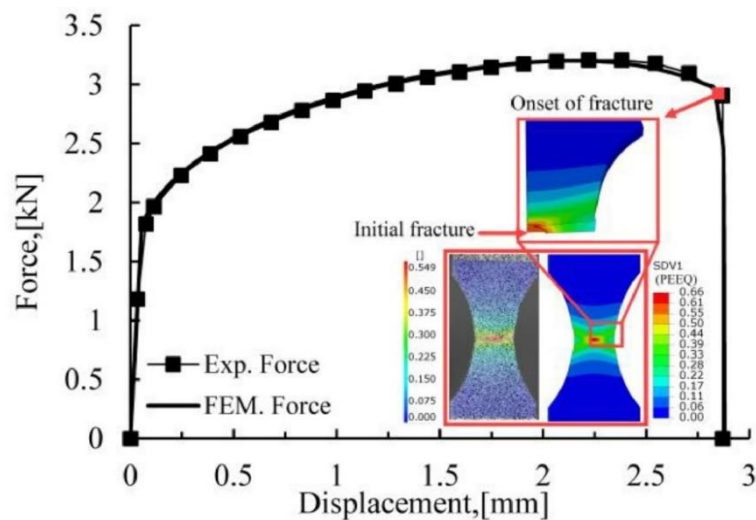


Figure 3.5. Comparison of Load-Displacement Curve, adopted from Quach et al. [140].

Using both these methods alongside each other is becoming an adopted methodology for validating fracture experiments. With using both FE and DIC no fracture model will be used. However, it is important to note, both of these methods have their own parameters that may lead to an accumulation of errors when modelling the deformation process (e.g., FE analysis: inadequate mesh refinement / DIC: poor quality of the speckle pattern).

3.2 Aims and Objectives

- Review present research to understand core principles and processes of DIC.
- Establish a standard of preliminary requirements to achieve the optimum experimental set up, by exploring parameters such as: equipment selection and what makes a suitable speckle surface.
- Investigate the effect of applying filtering during post processing of DIC data.
- Evaluate and summarise numerical and experimental potential DIC errors.

3.3 Basic Principles of Digital Image Correlation

The basic principles of DIC are relatively simple. Displacements are determined from a set of images taken before and during deformation of a specimen's surface, which typically has a distinguishable speckle pattern. Assumptions are made that features of the structure surface are displaced together and are preserved after deformation [141].

Pixel (px) is short for picture element; it is the smallest information in an image. A typical speckle pattern is shown in Figure 3.6a, the individual pixels of this image are represented using squares, as shown in Figure 3.6b. Intensity is known as the brightness level of light, and each pixel has its own level of intensity. A bit is the amount of tone variation in the obtained image, i.e. 16-bit image has more tones available for a given colour than an 8-bit image. For a greyscale 8-bit, the value of each pixel ranges from 0-255, where the lowest number represents black and the highest represents white, the range in-between is different shades of grey. This can be demonstrated by a histogram of the speckled pattern as shown in Figure 3.6c [142][143].

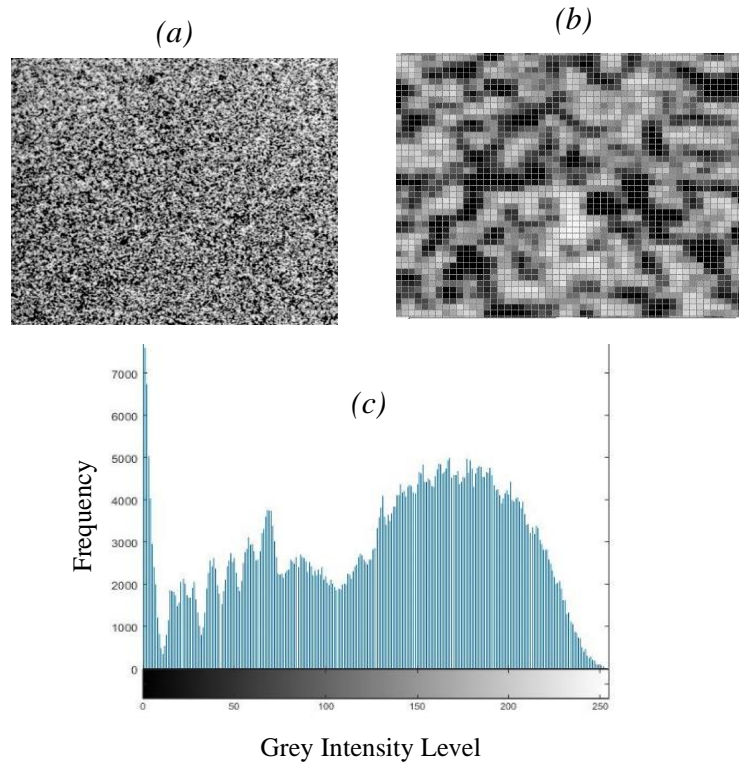


Figure 3.6. a) Typical Specimen Pattern b) Pixels of Pattern c) Histogram of Pattern.

A subset (also known as a facet) is a portion of the speckle pattern, which is selected during the reference state for calculation of the displacement throughout testing, as shown in Figure 3.7. The initial position of a subset from the reference image is matched to the deformed subset. DIC uses an optimisation algorithm to compute a field of displacements by tracking multiple subsets.

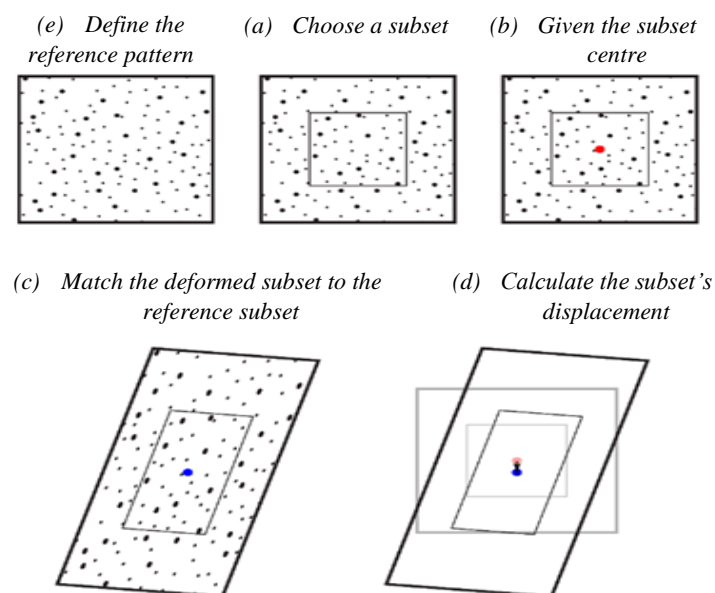


Figure 3.7. Subset Displacement during Deformation, adopted from LePage [144].

3.4 DIC Correlation Criteria

A predefined matching criterion (also known as the correlation criterion) and a optimisation algorithm is needed during the DIC process. Robustness, computational cost and reliability of a matching criterion are of great importance, as deviations during experiments such as unstable or uneven lighting and non-uniform contrast may occur [145]. Fundamentally, matching criteria must reduce the difference between the reference and moved subset. Sum of squared difference (SSD) Criteria is shown in Table 3.1 by Equation 38. The reference subset (as shown in Figure 3.8) $F(x_i, y_i)$ and the moved subset $G(x_i^*, y_i^*)$, are represented by the greyscale intensity of the i th pixel. This can be further simplified from $F(x_i, y_i)$ and $G(x_i^*, y_i^*)$ to F_i (greyscale intensity for reference subset) and G_i (greyscale intensity for deformed subset) respectively [141][146].

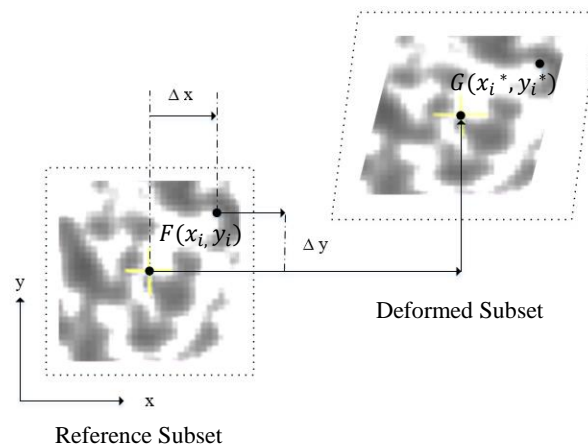


Figure 3.8. Deformation of Subset Before and After.

Sutton et al. [123] stated that the method of DIC owes its name to the cross correlation (CC) criterion. However, the CC criterion is one of many matching criteria. Literature includes a variation of additional criteria such as; sum of absolute difference (SAD), sum of squared difference (SSD), and parametric sum of squared difference (PSSD) as shown in Table 3.1 [146][123][147].

Table 3.1. Summary of Various Correlation Criterion [148][149][146].

Correlation Criterion		Equation	
Direct Cross-Correlation	(CC)	$\sum F_i G_i$	(38)
Zero-Mean Cross-Correlation	(ZCC)	$\sum [(F_i - \bar{F})(G_i - \bar{G})]$	(39)
Normalised Cross-Correlation	(NNC)	$\frac{\sum F_i G_i}{\sqrt{\sum F_i^2 \sum G_i^2}}$	(40)
Zero-Mean Normalised Cross-Correlation	(ZNCC)	$\frac{\sum \bar{F}_i \bar{G}_i}{\sqrt{\sum \bar{F}_i^2 \sum \bar{G}_i^2}}$	(41)
Sum of Squared Difference	(SSD)	$\sum (F_i - G_i)^2$	(42)
Zero-Mean Sum of Squared Difference	(ZSSD)	$\sum [(F_i - \bar{F})(G_i - \bar{G})]^2$	(43)
Normalised Sum of Squared Difference	(NSSD)	$\sum \left(\frac{F_i}{\sqrt{\sum F_i^2}} - \frac{G_i}{\sqrt{\sum G_i^2}} \right)^2$	(44)
Zero-Mean Normalised Sum of Squared Difference	(ZNSSD)	$\sum \left(\frac{\bar{F}_i}{\sqrt{\sum \bar{F}_i^2}} - \frac{\bar{G}_i}{\sqrt{\sum \bar{G}_i^2}} \right)^2$	(45)
Parametric sum of Squared Difference	(PSSD _{ab})	$\sum (aF_i + b + G_i)^2$	(46)
Sum of Absolute Difference	(SAD)	$\sum F_i - G_i$	(47)

The maximisation of the CC criteria is equivalent to the minimisation of the corresponding SSD criterion. Thus, subset matching can be intuitively achieved by minimising the difference between the reference and target subsets [146].

Deviations in lighting are challenging to regulate during experimental tests, the difference in viewing angles among cameras for a stereo rig set up may produce variances in the images illumination [123]. The main limitation of SSD Criteria is its inability to account for any change of the intensity of the moved subset [123][146]. In order to solve this issue and accommodate intensity changes, a variation of SSD criteria, PSSD_{ab} has been developed [146]. The software used in this project provided by Dantec Dynamics uses PSSD_{ab}, the correlation algorithm was predetermined with the software. The generalised PSSD_{ab} coefficient (as shown in Table 3.1)

has unknown parameters a and b to resolve for both the offset and scale changes of the intensity of the target subset.

Studies [148][146] found that correlation criterion such as; ZNSSD, PSSD and ZNCC, are acclaimed for their practical use as they are all insensitive to the scale and offset changes of the deformed image. Subset deformation is an important characteristic to capture, as subsets may deform with the deformation of the objects surface. When displacements are smaller than 1 pixel, the process detailed above does not apply, as this includes discrete pixels. This leads to a method for determination of displacement for subpixel resolution. There are a few subpixel algorithms such as; correlation coefficient curve-fitting method, the Newton–Raphson iteration and the gradient-based methods. These methods are found in DIC literature due to their accuracy and simplistic approach. The Newton–Raphson iteration has the highest accuracy and best stability but, has a much greater computation cost compared to the other algorithms due to the Hessian matrix. The Newton–Raphson iteration includes the rotation and deformation of subsets, which makes it an ideal subpixel registration algorithm at high strains and deformations [150][151].

3.4.1 DIC Set up and Definitions

Classification of DIC testing is composed of two main testing methods. Two dimensional methods using a single camera as shown in Figure 3.9 (also known as 2D-DIC) is associated with in-plane specimen testing [147]. If the 2D-DIC experiences any out of plane motion (e.g., due to misaligned grips) it causes significant errors, and if the specimen is of a curved surface, 2D-DIC testing method does not apply. The testing then requires two cameras, which is called stereo-DIC (also known as 3D-DIC) [148]. Overall, stereo-DIC is the preferred method if possible, but 2D-DIC can be used when two cameras do not fit within the rig layout [152].

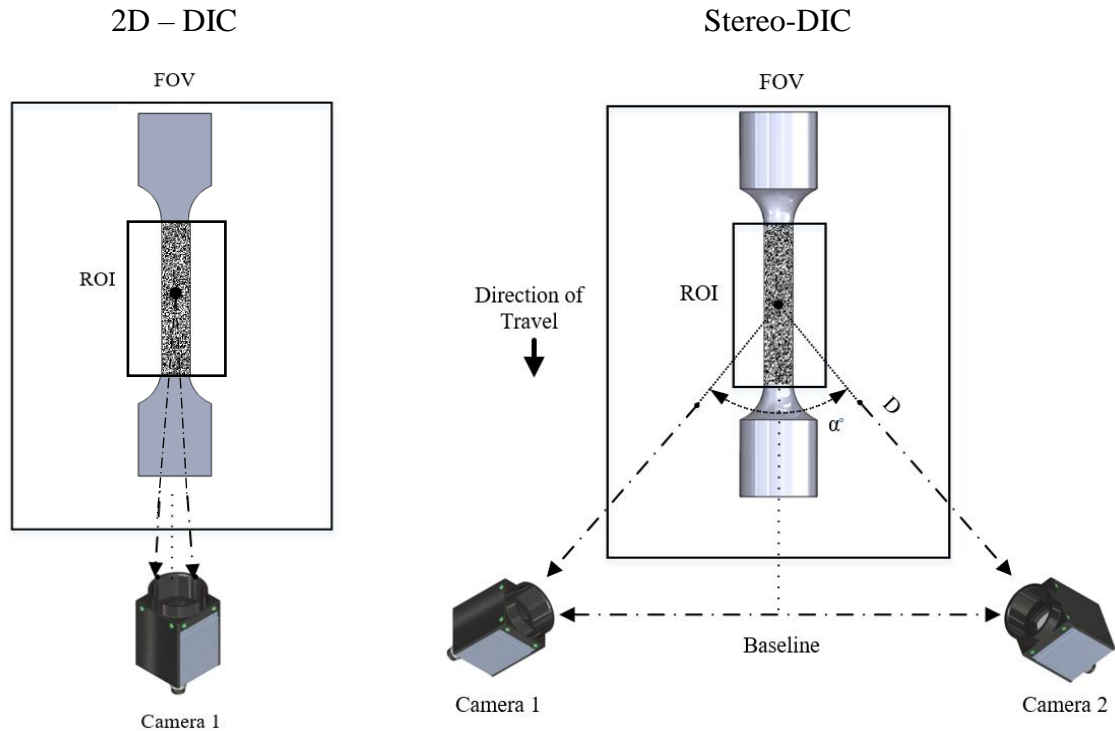


Figure 3.9 Diagram showing 2D Test Rig Set Up and Stereo Rig DIC Set Up.

In stereo-DIC there are two cameras used to take simultaneous images. The stereo rig design has a series of parameters which must be considered during the set-up phase. Part of these requirements are divided into intrinsic and extrinsic parameters. Intrinsic parameters relate a single camera image to the physical world, thus applying to both 2D-DIC and stereo-DIC. Intrinsic parameters include; focal length, image centre and scale. For a stereo rig set up, the extrinsic parameters are used to determine the relationship between the cameras coordinate system for triangulation. Extrinsic parameters include; stereo-angle, baseline and stand-off distance [152][153]. In order to obtain accurate measurements, high quality images need to be taken from a rigid test rig. The resolution of images is determined from a range of conditions such as, lens and speckle pattern quality, lighting conditions, camera noise and motion resolution [153]. Design of the DIC measurements is summarised in Appendix B with definitions and relative equations.

3.5 Main Processes for Digital Image Correlation

The core procedures of DIC are separated into 6 processes as shown below and by Figure 3.10.

- 1) **Design of DIC Measurements:** Determining the required measurements and any adjustments necessary. This consists of making sure the equipment's selection such as camera, lens and lighting is adequate. Within this process there must be a suitable speckle surface applied on the region of interest (ROI) of the specimen.
- 2) **Pre – Calibration:** Adjusting the DIC system until high quality images are obtained, this is done by reviewing the test procedure and setting up the hardware. Any environmental conditions that may affect testing must be considered, and any changes needed must take place during this process to ensure that conditions are stable during the experiment. Pre-calibration routine includes positioning the specimen and verifying the camera setup: taking account for the depth of field (DOF) and the specimens change in displacement during testing. DOF is defined as the distance between the closest and farthest regions of an image which is in focus. Taking static images at this stage, can highlight many issues including any glare, defects in speckle pattern and uneven lighting distribution. If there are any issues found, this process must be repeated iteratively. Thus, eliminating any issues until the system is acceptable to move onto the next procedure [152].
- 3) **Calibration:** Determines all of the intrinsic and extrinsic camera parameters, by extracting data points from a series of images using a calibration target. During the calibration process a number of images of the target are captured, this is done by rotating the target in view of both cameras [154].
- 4) **Post – Calibration:** Verifies the optical system calibration by analysing the noise-floor by taking a series of the static images. This is the final review of the DIC system before any testing takes place. All data acquisition systems need to be ready, such as the storage location of all the DIC images during testing and any triggering test frame signals such as force or displacement [152].
- 5) **Performing DIC Experiment:** Once the experiment starts, the DIC acquisition system takes a reference image, followed by a series of images taken until fracture occurs and the test is stopped.
- 6) **Post-Processing of DIC Images:** After the experiment has taken place the images obtained can be evaluated, producing full field data of the specimen from the reference image to failure. Digital filtering methods can then be applied for example; a low-pass filter can be used to soften the edges of a particularly sharp DIC pattern [152][155].

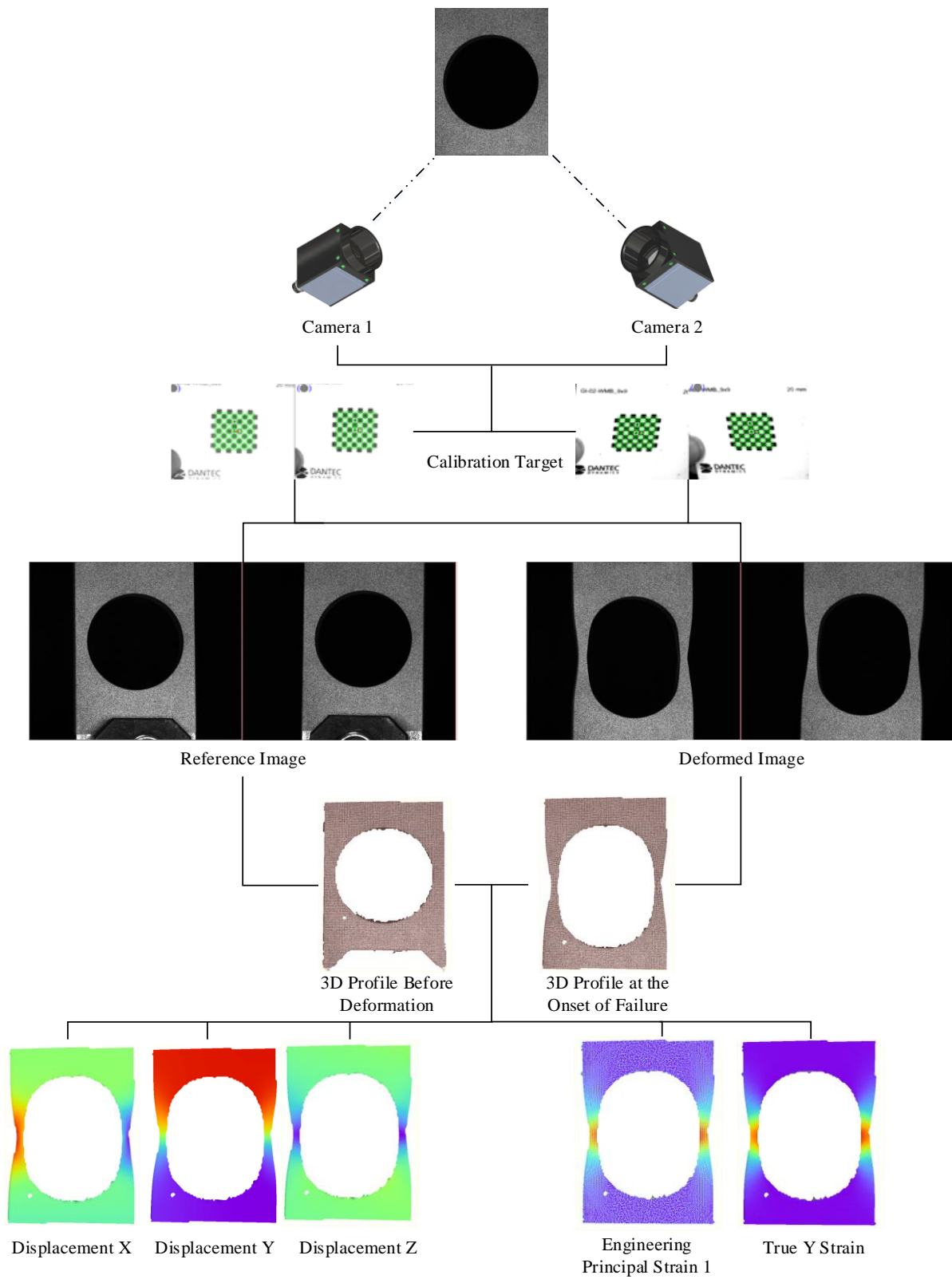


Figure 3.10. Flow Diagram displaying the Main Processes of DIC.

3.6 Preliminary Design of DIC Measurements

To determine the optimum experimental set up, intrinsic, extrinsic and other parameters need to be fully understood. This depends on the geometry being tested, as different specimen geometries require their own individual set up. This section investigates measurement requirements, equipment selection and what makes a suitable speckle surface.

The Dantec digital 3D Image correlation system Q-400 and Istra4D software was used to perform the experiments in this thesis. The experimental setup is shown in Figure 3.11. The two cameras used for all testing were VCXU-50M, the specification for the cameras is summarised in Table 3.2.

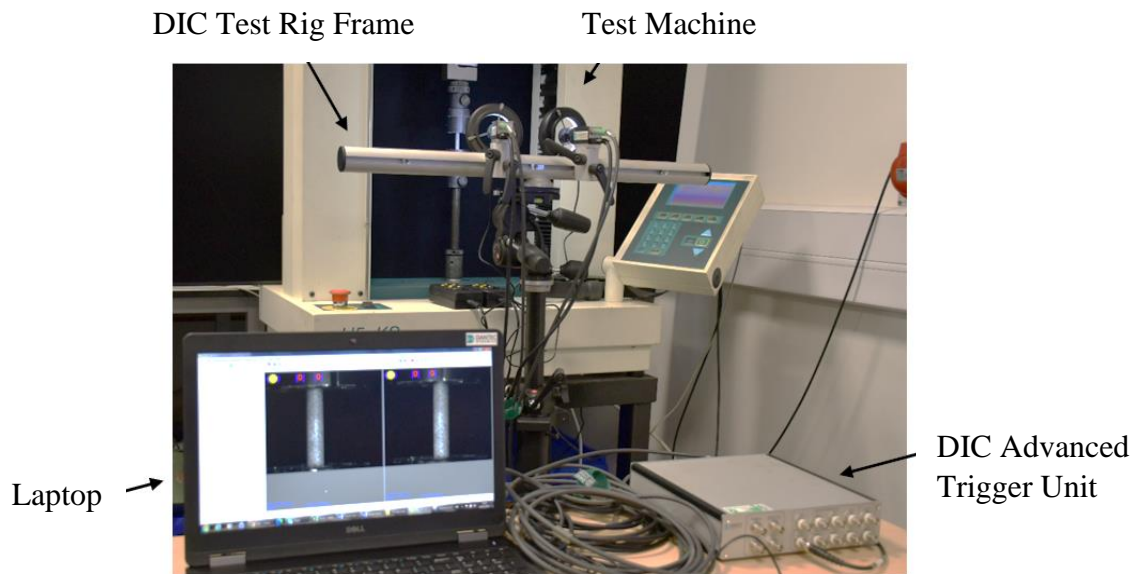


Figure 3.11. Dantec 3D Image Correlation System Q-400 and Istra4D Software Set Up.

Table 3.2. Camera Specification –VCXU- 50M

Sensor:	Sony IMX250 Gen2
Resolution:	2448 × 2048 px
Exposure Time:	0.001...60000ms
Pixel Size:	3.45 x 3.45 μm
Shutter Type:	Global shutter
Sensor Type:	2/3" CMOS
Acquisition:	Full Frame, 2448 × 2048 px, max. 77 fps

3.6.1 Lens Selection and Extension Tubes

There are two main characteristics that describe a lens, the focal length and the aperture. Focal length describes how much of the view is captured. The equipment provided with the Dantec package consists of 16mm and 50mm lenses, as well as a range of extension tubes ranging from 0.5mm to 40mm spacers (as shown in Figure 3.12). Different geometries have a range of field of view (FOV) and region of interest (ROI), meaning a variation of lens and extension tubes may need to be used.



Figure 3.12. Lens and Extension Tube Provided in DIC Package.

When the focal length is longer, the angle of view becomes narrower, and the magnification is increased. Thus, the shorter the focal length, the wider the angle of view and the magnification is reduced. Extension tubes can be used to increase the magnification [156].

As an example, the difference in between the 50mm and 16mm lens for a notched bar is displayed in Figure 3.13. The minimum working distance is very important, Figure 3.13b shows the effect of the limiting distance of the support frame relative to the specimen. The image cannot be in focus as a result of this. The images shown in Figure 3.13c/d display that when using a 16mm lens the FOV is too large for this particular set up.

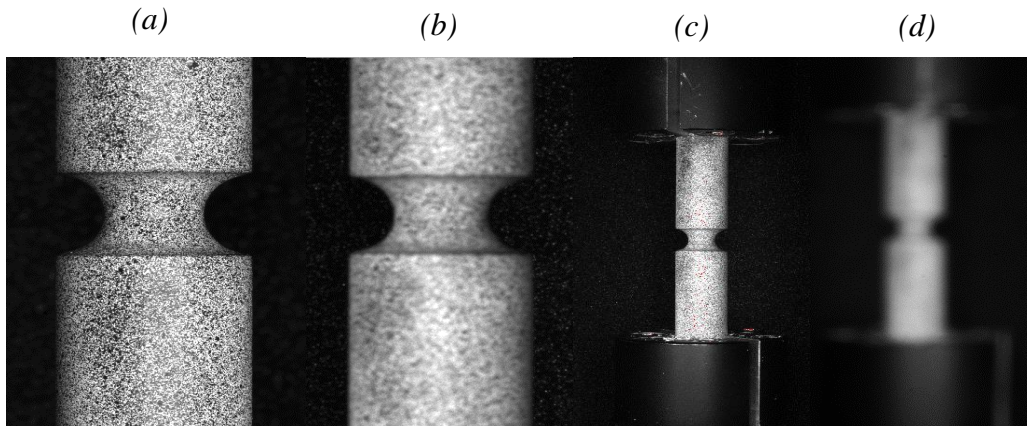


Figure 3.13. a) 50mm Lens + 10 mm Extension Tube, b) 50mm Lens + 5 mm Extension Tube
c) 16mm Lens d) 16 Lens + 5 mm Extension Tube.

The amount of light that passes onto a camera's sensor depends on the size of the opening in the lens, also known as aperture. Within a lens diaphragm are aperture blades, which are adjusted by an aperture ring. The size of the opening is determined by the magnitude of f-stops, where the bigger the f-stop the smaller the aperture, as shown in Figure 3.14. Whilst aperture controls the brightness of the image, it also directly affects the DOF.



Figure 3.14. Aperture Example [156].

During the initial DIC set up, the aperture depends on the required DOF. For example, Figure 3.15 displays a notched round specimen, which needs a large DOF in order to keep all of the geometry in focus.

Spatial resolution is dependent on the number of pixels that are used to construct a digital image. For example, when considering two images with the same dimensions of the imaging part, one may have more pixels than the other, meaning that it is the higher spatial resolution image. Spatial resolution is a measurement that can determine the quality of an image by referring to the smallest object that can be resolved by the camera's sensor [157], [158].

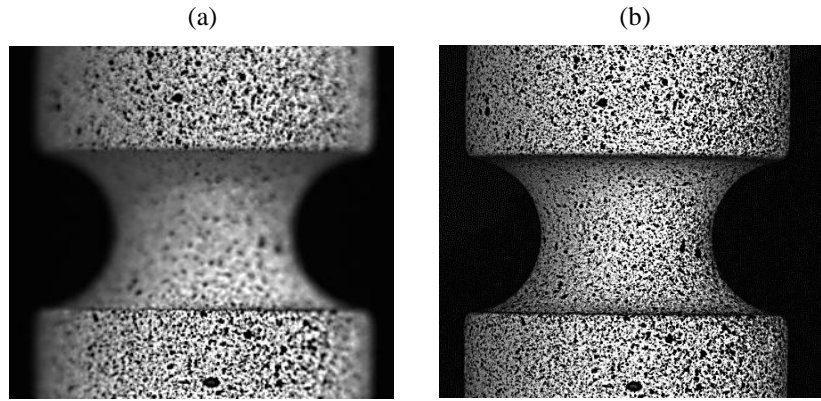


Figure 3.15. Depth of Field Example a) Image when using F2.8, b) Image when using F16.

3.6.2 Stereo Angle Selection

Stereo angle is an extrinsic parameter, defined as the angle between the two camera axes. Stereo angle is conditional on another extrinsic parameter, which is the distance between the two cameras (also known as the baseline). Reducing the baseline decreases the stereo angle. The stereo angle should be between 15° - 35° , depending on the geometry being tested. The narrower the specified stereo angle, the improved in-plane resolution but at cost of the out-of-plane resolution [159]. An example shown in Figure 3.16 displays the reduction in grid points matched when the stereo angle is increased. Whilst this may increase the out-of-plane resolution, any missing data points caused by the stereo angle selection for this geometry, means the data would not be captured during testing.

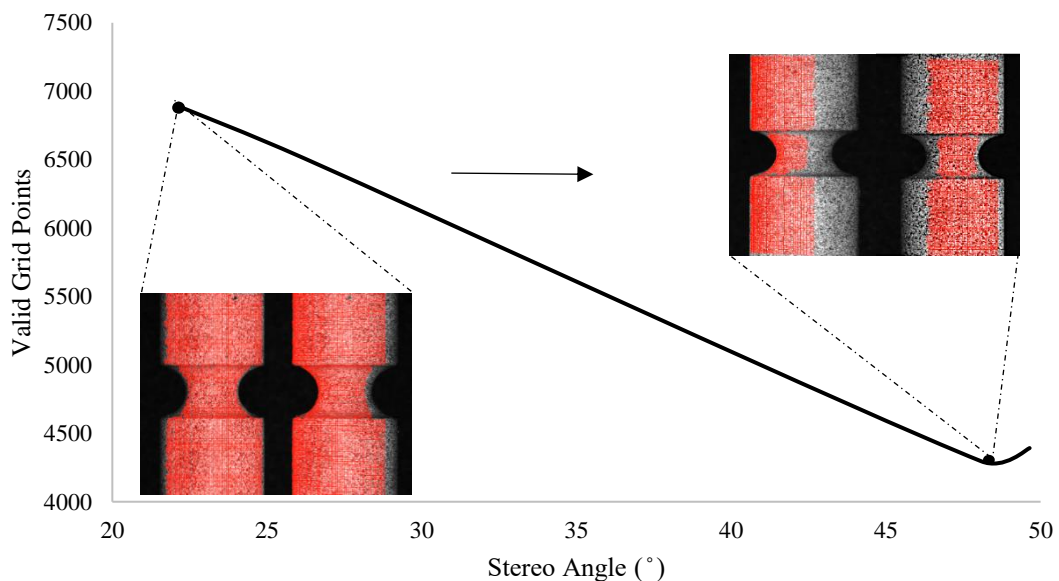


Figure 3.16. Graph showing the amount of Grid Points Depending on the Stereo Angle.

3.6.3 Specimen Pattern

Measurements for DIC cannot be recorded without a speckle surface on the ROI of the specimen. Therefore, the quality of the speckle pattern on the specimen is important when obtaining reliable and deformation measurements. The quality of the speckle pattern directly affects the resolution of the data produced [160][161]. There are four main attributes that make a speckle pattern; contrast, size and speckle edge and density. There is not one speckle pattern that can be used for all testing, because what is suitable for one test may not be for others. The purpose of a speckle pattern is to work in conjunction with lighting conditions to create a digital image that has a random high-contrast, low noise pattern. Increasing the gain of the camera amplifies the signal, increasing the number of counts recorded by the camera, however, this also generates more noise in the image [162].

The cameras used in this study have a resolution of 2448×2048 px as shown in Figure 3.17.

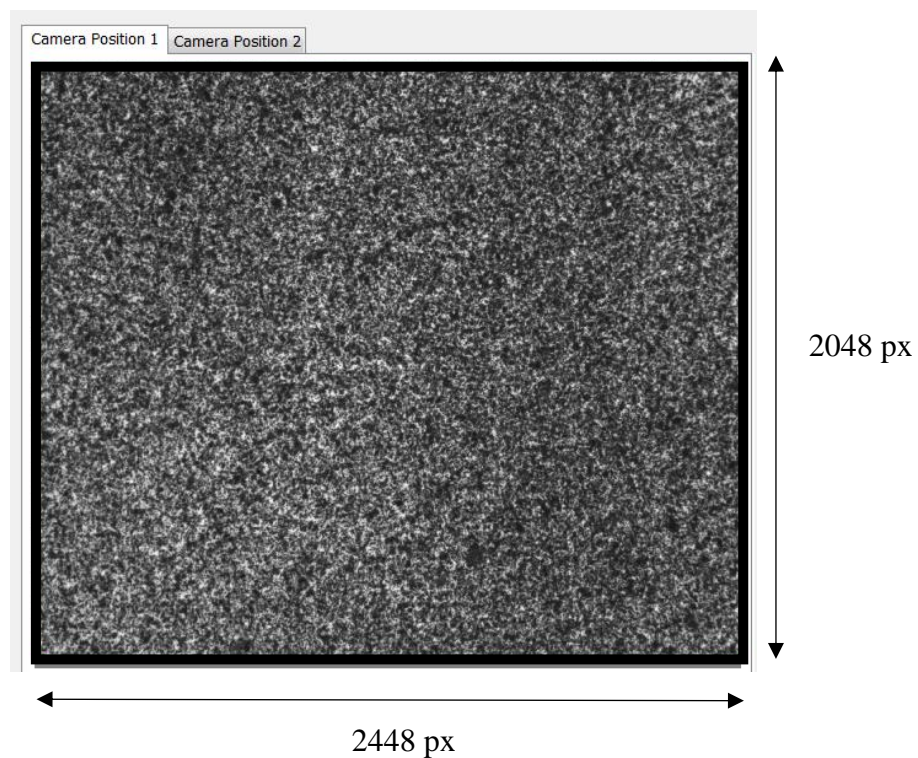


Figure 3.17. Resolution of Camera.

3.6.3.1 Speckle Size

Determining the optimum speckle size is challenging. The initial step is calculating the number of pixels the specimen has across the FOV for the mm/px. From this the physical size of speckles can be found by multiplying the pixel size (mm/px) by a factor of 3 [163]. Researchers have generated a general specification regarding speckle size as summarised below, this applies to not only the average but also the smallest or largest speckle [164][165][164][166]:

- A speckle must be ≥ 3 px in size (including white and black regions).
- If a speckle is ≤ 2 px in size, then they are too small and may cause aliasing.
- Speckles cannot be too big (e.g., 10 px in size) due to spatial resolution.
- Once an optimum speckle pattern is generated for a set FOV. Increasing the FOV makes the speckles too small. Whilst, decreasing the FOV increases the speckle size causing issues with spatial resolution.

Aliasing is caused by speckles being too small and happens when the image is processed through the camera. If aliasing takes place data maybe lost and it's not possible to recover in post-processing. One of the main issues with aliasing, is once a speckle is digitalised it's impossible to determine if it is aliased. An example of aliasing is shown in Figure 3.18. Figure 3.18a has white circles which represent a speckle 1 px in size, whilst in Figure 3.18b the speckle is at least 3 px in size. The diagram highlights the challenges locating the centre for when a speckle is only 1 px in size, whereas the shape of the speckle when at least 3 px in size is visibly defined [163].

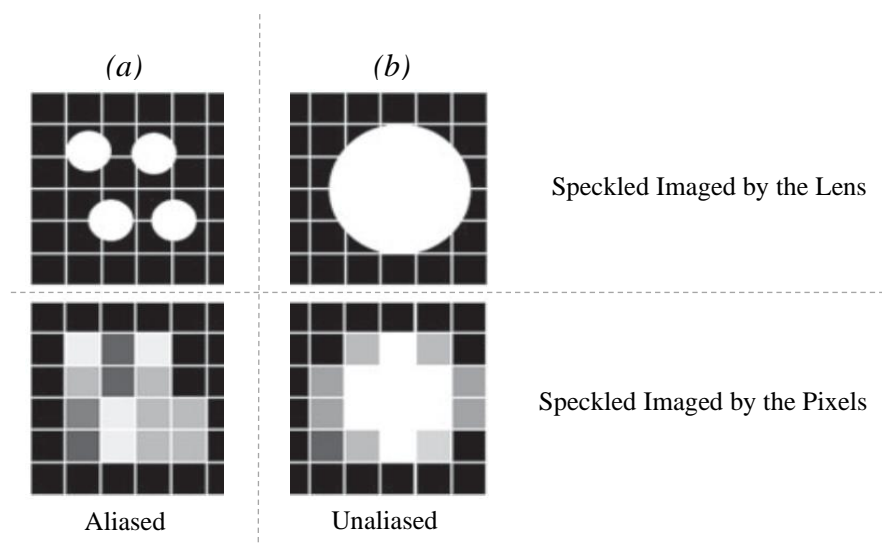


Figure 3.18. Diagram showing a) Aliased and b) Unaliased Speckle Images, adopted from Reu [163].

3.6.3.2 Contrast

For a speckle pattern, contrast is defined as the difference between grey levels (also known as counts) for the dark and light speckles [167]. High quality speckle patterns should have a contrast with the background to reduce the noise level during testing. By increasing the contrast of the speckle pattern particularly in the ROI, the displacement measurement accuracy of the DIC is enhanced [168]. As subsets are independently calculated, it is important that there is contrast within every subset. Histograms of speckle patterns can show the contrast range. The grey levels for an optimum pattern should cover a large range from 20-230 and at least 50-75 grey levels. Grey levels of 255 may cause saturation and should be avoided to ensure it does not affect the accuracy of the results [123], [169].

The range for intensity pattern contrast is achieved when selecting a camera which has more bits. This study uses pre-selected cameras as part of the Dantec DIC package, both cameras are limited to 8 bits [123]. However, it is possible to increase contrast and reduce the amount of noise by utilising parameters such as lighting conditions, and the method of applying the speckle pattern i.e. matt white paint [167].

Edge sharpness of a speckle is dependent on the speckling technique. Sharp-edged speckles characteristically have two grey levels between black and white regions. Whereas soft-edge speckles have a few more pixels in between the transition of the white and black regions. The main issue with sharp-edged speckles, is that they maybe aliased by the detector. However, to find the optimum balance between the discussed parameters such as speckle size, contrast and edge sharpness is difficult. Thus, it is necessary to assume the ideal edge sharpness to be of secondary importance [170].

The final property of a speckle to be discussed is density, also known as spatial distribution. The ideal spatial distribution is to have equal areas to black speckles and white areas. Speckles must be isotropic with no directionality, for subsets to be matched. Subset size is critical as it governs the spatial distribution and also the speckle size [169].

3.6.3.3 Different Methods to Produce Speckle Patterns

If a material has natural and semi-natural texture distribution characteristics on its surface, the texture can be used to perform DIC testing. However, this project only considers artificial speckle patterns [171][172].

There are a variety of methods to create the desired characteristics of a speckle pattern for specimens. Researchers have generated methods such as painted speckle technique, airbrushing and computer-generated random patterns [161]. A study conducted by Ashrafi and Tuttle [173], used two different methods. For the first method, the speckles were produced by using white and black spray, whilst the random-speckle pattern for the second method was generated digitally. Computer generated random patterns require perfect bonding between the surface of the specimen and the speckled paper. The contour plots in Figure 3.19, show a plate with hole specimen under tension loading conditions. The comparison found that the painted and printed speckles both accurately predicted strain fields.

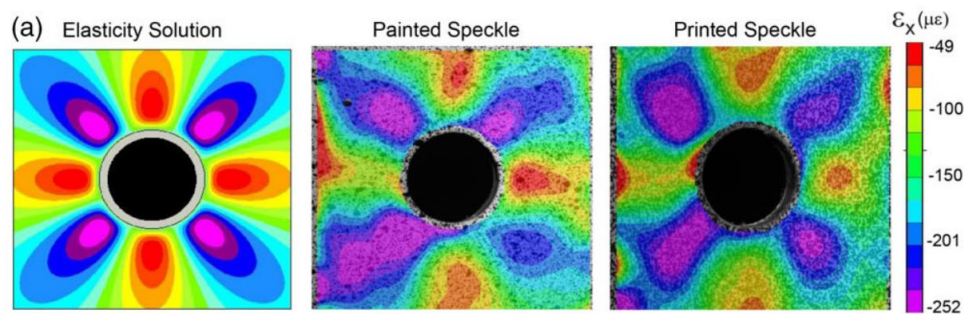


Figure 3.19. Plate with Hole Specimen using Painted and Printed Speckle Pattern [173].

The most common method of applying a speckle pattern is using spray paint, as it is easy to create a contrasting speckle pattern. In order to produce a pattern using spray paints, first matt white paint is applied to the specimen then it is left to dry, then black paint is sprayed on top. However, it can be problematic to achieve the necessary size contrast. Flexible paint is needed at the surface, especially when testing materials that have high deformations. The painting technique is typically done by applying thin coats of a spray paint primer. White paint should be applied not too thick but enough to cover the specimen surface [174]. Over spraying the ROI may compromise the contrast leading to speckles to become aliased [169]. The main limitation of spray paint is the prospect of failure of paint at high strains leading up to failure of the specimen. This means it is required to leave the period between painting and testing as

small as possible, it was found that between 30-60mins was the optimal time. Figure 3.20 shows a tensile specimen tested after 24 hours after being painted, the paint became separated from the specimen before failure meaning that deformation data was unable to be captured.

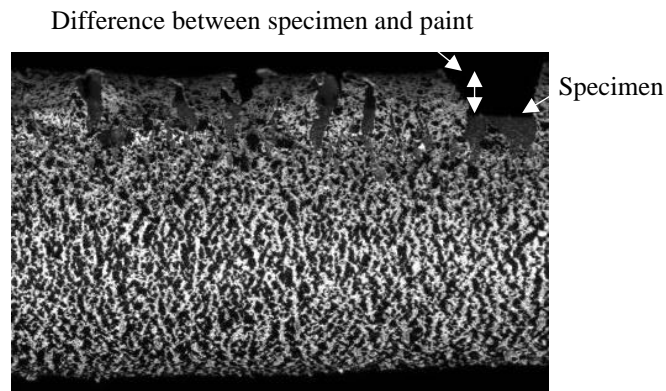


Figure 3.20. Paint Failure before the Specimen Fractures on a Tensile Test.

A preliminary experiment was conducted to find the optimum speckle pattern for a particular set up, as shown in Figure 3.21. Within this test, nine different speckles were produced using spray paints, with their relative histogram generated using MATLAB and grid of matched subsets produced by the DIC software. The results of all nine experiments are shown in Appendix C. Two of the results from the test are shown in Table 3.3.

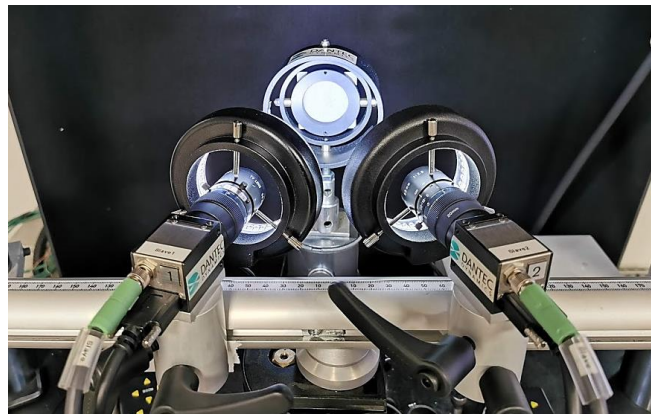
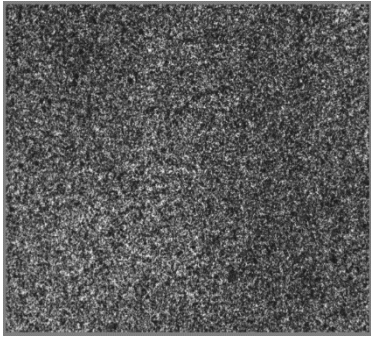
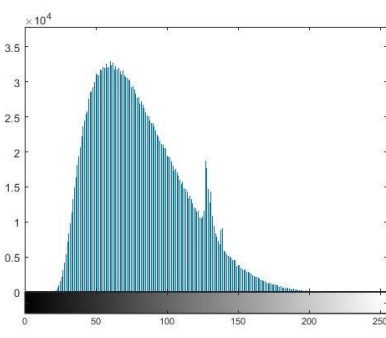
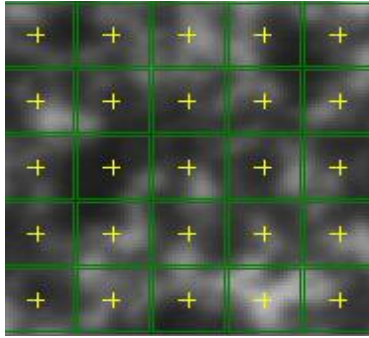
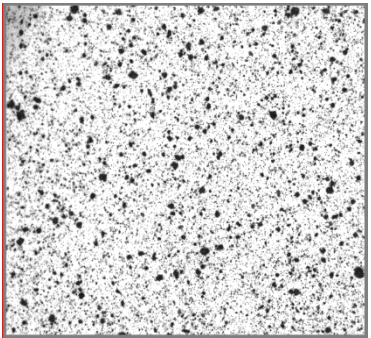
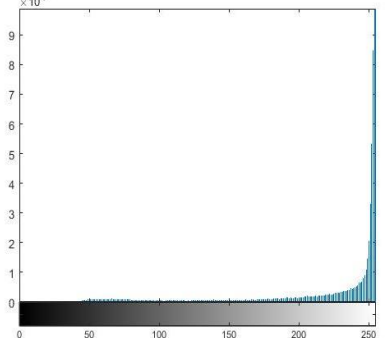
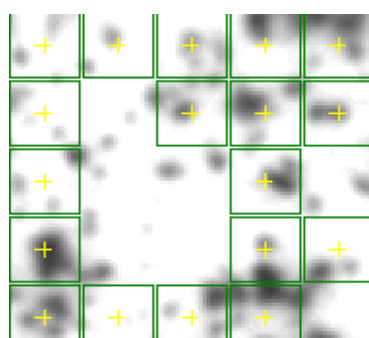


Figure 3.21. DIC set up for Speckled Pattern Tests.

Table 3.3. A Range of Speckle Patterns.

	Speckle Pattern	Histogram	Grid of Matched Subsets
Speckle Pattern A			
Speckle Pattern B			

For the majority of the speckle patterns created, the speckle size was too large and ranged throughout the pattern. The speckle pattern B shown in Table 3.3, had too many white regions in which there were no speckles within a subset. This was also displayed by the histogram for the speckle pattern B, as the pattern was showing mostly grey counts of 255. The result of this meant not all of the pattern was able to be matched or the data was not captured. The speckle pattern that had the best contrast was speckle pattern A, as demonstrated in the histogram as it was varied throughout, with a few grey levels of 255.

3.6.3.4 Subset Size

Selecting the subset size is important, as each subset is solved individually, the contrast within a subset is essential to ensure the pattern is matched. This means that a subset must contain more than one speckle [169].

Various subset sizes for the same speckle pattern are shown in Figure 3.22, with the relative true strain contour plots for the Y direction. For the subset size 9x9 pixels, the software would not finish evaluating all the steps. Therefore, the contour shown in Figure 3.22a is the last

evaluated step, demonstrating the subset size does not have enough contrast. A full field of data is achieved for larger subset sizes 21x21 pixels /33x33 pixels. Whilst the relative true strain contour plots for the Y direction for 21x21 pixels and 33x33 pixels look similar, the amount of contrast provided by subset size 33x33 pixels, overall reduces the contour statistical error radius for this particular pattern. The contour statistical error radius is the estimated uncertainty for the 3D coordinate of each data point on the contour mapped as a colour plot for an image.

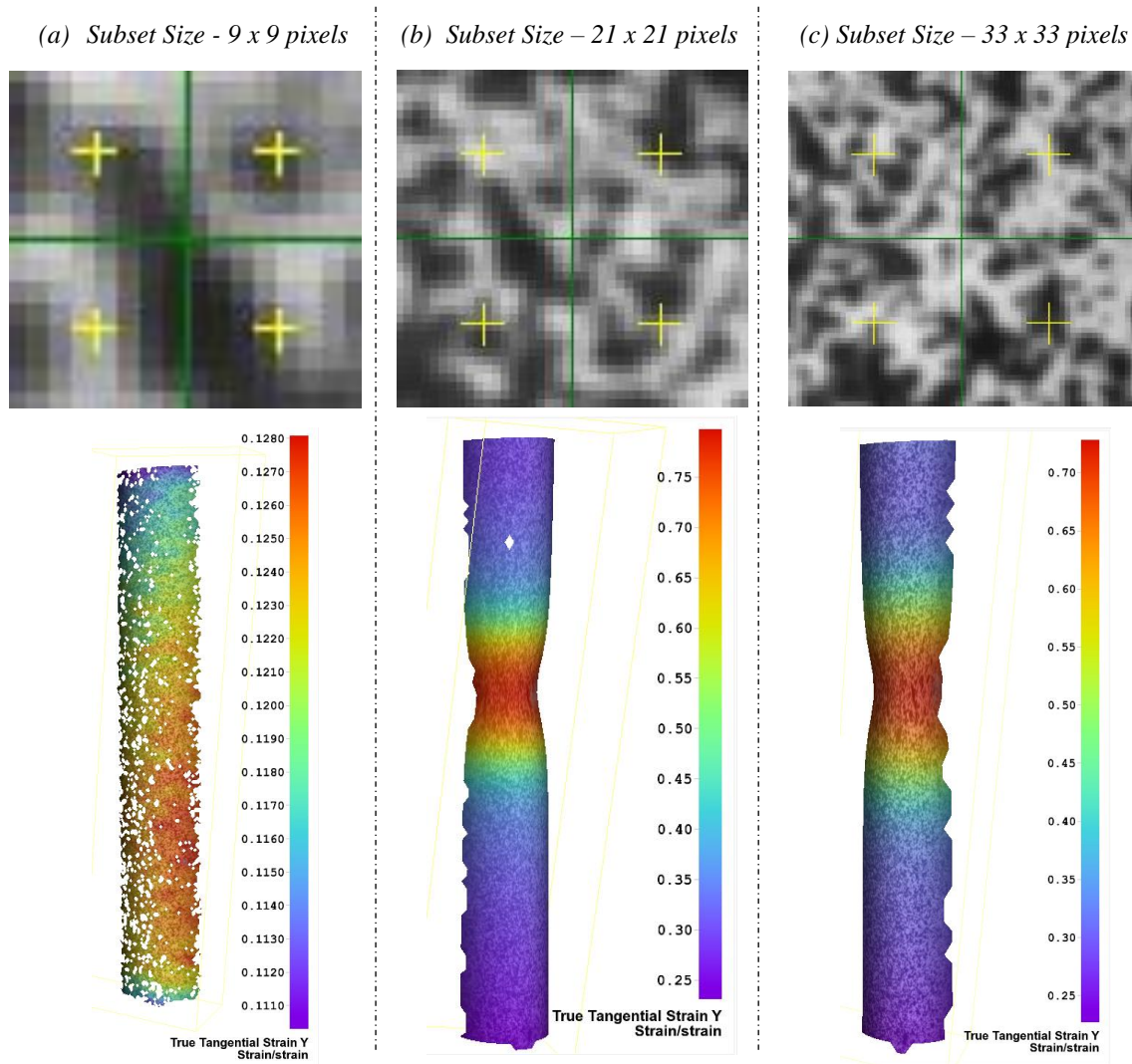


Figure 3.22. A range of Subset Sizes for the Same Speckle Pattern.

The distance between subsets is controlled by grid spacing. The overlap of subsets is used to increase the spatial resolution [175]. The influence of subset size on the quality of data is shown in Figure 3.23, this graph shows the contour statistical error radius depending on the subset size. As the subset size is increased, statistical error radius reduces for both the reference step

and at the onset of failure. Researchers Hunady et al. [176] also concluded the biggest error radius is found when using smaller subset sizes.

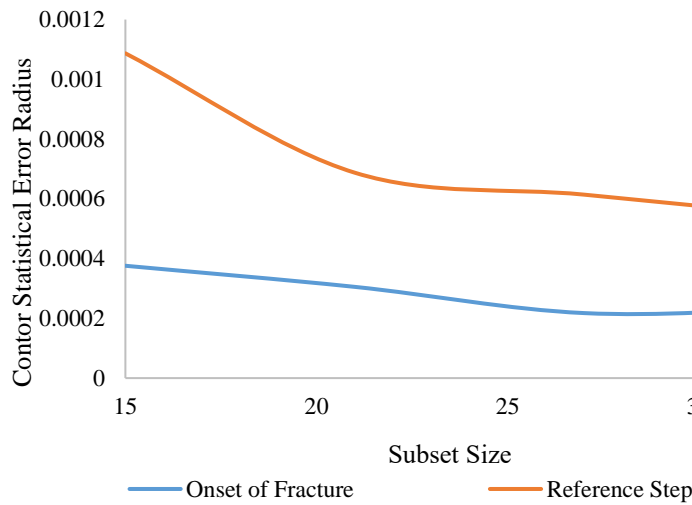


Figure 3.23. Influence of the Subset Size on the Contour Statistical Error Radius.

3.6.4 Lighting Conditions

The aperture is fixed depending on the ideal DOF for the specimen. Aperture, exposure time and external light are used to restrict motion blur and achieve sufficient contrast. These three parameters all work together, to ensure the contrast is uniform over the entire ROI of the image for both cameras and remains constant throughout time [152].

3.6.4.1 Exposure Time

Exposure time (also known as shutter speed) is defined as the amount of time the sensor is exposed to light. Exposure time can be altered to affect the amount the brightness in an image and also the appearance of motion. The diagram in Figure 3.24, displays how exposure time, aperture and camera gain all work alongside each other to produce an image. The aperture is pre-determined by the necessary DOF, and the camera gain must be kept low to reduce noise. A larger exposure time can be adjusted to show motion blur, whereas smaller exposure time (faster shutter speed) can be used to capture extremely fast motion of a specimen during deformation. During testing, motion blur needs to be eliminated meaning that a short exposure time is compulsory. Red circles in Figure 3.24 highlight what will generally be needed throughout DIC testing in this thesis. All three of these properties mean that the image of the

specimen has limited amounts of light. Thus, external lighting is needed to increase the contrast of the image.

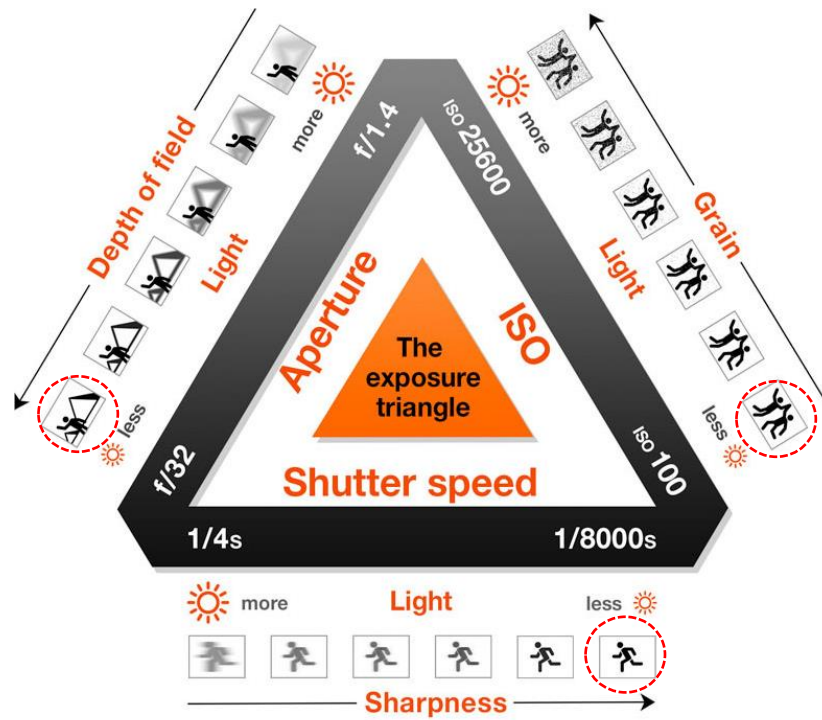


Figure 3.24. The Exposure Triangle [177].

3.6.4.2 External Lighting

External lighting must be uniform across the FOV and constant throughout time [152]. To demonstrate the challenges associated with lighting conditions, a range of types of lights and light mountings used during the research were investigated and are summarised in Table 3.4 and are presented in Figure 3.25.

Table 3.4. Range of Lighting Conditions.

Test No.	Type of Lights	Light Mounting	Distance / Baseline	
1	2x Flat Lights	Tripod	D = 0.7m	B = 0.2m
2	2x Flat Lights	Tripod	D = 0.95m	B = 0.8m
3	1x Flat Light	Tripod	D = 0.6m	B = 0m
4	2x LED Lights	On test rig bar either side of cameras	D = 0.26m	B = 0.24m
5	2x Ring Lights	Lens of camera	D = 0.26m	B = 0.07m

(a) – Test Setup Number 1



Flat Light Panels

(b) – Test Setup Number 2



Further away to diffuse the light before it reaches the specimen

(c) – Test Setup Number 3



Flat Light Panel

(d) – Test Setup Number 4



LED Spotlights

(e) – Test Setup Number 5



Inner segment turned off

Ring Lights

Figure 3.25. Different types of lights set ups for a variety of lighting conditions.

Three different types of lights were used during this preliminary lighting experiment. Test number 1-3 used LED camera light panels on tripods, which meant they could be moved around the test rig. Test set up number 2 was further away to allow the light to diffuse more evenly before it reached the object. The LED camera light panels have an adjusted brightness from 10-100%. However, all of the tests using the LED camera light panels caused an uneven contrast throughout the ROI. The two LED Lights shown in Figure 3.25b applied light more uniform. The LED spotlights were limited to three settings. The main limitation of the LED spotlights was that they caused the image to flicker. If the frame rate is near or faster than the AC supply/duty cycle frequency, then the intensity of the light can differ between images. Therefore, the change in contrast in images causes the camera to flicker [152]. Lastly, the ring lights have an adjusted brightness from 10-100% and were found to apply relatively flat lighting to the ROI. The ring lights are divided into four segments, meaning sections of the light can be turned on and off if required. Out of all the possible variations considered, the ring lights presented flat lighting, and when incorporating their adjusted brightness, ring lights were used throughout the DIC testing hereinafter.

3.6.5 Calibration

Before conducting any experiments, the cameras for the stereo rig are calibrated using a target which contains a grid pattern. Depending on the FOV the calibration target is selected, to ensure the target fills up the FOV as much as possible, the various sizes (each square in a grid ranges from 10mm to 60mm), are shown in Figure 3.26a. Once this is decided the target reference must be selected within the software, it is then rotated in a range of orientations whilst a series of images is taken, as shown in Figure 3.26b [178].

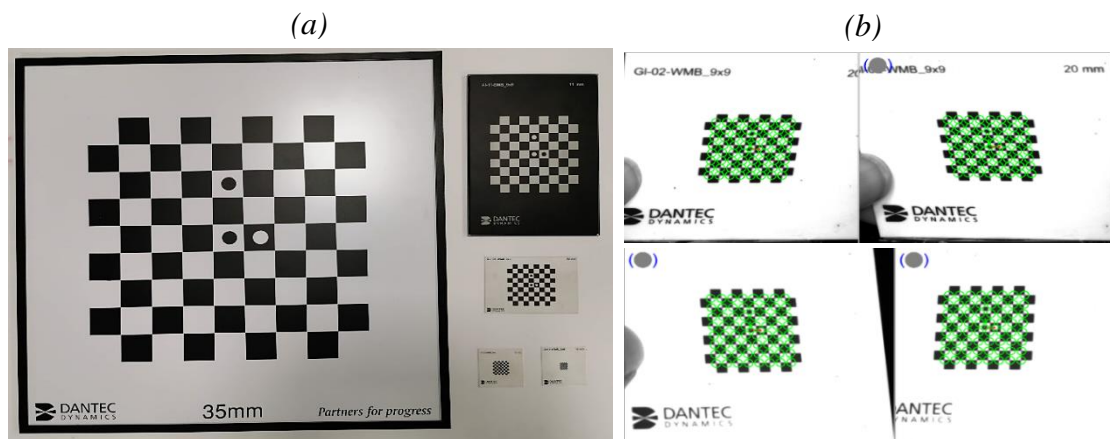


Figure 3.26. Image of Calibration Target in Different Orientations.

The purpose of calibration is to determine all of the intrinsic and extrinsic camera parameters, by extracting data points from the pattern on the target. A calibration point is calculated for each image and is then projected onto the sensor. The calibration quality is determined by the calibration residual, this is defined as the difference between the extracted point and the calculated point. Higher quality calibration images typically have a lower calibration residual [179]. Calibration should be conducted before any test, any movement of the cameras or lens after calibration will mean that a new calibration is needed [180].

3.7 Post Processing

The Dantec DIC software has a smoothing tab that defines the method and the strength of the filtering, which can be used during the evaluation of data. There are two filters to choose from, local regression filter which is based on adaptive spline polynomial algorithm (ACSP) and smoothing spline filter. The strength of the smoothing for a local regression filter is defined by the kernel size. The strength of smoothing for a spline filter depends on two parameters. The grid reduction factor and the smoothness factor. The grid reduction factor changes the density of the grid points relative to the data grid, increasing this constraint means less grid points and smoother data. The smoothness factor restricts the global curvature, by increasing this parameter the data will also be smoother.

Filters should be used with caution, whilst an increased filter smooths out the data and reduces the standard deviation of the data, it also decreases the spatial resolution. To demonstrate the effects of filtering, a strain profile from a uniaxial tensile test of AISI 304L is used at the onset of fracture. The settings for contour and displacement smoothing are independent and have been kept the same throughout comparison of the data. To evaluate the grid reduction factor, a range within the suggested limits are shown in Figure 3.27a. The graph in Figure 3.27b highlights increasing this factor will continue to smooth out the data, however this can hypothetically decrease the quality of the results.

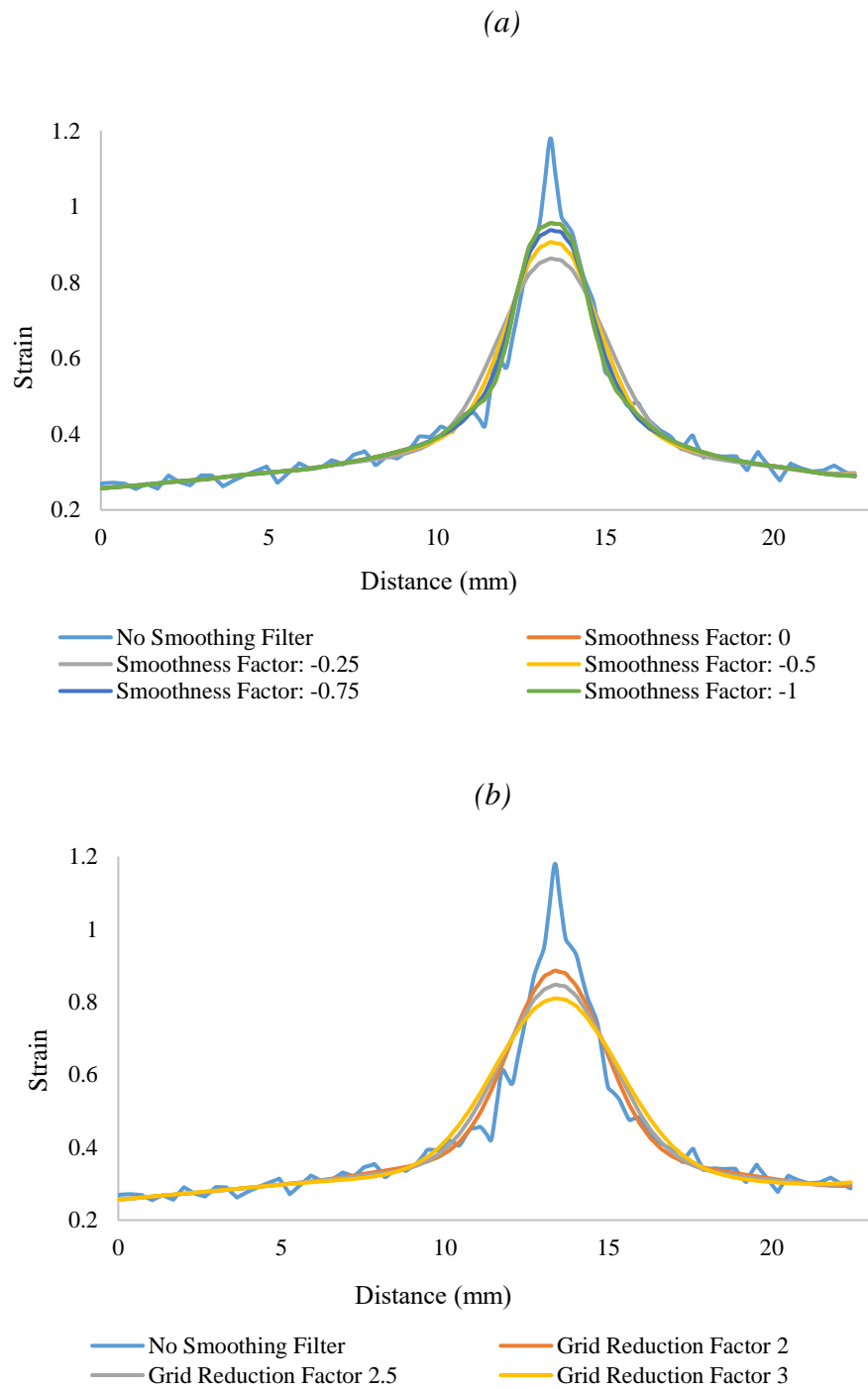


Figure 3.27. Major Strain before Failure of Tensile Test with a range of a) Local Regression Filters and b) Grid Reduction.

3.8 DIC Errors

Inaccuracies from DIC are typically divided into two main errors: numerical and experimental as shown in Figure 3.28.

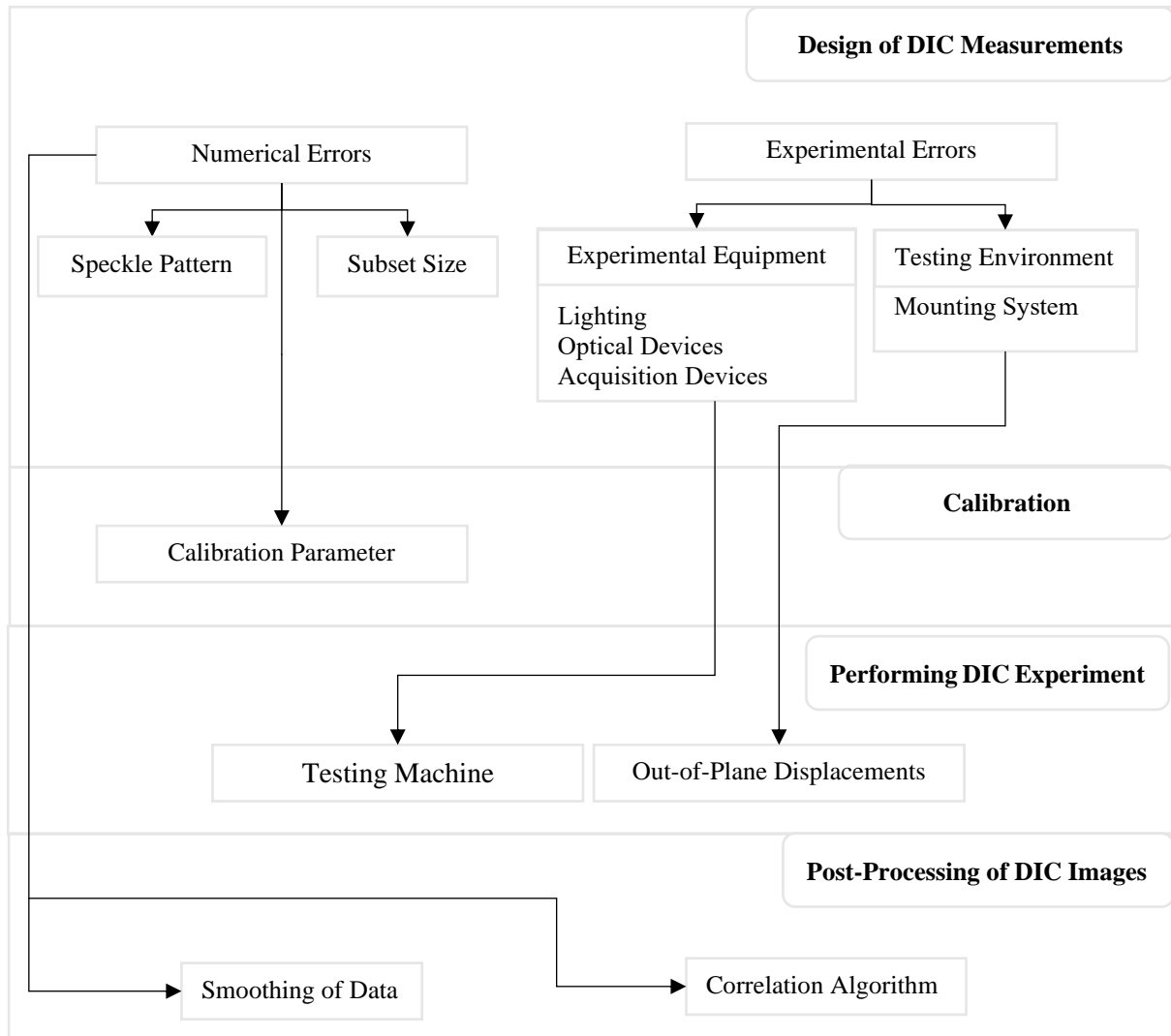


Figure 3.28. Diagram showing Different Types of Errors during the Different Processes of DIC.

Numerical errors can occur throughout DIC experiments from a range of parameters such as; inaccuracies in speckle pattern, subset size and algorithm used for correlation [149]. The quality of the speckle pattern directly affects the resolution of the data produced. As previously stated, speckle patterns have desired characteristics such as contrast, size and speckle edge and density. However, all these attributes can contribute to errors, if even one of these aspects is

not optimal it will introduce imprecisions into the overall error. Lecompte et al. [181] conducted an assessment on the quality of speckle patterns which concluded, the combination of the size of the speckles in a set speckle pattern, and the subset size, impact the accuracy of the measured displacements.

Determining the optimum subset size is crucial, as it impacts the reliability and accuracy of the data, as discussed previously in Section 3.6.3.4. Contrast inside a subset is needed, this can be achieved by the increasing amount of information. Researchers established increasing the size of subsets generally enhances the correlation quality and accuracy of results [182]. Although, it is important to note computational cost is increased with the subset size. Thus, there must be compromise between reducing both inaccuracies and computation time. It is important to note that past a critical size the subset will not provide any further improvements [183].

Poor focus can lead to extraction errors and will decrease the quality of the calibration. A number of poorly extracted points will cause calibration errors, resulting in a bias error. Poor calibration images typically occur where there is issues with extracting points, or when there is a problem with camera synchronisation, this can be indicated by a high calibration residual [179][184].

Experimental errors can be caused from experimental equipment and/or the environment during testing. Mounting systems must support both cameras rigidly together to avoid relative camera motion, as movement or vibrations of one camera with respect to the second camera will generate measurement errors [152]. Noise errors can also be known as variance errors. When observing a fixed object over time any fluctuations in the grey level intensity of a pixel, is known as noise produced by the camera detector. Quantifying camera noise is only essential when assessing the suitability of potential cameras. Noise-floor-analysis is an iterative process used to quantify noise errors after the experimental test, using static images taken just before the testing starts [152].

Suitable lighting conditions are important to reduce experimental errors, by limiting motion blur and providing sufficient contrast. This is controlled by three parameters; aperture, exposure time and external light sources (as discussed in Section 3.6.4). Jerabek et al. [185] discovered that light intensity just below overexposure provided best results. Researchers Haddadi and Belhabib [183], concluded the errors associated with variation of light seems to

be imperative, as any changes in the grey levels of the images affects the correlation accuracy. Thus, during the mechanical test; flat, uniform and adequate lighting is needed for the ROI.

Out-of-plane motions are typically inevitable. Out-of-plane motion when using 2D-DIC may corrupt the in-plane displacement measurements. However, as stereo-DIC calculates the 3D location beforehand, the user can calculate any out-of-plane displacement. M.A. Sutton et al. [186] found that stereo-DIC instantaneously measures all three components of displacement without presenting any in-plane displacement errors.

Lastly, when post processing the DIC data it is possible to apply filters to the experimental data. Whilst use of a filtration technique may considerably reduce strain measurements noise, it can also decrease the spatial resolution, leading to potential additional errors in the data [152].

3.9 Summary

- Lens selection is dependent on the ROI, as the focal length is increased so is the magnification, but the angle of view becomes narrower.
- Smaller stereo angle was necessary to capture more data of the round bars; however, this may decrease the out-of-plane resolution.
- Tests conducted were designed for various speckle patterns using spray paints for a fixed rig set up, this highlighted the challenges in achieving the optimum speckle pattern, such as contrast, density and the size of speckles.
- If using spray paint to generate a speckle pattern, the time between painting and testing should be limited, the optimum time was found to be between 30-60 mins. The main limitation of spray paint is the potential failure of paint before failure of the specimen.
- To ensure contrast is constant over the entire ROI, aperture exposure time and external light work cohesively. As the specimens used for this test were round, there needed to be a high aperture. To capture the testing whilst restricting motion blur, the exposure time must be small. Therefore, more light is needed this can be done using external light to improve the contrast of the image.

- External lighting must be uniform across the FOV. A range of lighting types and mountings were explored, which found the ring lights to be the most suitable source of external lighting.
- Calibration should be conducted before any experiments. Any movement of the cameras or lens after calibration will mean that a new calibration is needed, or this will lead to inaccuracies in data.
- Filters should be used with caution, whilst an increased filter smooths out the data and reduces the standard deviation of the data, it also decreases the spatial resolution.

4 Experimental Methodology

4.1 Introduction

This chapter firstly outlines the experimental testing programme, the schedule is divided into 4 main phases of testing and is composed of 15 specimens. Following this the methodology between FE analysis and DIC, which consists of three processes, preliminary, experimental and the post process is described. Experiment set up is thoroughly discussed. This shows all the equipment used and the testing procedures that are used throughout testing.

4.2 Aims and Objectives

- Provide an experimental testing programme with relevant loading conditions and geometries for each region of stress triaxiality.
- Outline the methodology for using DIC and FE analysis to obtain a fracture locus for AISI 304L and CA6NM.
- Provide a clear method for the experimental set up for each test, detailing the equipment used and parameters such as recording procedure of DIC software and sample preparation.

4.3 Experimental Testing Programme

To design the test programme the fracture locus constructed in Figure 2.19 provided indications of which geometry was necessary to obtain a data point in the desired region. The designs for the 15 specimens used in the experimental testing programme are shown in Figure 4.1, and the engineering drawings for all the specimens are presented in Appendix D.

The schedule for testing was split into 4 main phases, as shown in Table 4.1. For Phase 1 the focus was to obtain the material data for both AISI 304L and CA6NM. Determining the true stress strain data for the materials, provided the material data for all FE analysis. Phase 2 assessed the anisotropy of AISI 304L using a range of different rolling angles. The results of Phase 2 determined the AISI 304L was not anisotropic, therefore there were no additional specimens required at different rolling directions to be tested for Phase 3-4. Phases 3-4 used a range of different geometries under a variation of stress states. All testing was conducted at room temperature, under quasi-static conditions. The manufacture of the specimen's conformity and inspection report is shown in Appendix E all the samples used came from the same batch for the AISI 304L. The orientation of the samples for CA6NM was not further studied as this is a cast material, thus the material is isotropic.

Table 4.1 Phases of Testing Programme.

Phase	Name	Material	Stress State
1	Material Data	AISI 304L and CA6NM	Tension
2	Anisotropy	AISI 304L	Tension
3	High and Low Stress Triaxiality	AISI 304L and CA6NM	Tension / Tension and Shear / Shear
4	Negative Stress Triaxiality	AISI 304L and CA6NM	Compression

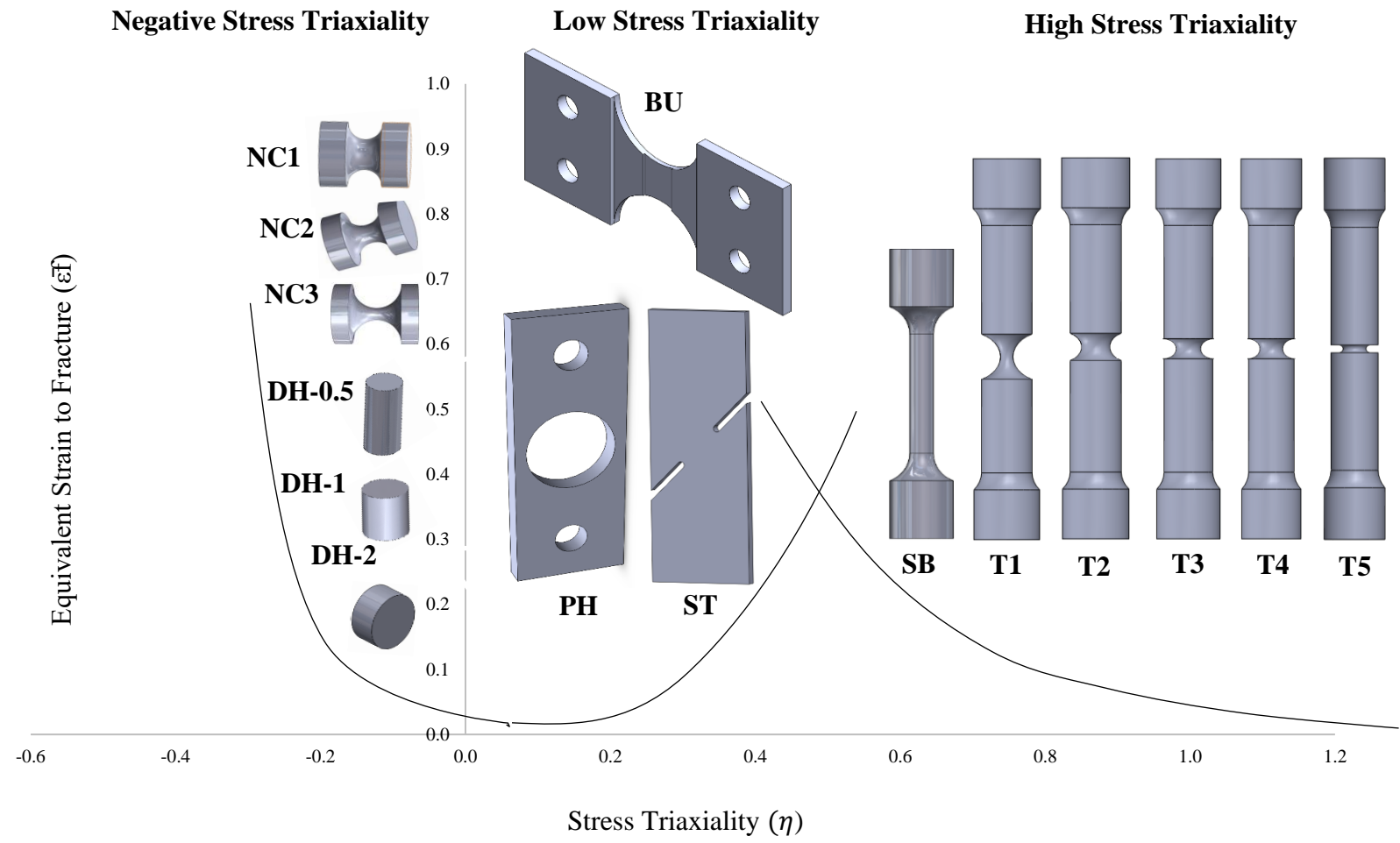


Figure 4.1. Range of Geometries for Experimental Programme.

4.4 Methodology between DIC and FE analysis

It was found in the background and literature review in Chapter 2 Bao and Wierzbicki [12] provided a general methodology used in constructing the fracture locus for any ductile material. The method consists of a series of tests and corresponding FE models, determining a test location of fracture initiation, to find the equivalent strain to fracture and the average stress triaxiality over the load history. In this thesis the methodology used by Bao and Wierzbicki has been adapted to include DIC, where DIC was used in parallel with FE analysis to provide material characterisation of AISI 304L and CA6NM. The range of geometries selected were to ensure there were sufficient amount of data points available in each region.

The methodology was divided into three main processes, preliminary, experimental and post processing as discussed below and shown in Figure 4.2.

- Preliminary Process: A series of different geometries including notched bars and plate with hole specimens were made out of AISI 304L to find the optimum setup for the DIC. Setup considerations include the equipment selection, lighting conditions and suitable speckle surface. Then, tensile tests were performed for AISI 304L to obtain the material data. This procedure explained in [187] was initially developed for AISI 304L, and was then repeated to obtain the material data for CA6NM.
- Experimental Process: Entailed choosing a geometry and setting up the DIC test rig for each specimen (see Figure 4.1). The tests were performed up to failure point, while the equivalent FE model was run in parallel using the material data obtained from the preliminary process.
- Post Process: During this stage suitable gauge parameters were used to extract displacement and strain data. The DIC images were used to identify the onset of failure, thus the displacement to fracture (u_f) could be found. By determining the critical location for each specimen, the stress state data was extrapolated from rerunning the parallel FE analysis, providing equivalent strain to fracture, the average stress triaxiality over the load history and the average Lode angle parameter over the load history.

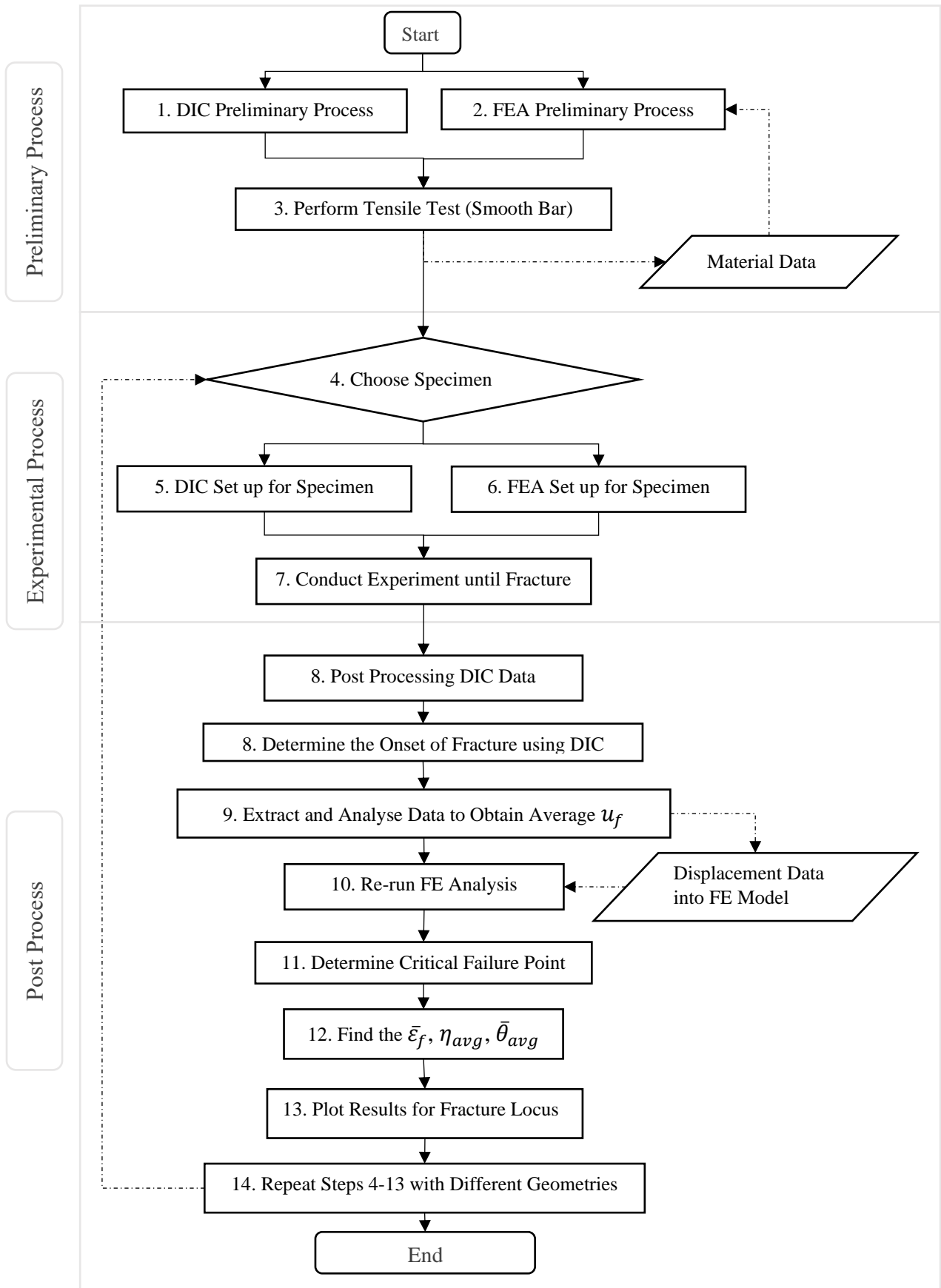


Figure 4.2. Methodology Flow Chart.

4.5 Experiment Set Up

At the start of a new DIC measurement it was important that the testing equipment was rigidly mounted to ensure both cameras were fixed together, to reduce relative camera motion. In order to level the DIC equipment and to centralise cameras, a laser level and a target grid were used as shown in Figure 4.3.

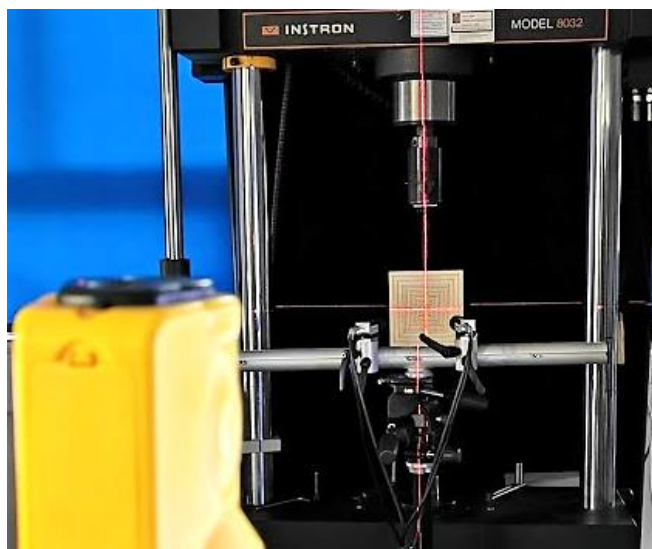


Figure 4.3. Levelling of Test Rig and Centralising Cameras.

Design of DIC measurements as previously discussed in section 3.5, were based on a variation of parameters such as, the geometry of the specimen being tested and the machine being used. Whilst the cameras and external lighting remained the same throughout, a variety of lens were used to ensure the FOV/ ROI was captured for each geometry, ensuring that the FOV accounted for the specimen to deform and remain in view. The summary of the DIC measurements for each geometry is presented in Appendix F.

The digital 3D Image correlation system Q-400 and Istra4D software was used in this study. The experimental setup is shown in Figure 4.4. The two cameras used for all testing were VCXU-50M which are specified in Table 3.2.

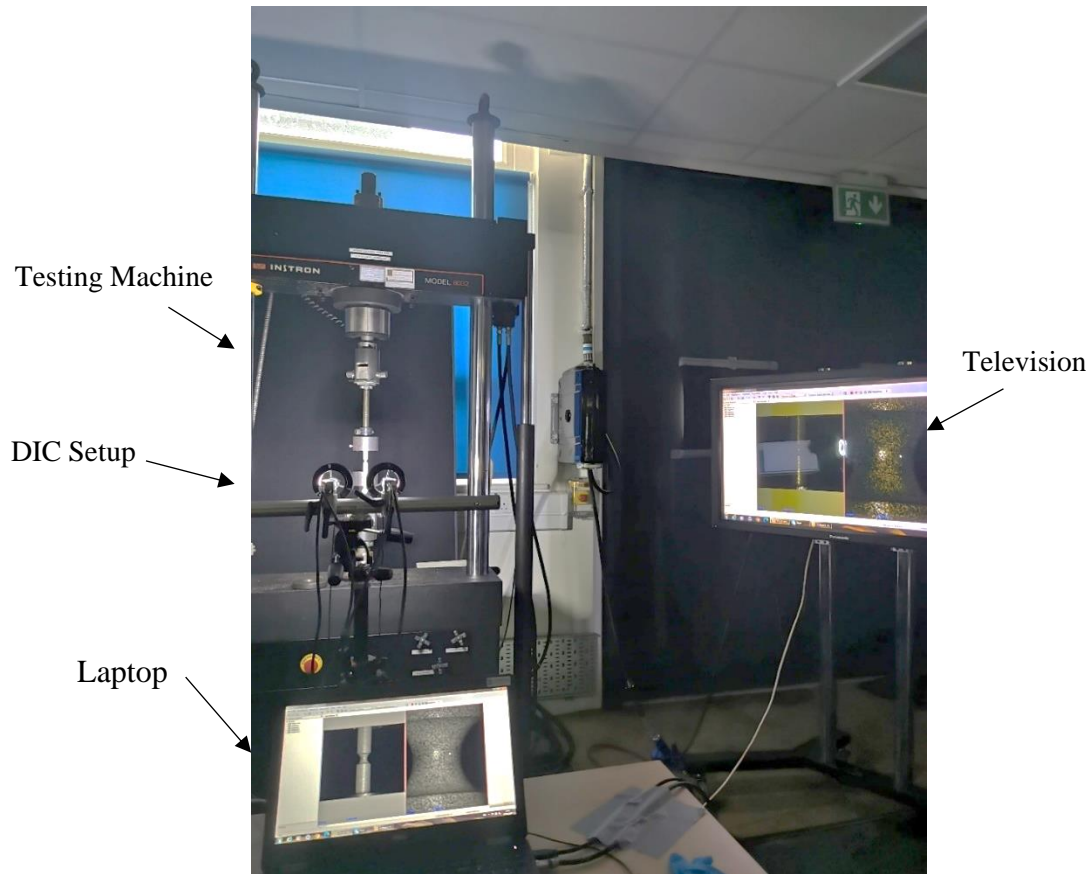


Figure 4.4. Experimental Test Set-Up - Example for T2 6mm Notched Bar.

Pre-calibration was conducted for individual setups extensively, adjusting the DIC system until high quality images were obtained. During this process the DOF and the specimens change in displacement during testing was estimated and was adjusted if necessary. Any issues such as: glare, defects in speckle pattern and uneven lighting distribution were eliminated before continuing with calibration.

Calibration was performed before every test. A variety of calibration targets were used depending on the set up to fill the FOV. During calibration, 20 images were captured when the target was rotated in front of the cameras. When completed the calibration residual was checked to ensure it was suitable. During post-calibration a series of static images were taken, so that the grid which is composed of subsets is distributed throughout and covers the ROI. Any final issues such as the lighting or speckle pattern that are detected at this point were corrected. As discussed in Chapter 3, if there were any changes to the system once it was calibrated, the calibration must be repeated.

Final checks for data acquisition systems were performed, such as ensuring the storage location of all the DIC images were correct. Each geometry had its own recording procedure during testing, which was set to take an image depending on the triggering test frame signals, this was controlled by the force input from the machine into the DIC software. An overall schematic of the testing machine and DIC software is shown in Figure 4.6. An example of a recording procedure is shown in Figure 4.5, where the first loop took an image every 1.1s until the load reached 15kN, this then triggered the first loop to stop and the second to begin. The second loop took an image each time the increment of force increased by 1kN, until the force reached 20kN. The recording procedure then went into the final loop, at which the software took an image every 1.1s, until the specimen failed, and the test is stopped. All the recording procedures used are detailed in Appendix G.

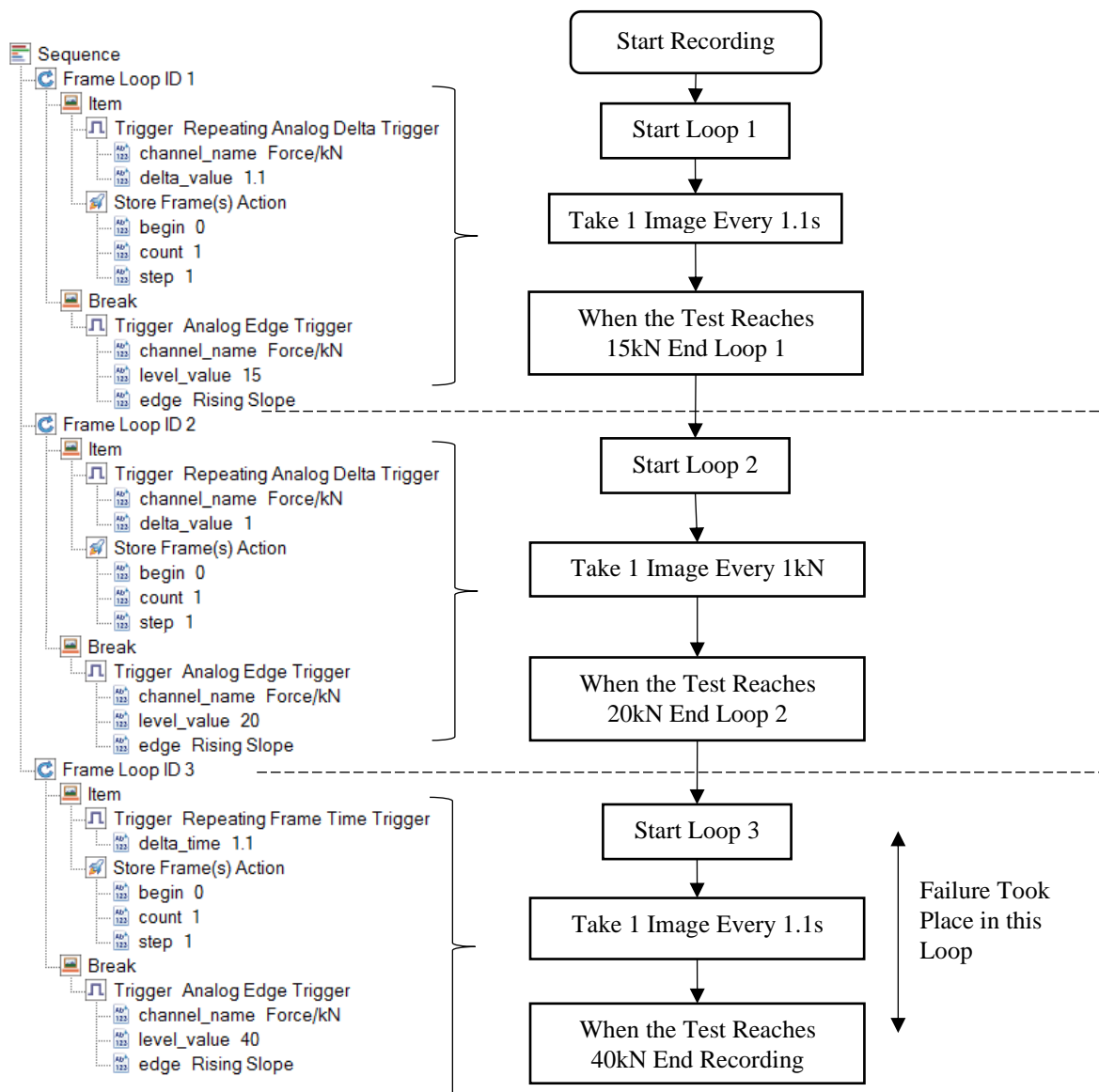


Figure 4.5. Recording Procedure Explained.

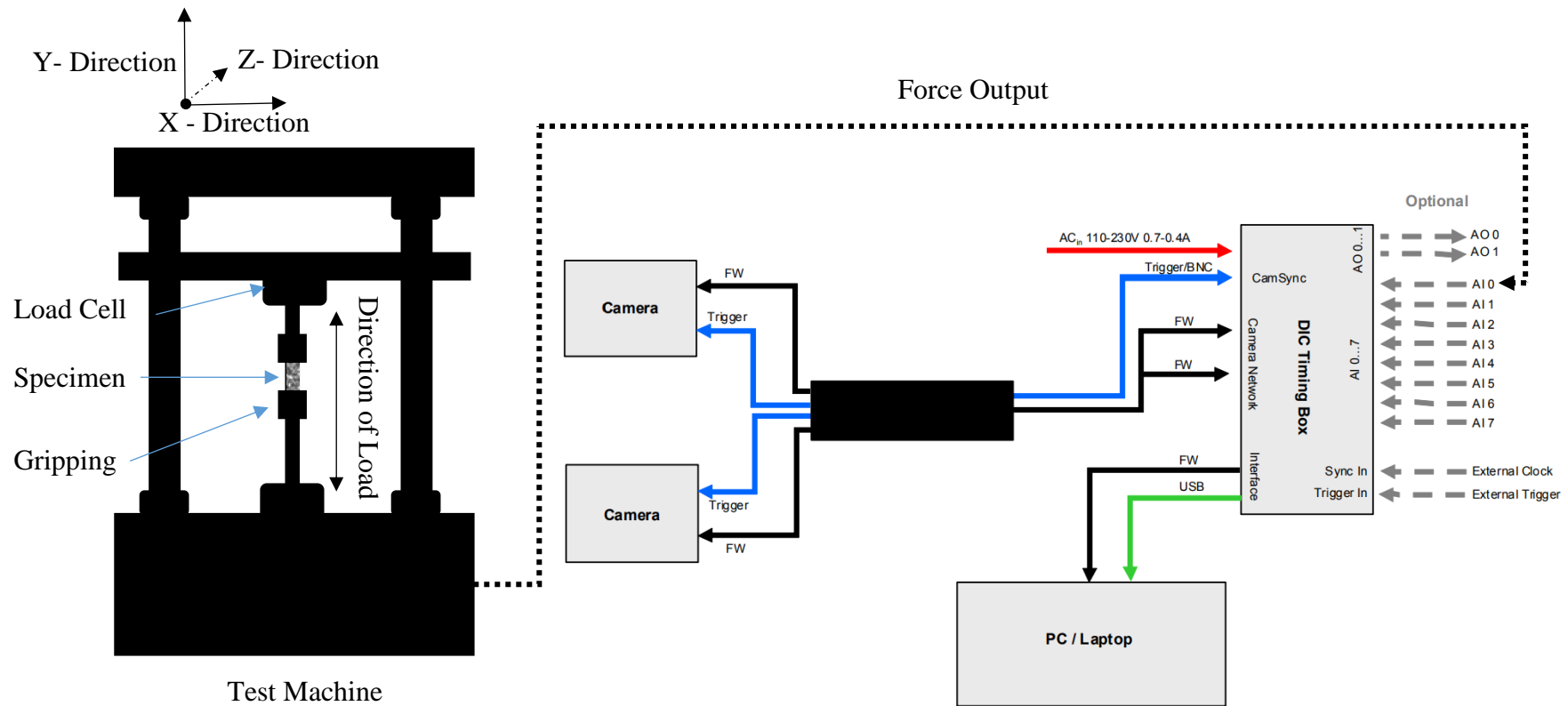


Figure 4.6. Testing Machine and DIC Software Schematic.

Lighting conditions were maintained throughout the duration of testing. As many of the specimens required a high DOF, the aperture used ranged between F8-F16, the shutter speed was high to ensure the moment of failure was captured. External lighting was used, creating different levels of intensity to produce enough contrast for the image, this was done using the ring lights proposed in Section 3.6.4.

Before the painting process the specimens were thoroughly degreased using isopropyl alcohol cleaner. They were left for at least 5 minutes, to ensure the specimens are fully dried. The specimens were painted in a spray booth as shown in Figure 4.7.



Figure 4.7. Specimen Spray Booth.

Following from the research conducted in Chapter 3, the white paint needed to be matt white, but also adhesive. Finding the right white paint was challenging as the AISI 304L was very ductile, it meant the paint had to be adhesive and stick to the specimen deforming up to 22mm. The processes of speckling a sample is shown in Figure 4.8. For each specimen the ROI is specific. Once the specimen was dry from being cleaned, as shown by Figure 4.8a, white paint was applied evenly to the specimen ensuring the specimen was covered, as shown by Figure 4.8b. The specimen was left for 7-10 minutes for it to dry depending on the geometry. If the white paint was too wet, then when the black speckles are applied it caused glare during the experiment. However, if left past a certain period this led to a lack of adhesion meaning the paint failed before the material.

For the final step the black speckle pattern was applied, as shown by Figure 4.8c. The technique of speckling the specimens black included spraying a mist of paint from a distance away from the specimen, which varied depending on the stress state and geometry. Following Section 3.6.3 speckling the specimens black needed to be random and provide contrast. If issues were detected after painting, the specimen was removed of all paint by using isopropyl alcohol cleaner and the process was repeated.

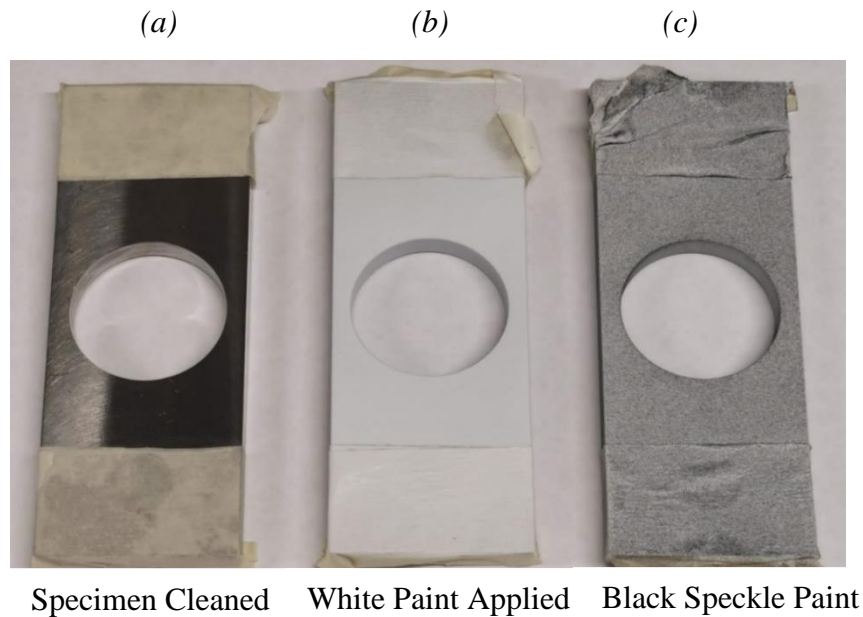


Figure 4.8. The Process of Speckling a Sample.

After the experiment was completed, the images obtained were evaluated, producing full field data of the specimen from the reference image to failure. All the specimens performed in this thesis were evaluated without filters.

4.6 Summary

- An experimental testing programme with relevant loading conditions and geometries for each region of stress triaxiality was presented.
- This chapter presented the methodology which will be used. In which both DIC and FE analysis are used to obtain a fracture locus for AISI 304L and CA6NM.
- The experimental set up was thoroughly detailed, presenting the equipment used and preparation necessary for samples to be ready for testing.

5 Results and Discussion

5.1 Introduction

Phase 1 of testing focused on obtaining the material data for AISI 304L and CA6NM which was used for the material model in FE simulations. A study was conducted using the direct measurement method to produce true stress strain data for both materials. Anisotropic behaviour of AISI 304L was investigated in Phase 2 of testing. Phase 3 focussed on obtaining data for the high and low stress triaxiality region with a range of tensile and shear experiments. The final phase of testing was Phase 4, which was a series of compression tests for data within the negative stress triaxiality region.

5.2 Aims and Objectives

- Provide a clear and accessible method to obtain accurate true-stress strain data, and to extend the limited material data beyond the ultimate tensile strength (UTS).
- Provide data for material properties used in the simulation for CA6NM and AISI 304L.
- Investigate anisotropic behaviour of AISI 304L, by testing the material for a range of rolling directions.
- Determine the various stress state data for high, low, and negative stress triaxiality.

5.3 Material Data

5.3.1 Introduction

Uniaxial tensile tests are used to determine a materials characteristics by observing the materials response when subjected to a load. This is divided into elastic and plastic regions. Beyond the necking region, strain is non-uniform along the gauge length. Literature suggests that in order to determine stress and strain data within the necking region, two methods can be used, inverse or direct. The inverse method incorporates experimental measurement with FE analysis to determine the true stress-strain curve [188]. Whereas the direct method uses instantaneous measured parameters from the surface of the specimen. The inverse method has been researched extensively [189][95][190]. In this method a reference stress-strain curve was iteratively adapted to reduce the divergence between the experimental data and FE analysis. Kamaya and Kawakubo [191] proposed a methodology which used the inverse process, to determine the true stress-strain curve of an hourglass type specimen, with a range of FE analysis and DIC. Implementing the inverse method is more time consuming when compared to the direct method.

As the direct method uses instantaneous measured parameters, optical systems such as DIC can be used. DIC can produce data throughout testing, allowing for measurements such as true strain and instantaneous cross-sectional area up to failure to be extracted. With this data the true stress can be calculated. Li et al., [192] used DIC to determine the true stress-strain curve of advanced high-strength steel D9780. Results were validated by comparing the direct approach to a range of methods, which found the direct measurement method delivered a more accurate stress-strain curve at large strains. Literature on the direct method [193][194][195] is limited. Previous work cited relating to the direct method did not present much detail for different parameters, such as various subset sizes or filtering options. However, subset sizes ranging from 21 x 21 pixels to 81 x 81 pixels, with increments of 6 x 6 pixels were investigated by Yaofeng and Pang [196]. The results found the optimal subset size is a trade-off between the influence of random errors and systematic errors. A study investigating different filtering strategies used adaptive low-pass filters and notch filters to eliminate noise, although this type of filtering was found to increase errors [197]. There is no study that has investigated the effect of subset size and the parameters used during the post processing of DIC data. This gap in

research has been investigated in this thesis and is of importance in order to determine accurate stress-strain data.

True stress-strain curves to failure for AISI 304L were produced by Blandford et al. [198]. However, the research stated that tensile testing did not include a method of continuous monitoring of the neck area but used extrapolation to the fracture point. Extrapolation method is regularly used to extend true stress-strain data past the uniform elongation and occasionally those extrapolations are based on an arbitrary assumption [192]. This research proposes using the direct method to obtain three parameters needed to determine true stress-strain data; displacement, cross-section area (of necking region) and true strain until the onset of failure. Post-processing DIC results is of importance, as different filtering and/or subset size results in different true stress-strain curves. Literature available shows there has been insufficient research carried out to compare the variation in parameters. The aim of this section is to not only extend data available post UTS for AISI 304L and CA6NM, but to provide a clear and accessible method to obtain accurate true-stress strain data. Validation is achieved by matching the force displacement curves from the experimental tests.

5.3.2 Methodology

In order to accurately determine the required true stress-strain data, post-processing of the DIC data will be used in an FE analysis to be compared to the experimental force displacement response. The approach is briefly described below:

1. Perform a series of experimental tensile tests using DIC, taking a series of images throughout testing until failure.
2. Determine the onset of failure.
3. Determine which gauge visualisation parameters to use to extract data.
4. Plot an experimental force displacement response.
5. Decide subset size and filtering parameters to run evaluation.
6. Determine the instantaneous cross-sectional area and true strain in order to plot a true stress-strain curve.
7. Input the true stress-strain data and displacement at failure (from DIC) into FE model and run analysis.

8. Plot the force displacement response for the FE model and compare to the DIC force displacement curve. If they match, then the true stress-strain data is correct, and the analysis accurately replicates the experiment. If the curves do not match, then steps 5 to 8 must be repeated.

5.3.3 Experimental Test

Tensile specimens were tested on a 100kN Instron Servo Hydraulic testing machine using displacement control at a rate of 5 mm/min. The chemical composition of AISI 304L and CA6NM are shown in Table 5.1.

Table 5.1 Chemical Composition of AISI 304L and CA6NM.

AISI 304L							
Carbon (C)	Manganese (Mn)	Silicon (Si)	Phosphorous (P)	Sulphur (S)	Chromium (Cr)	Cobalt (Co)	Nitrogen (N)
0.012%	1.08%	0.27%	0.028%	0.001%	8.7%	0.12%	0.07%
CA6NM							
Carbon (C)	Manganese (Mn)	Silicon (Si)	Phosphorous (P)	Sulphur (S)	Chromium (Cr)	Molybdenum (Mo)	Nickle (Ni)
0.012%	0.735%	0.475%	0.023%	0.001%	12.78%	0.545%	4.43%

5.3.4 Specimen

The design of the cylindrical dog-bone tensile specimens were based on the British Standards: ISO 6892-1:2019, the dimensions in mm are shown in Figure 5.1 [199]. The manufacture of the specimens was from a 25 x 2000 x 60000 mm plate. Which is representative of the material used in the construction of flasks, the material was provided for the project by NTS.

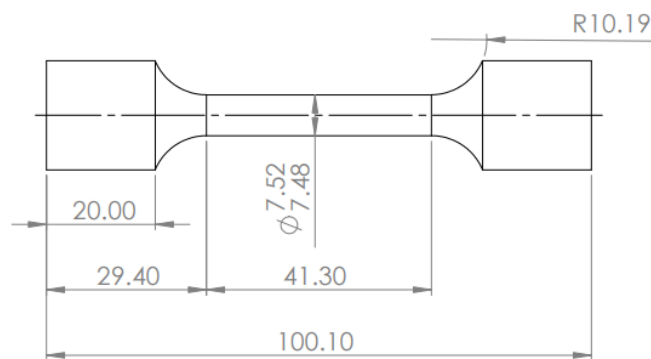


Figure 5.1. Tensile Specimen Dimensions.

5.3.5 Results and Discussion

Physical changes at microscopic and macroscopic levels are used as indicators to predict the onset of fracture. In order to determine the failure strain, fracture initiation must first be determined. In this study, fracture initiation of the tensile specimens was shown by two factors: the first was by the sudden load drop as shown in Figure 5.2a, and the second was found when post processing using the DIC software, as the image just before a failure crack was observed. For example, Figure 5.2b shows step 269 and step 270, where step 269 was taken as the onset of failure. The image number taken during testing is referred to as the step. During the post processing of the data the accuracy was set to 0.1 pixels.

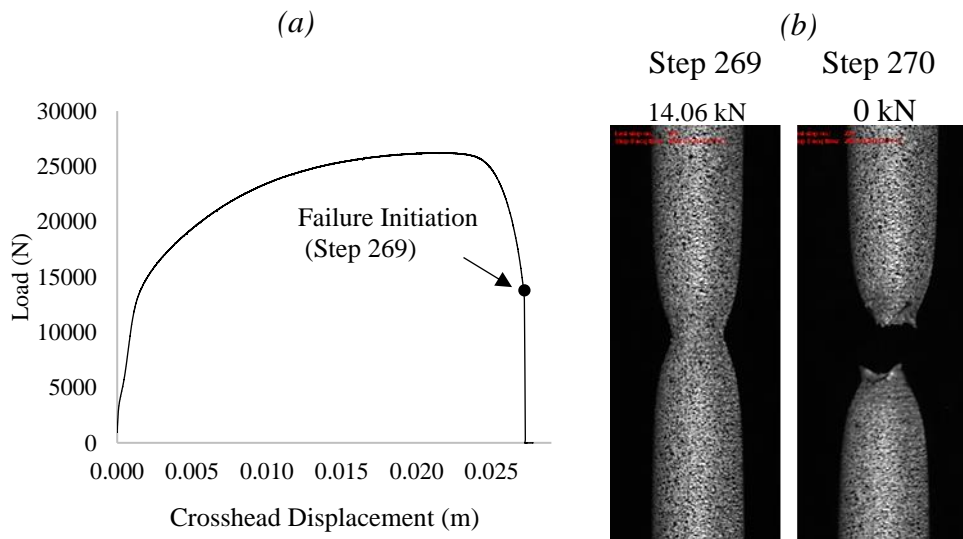


Figure 5.2. a) Force-Crosshead Displacement Graph using Machine Data b) Fracture Initiation of Tensile and Failure of Specimen.

The sudden drop in the load displacement curve matches the load shown in the step where the onset of failure has been defined. As the DIC captures the moment before fracture, failure initiation is defined as the step before the first detectable failure crack, which aligns with the sudden drop in the load displacement curve.

5.3.6 Extraction of DIC Data

When post processing DIC data it is important to use suitable gauge parameters depending on necessary requirements. There are three main data sets to be extracted from the tensile tests

performed including; displacement, cross-sectional area (of necking region) and true strain until the onset of failure.

Displacement: Change in length of the vertical line AB as shown in Figure 5.3a.

Cross-Sectional Area: To calculate the true stress the actual cross-sectional area was needed. An assumption was made that the cross-section of the cylindrical specimen remains as a circle during the experiment [194]. The cross-sectional area of the specimen can be obtained by calculating the curvature of the surface shape with the DIC software. This has been determined by using the change in length of the horizontal line CD as shown in Figure 5.4. Line CD was positioned in the region of strain localisation. Strain localisation occurs in the necked region of the specimen. The strain localisation graph in Figure 5.3b was obtained using the vertical line AB shown in Figure 5.3a and plotting the true strain in the Y direction every step until failure.

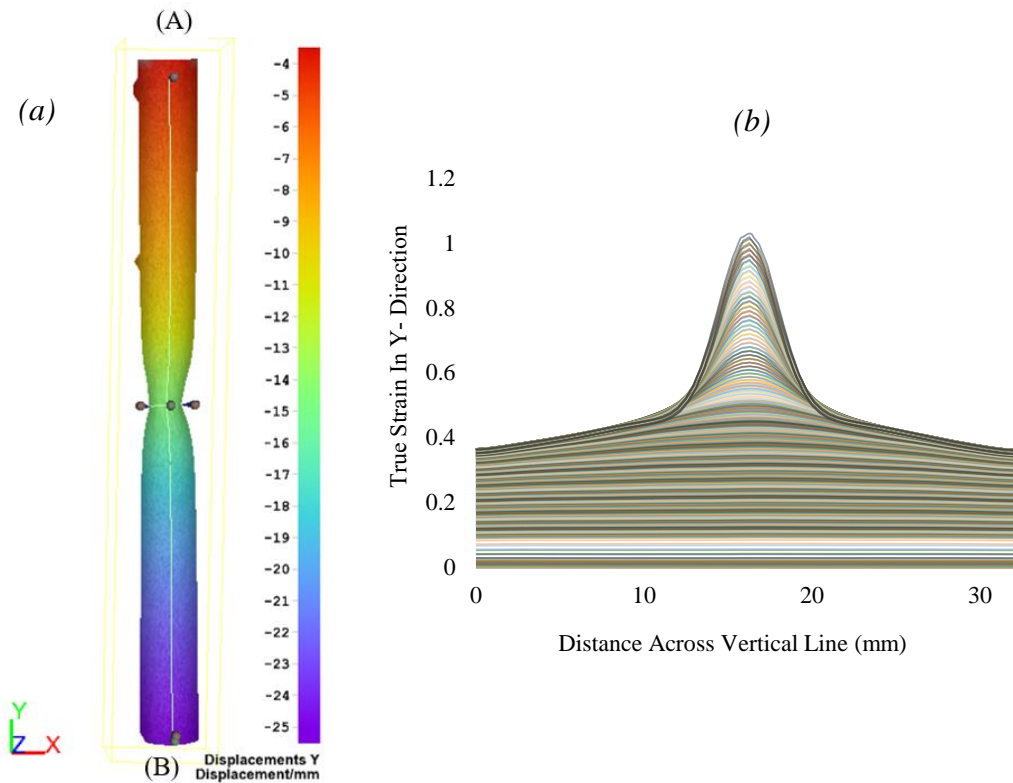


Figure 5.3. a) Contour of Displacement in Y-direction b) Measured True Strain in Y Direction against Distance Along the Vertical Line.

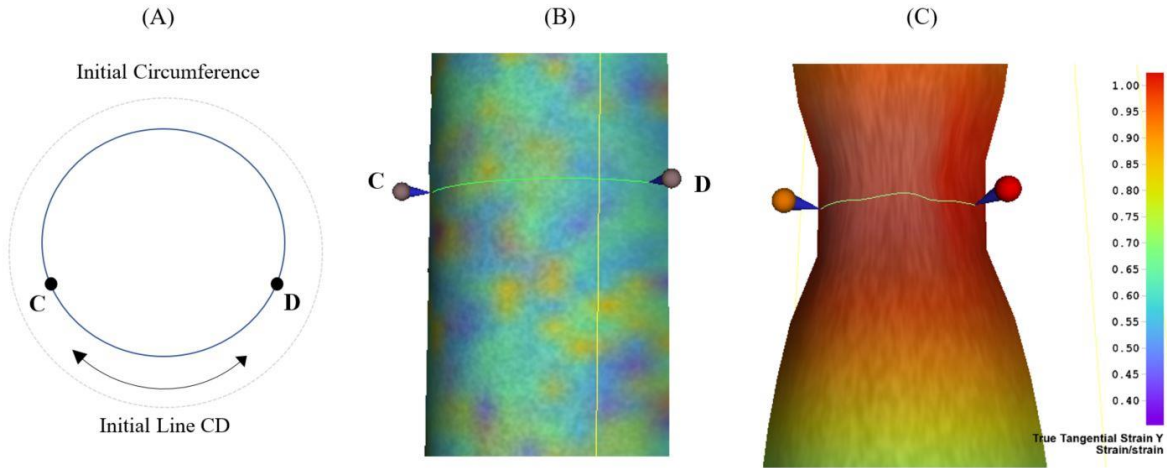


Figure 5.4. Contour Plot of Horizontal Line used to find the Instantaneous Cross-Sectional Area Until failure a) Line CD at Step 0 b) Line CD at Step 269.

The instantaneous area was calculated by first finding the ratio between the line CD and the initial circumference, as shown in Figure 5.4. The length change of line CD was extracted from the DIC data and multiplied by the ratio to determine the direct circumference. This was then used to calculate the radius. Therefore, the study was able to find the change in area throughout testing.

True Strain: Two ways of extracting true strain are shown in Figure 5.5, by a gauge point and a polygon around the necking area. The maximum strain from contour is limited to 2 decimal places. The range in failure strains are shown in Table 5.2.

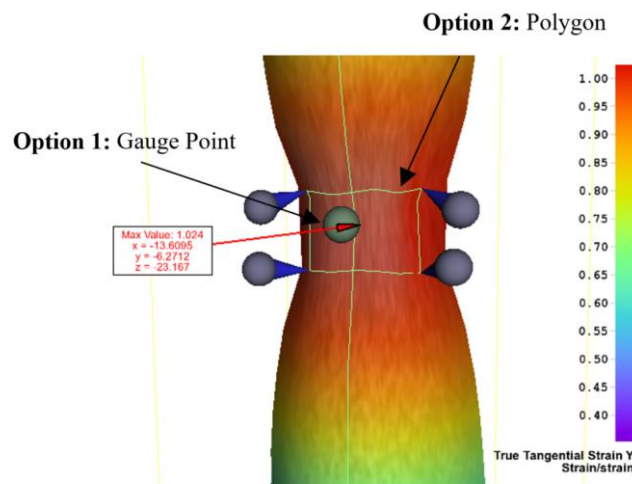


Figure 5.5. Contour Plot showing different Gauge Parameters.

Table 5.2. Failure Strains using a Range Gauge Parameters.

Gauge Point	Polygon - Max over surface	Max Strain from Contour (2dp)	Polygon - Mean over surface	Polygon - Min over surface
1.0230	1.0243	1.0240	1.0236	1.0218

Using different gauge parameters has a minor effect on the strain data throughout testing. However, by using the polygon - maximum strain over surface ensures that the highest failure strain is included, and this was used to extract true strain data.

5.3.7 Finite Element Model

A FE model was built in ABAQUS/STANDARD to simulate the uniaxial tensile test using a standard von Mises plasticity model as shown in Figure 5.6. An axisymmetric model was used, with symmetry boundary conditions applied along the horizontal symmetry line at the centre of the specimen, a displacement boundary condition was introduced to the remote point which was coupled to the top surface. The radial constraint on the Y axis shown in Figure 5.6 is not necessary but will not impact the analysis. Axisymmetric elements CAX4R were used. A mesh convergence study found the optimum number of nodes and elements were 2245 and 2096 respectively.

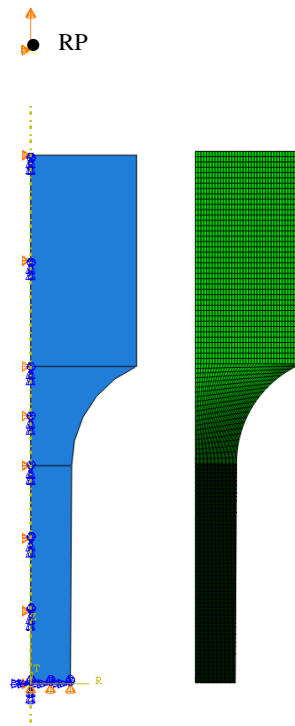


Figure 5.6. FE Model of a Tensile Specimen.

5.3.8 True Stress-Strain Curve

Once the failure initiation and gauge parameters have been determined, true stress-strain curves can be obtained. However, as discussed previously the subset size and smoothing of data will affect the data of the parameters being extracted. Using a range of subset sizes the true stress-strain curves have been obtained, as shown in Figure 5.7a. The true stress-strain curves initially agree however, the results deviate at larger strains. The true stress-strain data for the range of subsets are used in FE analysis. The force displacement responses from the FE analysis are shown in Figure 5.7b, this was compared to the experimental force displacement data (DIC Data). All of the FE analysis for various subsets underestimates the force. However, the true stress-strain data provided when using a 25 x 25 pixels subset size gives the best match and follows the experimental curve.

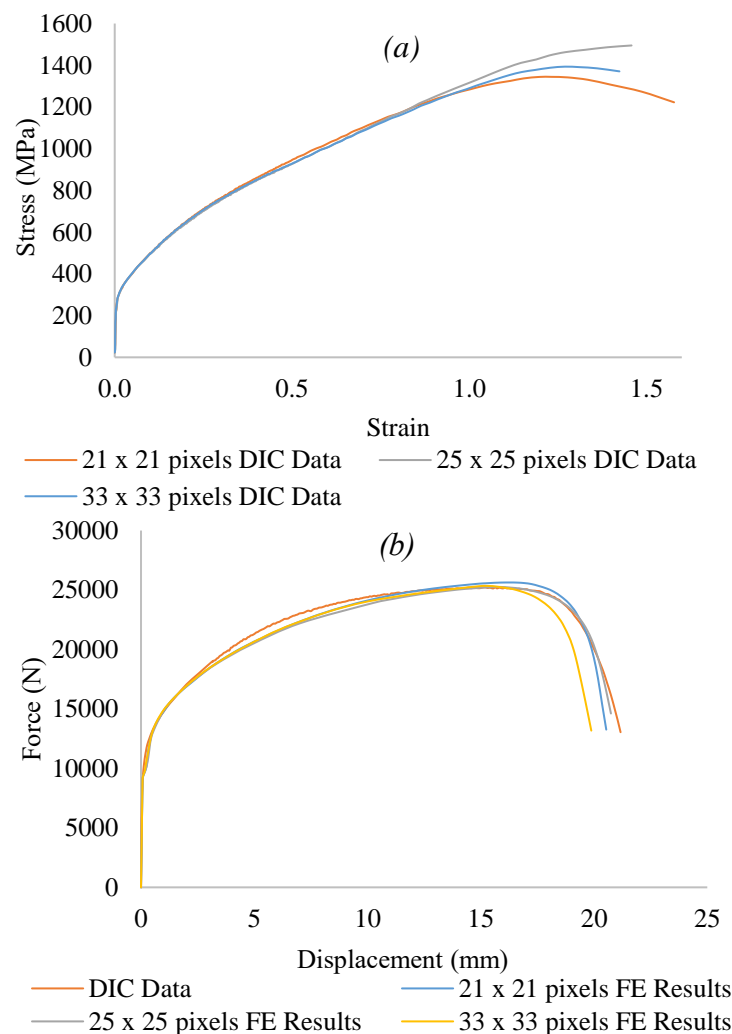


Figure 5.7. a) True Stress-Strain Curves b) Force Displacement Curves for a Range of Subsets.

The ratio calculated from the original circumference and the line CD has a significant influence on the calculated area when using the direct method. The original force displacement responses shown that the stress should have been higher than calculated.

From measuring the diameter from the failed specimen, the failure area and stress can be determined. The calculated radius at failure initiation was then compared to the actual measured value of the specimen. The original calculated area was found to be 4.2% larger than the measured area. Line CD as shown in Figure 5.4c started as a circumferential line, however it does not end up as the shortest circumferential distance between points C and D, due to deformation in the necking area. In order to correct the data, the calculated ratio of the circumference was altered. Decreasing the calculated ratio increases the stress. Thus, the ratio of the circumference was iteratively reduced by 0.1%, until reaching 2.7% as the calculated force displacement curve matched the experimental force displacement curve when using a subset size of 25 x 25 pixels, as shown in Figure 5.8.

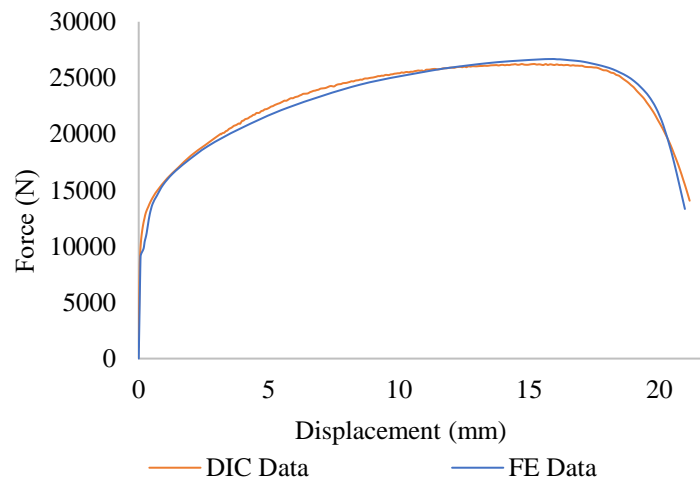


Figure 5.8. Matched Force Displacement Curves.

Table 5.3 compares the original and corrected calculated failure parameters. Demonstrating the accuracy of the corrected calculated true stress-strain data.

Table 5.3. Failure Measurement Comparisons.

	Measured Data	Original Calculated	Corrected Calculated
Failure Radius (mm)	1.70	1.73	1.68
Failure Area (mm ²)	9.03	9.41	8.90
Failure Stress (MPa)	1558	1495	1579

Deformation of the FE analysis shows good agreement with the DIC image at the onset of failure. This is shown in Figure 5.9 by the contours displaying true Y failure strain.

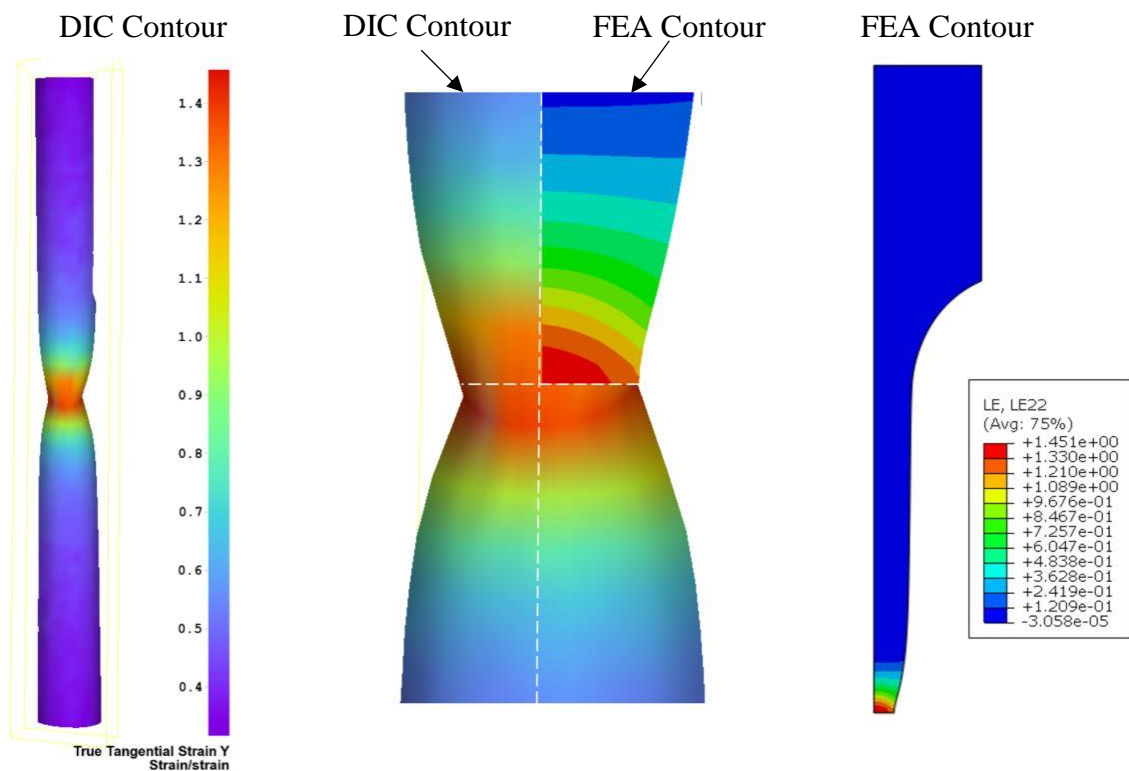


Figure 5.9. Contours of True Y strain for DIC image and FE model at the Onset of Failure.

In order to demonstrate the effect for a range of local regression and smoothing spline filter, true stress-strain curve was plotted against data when no filtering is applied, as shown in Figure 5.10a. By using these sets of data in FE analysis the force displacement responses from the FE analysis are shown in Figure 5.10b. This shows that as the smoothing of the data reduces the failure stress and strain the data does not predict the correct true stress-strain data. Applying any filters reduces the standard deviation of the data and decreases the spatial resolution. When

the data has no filtering applied this was found to be the best match for the experimental force displacement curve.

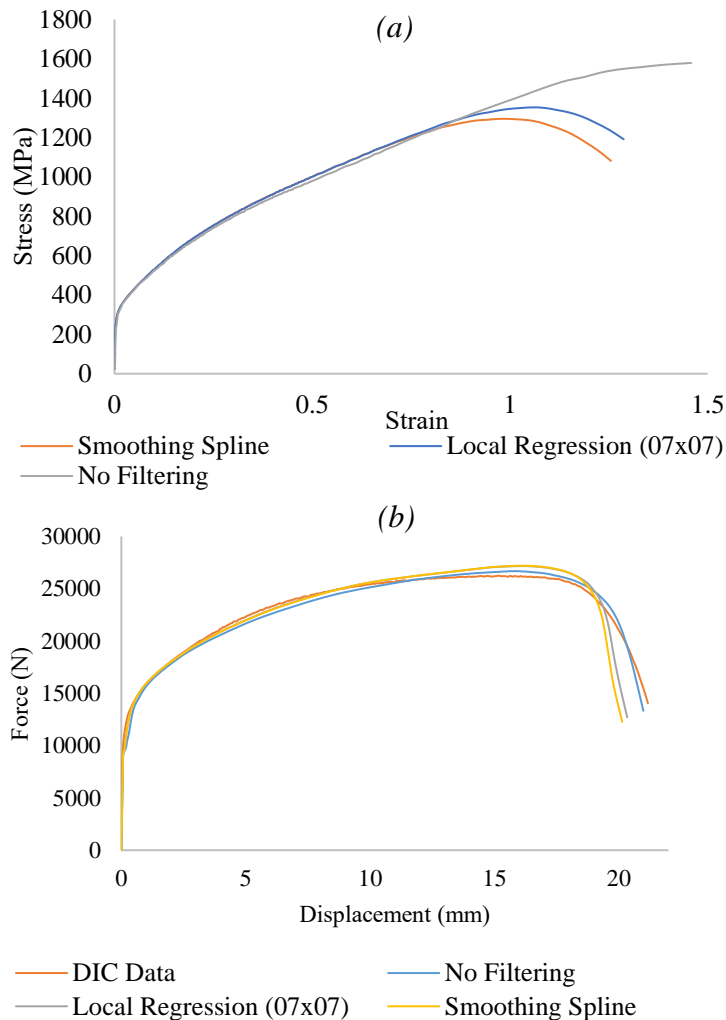


Figure 5.10. a) True Stress-Strain Curves b) Force Displacement Curves for a Range of Filtering.

5.3.9 Conclusion

A series of uniaxial tensile tests were performed. DIC was used during the experiments in order to extract data such as true strain and instantaneous cross-sectional area up to failure. The direct measurement method was used to provide true stress-strain data throughout the whole test, including beyond UTS. DIC post process study, investigated the effect of using different filtering and subset size results when producing true stress-strain data. FE analysis was executed using the different true stress-strain data sets to compare the force displacement

responses. In this study, it was found that the post processing of the DIC software significantly influenced the extracted data. A subset size of 25 x 25 pixels and no filtering, produced true stress-strain data that was in agreement with the experimental results, as shown in Figure 5.11. The vertical line shown on Figure 5.11 shows the upper strain limit which can be obtained before non-uniform deformation takes place.

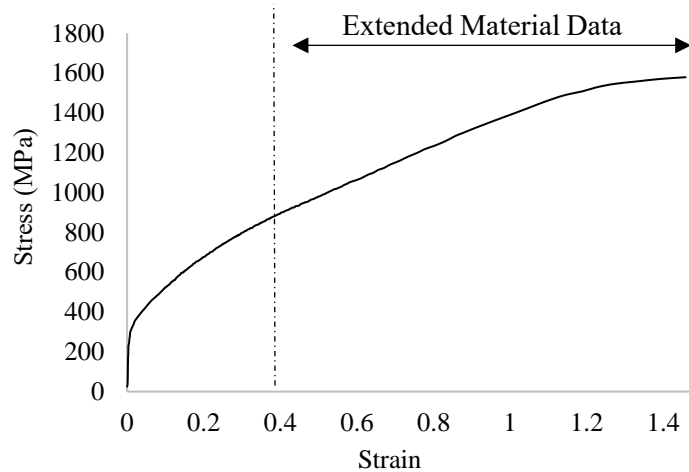
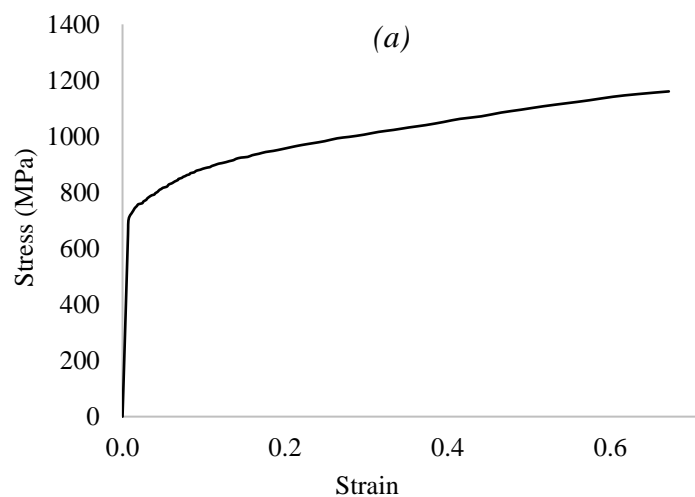


Figure 5.11. Final True Stress-Strain Data for AISI 304L.

When applying a subset size of 25 and no filtering to the CA6NM DIC data, this produced accurate true stress strain data shown in Figure 5.12a, the agreement is shown by the force displacement curve in Figure 5.12b.



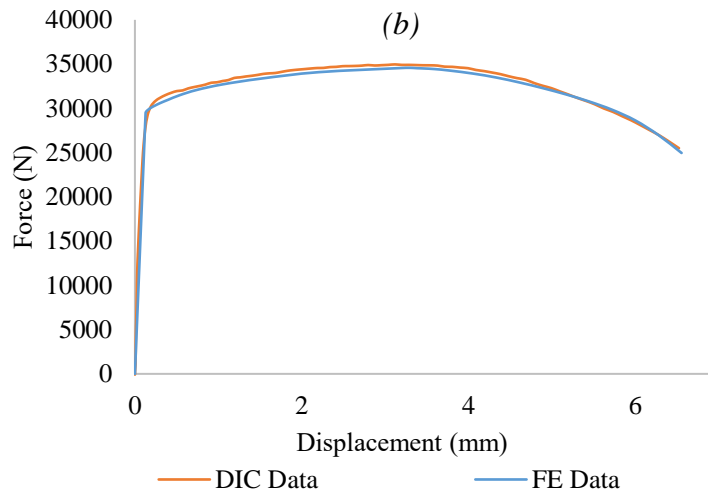


Figure 5.12. a) Force Displacement Curves for CA6NM b) True Stress-Strain Data for CA6NM.

Different geometries of specimens will need their own individual experimental set ups and a subset size is dependent on the speckle pattern applied. Therefore, the general methodology applied to this study should be used to ensure the true stress-strain data is correct and the analysis accurately replicates the experiment.

From the study conducted to obtain the material data the material properties used in the simulations are listed in Table 5.4.

Table 5.4. Material Properties used in the Simulation for CA6NM and AISI 304L.

Material	Density	Poisson Ratio	Young's Modulus	Yield stress and plastic strain
AISI 304L	7.9e+3 Kg/m ³	0.265	2.03e+5 MPa	See tabulated data points in Appendix H
CA6NM	7.6e+3 Kg/m ³	0.3	1.98e+5 MPa	

5.4 Anisotropy of AISI 304L

Anisotropy is defined as the directional variation of mechanical properties. If a material is anisotropic, it displays diverse material behaviours in different directions, this can affect the materials mechanical properties. Isotropy is the opposite to anisotropy, where the material shows identical properties in all directions. Anisotropy in metals are less expected in cast structures and products manufactured from powders by isostatic pressing [200].

This study focuses on two materials CA6NM and AISI 304L. As CA6NM is a cast material, only AISI 304L sheet metals will be investigated for anisotropic behaviour. Manufacturing of the specimens will be for rolling direction 0° , 45° and 90° as shown in Figure 5.13, to determine if directions of the material also have an influence in the fracture behaviour.

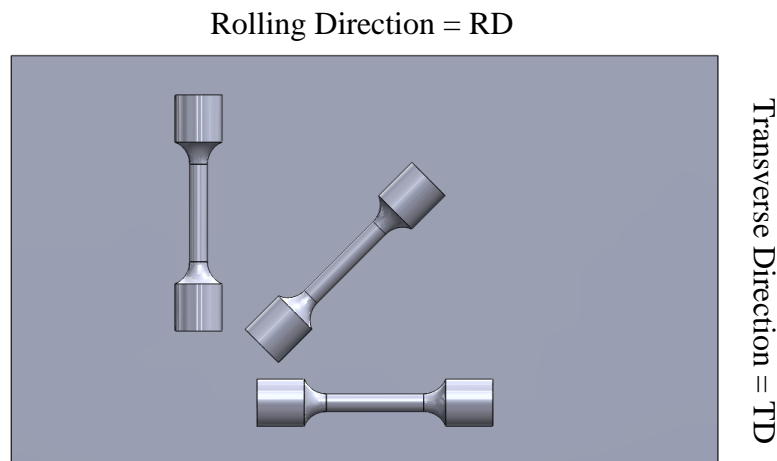


Figure 5.13. Rolling Directions of Tensile Specimens.

Five of each uniaxial tensile tests were performed for each direction. DIC was used during the experiments, therefore true stress-strain data was obtained throughout the whole test, including beyond UTS. By critically evaluating the data produced, the material AISI 304L is assumed to be isotropic, as it did not exhibit any significant anisotropic behaviour. The graphs shown in Figures 5.14 and 5.15 demonstrate that the results were not affected by the range of directions. The failure stresses in Figure 5.15 are marginally different due to the force at which the material failed, and there is no correlation between the rolling directions affecting the true stress strain curves. Scatter of data for at higher stresses and strains are shown in Figure 5.15, this is due to

the difference in forces at which the samples failed, this is shown in Figure 5.14 but the scales of strain in Figure 5.15 presented this more evident.

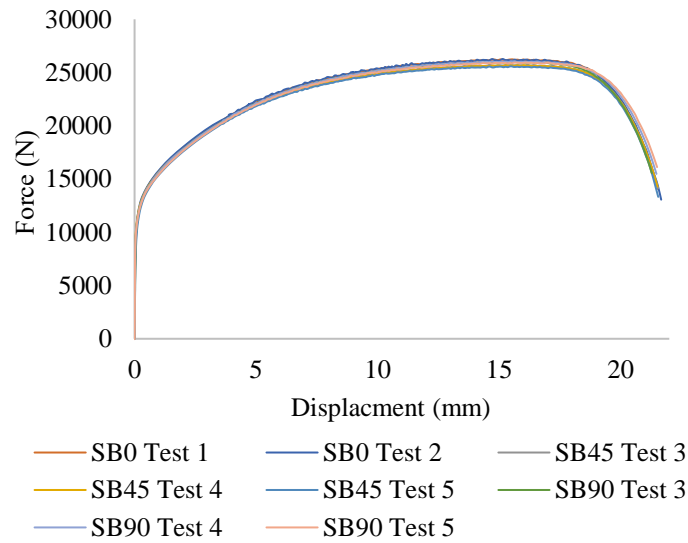


Figure 5.14. Force Displacement Curves for a Range of Rolling Directions.

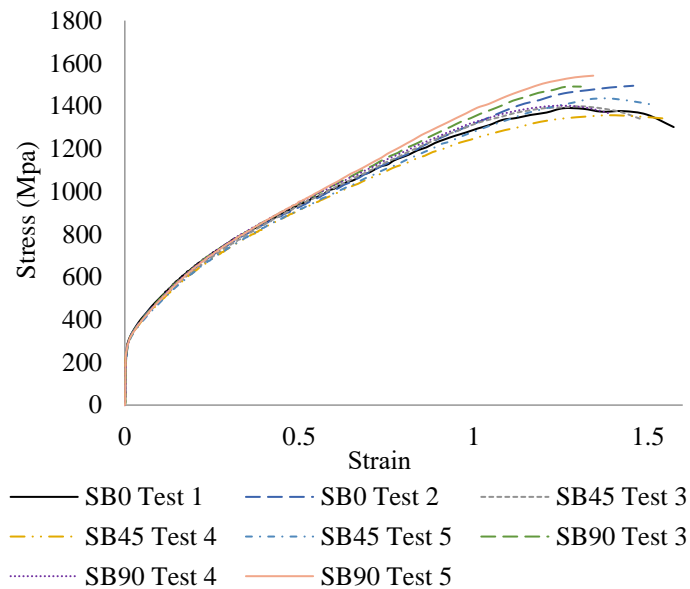


Figure 5.15. True Stress-Strain Curves for a Range of Rolling Directions.

In this study anisotropic structure for plane stress conditions was tested for a range of rolling directions; 0° , 45° and 90° , to see if the different rolling directions of materials had an influence on the fracture behaviour. In conclusion, this thesis will assume AISI 304L to be isotropic and will not investigate various rolling directions further.

5.5 High and Low Stress Triaxiality

5.5.1 Introduction

To construct a fracture locus for the high and low stress triaxiality regions for AISI 304L and CA6NM. A series of 9 geometries as shown in Figure 5.16 were each tested to failure 5 times, for a total of 110 tests, at ambient temperature under quasi-static conditions. The axial displacement was measured using the method shown in Section 4.6.6. The tests have been repeated five times to assure the consistency of the results.

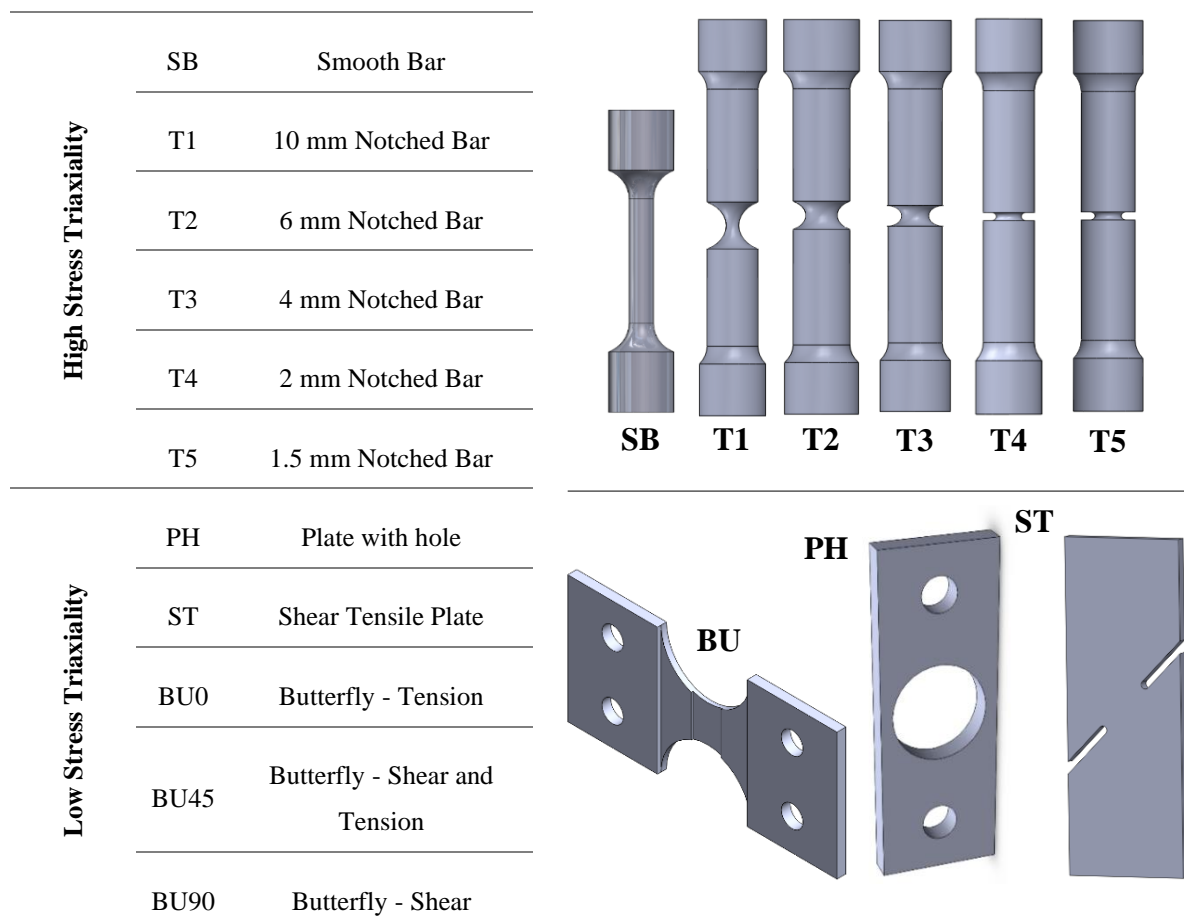


Figure 5.16. High and Low Stress Triaxiality Specimens.

5.5.2 Experiments and Results

For all post processing of DIC results a subset size of 25 and a grid spacing of 17 was used. The parallel numerical simulations of all the 9 geometries were performed using ABAQUS/STANDARD, using a standard von Mises plasticity model, isotropic hardening, Mises yield surface, associative plasticity defined using the *PLASTIC keyword. Reduced integration elements were used for nonlinear static analysis, this was preferred as the integration was performed on a single integration point which reduces the computational time.

5.5.2.1 Smooth and Notched Bar Experiments

Specimens in the high stress triaxiality region were tested on an Instron Servo Hydraulic testing machine (100 kN capacity). An example showing the experimental test set up for T2 was previously shown in Figure 4.4. DIC Contours for True Tangential Y Strain for T3 are shown for both AISI 304L and CA6NM in Figure 5.17.

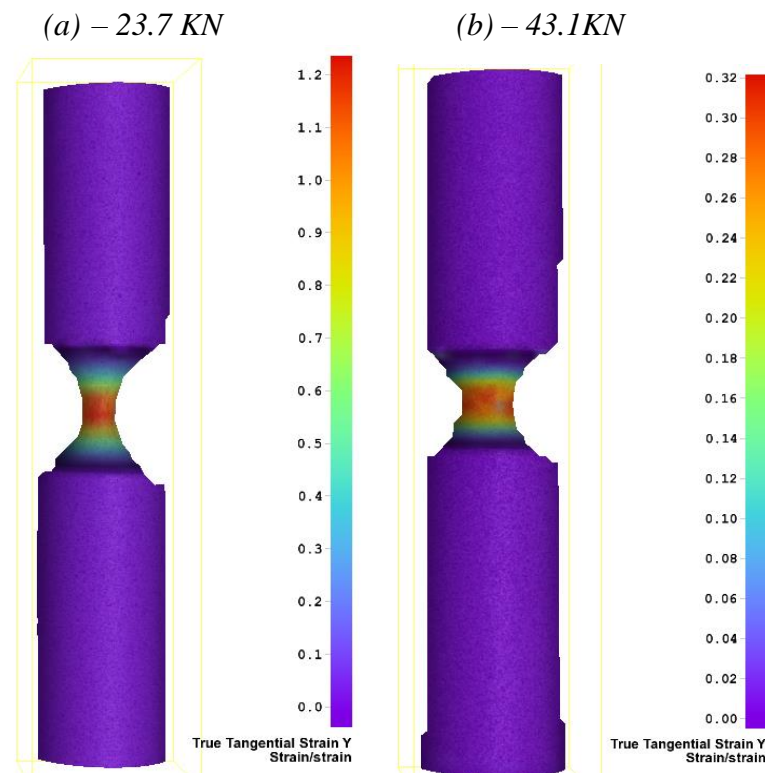


Figure 5.17. 4mm Notched Bar (T3) DIC Contour for True Tangential Strain Y, a) AISI 304L, b) CA6NM.

For the FE models regarding the uniaxial tensile tests for smooth bar (SB) and notched bars (T1-5), half axisymmetric models with CAX4R elements were used. CAX4R elements were used as they have good high deformation plasticity. Symmetry boundary conditions were applied along the horizontal symmetry line at the centre of the specimen, and a displacement boundary condition was introduced to the remote point, which was coupled to the top surface, as shown in Figure 5.18a. In order to study the possible mesh size sensitivity, three different meshes were developed as shown in Figure 5.18b. The equivalent plastic strain for the different three meshes is shown in Figure 5.18c, with the normal mesh being selected due to the convergent result. Mesh sensitivity was investigated for all FE simulations in this thesis.

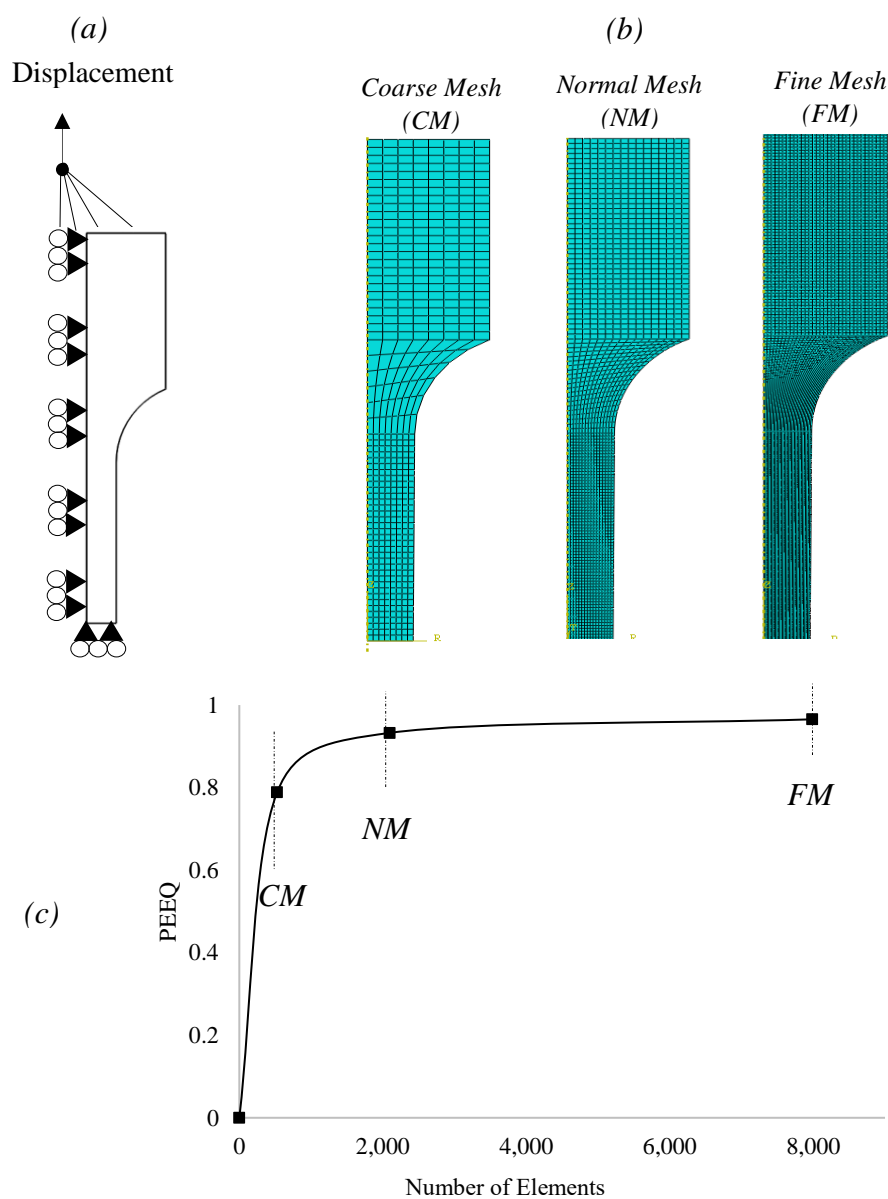


Figure 5.18. Smooth Bar (SB) a) Loading and Boundary Conditions b) Three Different Meshes c) Equivalent Plastic Strain for the Different Meshes.

An example showing the force displacement curves for T3 for both AISI 304L and CA6NM is shown in Figure 5.19. The experimental results for the smooth and notched bars showed an excellent agreement within the plastic region with the FE equivalent results. However, there is an observable difference in the elastic region for CA6NM as shown in Figure 5.19b, this was also observed in Figure 5.19c, which shows the elastic region of the AISI 304L. The discrepancy in the elastic region is due to the DIC software not being able to capture small stains with accuracy, however, this does not affect this study as this thesis is solely focused on characterising the plasticity and fracture behaviour. This agreement up to failure has been seen for all the high stress triaxiality specimens as shown in Appendix I.

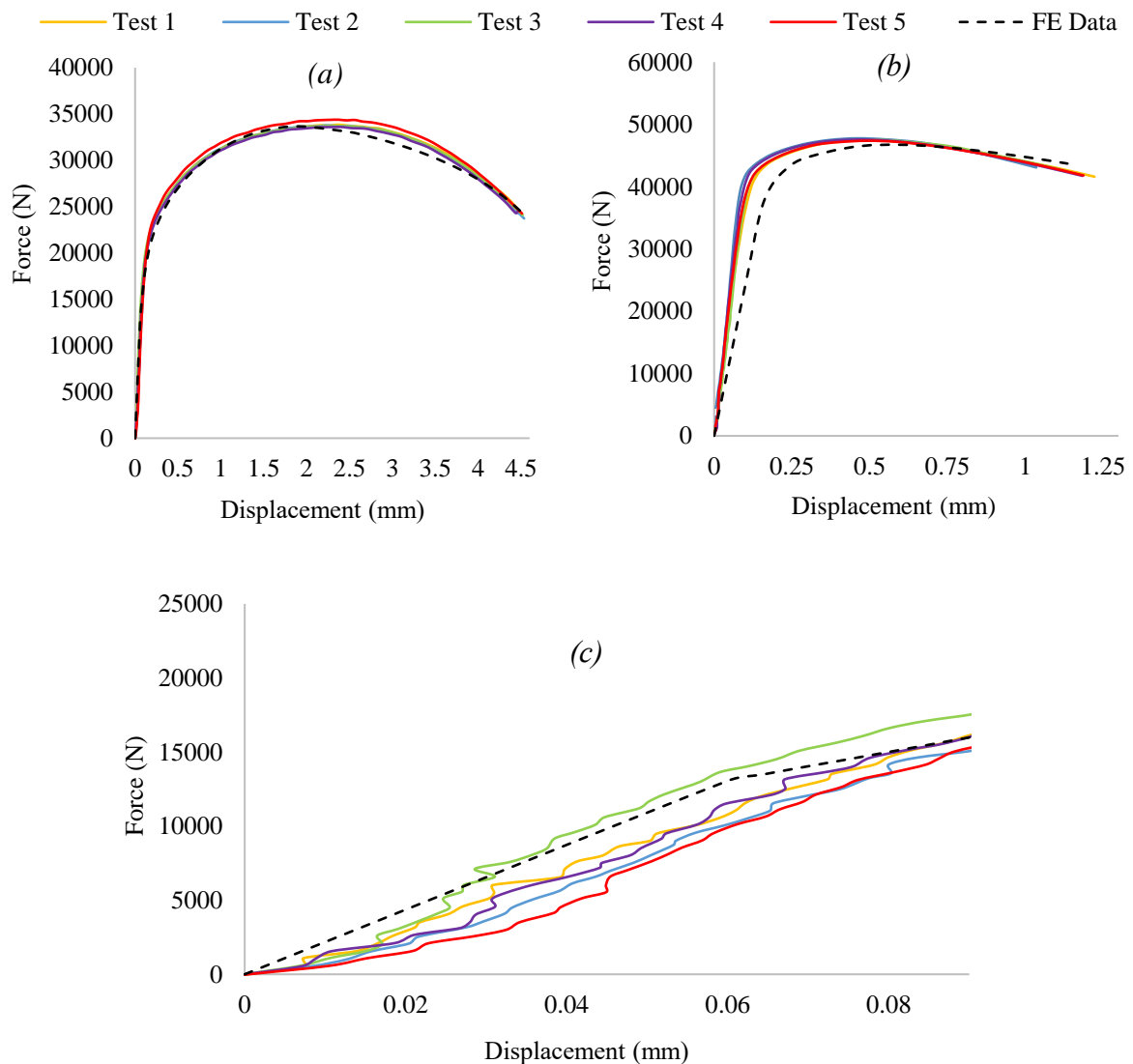


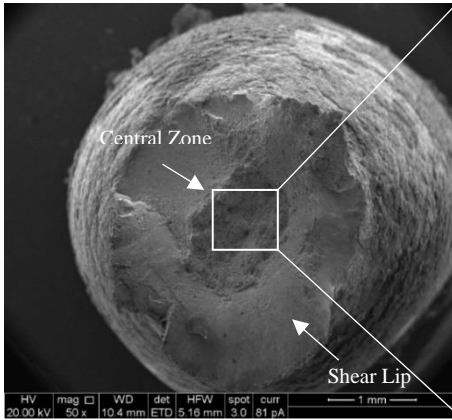
Figure 5.19. 4mm Notched Bar (T3) Force Displacement Curves a) AISI 304L, b) CA6NM, c) AISI 304L Elastic Region

Scanning electron microscope (SEM) uses focused beam of high-energy electrons to generate a variety of signals at the surface of solid specimens. The signals that derive from electron-sample interactions reveal information for failure surfaces can provide fractographic characteristics offering indications of the mode of failure [201]. A SEM investigation was carried out using the Quanta 200 3D Dual Beam FIB-SEM machine model. To prepare the specimens, they were cut down to size to fit within the machine and were carefully cleaned and dried.

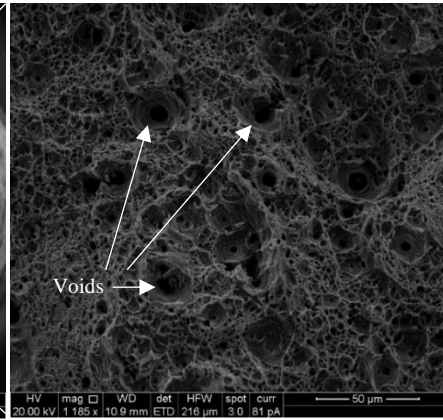
The fracture regarding the material AISI 304L was a typical ductile fracture, this is shown in Figure 5.20a and Figure 5.20c by dimple rupture. The fracture surface includes a central fibrous region and shear lips around the outer edge. Typically, in the high stress triaxiality region as stress triaxiality decreases, fracture strain increases, thus the voids in the material grow and coalesce as the time of deformation increases, hence the dimples are larger and deeper in the central zone for SB compared to T1 when observing the same scale, as shown in Figure 5.20b and Figure 5.20f.

For the same notched bar T4, the SEM images for the fracture surface for AISI 304L and CA6NM are shown in Figure 5.20c-d and Figure 5.20g-h respectively. The failure mechanism for CA6NM is difficult to conclude. There are no observable brittle features, the failure of CA6NM could be affected by many issues including matrix, inclusions, interface between matrix and secondary particles. Without detailed understanding supported by further specific systematic research, it is difficult to be conclusive.

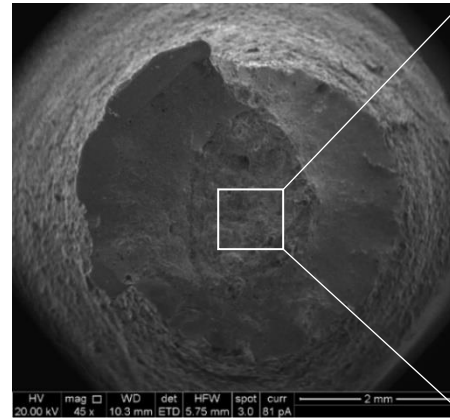
(a) - AISI 304L - SB
Whole Region



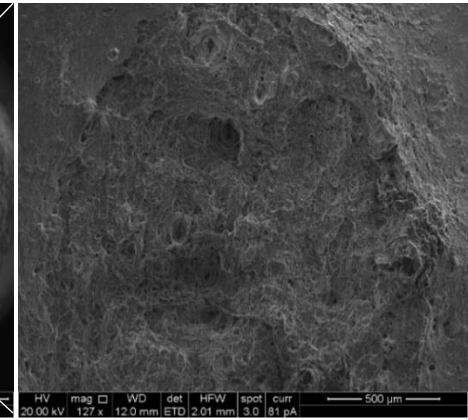
(b) - AISI 304L - SB
Central Region 50 μ m



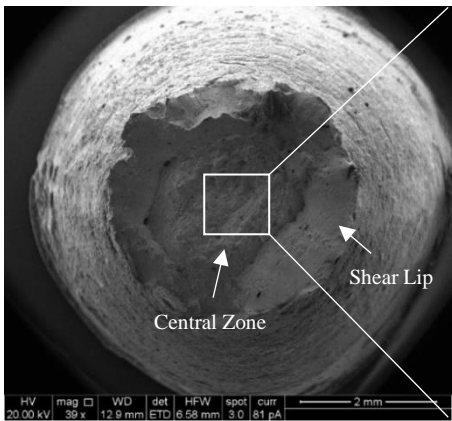
(c) - AISI 304L - T4
Whole Region



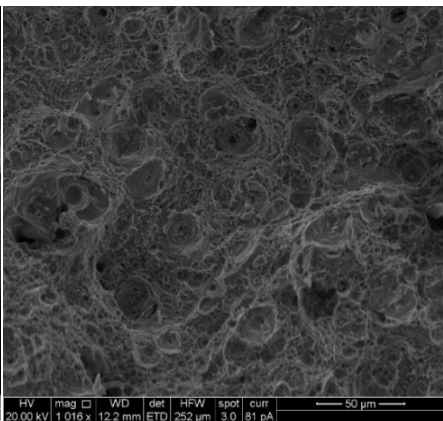
(d) - AISI 304L - T4
Central Region 500 μ m



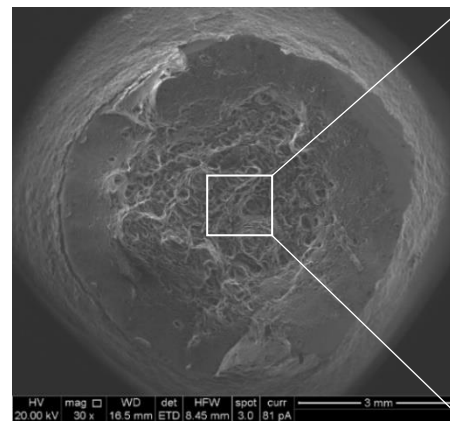
(e) - AISI 304L - T1
Whole Region



(f) - AISI 304L - T1
Central Region 50 μ m



(g) - CA6NM - T4
Whole Region



(h) - CA6NM - T4
Central Region 500 μ m

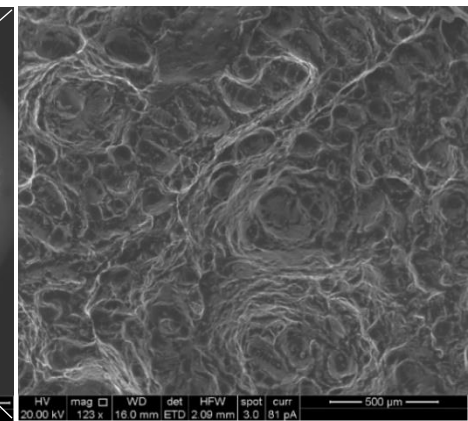


Figure 5.20. Fracatograph for a Range of Tensile Specimens.

5.5.2.2 Plate with Hole Experiments

All the plate with hole (PH) specimens were tested on an Instron Servo Hydraulic testing machine (100 kN capacity). An example showing the experimental test set up for a PH specimen is shown in Figure 5.21.



Figure 5.21. Experimental Test Set-Up for Plate with Hole (PH) Specimen.

DIC Contours for True Tangential Y Strain for the PH specimen are shown for both AISI 304L and CA6NM in Figure 5.22.

For the FE models regarding the PH specimen C3D8R elements were used. To simulate this experiment, remote points were kinematically coupled to the hole's inner surface at the centre of each gripping hole. One of the remote points was fixed and the other was used to apply loading as a prescribed displacement, as shown in Figure 5.23a. The constraint used in Figure 5.23a is an inaccurate representation of a pin in a hole. However, it is shown in Figure 5.23b, that the effects around the pin hole were localised and this constraint does not impact on the results to be compared with the DIC results. Figure 5.23c shows the mesh density of the FE model, with the mesh being more dense around the failure region.

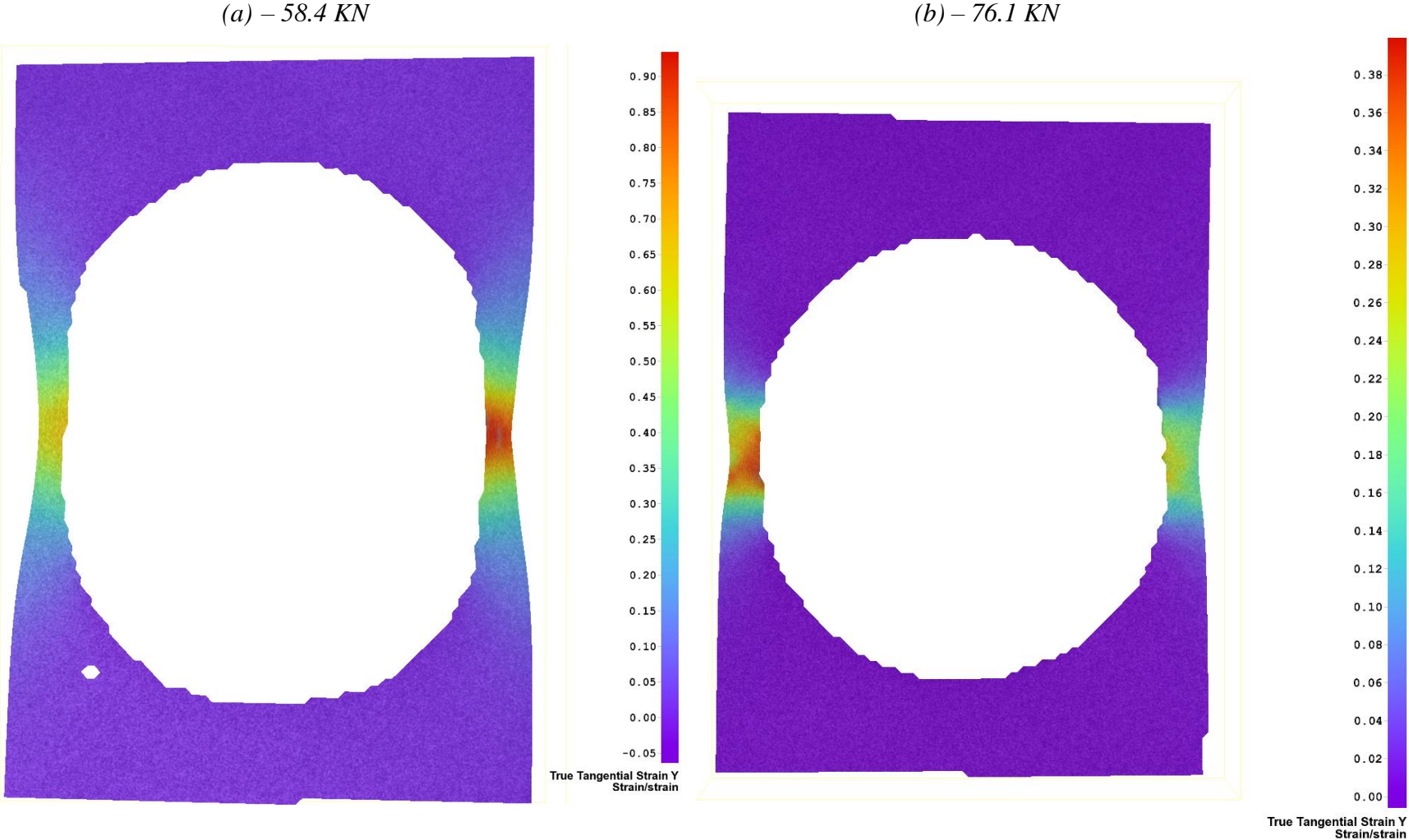


Figure 5.22. Plate with Hole (PH) Specimen DIC Contour for True Tangential Strain Y a) AISI 304L, b) CA6NM.

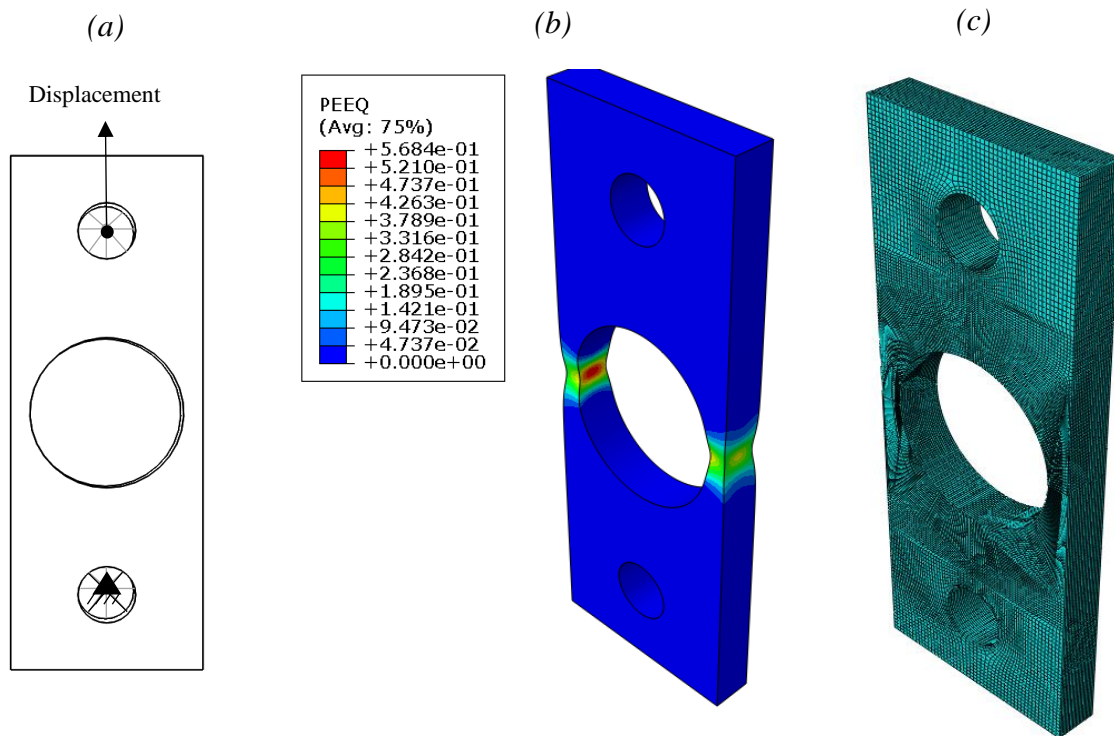


Figure 5.23. a) Loading and Boundary Conditions of Plate with Hole (PH) b) FE Plastic Equivalent Strain Contour Example c) Mesh density of FE model.

Force displacement curves for the PH specimens for both AISI 304L and CA6NM are shown in Figure 5.24.

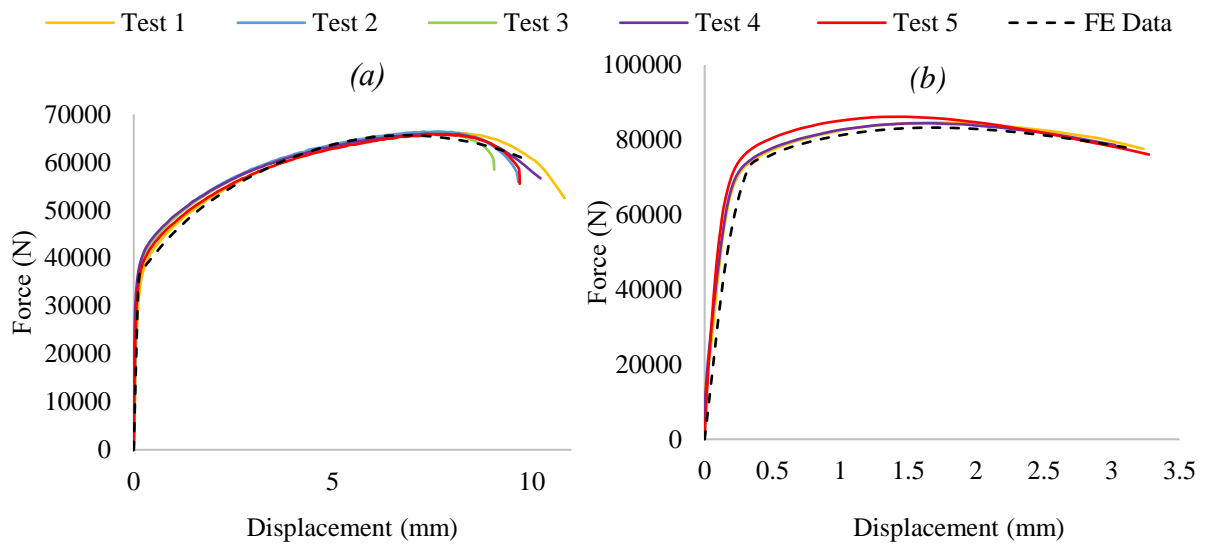


Figure 5.24. Plate with Hole (PH) Force Displacement Curves a) AISI 304L, b) CA6NM.

5.5.2.3 Shear Tensile Plate Experiments

The shear and tension (ST) specimens were tested on a Mays Servo Hydraulic testing machine (600 kN capacity) due to loading and gripping requirements of the specimen. An example showing the experimental test set up for a ST specimen is shown in Figure 5.23.

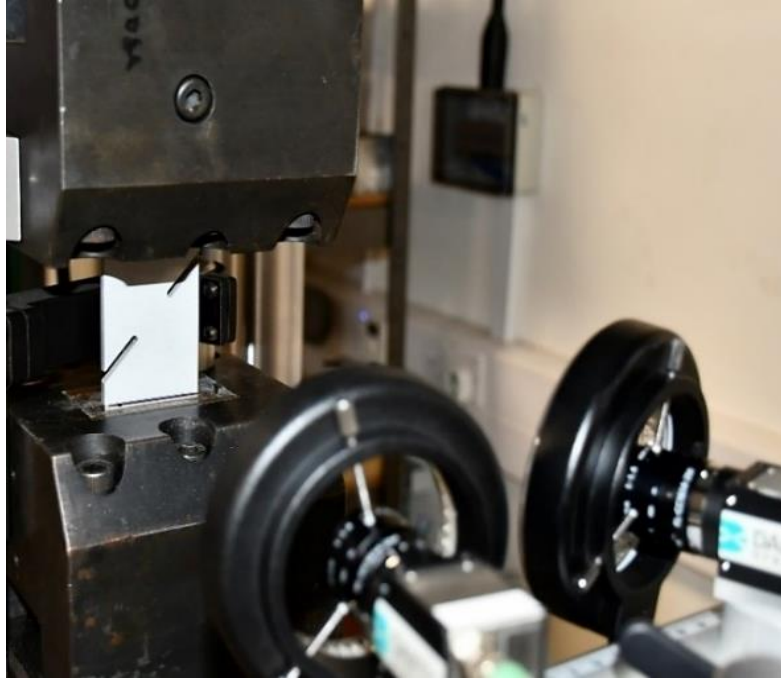


Figure 5.25. Experimental Test Set-Up for Shear and Tension (ST) Specimen.

DIC Contours for True Tangential Y Strain for ST Specimens are shown for both AISI 304L and CA6NM in Figure 5.26.

To model the ST specimen a displacement boundary condition, was introduced to a remote point which was coupled to the top section for the shear plate specimen, the bottom section was fixed as shown in Figure 5.27a. For the ST specimen C3D8R elements were used, the mesh density is shown in Figure 5.27b.

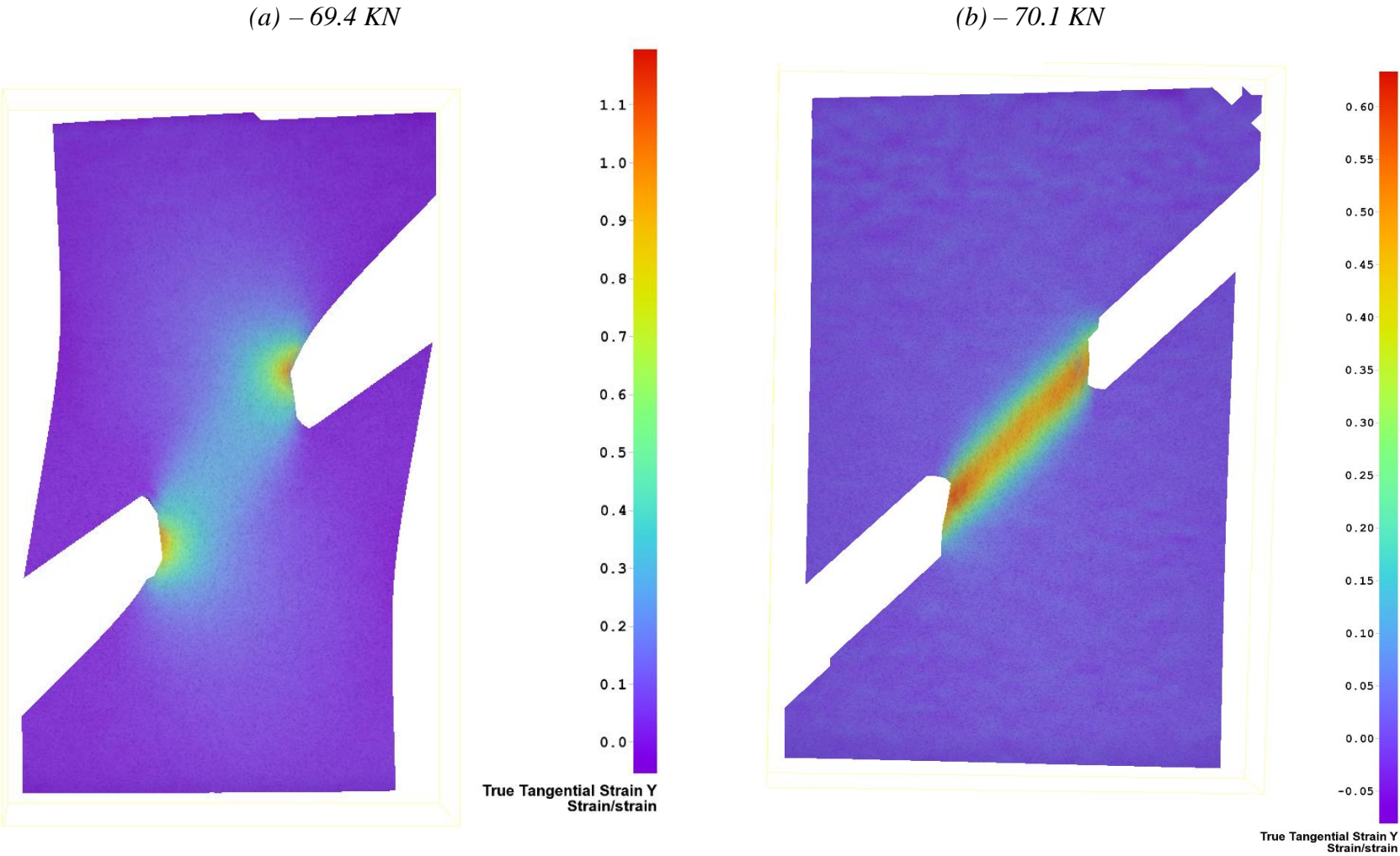


Figure 5.26. Shear and Tension (ST) Specimen DIC Contour for True Tangential Strain Y a) AISI 304L, b) CA6NM.

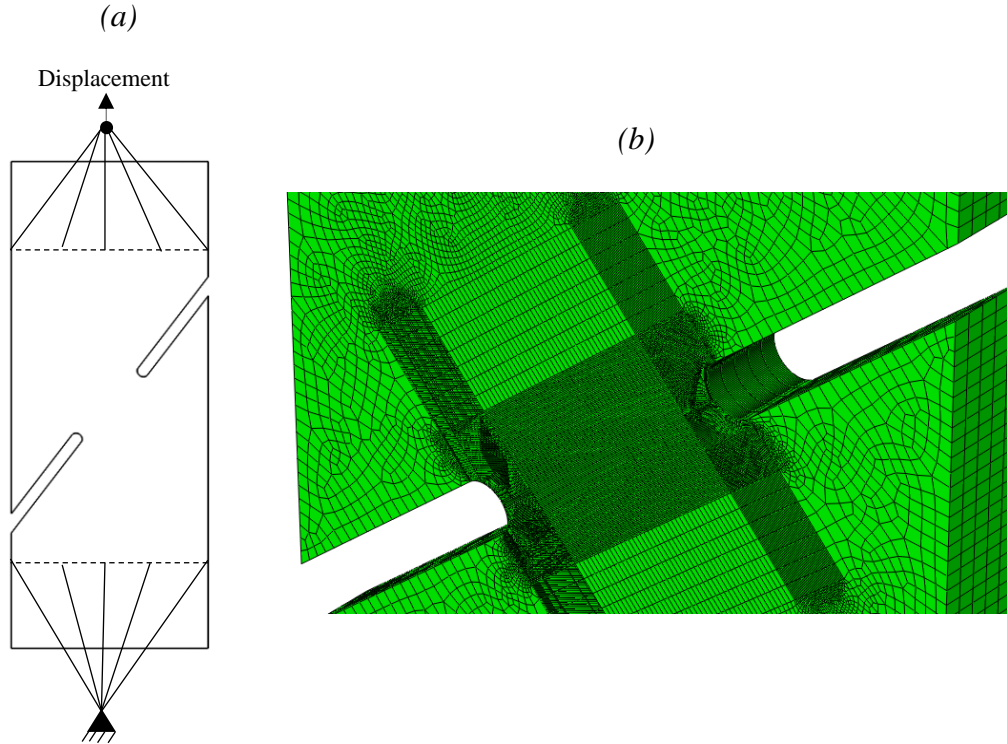


Figure 5.27. a) Loading and Boundary Conditions of Shear and Tension (ST), b) Mesh Density for the Failure Region.

Force displacement curves for the ST specimen for both AISI 304L and CA6NM are shown in Figure 5.28.

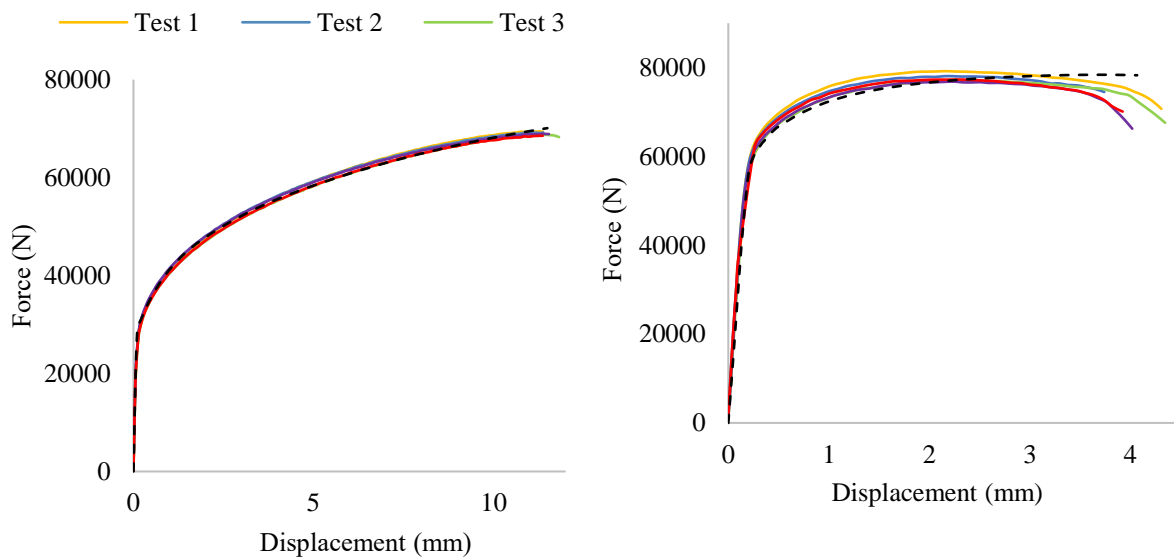


Figure 5.28. Shear and Tension (ST) Specimen Force Displacement Curves a) AISI 304L, b) CA6NM.

5.5.2.4 Butterfly Specimen Experiments

The butterfly specimens were tested on a Instron Servo Hydraulic testing machine (100 kN capacity). The experimental test set up for the butterfly specimen (BU) for the various loading angles is shown in Figure 5.29.

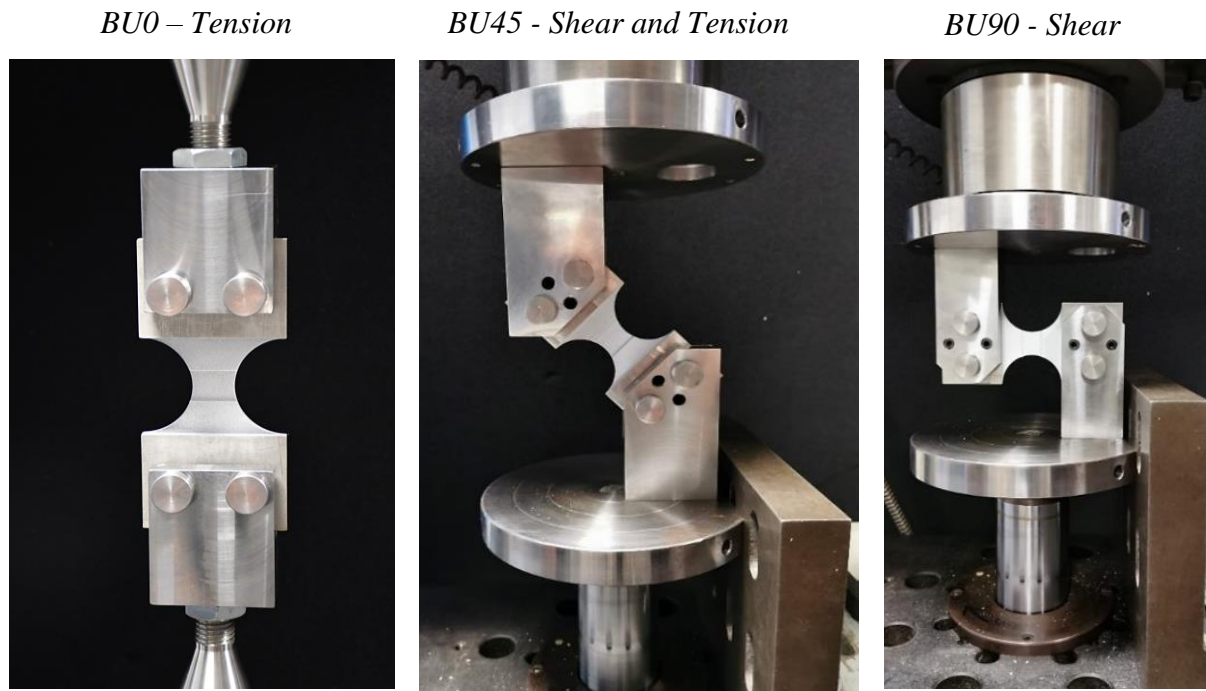


Figure 5.29. Experimental DIC Set Up for Butterfly Specimens.

DIC Contours for True Tangential Y Strain for BU0/45/90 are shown for both AISI 304L and CA6NM in Figure 5.30 and Figure 5.31.

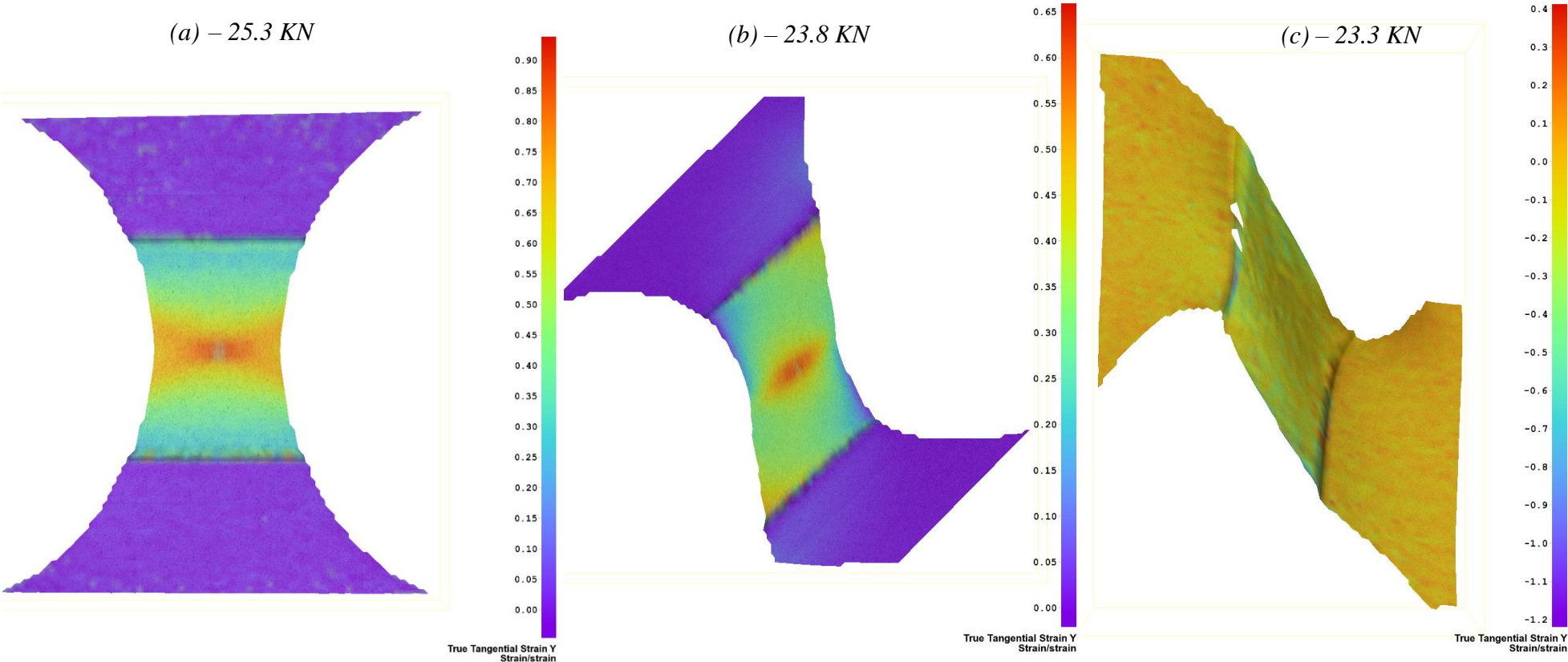


Figure 5.30. AISI 304L Butterfly Specimen DIC Contours for True Tangential Strain Y.

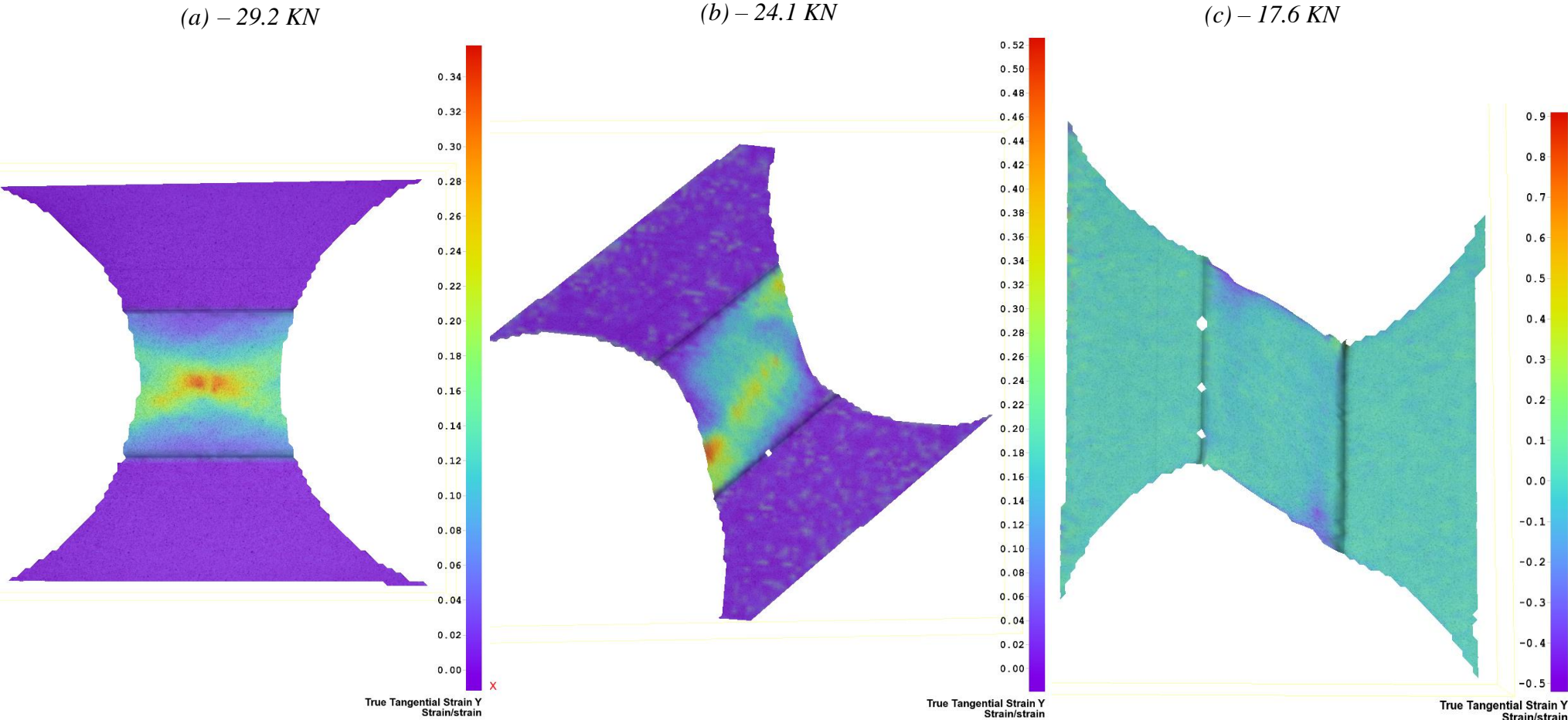


Figure 5.31. CA6NM Butterfly Specimen DIC Contours for True Tangential Strain Y.

The butterfly specimen had four holes for gripping, remote points were kinematically coupled to the hole's inner surface at the centre of each gripping hole. A displacement boundary condition was introduced to two of the holes and the other two were fixed. The geometry was then rotated depending on the loading condition required, as shown in Figure 5.32.

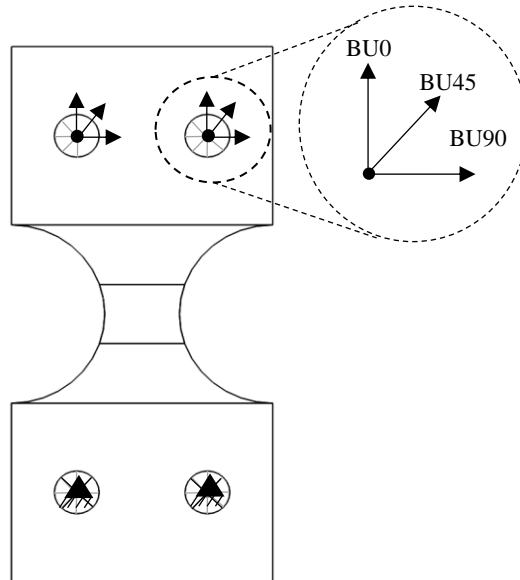


Figure 5.32. Loading and Boundary Conditions of Butterfly Specimen (BU0/45/90).

An example showing the force displacement curves for the shear loading for a BU90 specimen for both AISI 304L and CA6NM are shown in Figure 5.33.

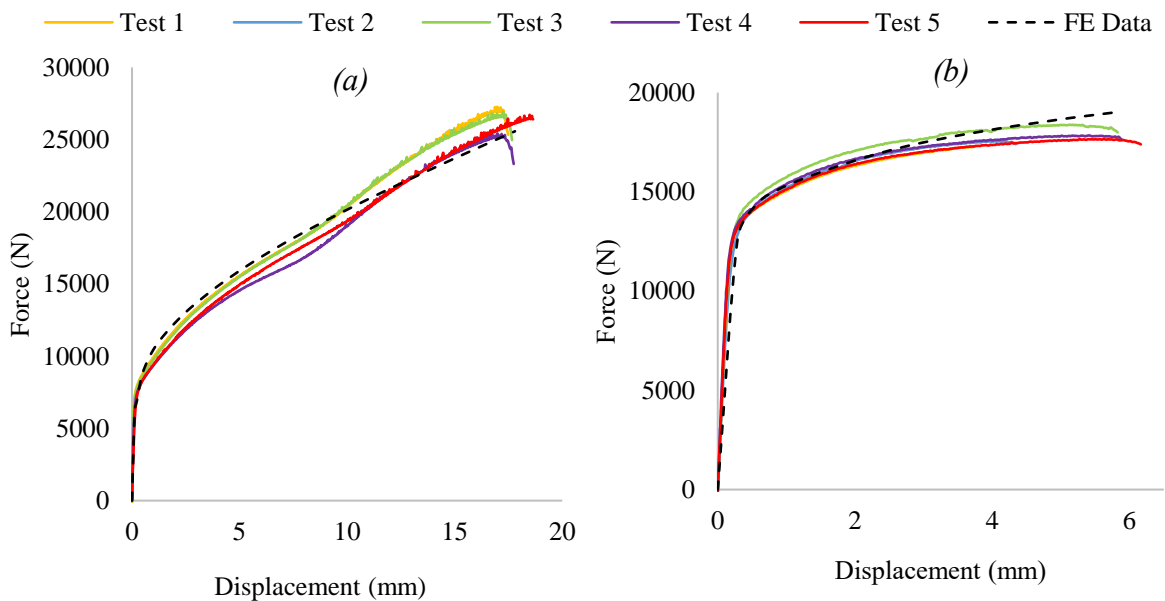


Figure 5.33. Butterfly Specimen BU90 Force Displacement Curves a) AISI 304L, b) CA6NM.

5.5.3 Summary of Low and High Stress Triaxiality

To obtain the equivalent fracture strain, average stress triaxiality and the average Lode angle parameter, the instance which failure occurred and where failure initiated (critical location) was needed. For all specimens tested, the moment of fracture initiation was assumed to be the first detectable discontinuity at the specimen surface when observing the DIC images. Following Table 2.2 which summarised the critical location from various researchers, the critical location was taken at the maximum plastic equivalent strain. Examples displaying the critical location for a few geometries are shown in Figure 5.34. The critical location for SB and all the notched bars T1-5 was taken as the centre of the equatorial area, as shown in Figure 5.34a. The critical location for PH specimen as shown in Figure 5.34b, was taken at the middle of the circumferential surface of the hole perpendicular to the loading. For the ST specimen the critical location, as shown in Figure 5.34c, was taken at the middle of the gauge surface perpendicular to the loading.

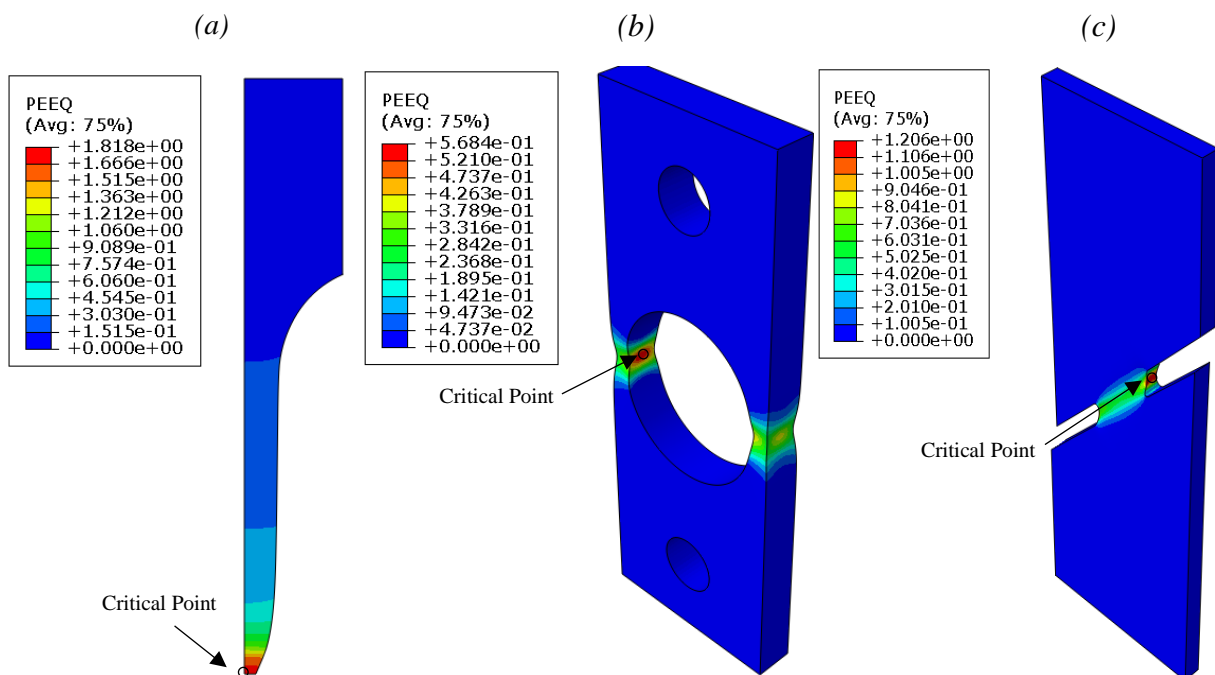


Figure 5.34. Plastic Equivalent Strain Contours showing Critical Locations.

To obtain the Lode angle parameter from ABAQUS, a python script was used in the application programming interface (API), as shown in Appendix J-1. The first step of the code was to calculate the normalised third invariant for the FE model for each frame, this was executed

using which used Equation 31 (line 63). Next, the lode angle parameter was calculated using Equation 37 (line 64).

As previously discussed, for each geometry there were three parameters that were required: the equivalent fracture strain, average stress triaxiality and the average Lode angle parameter. To clarify how this was conducted for each geometry, an example using the FE results from AISI 304L T3 is shown in Figure 5.35a. The average displacement at failure (u_f) for the 5 experimental tests performed was used for the displacement boundary condition in the FE model. Data was then extracted from the FE model at the critical location, as shown in Figure 5.35a. The equivalent fracture strain was taken as the final equivalent plastic strain (PEEQ) value, the value for stress triaxiality and Lode angle parameter was averaged over the load history, as shown on the graph in Figure 5.35b. Triaxiality and Lode angle parameter were averaged over the load history, whilst their variability with displacement is due to local changes in geometry, taking the average captures the plasticity behaviour as well as failure, which provides a conservative result, compared to taking the point of failure, this method has been done by previous researchers Bao and Wierzbicki [12].

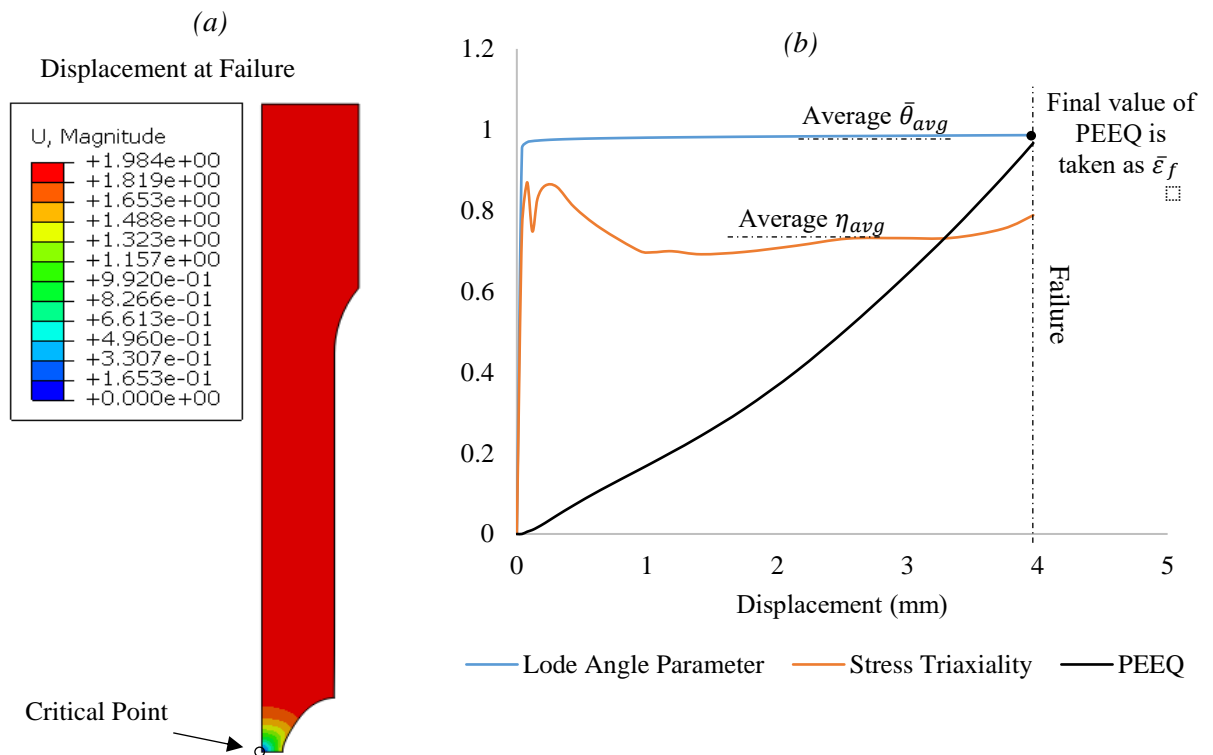


Figure 5.35. An example showing how the equivalent fracture strain, average stress triaxiality and the average Lode angle parameter is obtained a) Contour plot of the displacement for AISI 304L T3 at failure, b) Graph showing how the data was extracted.

FE contours for Lode angle parameter and stress triaxiality show how the material is responding to the loading conditions, an example is shown in Figure 5.36 of AISI 304L PH at the onset of failure.

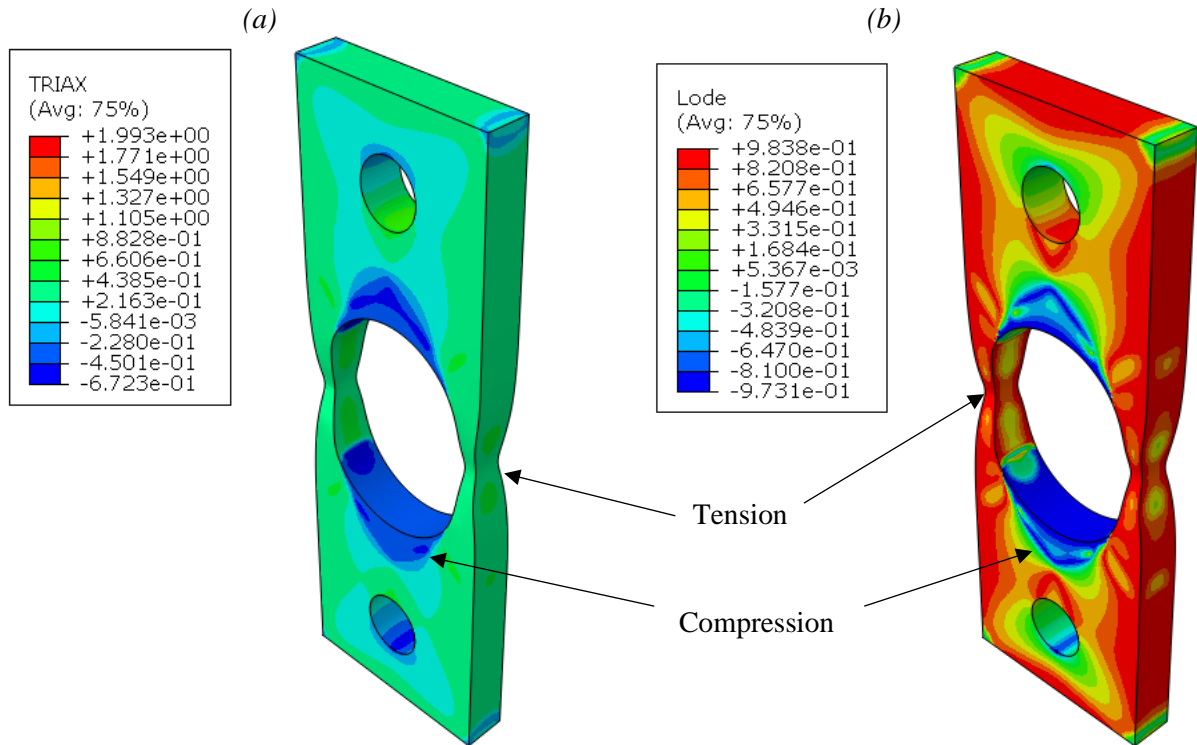


Figure 5.36. AISI 304L Plate with Hole at Failure.

An example comparing the FE analysis and DIC contour of AISI 304L PH at the onset of failure is shown in Figure 5.37, the deformation and the Y-strain are shown to be equivalent.

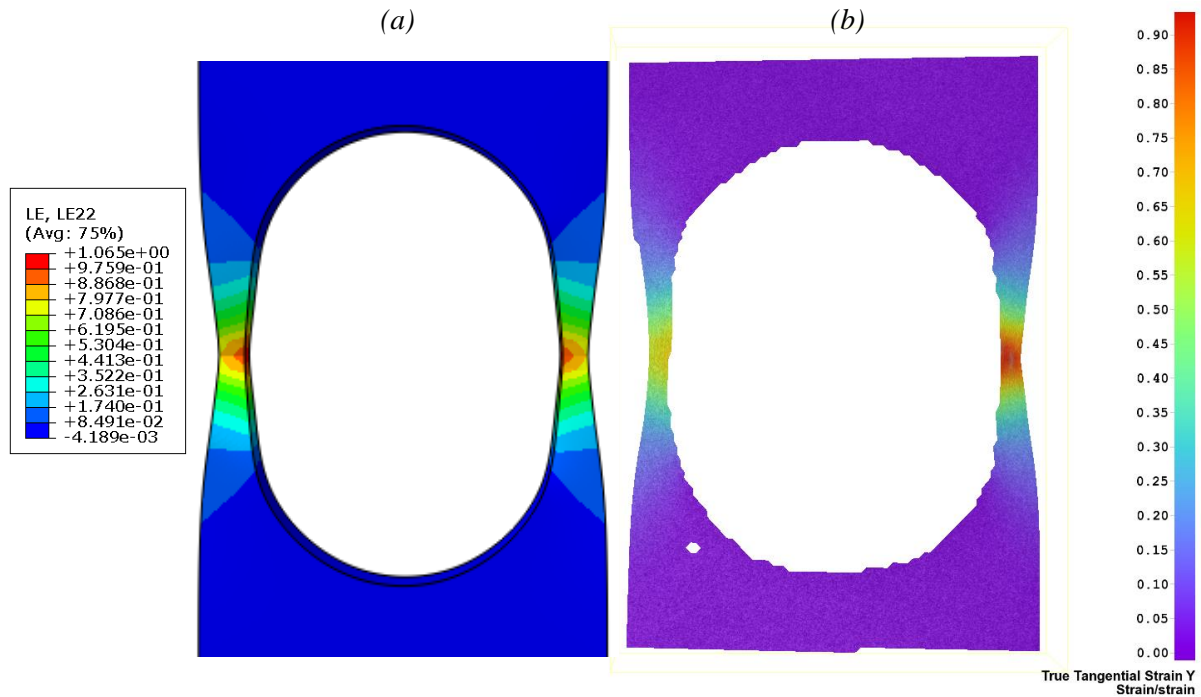


Figure 5.37. AISI 304L PH a) FE Contour Y-True Strain b) DIC Contour Y-True Strain.

A 2D fracture locus was used in this thesis instead of a 3D fracture locus, as it was easier to interpret the results. Thus, there are two graphs for each material, the first is the traditional 2D fracture locus, where equivalent fracture strain is against average stress triaxiality, and the second is the average Lode angle parameter data against average stress triaxiality, this is conducted for both AISI 304L and CA6NM, as shown in Figure 5.38. Tabulated data for AISI 304L and CA6NM for the equivalent fracture strain, stress triaxiality and the lode angle parameter is shown in Table 5.5.

Error bars shown in the graphs presented, were determined by using the minimum and maximum u_f of each geometry as value for the displacement boundary condition in the FE model, to find the relative equivalent fracture strain, average stress triaxiality and average Lode angle parameter. The trend lines were found using Matlab curve fitter app, by comparing numerical fit results, including the fitted coefficients and goodness-of-fit statistics. The points used for each trend line depended on which region the stress triaxiality was in, for example points used for the low stress triaxiality region were PH, ST, BU0, BU45 and BU90.

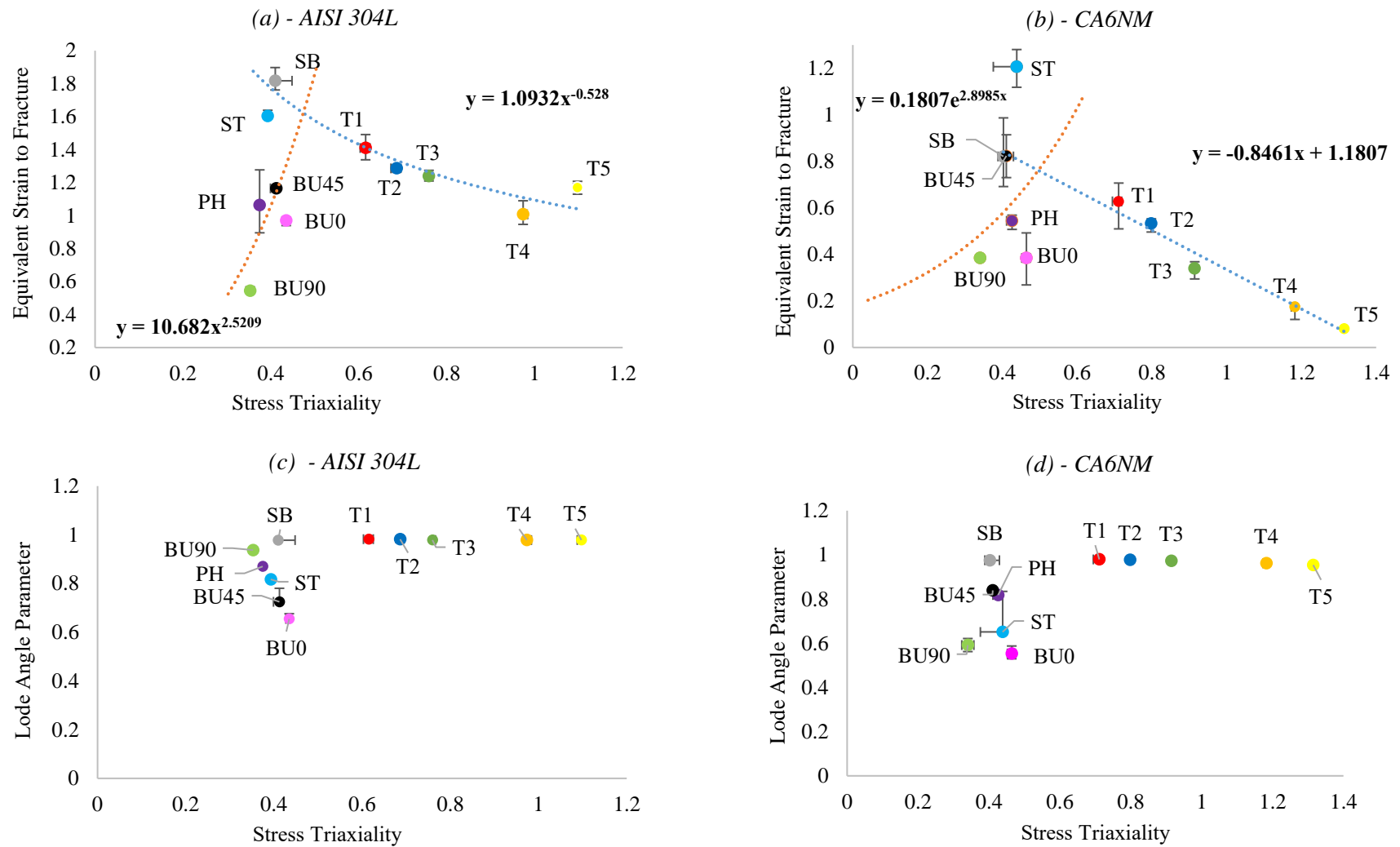


Figure 5.38. Fracture Loci for High and Low Stress Triaxiality Region and Lode Angle Parameter as a function of Stress Triaxiality for both AISI 304L and CA6NM.

Table 5.5. Tabulated data for AISI 304L and CA6NM for Equivalent Fracture Strain, Stress Triaxiality and the Lode Angle Parameter.

Name of Specimen	AISI 304L				CA6NM			
	u_f	$\bar{\epsilon}_f$	η_{Avg}	$\bar{\theta}_{Avg}$	u_f	$\bar{\epsilon}_f$	η_{Avg}	$\bar{\theta}_{Avg}$
SB	21.5052	1.8178	0.4096	0.9782	6.2664	0.8210	0.4028	0.9757
T1	5.9330	1.4099	0.6152	0.9820	2.2021	0.6280	0.7113	0.9794
T2	5.1796	1.2865	0.6862	0.9817	1.7476	0.5333	0.7985	0.9771
T3	3.9679	1.2392	0.7594	0.9786	1.1533	0.3406	0.9146	0.9725
T4	3.8697	1.0078	0.9735	0.9783	0.7130	0.1750	1.1827	0.9619
T5	3.9679	1.1691	1.0973	0.9785	0.5302	0.0808	1.3147	0.9541
PH	9.8911	1.0640	0.3745	0.8700	3.1788	0.5443	0.4260	0.8184
ST	11.4921	1.6042	0.3927	0.8170	4.0669	1.2067	0.4384	0.6510
BU0	10.3419	0.9707	0.4347	0.6545	2.2499	0.3845	0.4642	0.5538
BU45	16.2880	1.1652	0.4124	0.7248	5.2165	0.8234	0.4108	0.8392
BU90	17.8048	0.5446	0.3526	0.9373	5.8294	0.3849	0.3405	0.5919

In the high stress triaxiality region for both materials, as the stress triaxiality increased, the equivalent plastic strain to fracture decreased [102]. This region exhibits trends consistent with those reported for a range of materials [202]. Although, material properties have an effect on the magnitude of stress triaxiality, when comparing the general trend of the stress triaxiality of tensile tests with the results obtained by Bao and Wierzbicki [12], as shown in Figure 5.39 the results are shown to be similar.

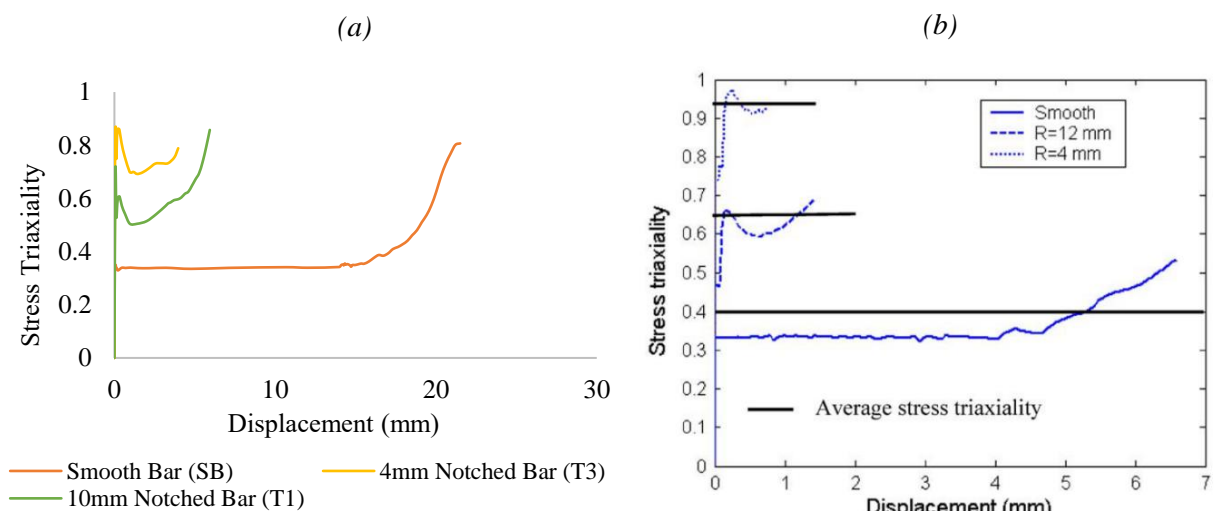


Figure 5.39. Evolution of Stress Triaxiality for Tensile Tests, a) Results from AISI 304L b) Results from AL2024-T35, adopted from Bao and Wierzbicki [12].

Lode angle parameter data presented for the high stress triaxiality specimens, as shown in Figure 5.40b and Figure 5.40d are all approximately $\bar{\theta} = 1$, which corresponds to axisymmetric tension as estimated in [107][84].

When constructing a fracture locus pure shear experiments are used for the low stress triaxiality region, as typically the hydrostatic pressure and Lode angle parameter are approximately zero or very small compared to the equivalent stress at fracture locations [12]. The BU90 specimen as shown in Figure 5.1 were designed to provide pure shear data; although, fracture initiation at the critical location of the specimen occurred at the point of maximum tensile stress. An example is shown in Figure 5.40, which the location of the propagated failure crack was confirmed by the DIC image. The change in stress state from compression to tension is shown in Figure 5.40c. Whilst the specimen's critical location was assumed to be the point at maximum plastic equivalent strain, the bulk material in the cross-section shown in Figure 5.40 was subjected to pure shear conditions. A parametric study [203] considering over 600 novel shear specimen geometries concluded that no single geometry can be used for a wide range of materials, as shear stress state failure is dependent on a materials ductility and hardening behaviour.

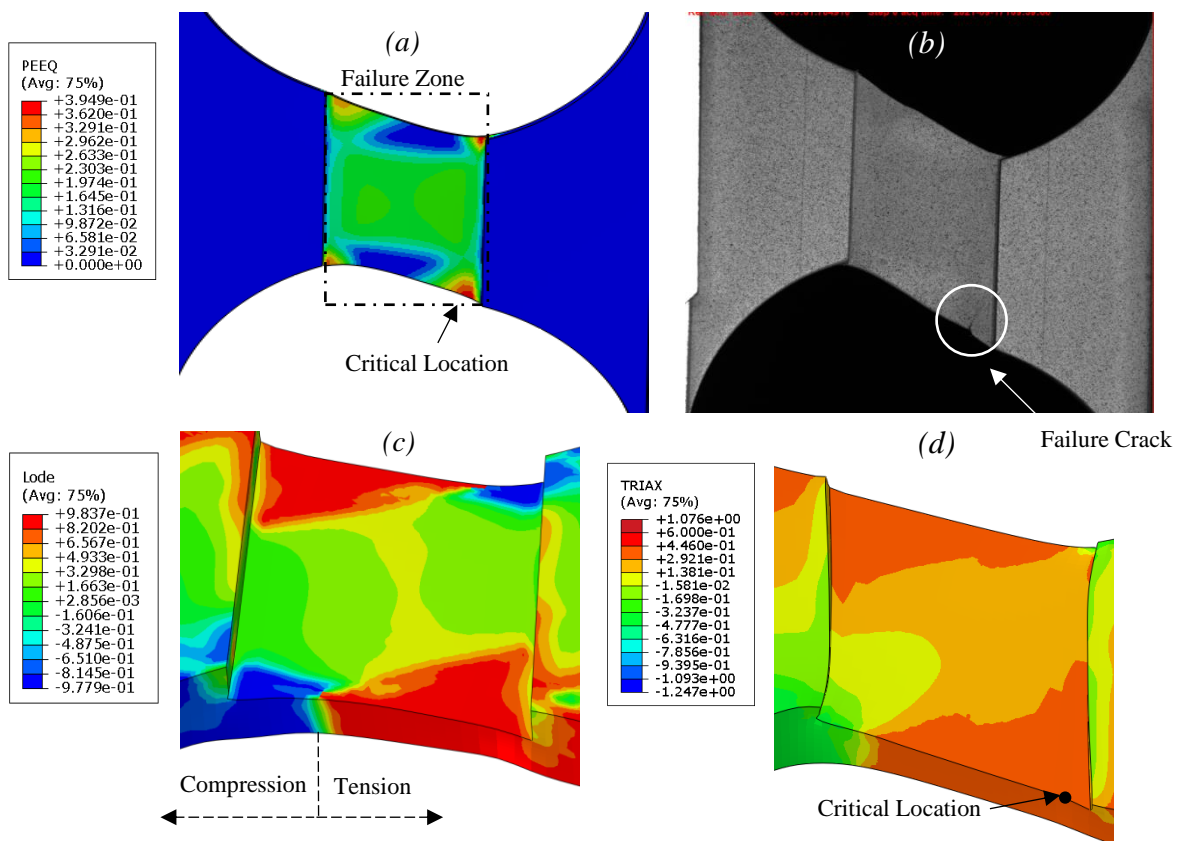
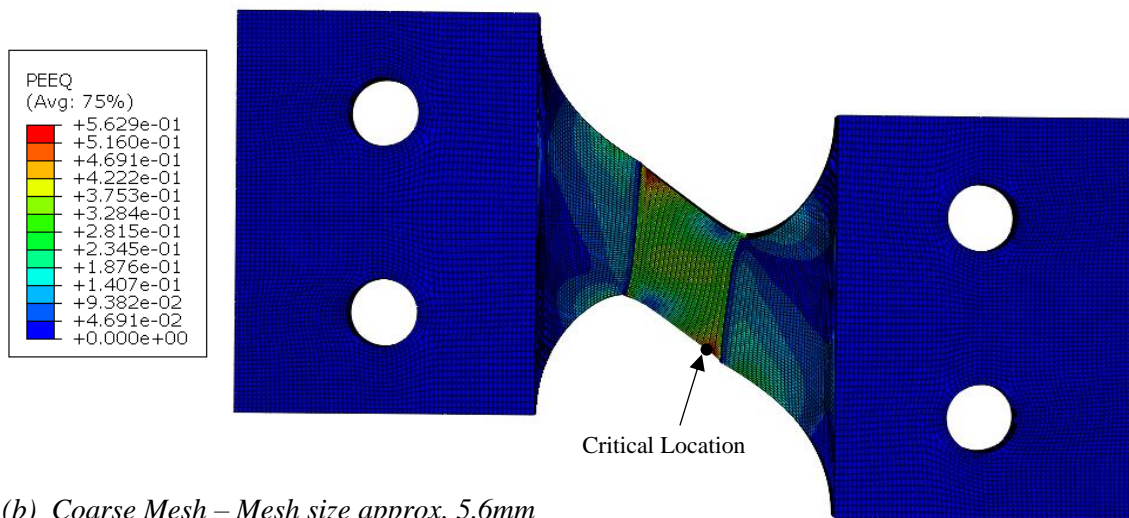


Figure 5.40. The Onset of Failure for AISI 304L BU90 a) FE Equivalent Plastic Strain Contour b) DIC Image c) FE Lode angle Parameter Contour d) FE Stress Triaxiality Parameter Contour.

FE analysis for nuclear transport packages is currently used in their development, as well as part of demonstrating their performance to meet regulatory compliance. When using FE analysis to demonstrate the impact performance of nuclear transport packages, the design of the FE mesh is of importance in order to obtain robust results [204]. When designing mesh for a nuclear transport package, due to the large size and complexity of the model, the mesh is optimised between the validity of results and the computational cost, this means that a coarse mesh maybe used. For the BU90 specimen the model was re-run with a coarser mesh and compared to the finer mesh selected during the mesh sensitivity study, as shown in Figure 5.41. When a coarser mesh was used, the critical location moved to the centre of the specimen, where the bulk of the material is under shear loading conditions, instead of the tensile failure location which was obtained with the finer mesh.

(a) Fine Mesh used in study – Mesh size approx. 0.8mm



(b) Coarse Mesh – Mesh size approx. 5.6mm

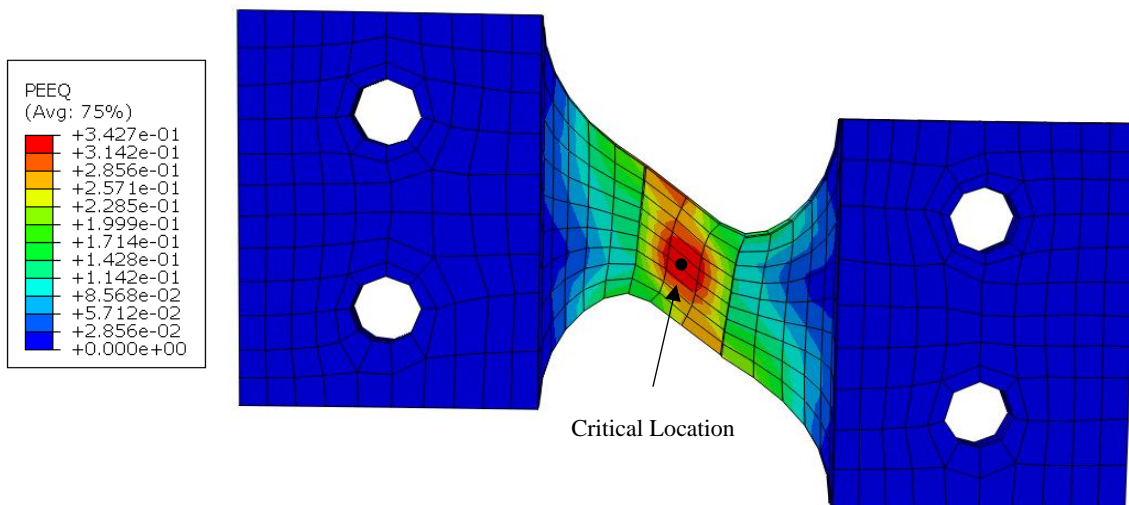


Figure 5.41. The Onset of Failure for AISI 304L BU90 FE Equivalent Plastic Strain Contour, a) Fine Mesh used in Study b) Coarser Mesh.

Structural integrity assessments of nuclear transport packages have local and global criteria to evaluate and determine whether a structure fails [204]. There are two options regarding the strain limits for the structural performance criteria; the first considers the critical location being away from any structural discontinuity, and the second considers that the structure will fail in the vicinity of a stress concentration. The allowable strain criteria for both are based on either, taking the average section failure, or the maximum plastic equivalent strain in the section. The fracture locus presented in Figure 5.38, considered the structure will fail in the vicinity of a stress concentration, by taking the critical location as the maximum plastic equivalent strain. However, a conservative estimate of shear failure strain could have been used instead, by extracting data from a central node located in the shear region or averaging the whole of the failure zone of the specimen.

Therefore, to further investigate two methods are introduced, as discussed below,

- **Method 1:** This was based on the critical failure point being taken at the maximum plastic equivalent strain, as shown in Figure 5.42 by point A. Results of this method were shown previously in Figure 5.38.
- **Method 2:** Following **Method 1**, the critical failure point was taken at the maximum plastic equivalent strain, however, for the shear specimens (this included ST/BU45/BU90) the critical failure point was taken at the centre of the specimen, on the outer surface, as shown in Figure 5.42 by point B.
- **Method 3:** A spatial averaging method was used, where the failure process zone was averaged for equivalent fracture strain, average stress triaxiality and the average Lode angle parameter, as shown in Figure 5.42 as section C.

There are a range of specimens shown in Appendix K, for the variation of locations used to extract data for the different methods. It is important to note, the moment of failure did not change throughout the variety of methods. Hence, the displacement boundary condition from the minimum, average, and maximum u_f , which were applied to the FE model remained the same.

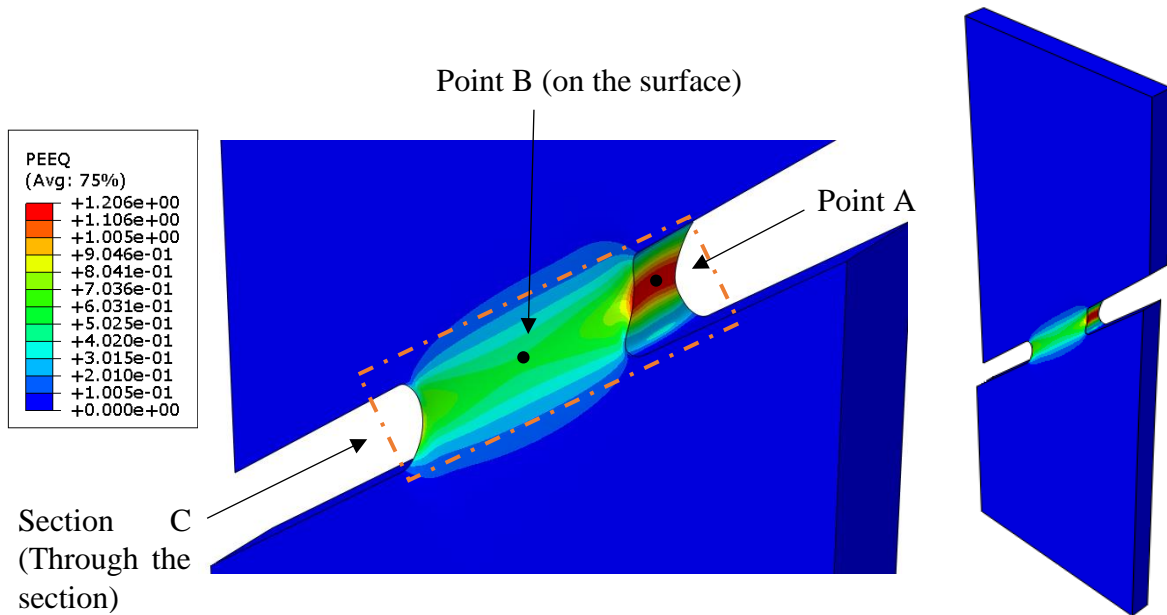


Figure 5.42. Plastic Equivalent Strain Contour of CA6NM ST, showing the Range of Locations Depending on the Fracture Locus.

The graphs for **Method 2** for both AISI 304L and CA6NM are shown in Figure 5.43, first is the traditional 2D fracture locus, shown by Figure 5.43a and b, and the second is the average Lode angle parameter data against average stress triaxiality by Figure 5.43a and b. Tabulated data for AISI 304L and CA6NM for the equivalent fracture strain, stress triaxiality and the lode angle parameter for **Method 2** is shown in Table 5.6.

The high stress region remained the same as Figure 5.38 when using **Method 1**. The data produced for the low stress triaxiality regime was what was expected when referring to Figure 2.11, where the shear geometries for both the Lode angle parameter and the stress triaxiality are closer to 0.

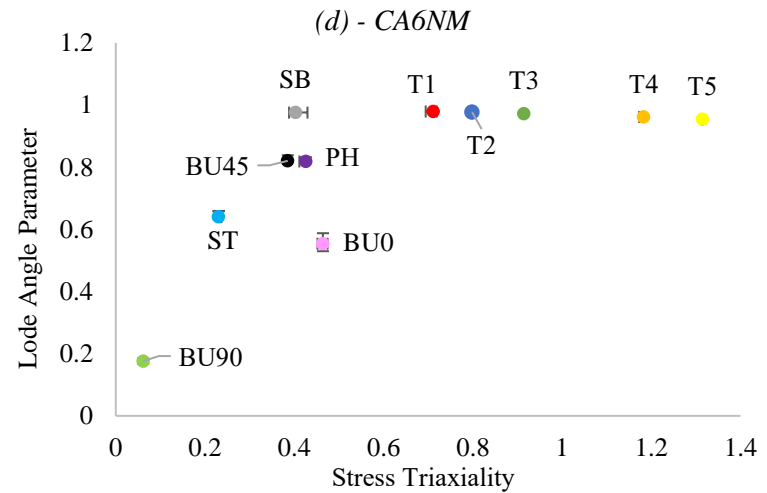
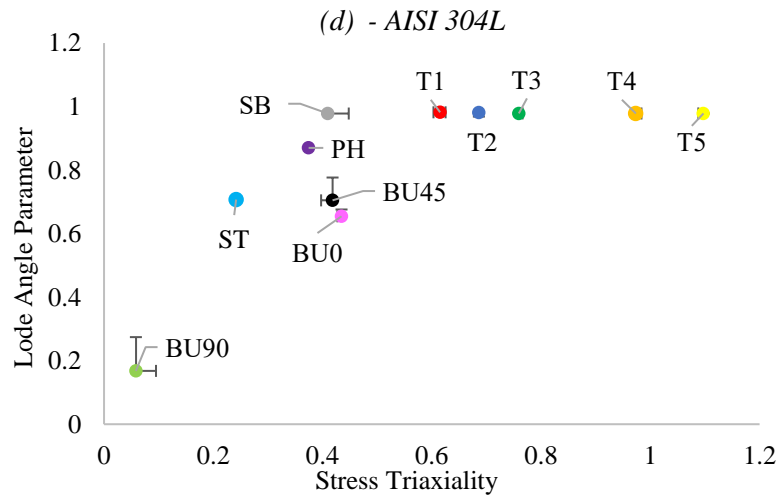
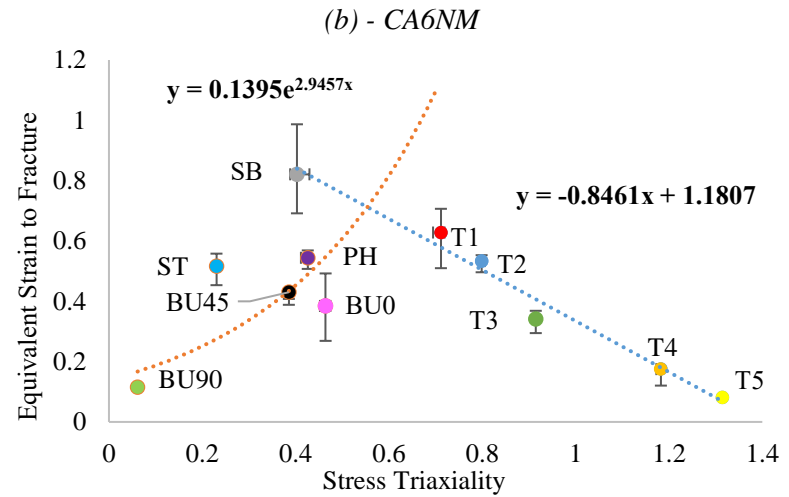
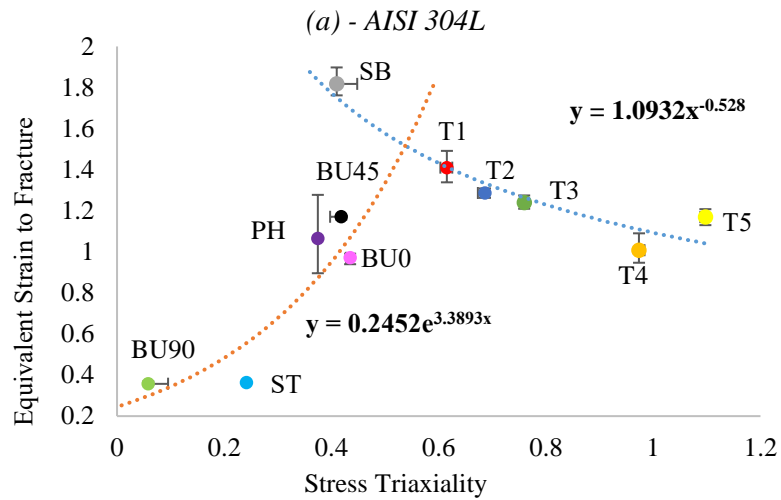


Figure 5.43. Method 2 - Fracture Loci for High and Low Stress Triaxiality Region and Lode angle Parameter as a function of Stress Triaxiality for both AISI 304L and CA6NM.

Table 5.6. Method 2 - Tabulated data for AISI 304L and CA6NM for Equivalent Fracture Strain, Stress Triaxiality and the Lode Angle Parameter.

Name of Specimen	AISI 304L				CA6NM			
	u_f	$\bar{\epsilon}_f$	η_{Avg}	$\bar{\theta}_{Avg}$	u_f	$\bar{\epsilon}_f$	η_{Avg}	$\bar{\theta}_{Avg}$
SB	21.5052	1.8178	0.4096	0.9782	6.2664	0.8210	0.4028	0.9757
T1	5.9330	1.4099	0.6152	0.9820	2.2021	0.6280	0.7113	0.9794
T2	5.1796	1.2865	0.6862	0.9817	1.7476	0.5333	0.7985	0.9771
T3	3.9679	0.9671	0.7594	0.9786	1.1533	0.3406	0.9146	0.9725
T4	3.8697	1.0078	0.9735	0.9783	0.7130	0.1750	1.1827	0.9619
T5	3.9679	1.1691	1.0973	0.9785	0.5302	0.0808	1.3147	0.9541
PH	9.8911	1.0640	0.3745	0.8700	3.1788	0.5443	0.4260	0.8184
ST	11.4921	0.3634	0.2418	0.7073	4.0669	0.5162	0.2304	0.6408
BU0	10.3419	0.9707	0.4347	0.6545	2.2499	0.3845	0.4642	0.5538
BU45	16.2880	1.1708	0.4183	0.7048	5.2165	0.4301	0.3855	0.8206
BU90	17.8048	0.3580	0.0583	0.1678	5.8294	0.1150	0.0613	0.1760

Lastly, **Method 3** used a spatial averaging method, where the equivalent fracture strain, stress triaxiality and the Lode angle parameter, was averaged over the failure process zone. To obtain the spatial averaging values two python scripts were used. An example using an FE model of AISI 304L BU0 is used to further explain this method, as shown in Figure 5.44.

The first script as shown in Appendix J-2 was used for the equivalent fracture strain. Elements within the failure process zone were selected (lines 36-38), the equivalent fracture strain value of the selected elements for the last frame was extracted (lines 43-54). This produced one value per element, which was then averaged for all the elements selected to give the final equivalent fracture strain.

The second script as shown in Appendix J-3 was used for the average stress triaxiality and the average Lode angle parameter. Elements within the failure process zone were selected (lines 42-44), then the code calculated the average stress triaxiality and Lode angle parameter over the load history for one element, this then was repeated for all the selected elements (lines 52-100). Data was then produced for all the elements and their relative value over the load history (lines 104-107), an average was then taken for all the elements, to output the final average stress triaxiality and the average Lode angle parameter.

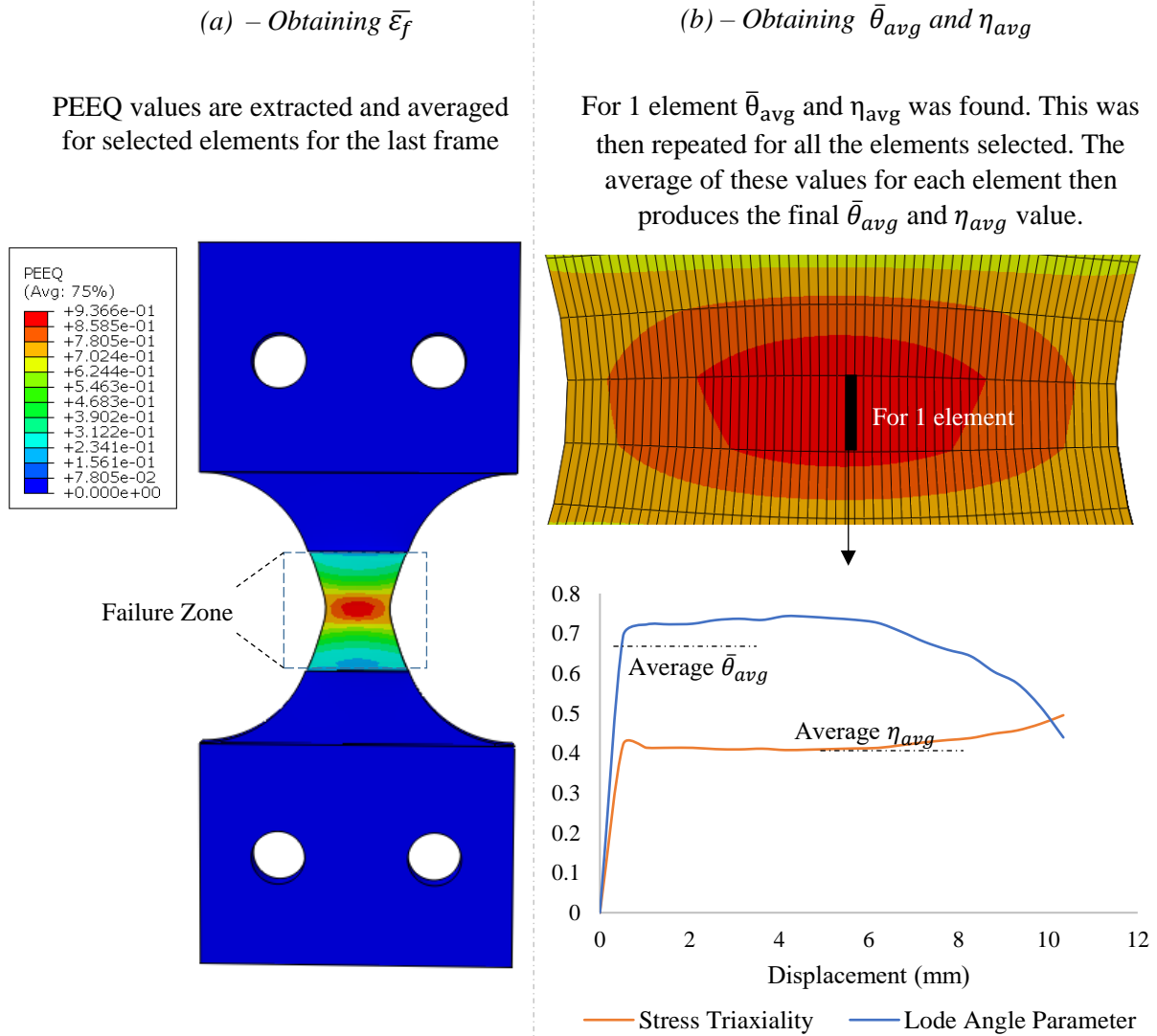


Figure 5.44. An Example using an FE Model for AISI 304L BU0 to Show the Spatial Averaging Method.

For the high stress triaxiality specimens there was two things to consider; firstly, the challenge in selecting the failure process zone, 50% of the failure strain and everything above was taken as the failure process zone to keep consistency of the method. Secondly, as the high stress triaxiality specimens were axisymmetric models, the element volume needed to be incorporated for when using the spatial averaging method, to account for the radius across the swept volume. To do this an additional python script was constructed, as shown in Appendix J-4 and is explained in Figure 5.45.

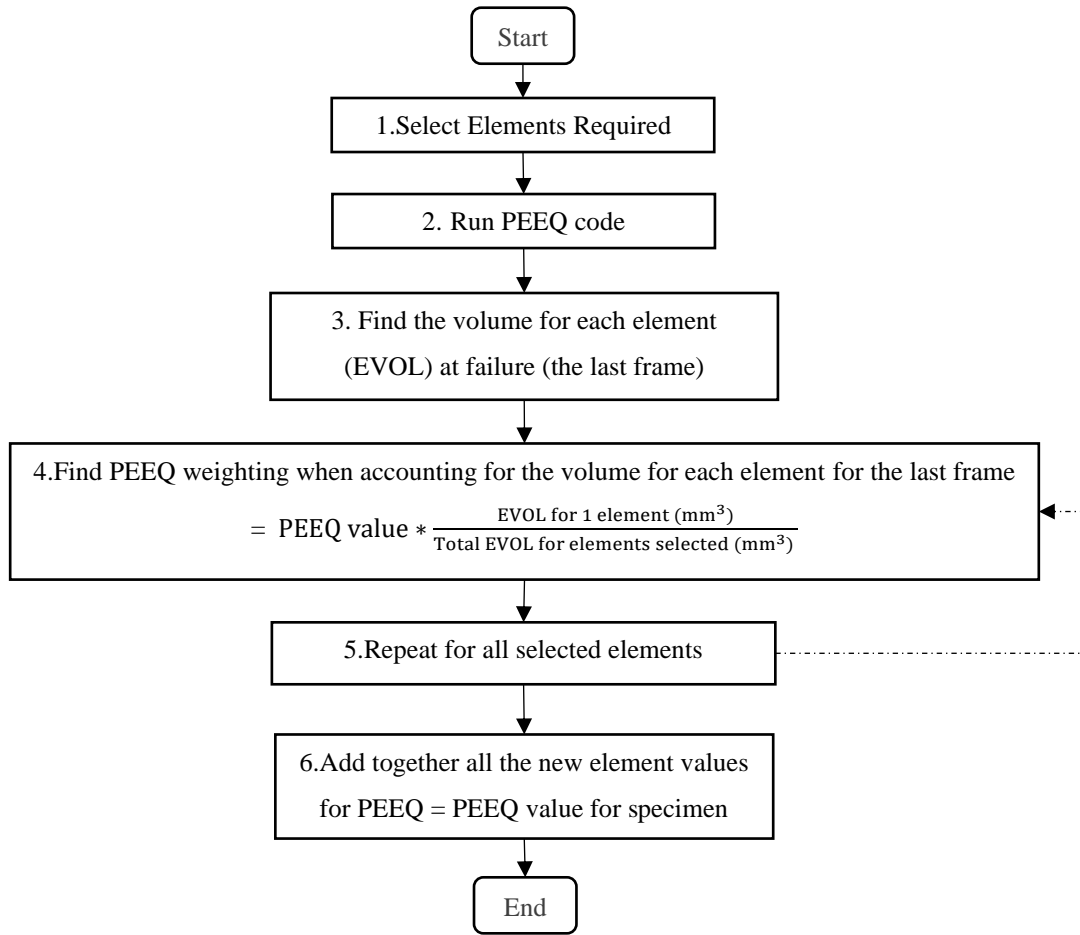


Figure 5.45. Flow Chart Showing the Process of Accounting for the Element Volume for Axisymmetric Models.

The graphs for **Method 3** for both AISI 304L and CA6NM are shown in Figure 5.46, first is the traditional 2D fracture locus, shown by Figure 5.46a and b, and the second is the average Lode angle parameter data against average stress triaxiality by Figure 5.46a and b. Tabulated data for AISI 304L and CA6NM for the equivalent fracture strain, stress triaxiality and the lode angle parameter for **Method 3** is shown in Table 5.7.

The general trend of the high stress region remained the same as the previous methods, whilst the data produced are more conservative than the results when using **Method 1 and 2**. This is to be expected as **Method 3** used the average data values from the selected failure zone, instead of extracting data based of the maximum plastic equivalent strain location. The data produced for the low stress triaxiality regime is more difficult to compare. Thus, graphs were constructed to include all the methods for each fracture locus on one graph, for both AISI 304L and CA6NM as shown in Figure 5.47 and Figure 5.48.

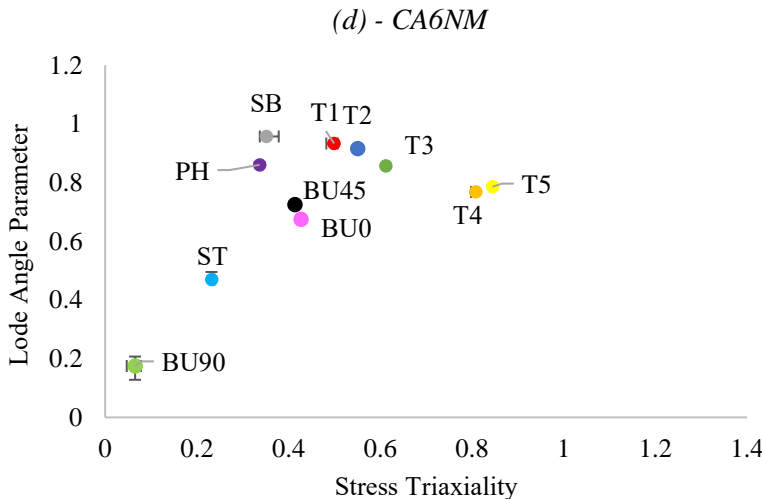
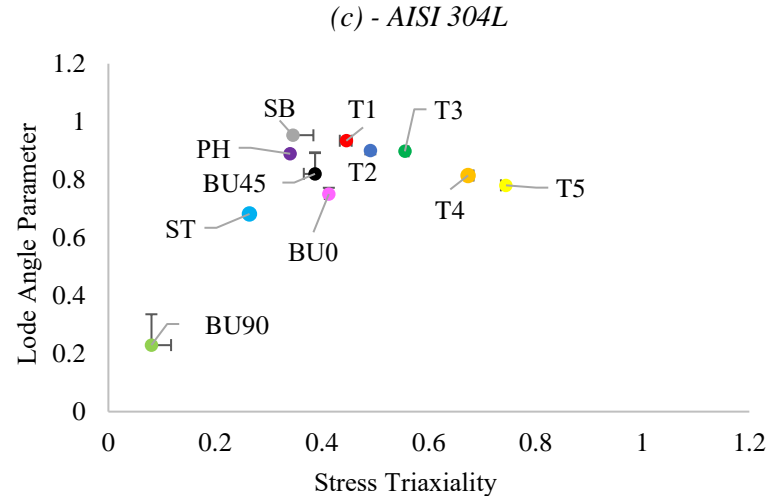
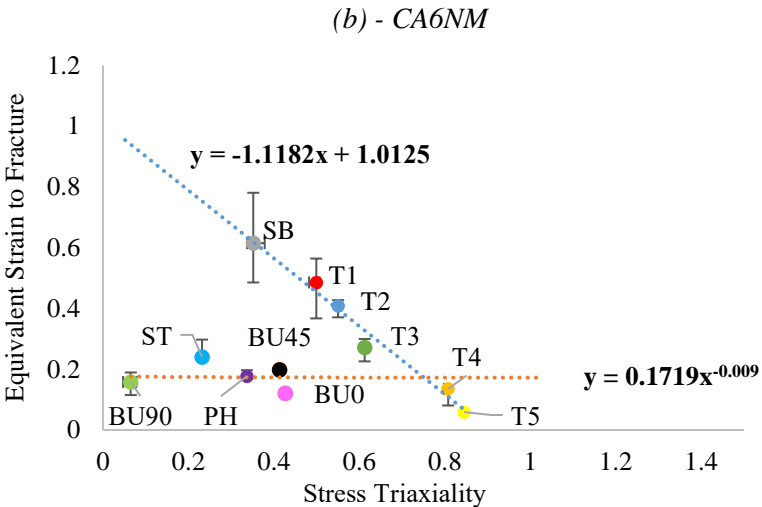
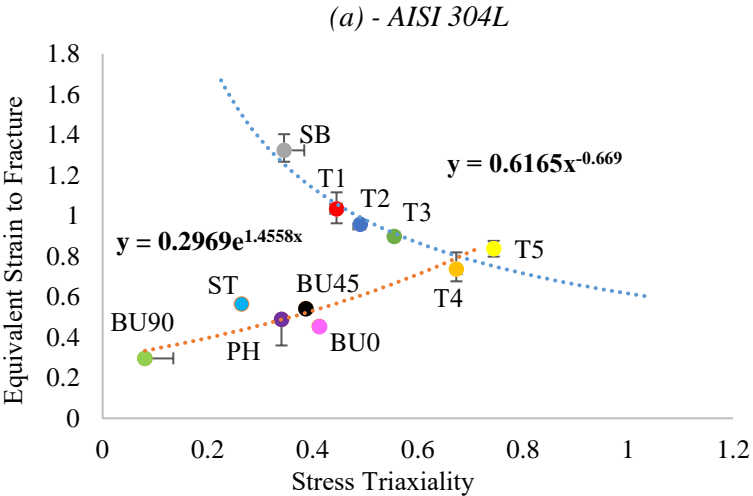


Figure 5.46. Method 3 - Fracture Loci for High and Low Stress Triaxiality and Lode angle Parameter as a function of Stress Triaxiality for both AISI 304L and CA6NM.

Table 5.7. Method 3 - Tabulated data for AISI 304L and CA6NM for Equivalent Fracture Strain, Stress Triaxiality and the Lode Angle Parameter.

Name of Specimen	AISI 304L				CA6NM			
	u_f	$\bar{\epsilon}_f$	η_{Avg}	$\bar{\theta}_{Avg}$	u_f	$\bar{\epsilon}_f$	η_{Avg}	$\bar{\theta}_{Avg}$
SB	21.5052	1.3235	0.3455	0.9531	6.2664	0.6149	0.3519	0.9572
T1	3.9679	0.8377	0.7444	0.7806	0.5302	0.0589	0.8451	0.7859
T2	3.8697	0.7375	0.6734	0.8144	0.7130	0.1352	0.8081	0.7681
T3	3.9679	0.8980	0.5551	0.8978	1.1533	0.2718	0.6126	0.8569
T4	5.1796	0.9577	0.4904	0.9006	1.7476	0.4078	0.5505	0.9159
T5	5.9330	1.0347	0.4455	0.9343	2.2021	0.4856	0.4994	0.9332
PH	9.8911	0.4880	0.3405	0.8894	3.1788	0.1769	0.3370	0.8606
ST	11.4921	0.5653	0.2643	0.6817	4.0669	0.2400	0.2320	0.4696
BU0	10.3419	0.4525	0.4128	0.7505	2.2499	0.1204	0.4271	0.6751
BU45	16.2880	0.5415	0.3868	0.8201	5.2165	0.1977	0.4136	0.7250
BU90	17.8048	0.2963	0.0806	0.2294	5.8294	0.1579	0.0652	0.1750

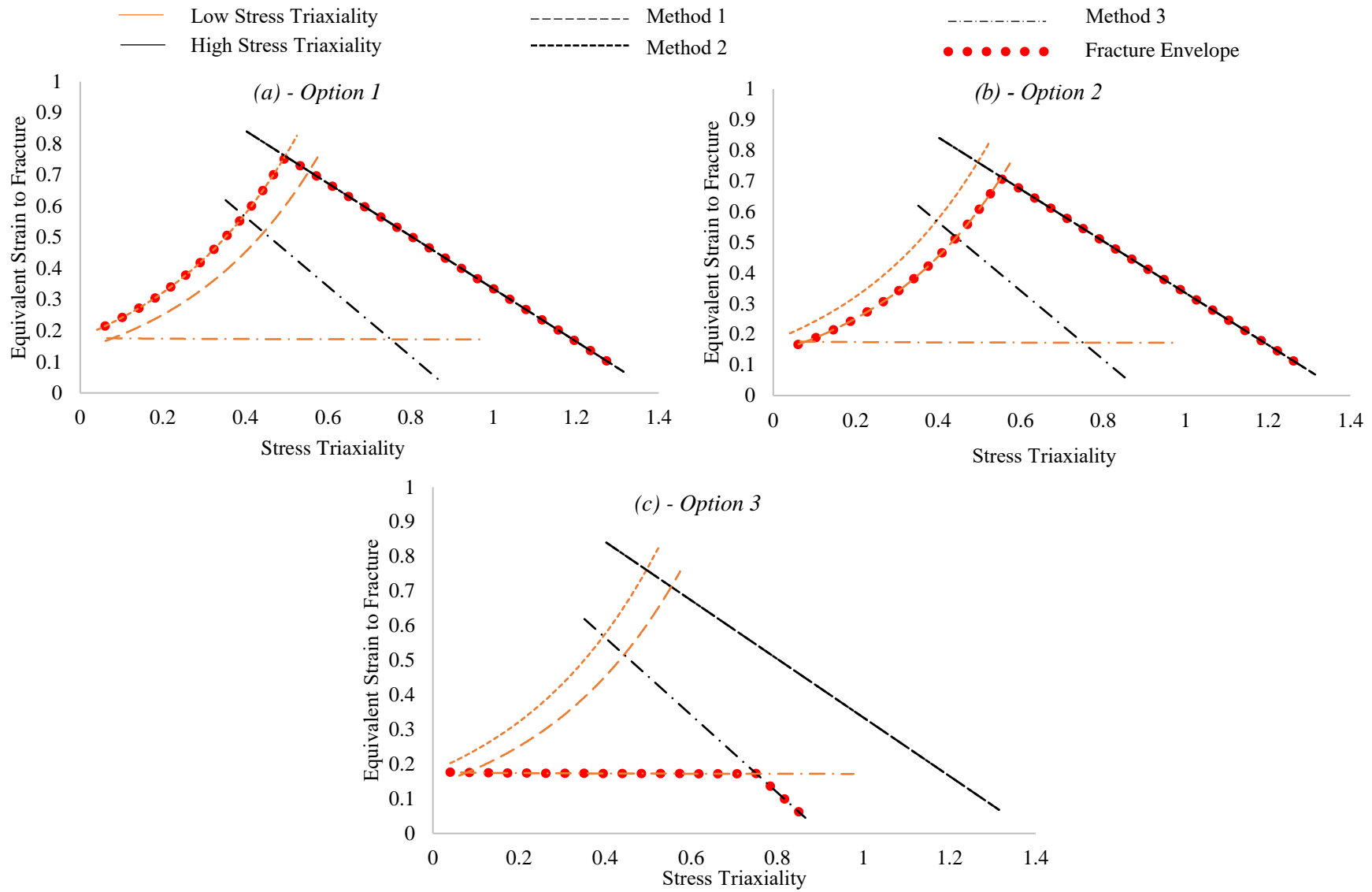


Figure 5.47. Fracture Loci for Various Methods for High and Low Stress Triaxiality for CA6NM.

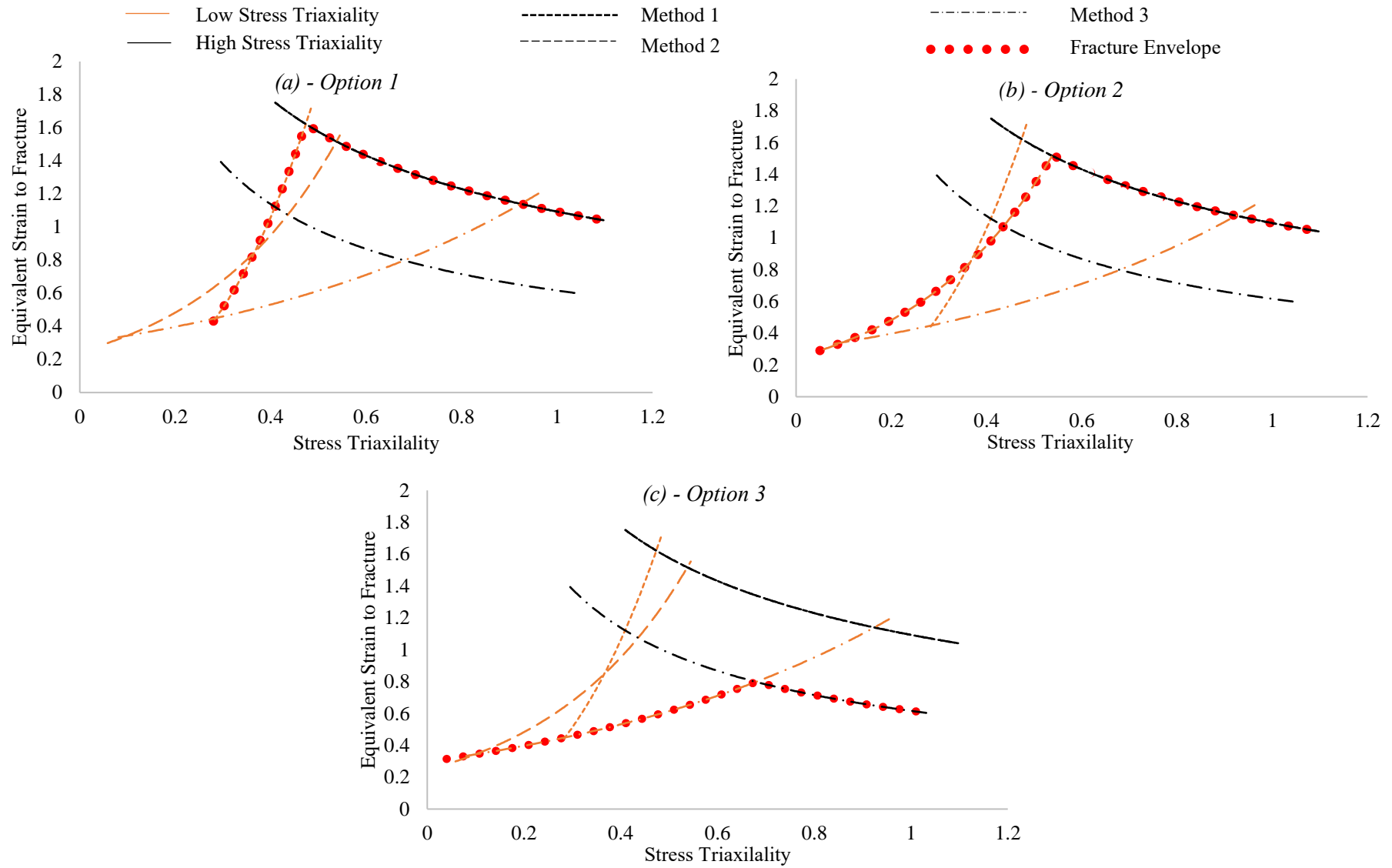


Figure 5.48. Fracture Loci for Various Methods for High and Low Stress Triaxiality for AISI 304L.

The fracture loci for the various methods for high and low stress triaxiality for both CA6NM and AISI 304L are shown in Figures 5.47 and 5.48. All the methods investigated are presented on the same graph, with the different options of choosing a method highlighted by the fracture envelope. The analytical expressions for the graphs are summarised in Table 5.8.

Table 5.8. Analytical Expressions for Various Methods for AISI 304L and CA6NM.

	AISI 304L	Range for η	CA6NM	Range for η
Method 1	$\bar{\varepsilon}_f = 10.682\eta^{2.5209}$	0-0.67	$\bar{\varepsilon}_f = 0.1807e^{2.8985\eta}$	0-0.5
	$\bar{\varepsilon}_f = 1.0932\eta^{-0.528}$	0.68-1.2	$\bar{\varepsilon}_f = -0.8461\eta + 1.1807$	0.5-1.4
Method 2	$\bar{\varepsilon}_f = 0.2452e^{3.3893\eta}$	0-0.54	$\bar{\varepsilon}_f = 0.1395e^{2.9457\eta}$	0-0.55
	$\bar{\varepsilon}_f = 1.0932\eta^{-0.528}$	0.55-1.2	$\bar{\varepsilon}_f = -0.8461\eta + 1.1807$	0.56-1.4
Method 3	$\bar{\varepsilon}_f = 0.2969e^{1.4558\eta}$	0-0.47	$\bar{\varepsilon}_f = 0.1719\eta^{-0.009}$	0-0.74
	$\bar{\varepsilon}_f = 0.6165\eta^{-0.669}$	0.48-1.2	$\bar{\varepsilon}_f = -1.1182\eta + 1.0125$	0.75-1.4

5.5.4 Conclusion

To further characterise the plasticity and fracture behaviour of AISI 304L and CA6NM, experimental tests using DIC were performed to failure at ambient temperature under quasi-static conditions, for a series of geometries such as notched bars, shear plates, and for various loading conditions including tensile and shear loading. A combination of the agreement of force displacement curves and the comparison of the contour plots from the FE analysis and the DIC, show the results obtained represent the true stress state data.

There were three methods presented that investigated different ways to extract the equivalent fracture strain, average stress triaxiality and the average Lode angle parameter. **Method 1** followed the adopted method shown in Table 2.2, where the critical failure point was taken at the maximum plastic equivalent strain. The data produced for both materials when using this method for the high stress triaxiality region exhibited trends consistent with those reported for a range of materials [18][19][22]. However, for the low stress triaxiality region the shear specimens did not produce the results expected as the critical location of the specimens occurred under pure tension. Due to the large size and complexity of designing mesh for a nuclear transport package, a coarse mesh maybe used. Thus, the BU90 specimen FE model was

re-run with a coarser mesh and compared to the finer mesh selected during the mesh sensitivity study, which shown when using the coarse mesh the critical location moved to the centre of the specimen, where the bulk of the material was under shear loading conditions. This then led to **Method 2** which was the same as **Method 1**, but for the shear specimens (ST/BU45/BU90) the critical failure point was taken at the centre of the outer surface on the specimen. Therefore, the high stress region remained the same, however, the data produced for the low stress triaxiality regime was closer to the initial expected stress states. Lastly, **Method 3** used the spatial averaging method from the selected failure zone.

The fracture loci developed for all three methods were combined into one graph, leading to the development in a strain-based criterion for AISI 304L and CA6NM. Analytical expressions of the fracture envelope found for each method can be utilised for practical relevance, regarding nuclear transport packages depending on the failure model. A strain-based criterion for AISI 304L and CA6NM was produced. Interpretation of the constructed graphs and the analytical expressions for practical relevance regarding nuclear transport packages is dependent on the failure model. As previously discussed, structural integrity assessments of nuclear transport packages have local and global criteria to evaluate and determine whether a structure fails [204]. The strain criteria are based on taking either the maximum plastic equivalent strain or the average plastic equivalent strain across a section in the region of interest. **Method 1** and **Method 2** could be applied when looking at the failure strain at a specific point, however, these methods may not be appropriate when considering a gross failure in the section. Thus, **Method 3** could be potentially utilised when considering the gross failure criteria throughout the section of local structural discontinuity. The choice of method is at the discretion of the analyst and will vary on a situational basis.

For example, CA6NM is typically used for thick wall castings, this means that when performing a structural integrity assessment, the design envelope expressed by the analytical expression in Table 5.8 by **Method 3** could be applied. Whereas, if AISI 304L is used for thin-walled castings, the maximum plastic equivalent strain at the local structural discontinuity should be considered, which will use the strain-based criteria proposed by **Method 1** or **Method 2**.

5.6 Negative Stress Triaxiality

5.6.1 Introduction

To construct a fracture locus for the negative stress triaxiality region, DIC has been used in parallel with FE analysis to provide compressive material characterisation of AISI 304L and CA6NM.

Typically, experiments for negative stress triaxiality use conventional upsetting tests as previously discussed in Section 2.6.1.3 [119]. During upsetting tests, short cylinders of materials are compressed between flat platens. As the loading is applied, friction between specimens and the platens generates barrelling of the specimen near the equator which can cause fracture. The other geometry used for compression testing is a round bar with a notched small gauge section in the middle. A series of 6 geometries as shown in Figure 5.49 were each tested to failure 5 times, for a total of 60 tests, at ambient temperature under quasi-static conditions.

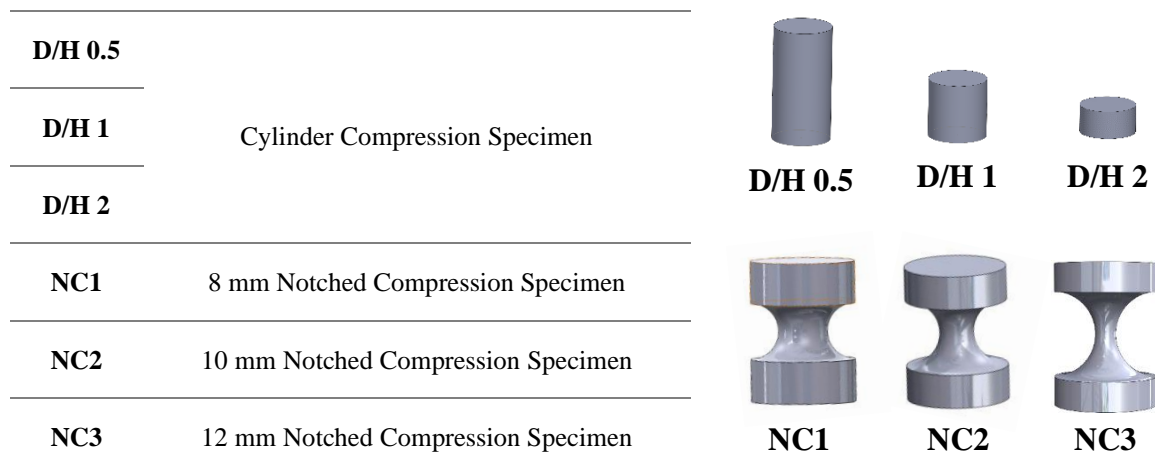


Figure 5.49. Negative Stress Triaxiality Specimens.

5.6.2 Experiments

The experimental setup for the 12mm notched compression specimen (NC3) is shown in Figure 5.50a and an example of the cylinder compression specimen D/H 0.5 is shown in Figure 5.50b. Compression specimens were tested on a Mayes Servo Hydraulic testing machine using stroke control at a rate of 1 mm/min. In order to ensure that the specimen remained central an alignment guide was used during the experiment and a linear variable differential transformer (LVDT) was utilised to measure the displacement. The top platen was fixed, whilst the bottom platen was used to apply the required loading, the top platen consists of two plates with a spherical ball bearing in the middle to eliminate any misalignment from the system.

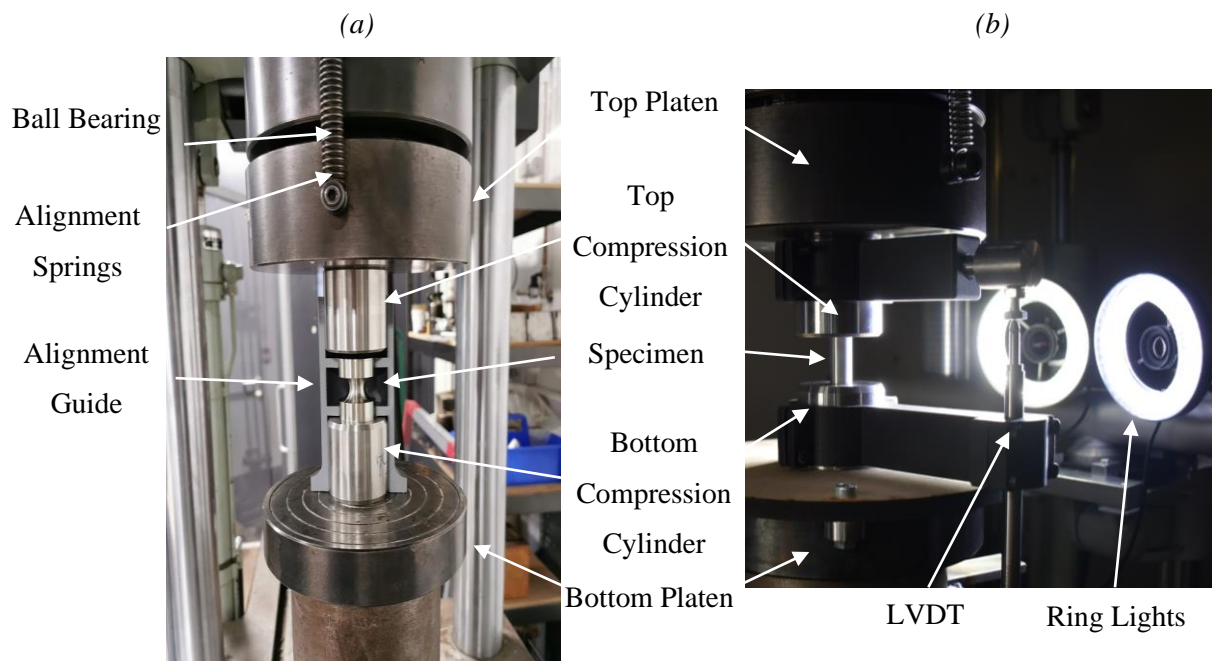


Figure 5.50. Notched Compression Specimen Experimental Set Up.

5.6.3 FE Analysis

All FE models were created in ABAQUS and were modelled with CAX4R elements. To simulate the notched compression specimens (NC1-3), axisymmetric models were used as shown in Figure 5.51a. For the upsetting tests (D/H 0.5-2) half axisymmetric models were created, using symmetry boundary conditions applied along the horizontal symmetry line at the centre of the specimen, as shown in Figure 5.51b. For all FE models used in this study the compression platens were modelled as rigid surfaces. Surface-to-surface contact with the

penalty friction formulation was used to model the interaction between the platen and the specimen. A pre-described displacement was applied at the top platen while the bottom platen was fixed. The displacement for the DIC data was measured on the specimens as shown in Section 4.6.6, and the displacement for the FE data was extracted for the relevant time step from the analysis, which follows the method used in Section 4.8. The same mesh sensitivity methodology used in Section 4.8.2 was used for investigating all FE simulations in order to obtain converged results.

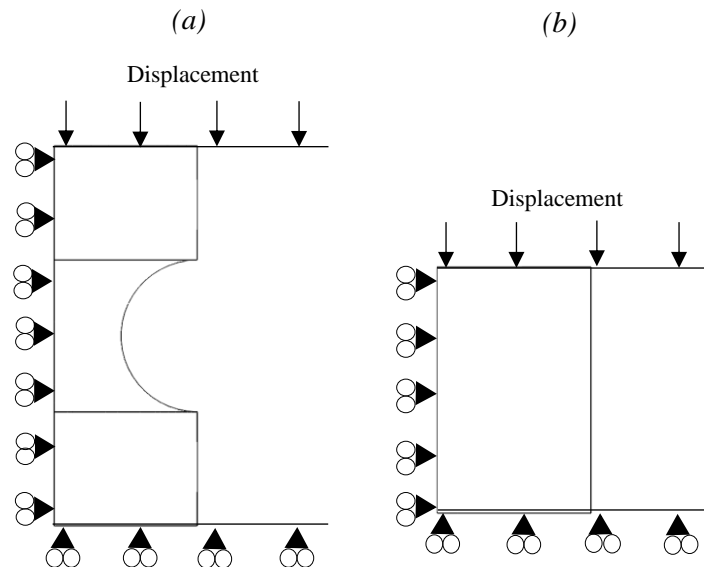


Figure 5.51. Loading and Boundary Conditions for Compression Specimens.

Coefficient of friction study between the specimens and the platen surface was conducted for both geometries as shown in Figure 5.52. The notched bar shows no dependency on the coefficient of friction which is in agreement with [12]. The coefficient of friction for the upsetting tests was found to be 1, as there was less scatter when this value was used, this meant that it aligned with the DIC data more accurately.

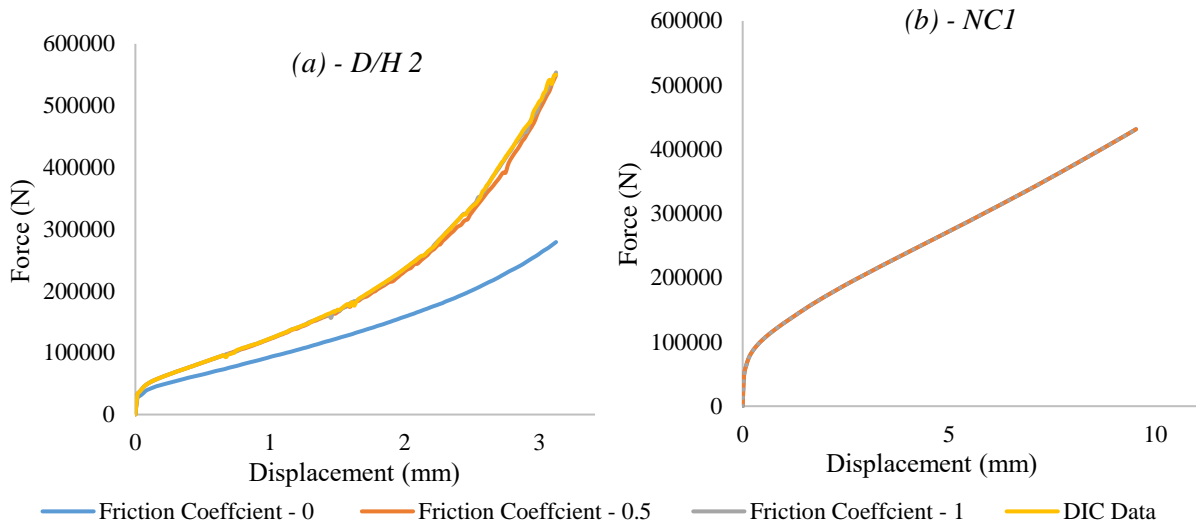


Figure 5.52. Comparison of Force Displacement Curves for a Range of Coefficient of Friction.

5.6.4 Results and Discussion

For all post processing of DIC results a subset size of 45 and a grid spacing of 37 was used. The tests have been repeated five times to assure the consistency of the results.

To determine the stress state of a material the onset of fracture is required. Methods for finding fracture initiation for tensile and shear geometries are well established [12][95][56][51] however, there is restricted research for compression of ductile materials [79]. Brittle material reaches their ultimate compressive strength when the load applied drops drastically. For compression tests of cylindrical specimens with different geometrical aspect ratios for materials such as aluminium alloys 2024-T351, Al-6061, AISI 1040 and 1045 steel have been researched [12][120][121][102], however data regarding AISI 304L is limited [205], [206] and there is no known published data regarding compression testing of CA6NM with regard to constructing a fracture locus.

The moment of failure initiation for the compression specimens was more challenging, as the paint tends to gather and fold over when the material gets near failure, as shown in Figure 5.53. Therefore, to ensure the failure crack was observed there was a part of the specimen that was not painted, and a separate camera was used as well as the DIC set up. The main limitation of the DIC set up for the compression specimens was the DOF on some specimens were limited to the maximum aperture of the lens.

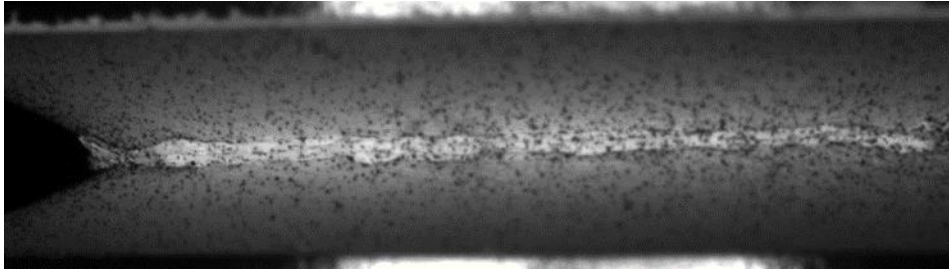


Figure 5.53. Accumulation of Paint on a Compression Specimen.

To define the instant of failure for AISI 304L a range of loads were used. The specimens are shown in Figure 5.54. The specimen in Figure 5.54i has failed, however this has gone past the onset of failure. In order to determine at which, load the specimen fails a microscopic analysis was needed. Three options were selected in order to observe failure crack in the middle of the specimens, this is shown in Figure 5.55.

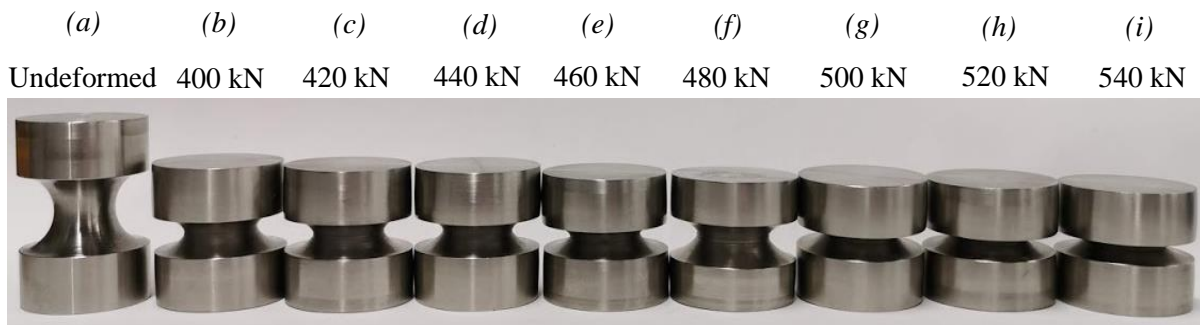


Figure 5.54. Deformed Compression Specimens at Various Loads Compared to an Undeformed Specimen.

When the metallographic specimen is being cut from the main body of the specimen it may alter the structure of the material. Therefore, caution was exercised when sectioning to minimise any alteration of the microstructure [207]. To ensure that the metal was not influenced by the quality of the cut the specimens were machined by the CNC milling machine using substantial amounts of coolant.

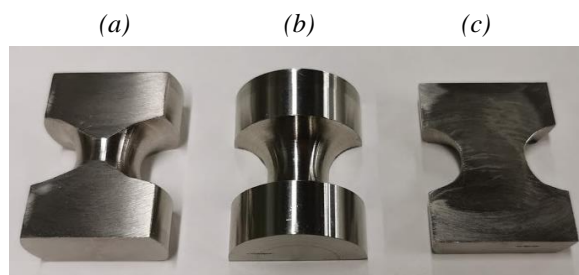


Figure 5.55. A Range of Options in Order to Observe the Centre of the Specimen.

The specimens were then manually ground and polished. Failure cracks existed in all the specimens that had been subjected to loads exceeding 500kN. On the lead up to failure there is a slight barrelling effect around the equator from the specimen at 480kN (as shown in Figure 5.56a). Whereas the specimen subjected to 500kN (as shown in Figure 5.56b) shows visible cracks. The failure crack in the middle of the specimen is shown in Figure 5.56c and was measured to be 0.00835mm respectively.

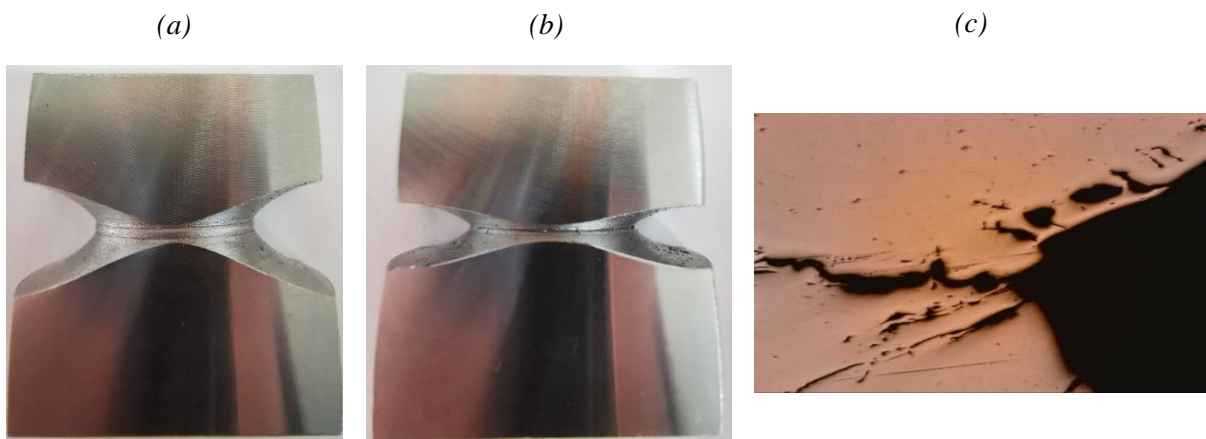


Figure 5.56. a) 480KN Compression Specimen b) 500KN Compression Specimen c) Magnification 20x - 500KN Right Side.

The onset of failure for the compression experiments aligns with the first visible macroscopic crack at the equatorial area. The main conclusion for the series of experiments found that the onset of failure takes place in conjunction with the first visible macroscopic crack. Thus, for the experimental test set up a camera was used, this was projected on to a screen throughout testing to ensure that the observable failure crack the force was recording and the test was stopped. There was no failure crack observed for any of the upsetting tests conducted and for the CA6NM NC1 (as shown in Figure 5.57) this was due to the materials failure strain exceeding the capabilities of the servo-hydraulic machine used. To protect the machine all tests were stopped before reaching the maximum capacity of the load cell, this issue has been seen in research previously by [102]. The failure of geometries has been characterised this is summarised in Table 5.9 below, where circumferential failure is as shown in Figure 5.58a, and shear failure as shown in Figure 5.58b.

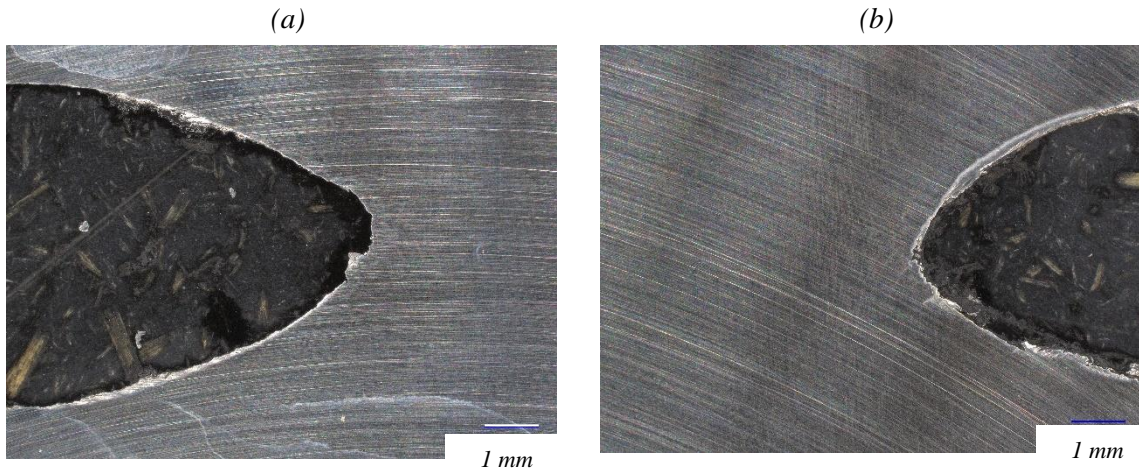


Figure 5.57. CA6NM NC1 No failure Observed a) Left Side b) Right Side.



Figure 5.58. a) AISI 304L NC3 b) CA6NM NC3 Compression Specimen.

Table 5.9. Compression Specimens Characterisation of Failure

	No Failure		Circumferential Failure		Shear Failure	
	AISI 304L	CA6NM	AISI 304L	CA6NM	AISI 304L	CA6NM
NC1						
NC2						
NC3						
D/H 0.5						
D/H 1						
D/H 2						

For the specimens that did not fail, their data cannot be used in the construction of the fracture locus. The specimens that did fail, their experimental results showed an excellent agreement within the plastic region with the FE equivalent results (as shown in Figure 5.59). This agreement up to failure is shown for all the compression specimens in Appendix L.

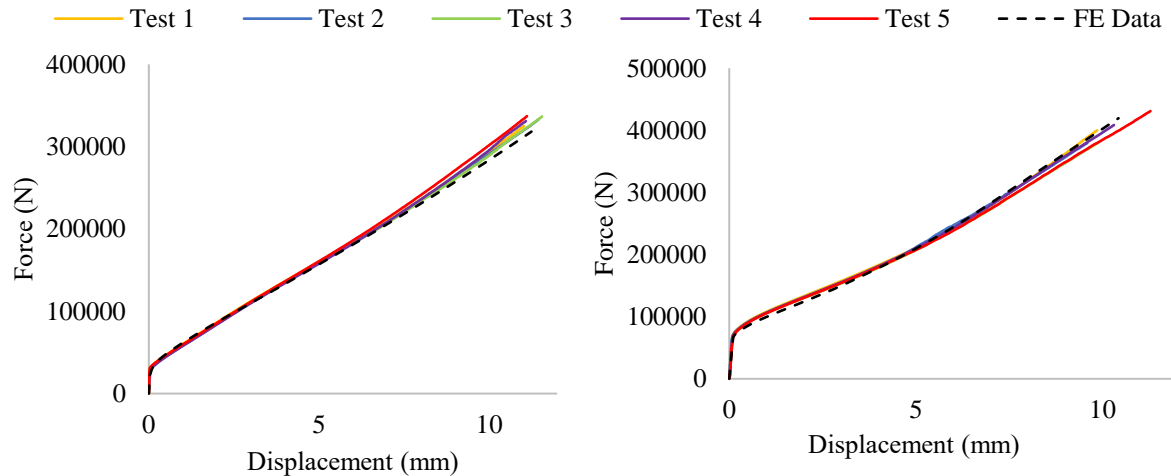


Figure 5.59. CN2 Compression Specimen Force Displacement Curves a) AISI 304L, b) CA6NM.

An example comparing the FE model, DIC contour and the deformed specimen of AISI 304L NC3 at the onset of failure is shown in Figure 5.61, the deformation and the displacement are shown to be equivalent. To obtain the equivalent fracture strain, average stress triaxiality and the average Lode angle parameter, the instance which failure occurred and where failure initiated (critical location) was needed, as discussed in Section 5.53. For all specimens tested, the moment of fracture initiation was assumed to be the first detectable discontinuity at the specimen surface when observing the DIC images, as previously discussed. Researchers Bao and Wierzbicki [12], took the critical location for this geometry at the equatorial area on the surface of the specimen. However, for the CA6NM specimens the maximum plastic equivalent strain was not at the surface of the equatorial area. There were three potential options that were investigated, as shown in Figure 5.60; Point A was at the maximum plastic equivalent strain, Point B was at the equatorial area on the surface of the specimen. Lastly, line C took an average of all the elements between Point A and B.

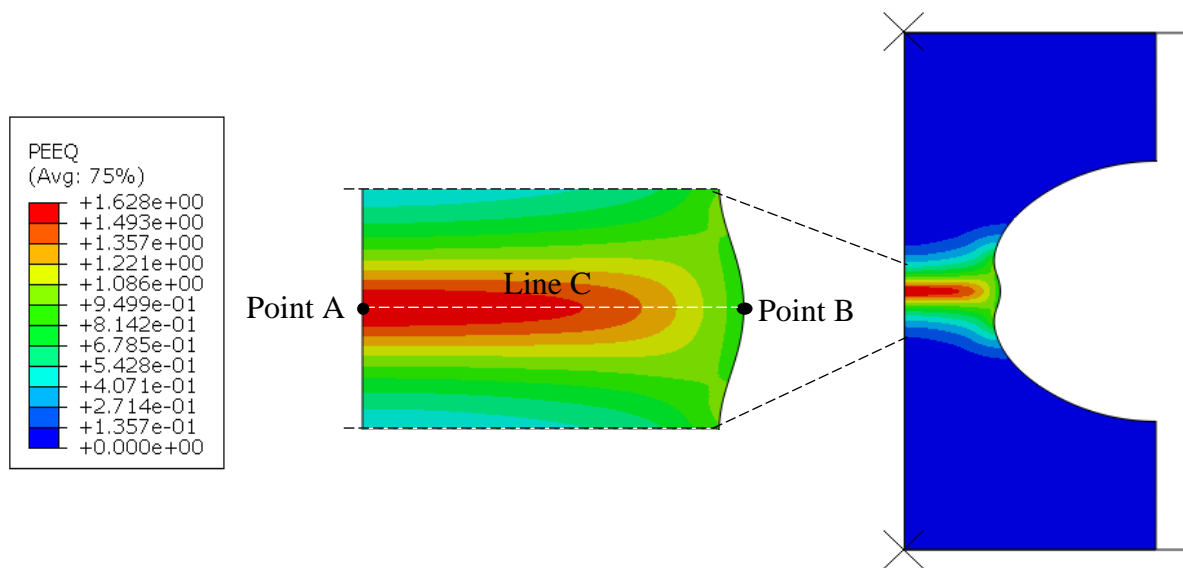


Figure 5.60. Plastic Equivalent Strain Contour of CA6NM NC3, showing the Range of Locations.

The evolution of stress triaxiality and Lode angle parameter for the range of locations is shown in Figure 5.62. The average Lode angle and stress triaxiality was taken following Section 4.8.3. This demonstrated that only when Point B was used as the critical location was the stress triaxiality value within the cut-off limit. For the CA6NM specimens both Point A and Point B were used for the critical location. The critical locations for all the compression specimens are shown in Figure 5.63.

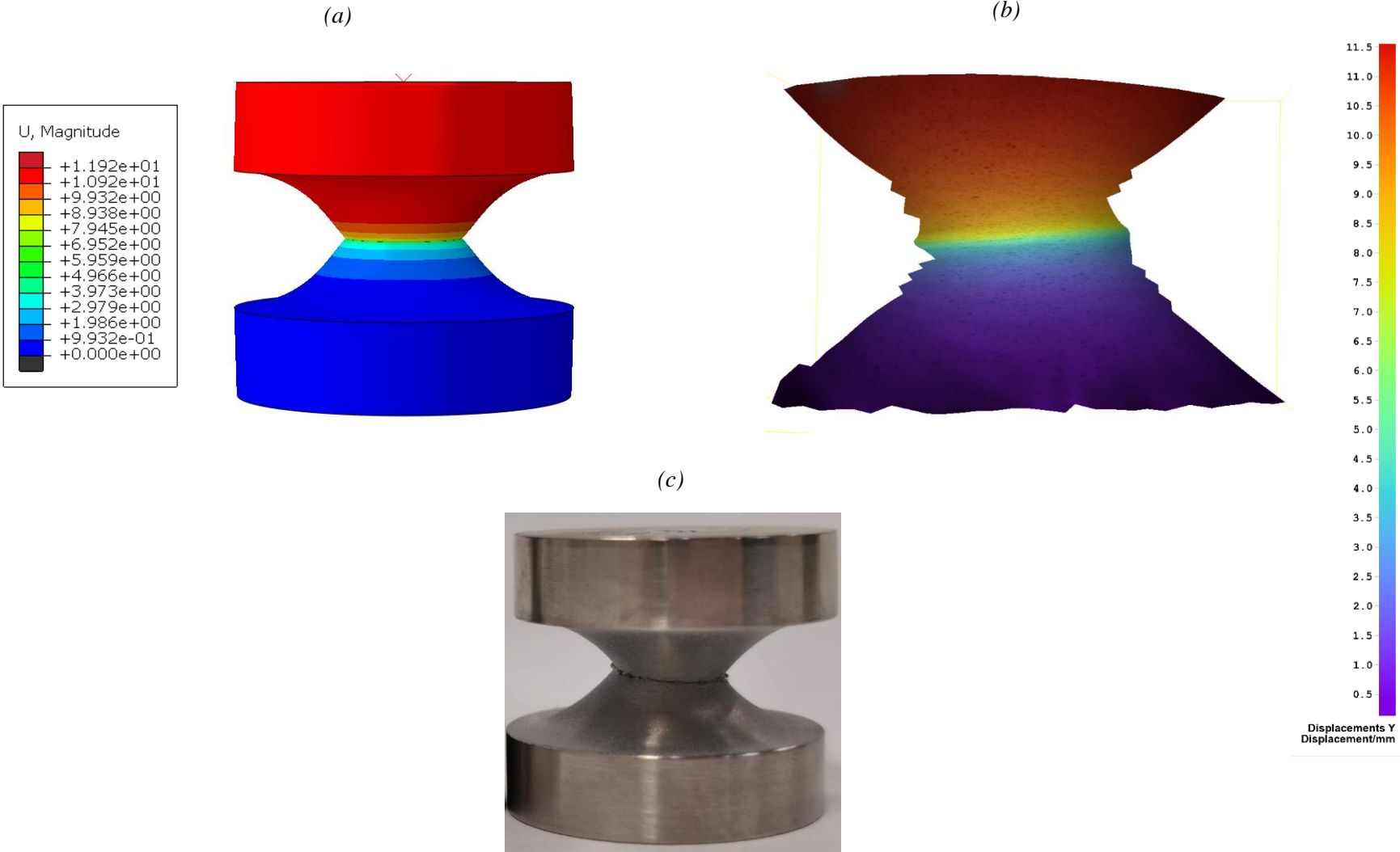


Figure 5.61. AISI 304L NC3 at Failure a) FE Model Displacement Contour b) DIC Displacement Contour c) Deformed Specimen.

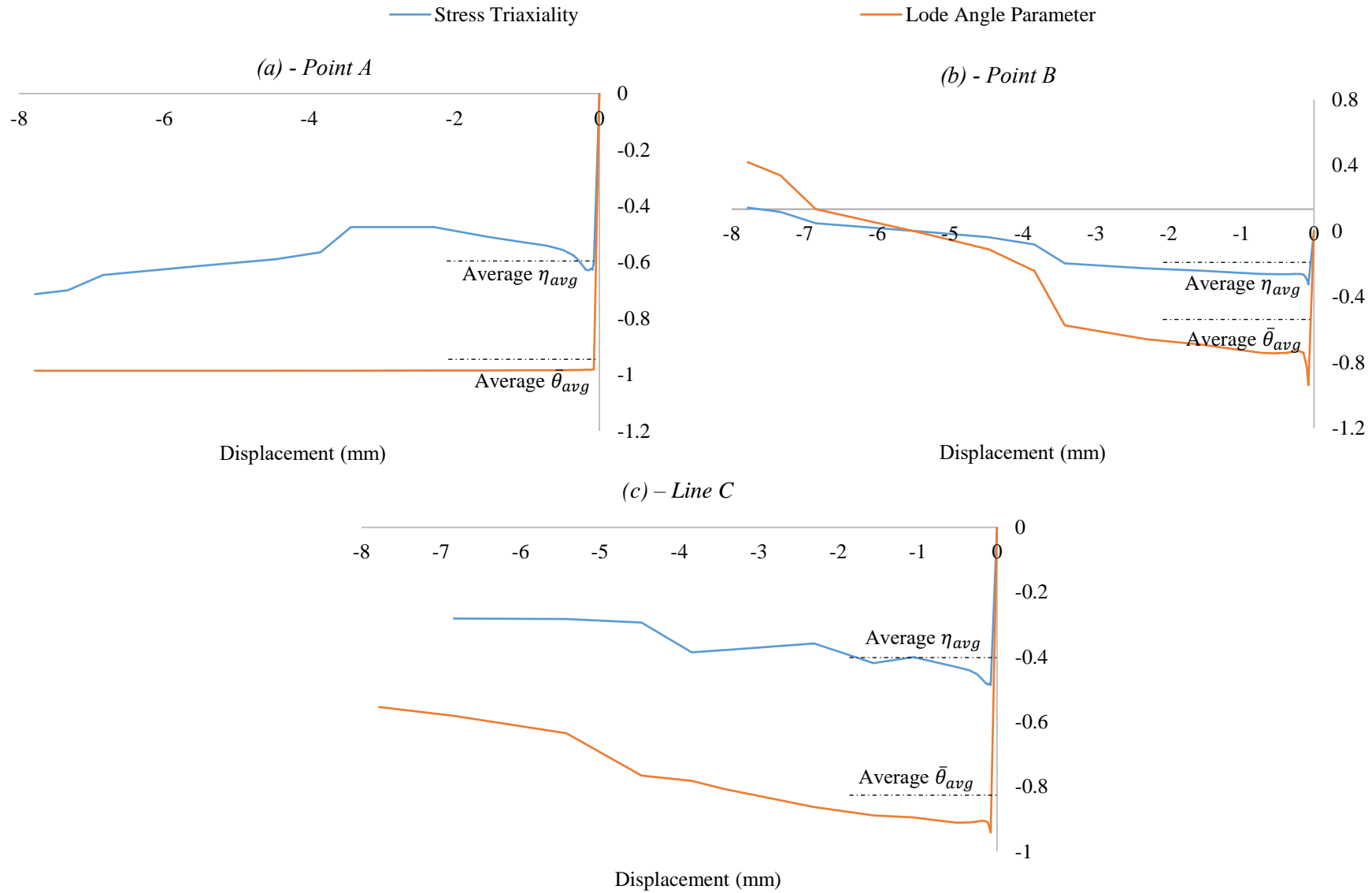


Figure 5.62. Evolution of Stress Triaxiality and Lode Angle Parameter showing the Range of Locations for CA6NM NC3.

To obtain the three parameters: the equivalent fracture strain, average stress triaxiality and the average Lode angle parameter, the same process utilised for the high and low stress triaxiality region was used. Fracture loci for negative stress triaxiality region and lode angle parameter as a function of stress triaxiality for the compression specimens and different points is shown in Figure 5.64. Error bars shown in the graphs presented were determined by using the minimum and maximum u_f of each geometry as value for the displacement boundary condition in the FE model, to find the relative equivalent fracture strain, average stress triaxiality and average Lode angle parameter.

As previously discussed in Section 2.6.1.3, when constructing a fracture locus compression experiments are used for the negative stress triaxiality region. The results for the AISI 304L were past the cut-off value, whereas when using Point B for the CA6NM the values were in the expected range. It was suggested by Bao and Wierzbicki [90] that negative stress triaxiality has a cut-off value of $-1/3$, below which fracture will never occur. Although, Khan and Liu [89] hypothesis contradicted the critical cut-off value of stress triaxiality, proposing that the cut-off value is not constant but depends on the stress state [89]. This highlighted issues regarding the proposed hypothesis, that the material will not fail for stress triaxiality values less than the cut-off value. Exceeding the limit value proposed could depend on the ductility of the material, the ductility of the materials tested in this study meant there was specimens that did not fail. Thus, there was not enough data points in the negative stress tri region to combine with the data in the high and low region.

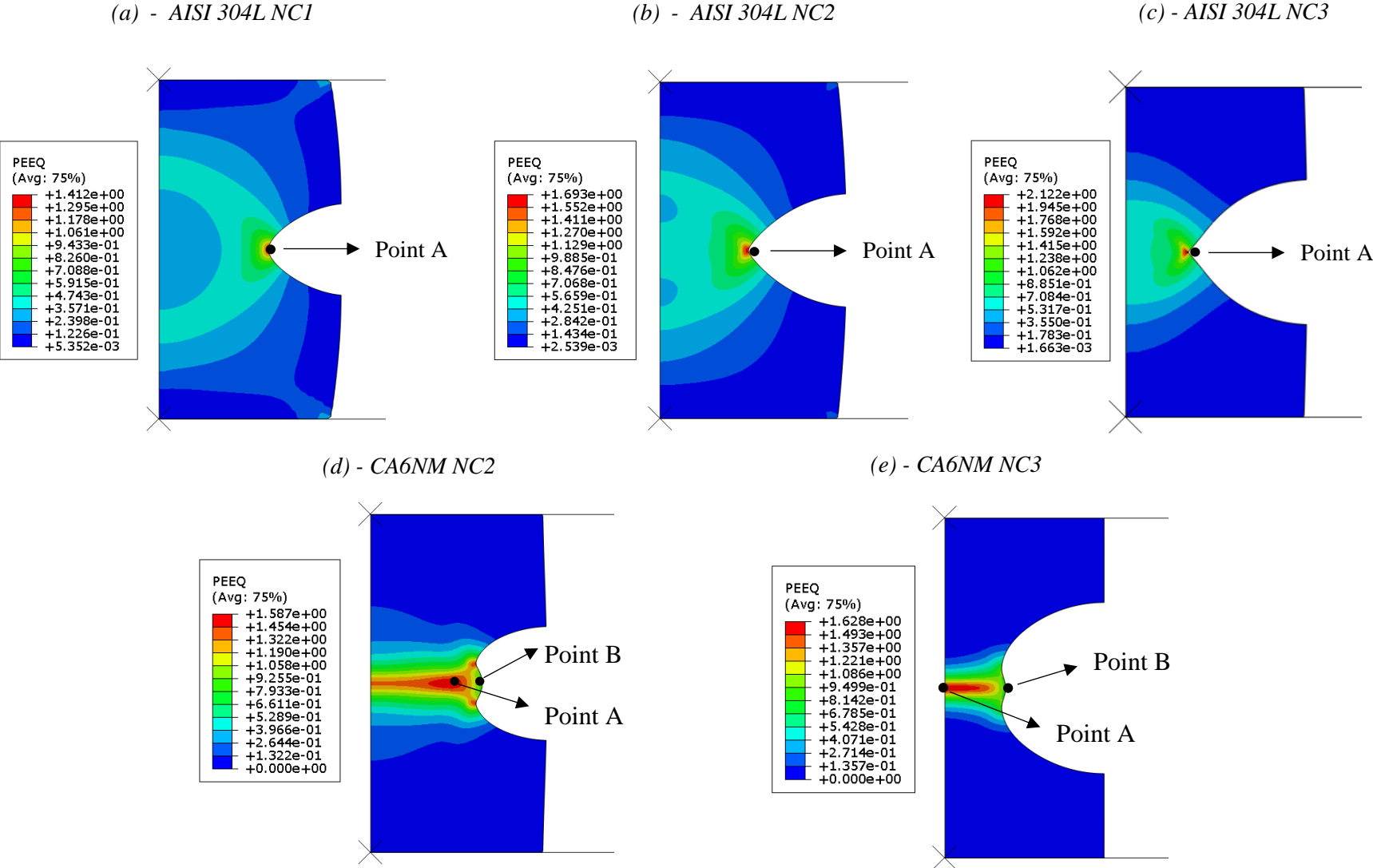


Figure 5.63. Plastic Equivalent Strain Contours for Compression Specimens showing Critical Locations.

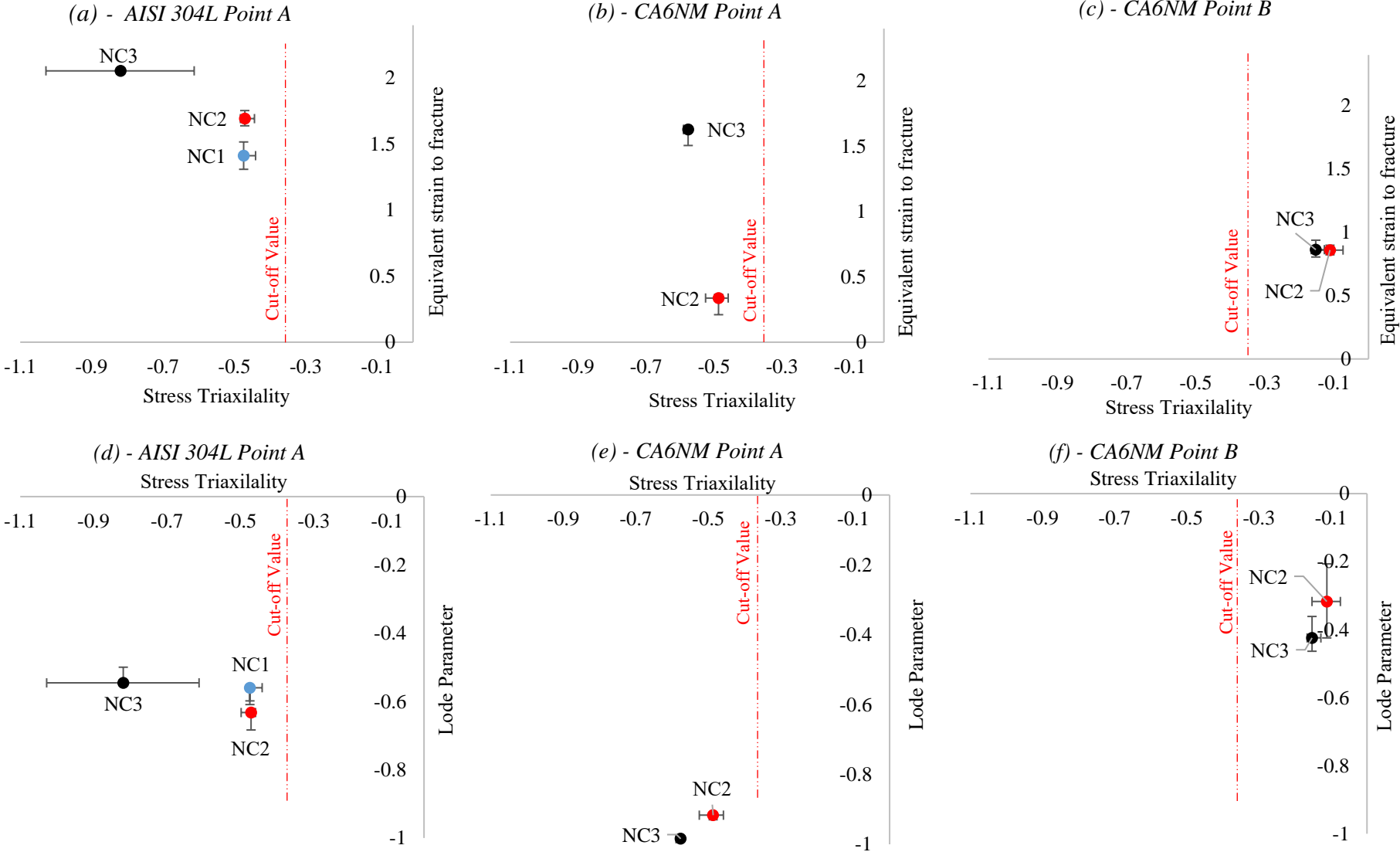


Figure 5.64. Fracture Loci for Negative Stress Triaxiality Region and Lode angle Parameter as a Function of Stress Triaxiality.

5.6.5 Conclusion

To further characterise the plasticity and fracture behaviour of AISI 304L and CA6NM, experimental compression tests using DIC were performed to failure at ambient temperature under quasi-static conditions, for a series of round bars with a notched small gauge section and short cylinders. The results obtained represent the true stress state data, as shown by the agreement of the force displacement curves and the contours shown in Figure 5.61.

The onset of failure was found to take place in conjunction with the first visible macroscopic crack. For a series of specimens, the failure strain exceeded the capabilities of the servo-hydraulic machine used. Therefore, there was not enough data points produced in the negative stress triaxiality region, to combine with the data obtained in the high and low stress triaxiality region.

A variety of critical locations were investigated. The results for the AISI 304L were past the cut-off value, whereas when using Point B for the CA6NM the values were in the expected range. There are two main factors that made obtaining the fracture loci for the negative region challenging, the first was the moment of failure which was hard to determine due to the gathering of paint during deformation. Secondly, was the decision on where to take the critical location. Whilst different locations were investigated the results are difficult to conclude. Defining fracture initiation is the weakest point of the fracture theory, there is no unique way of doing it, for compressive fracture is even more complicated [208]. Further investigation is needed into the best way to perform ductile compression tests with the DIC is needed. Additional testing with more ranges of notches could increase the amount of data on the fracture loci.

5.7 Summary

- To provide true stress-strain data including beyond UTS for AISI 304L and CA6NM, the direct measurement method was used. DIC produced data allowing for measurements such as true strain and instantaneous cross-sectional area up to failure to be extracted.
- Post process DIC study, investigated the effect of using different filtering and subset size results when producing true stress-strain data. Post processing of the DIC software was found to significantly influence the extracted data. For this study a subset size of 25 x 25 pixels and no filtering, produced true stress-strain data that was in agreement with the experimental results.
- AISI 304L was investigated to see if the material displayed any directional variation of mechanical properties. The experiments conducted shown the material AISI 304L did not exhibit any significant anisotropic behaviour.
- The results obtained for the high, low and negative stress triaxiality region represented the true stress state data, as shown by the agreement of force displacement curves and the comparison of the contour plots from the FE analysis and the DIC.
- For the high and low stress triaxiality region there were three methods presented that investigated different ways to extract the equivalent fracture strain, average stress triaxiality and the average Lode angle parameter. From this a strain-based criterion for AISI 304L and CA6NM was produced.
- For the negative stress triaxiality region, the failure strain for a series of specimens exceeded the capabilities of the servo-hydraulic machine used. Therefore, there was not enough data points produced in the negative stress triaxiality region, to combine with the data obtained in the high and low stress triaxiality region.
- By repeating each test 5 times, errors were observed using differences in force displacement curves. A combination of the agreement of force displacement curves and the comparison of the contour plots from the FE analysis and the DIC, show the results obtained represent the true stress state data.

6 Conclusion and Recommendations for Further Work

6.1 Conclusion

Overall, the aim of this thesis was to characterise the plasticity and fracture behaviour of two grades of stainless steel, AISI 304L and CA6NM by producing a fracture locus for each material. The fracture locus details the materials ductility in terms of fracture strain, which can aid in the design of nuclear transport packages.

The background and literature review in **Chapter 2**, firstly discussed the material properties of AISI 304L and CA6NM. Literature concerning ductile fracture including its history has been reviewed, this found research regarding ductile fracture was continuously being extended. Fundamentals of stress state, regarding stress triaxiality and Lode angle parameter and how they relate to a fracture locus were outlined. A novel fracture locus was constructed using a variety of data points from previous researchers, to show the different geometries and their relative loading conditions necessary to obtain data within each region.

Chapter 3 highlighted the core principles and processes of DIC. This chapter methodically discussed and investigated various parameters affecting DIC operation and results. A series of preliminary experiments were performed in order to understand the requirements needed to achieve an optimum test. Tests for various speckle patterns using spray paints highlighted challenges in achieving the optimum speckle pattern as parameters such as contrast, density and the size of speckles needed to be considered. When performing a DIC test contrast over the entire ROI needed to be constant to attain this, it was found that aperture, exposure time and external light needed to work cohesively. High aperture, small exposure time was used to keep the geometry in focus and to restrict motion blur. External light was needed to improve the contrast of the image, a range of lighting types and mountings were investigated, which concluded the ring lights were the most suitable source of external lighting. During the post processing of DIC data, the Dantec DIC software had a smoothing tab that defined the method and the strength of the filtering. There were two filters to choose from, local regression filter which is based on adaptive spline polynomial algorithm (ACSP) and smoothing spline filter.

CHAPTER 5. CONCLUSION AND RECOMMENDATIONS FOR FURTHER WORK

This study found that filters should be used with caution, whilst an increased filter smoothed out the data and reduce the standard deviation of the data, it also decreased the spatial resolution.

The experimental methodology in **Chapter 4**, introduced the experimental testing programme which had 4 main phases of testing, a total of 200 tests were performed at ambient temperature under quasi-static conditions on test specimens having 15 different geometries. The methodology used DIC in parallel with FE analysis, to find the equivalent fracture strain, average stress triaxiality and the average Lode angle parameter over the load history. Utilising both DIC and FE analysis was a direct and efficient approach, as shown throughout this thesis by the agreement between the experimental data and FE analysis force-displacement curves.

For *Phase 1* the focus was to obtain material data for both AISI 304L and CA6NM. To provide true stress-strain data including beyond UTS, the direct measurement method was used. DIC produced data allowing for measurements such as true strain and instantaneous cross-sectional area up to failure to be extracted. The effect of using different filtering and subset size results when producing true stress-strain data was investigated. FE analysis was executed using the different true stress-strain data sets to compare the force displacement responses. The results shown post processing of the DIC software influenced the extracted data. For this particular study a subset size of 25 x 25 pixels and no filtering, produced true stress-strain data that was in agreement with the experimental results. The general methodology developed can be used to obtain true stress-strain data, however, parameters found in this study may not be applicable to different materials or geometries as they will need their own experimental set up.

Phase 2 evaluated the anisotropy of AISI 304L by testing a series of uniaxial tensile tests, for the rolling directions: 0°, 45° and 90°, to see if the directions of the material had an influence on the materials fracture behaviour. This study concluded AISI 304L is isotropic, as it did not exhibit any significant anisotropic behaviour.

Experiments for the high and low stress triaxiality region were conducted for *Phase 3*. To obtain a specimens failure data, for the equivalent fracture strain, average stress triaxiality and average Lode angle parameter over the load history, the instance which failure occurred and where failure initiated (critical location) was needed. The moment of fracture initiation was assumed to be the first detectable discontinuity at the specimen surface when observing the DIC images. Following previous researchers, the critical failure point was taken at the

CHAPTER 5. CONCLUSION AND RECOMMENDATIONS FOR FURTHER WORK

maximum plastic equivalent strain. However, the initial assumed method for the critical location was further investigated, as the fracture initiation at the critical location of the shear specimens occurred at the point of maximum tensile stress. Thus, there were three methods presented that investigated different ways to extract the equivalent fracture strain, stress triaxiality and Lode angle parameter. Following previous researchers, Method 1 was based on the critical failure point being taken at the maximum plastic equivalent strain. The substantial size and complexity of designing mesh for a nuclear transport package means that a coarse mesh maybe employed. When a coarser mesh was applied compared to the finer mesh selected during the mesh sensitivity study, the critical location moved to the centre of the specimen, where the bulk of the material was under shear loading conditions, instead of the tensile failure location. Method 2 was similar to Method 1, except for the shear specimens where the critical failure point was taken at the centre of the specimen on the outer surface. Method 3 averaged the stress state data for the whole of the failure zone of the specimen. The fracture loci developed for all three methods were combined into one graph, leading to the development of a strain-based criterion for AISI 304L and CA6NM. Analytical expressions of the fracture envelope found for each method can be utilised for practical relevance, regarding nuclear transport packages depending on the failure model.

Lastly, *Phase 4* tested a series of round bars with a notched small gauge section and short cylinders under compressive loading conditions, to obtain data regarding the negative stress triaxiality region. The onset of failure was found to take place in conjunction with the first visible macroscopic crack. However, as the material deformed the paint gathered making the failure crack challenging to observe. For a series of specimens, the failure strain exceeded the capabilities of the servo-hydraulic machine used. Therefore, there was not enough data points produced in the negative stress triaxiality region, to combine with the data obtained in the high and low stress triaxiality region. The results for the AISI 304L were past the proposed cut-off value. Whereas, for the CA6NM the values were in the expected range when using Point B which was at the equatorial area on the surface of the specimen. Whilst different locations were investigated the results are difficult to conclude. The weakest point of the fracture theory, is how to define fracture initiation, for compressive fracture it is even more complicated [208].

The method of evaluating DIC test data to produce a fracture locus provides a new understanding of the failure behaviour of the two materials. Both the method for modelling plasticity and the method for assessing fracture behaviour are advancements that can be used

to reduce development risk and provide additional confidence in nuclear transport package design and substantiation.

When considering the analysis of transport flasks, due to the fact CA6NM is a cast material it may perhaps be necessary in addition to failure analysis described in this thesis, to undertake a fracture mechanics assessment using a postulated flaw size to satisfy a design code such as BS7910.

6.2 Contributions to Knowledge and Novel Techniques Developed

6.2.1 Contributions to Knowledge

- **DIC Data Analysis** – Investigated the effect of applying filtering during post processing of DIC data. This information and data can be used as a bases for DIC testing for future engineers or researchers, as there is no present knowledge regarding the effect of filtering as presented in this thesis for obtaining accurate true stress-strain data of uniaxial tensile tests.
- **Methodology** – Created a methodology which uses both DIC and FE analysis, to obtain data which was then used to create fracture loci for AISI 304L and CA6NM. As presented in the research gap in Section 2.8, the method developed in this thesis contributes to the ductile fracture knowledge, as it can be used for obtaining a fracture locus for various materials and geometries.
- **True Stress-Strain Data** - Provided true stress-strain data including beyond UTS for AISI 304L and CA6NM. As the material data produced in this thesis is past the UTS, up to failure it can be used by a nuclear company such as INS for FE analysis to understand how materials react to impact scenarios regarding a nuclear transport package. This data could provide insight for the nuclear transport industry regarding CA6NM for FE analysis, as there is limited data for CA6NM in complex stress-states.

6.2.2 Novel Techniques Developed

- **DIC Optimum Experimental Set Up** - Established standard a series of preliminary requirements to achieve the optimum experimental set up, by exploring various parameters such as: equipment selection and what makes a suitable speckle surface. These novel

techniques can be used by other researchers, university students and also industry to study ductile fracture behaviour.

- **Methods of Obtaining Data** - Three methods were introduced for creating fracture loci, they investigated different ways to extract the equivalent fracture strain, average stress triaxiality and the average Lode angle parameter. From this a strain-based criterion for AISI 304L and CA6NM was produced. The different methods for assessing fracture behaviour are advancements that can be used to reduce development risk and provide additional confidence in nuclear transport package design and substantiation. These methods can be used regarding any study of materials regarding ductile fracture, to provide an insight into how the material fails under different loading conditions, to providing information if the material is suitable to its desired application.

6.3 Recommendations for Further Work

Although comprehensive studies have been performed in this thesis on characterising the plasticity and fracture behaviour of AISI 304L and CA6NM, the following topics are suggested for future studies:

- **Various Strain Rates and a Range of Temperatures** - Testing standards are regulated by the IAEA before nuclear transport packages can be licenced for use, a series of tests are performed in which, the package may be subjected to various tests including mechanical, thermal and water immersion tests. This thesis focused solely on obtaining quasi-static ambient temperature data, however, these materials are subjected to impact testing at various temperatures. The methods used in this thesis could be explicitly used to obtain experimental data for a variety of strain rates and a range of temperatures (-40° - 500° , as shown in Figure 2.1), providing further insight into the failure of materials, which could then be applied to real assessments.
- **SEM Investigation** – It is recommended that material focused research should be conducted on characterising potential brittle modes of failure regarding the observations for CA6NM and further micromechanical modelling to investigate the failure process.
- **Negative Compression Testing** – Defining fracture initiation for compressive fracture is complicated, the critical location for compression tests should be further explored. Further investigation is needed into the best way to perform ductile compression tests with the DIC, to reduce the folding of paint to obtain more accurate results. Lastly, additional testing with more ranges of notches could increase the amount of data on the fracture loci.

References

- [1] World Nuclear Association, “Nuclear Power in the World Today.” <https://www.world-nuclear.org/information-library/current-and-future-generation/nuclear-power-in-the-world-today.aspx>.
- [2] U.S Energy Information Administration, “Nuclear explained,” 2019. <https://www.eia.gov/energyexplained/nuclear/nuclear-power-plants.php> (accessed Jul. 12, 2021).
- [3] Nuclear Energy Agency, “Radioactive Waste in Perspective,” 2010.
- [4] International Atomic Energy Agency, “Regulations for the safe transport of radioactive material, 2018 edition,” 2018. [Online]. Available: <http://www-ns.iaea.org/standards/>.
- [5] National Research Council, *Going the Distance?: The Safe Transport of Spent Nuclear Fuel and High-Level Radioactive Waste in the United States*. Washington, D.C.: National Academies Press, 2006.
- [6] Office for Nuclear Regulation, “Transporting radioactive material.” <https://www.onr.org.uk/transport/> (accessed Jul. 12, 2021).
- [7] U.S. Department of Energy, “Radioactive Material Shipping Packages, Transportation Emergency Preparedness Program (TEPP),” pp. 1–12.
- [8] B. Sievwright, U. Kingdom, P. Dixon, and R. W. E. Nukem, “The Development of a Type B (U) Transport Container Design in Cast and Forged Stainless Steel for the Transport of Immobilised Intermediate Level Waste,” no. PATRAM, 2004.
- [9] N. A. C. I.A. Grainey, A.D. Cummings, “Development Of A Large Waste Transport Container (LWTC) For Disposal Of Legacy ILW To A Geological Disposal Facility In The UK,” vol. 44, no. 0, 2013.
- [10] S.Porter S.Perry and IA.Grainey, “INS ENG R 18 740 Rev 1: TDP021: RWM PROGRAMME - Handling and Operational Review of the LWTC Concepts Description,” 2019.
- [11] L. Waste and T. Container, *Large Waste Transport Container Summary Report*, no. May. 2021.
- [12] Y. Bao and T. Wierzbicki, “On fracture locus in the equivalent strain and stress triaxiality space,” *Int. J. Mech. Sci.*, vol. 46, no. 1, pp. 81–98, Jan. 2004, doi: 10.1016/j.ijmecsci.2004.02.006.

- [13] X. Gao, G. Zhang, and C. Roe, "A study on the effect of the stress state on ductile fracture," *Int. J. Damage Mech.*, vol. 19, no. 1, pp. 75–94, Jan. 2010, doi: 10.1177/1056789509101917.
- [14] K. S. Zhang, J. B. Bai, and D. François, "Numerical analysis of the influence of the Lode parameter on void growth," *Int. J. Solids Struct.*, vol. 38, no. 32–33, pp. 5847–5856, 2001, doi: 10.1016/S0020-7683(00)00391-7.
- [15] R. Kiran and K. Khandelwal, "A triaxiality and Lode parameter dependent ductile fracture criterion," *Eng. Fract. Mech.*, vol. 128, no. C, pp. 121–138, 2014, doi: 10.1016/j.engfracmech.2014.07.010.
- [16] Instron, "The challenges and benefits of implementing strain control - Instron." <https://www.instron.us/testing-solutions/industry-solutions/materials/metals/solutions-for-sheet-metal-testing/strain-control> (accessed Dec. 09, 2020).
- [17] H. Jin, B. Sanborn, W. Y. Lu, and B. Song, "Mechanical characterization of 304L-VAR stainless steel in tension with a full coverage of low, intermediate, and high strain rates," *Mech. Mater.*, vol. 152, p. 103654, Jan. 2021, doi: 10.1016/j.mechmat.2020.103654.
- [18] E. Cadoni, D. Forni, R. Gieleta, and L. Kruszka, "Tensile and compressive behaviour of S355 mild steel in a wide range of strain rates," *Eur. Phys. J. Spec. Top.*, vol. 227, no. 1–2, pp. 29–43, 2018, doi: 10.1140/epjst/e2018-00113-4.
- [19] N. K. Singh, E. Cadoni, M. K. Singha, and N. K. Gupta, "Mechanical characterization of multi phase steel at different rates of loading," *Mater. Sci. Forum*, vol. 710, no. May 2014, pp. 421–426, 2012, doi: 10.4028/www.scientific.net/MSF.710.421.
- [20] X. Jin *et al.*, "Quasi-static and dynamic experimental studies on the tensile strength and failure pattern of concrete and mortar discs," *Sci. Rep.*, vol. 7, no. 1, pp. 1–15, 2017, doi: 10.1038/s41598-017-15700-2.
- [21] Ove Arup & Partners, "Development Work To Establish The Feasibility Of Manufacturing The ILW Transport Containers By Casting - Phase One, Report No. IE 91-38 Issue : A," 1993.
- [22] V. Kain, *Stress corrosion cracking (SCC) in stainless steels*. Woodhead Publishing Limited, 2011.
- [23] "Waste Package Specification and Guidance Documentation Guidance on the design of waste containers for waste packages containing low heat generating waste," 2019. [Online]. Available: www.gov.uk/guidance/generic-waste-package-specification.
- [24] Y. Dong *et al.*, "Microbiologically influenced corrosion of 304L stainless steel caused by an alga associated bacterium *Halomonas titanicae*," *J. Mater. Sci. Technol.*, vol. 37,

- pp. 200–206, 2020, doi: 10.1016/j.jmst.2019.06.023.
- [25] W. C. Niu and Y. L. Ju, “System design and experimental verification of an internal insulation panel system for large-scale cryogenic wind tunnel,” *Cryogenics (Guildf)*., vol. 115, no. February, 2021, doi: 10.1016/j.cryogenics.2021.103279.
- [26] F. C. Campbell, “Fatigue and Fracture: Understanding the Basics,” *J. Chem. Inf. Model.*, 2012.
- [27] “DESIGN GUIDELINES FOR THE SELECTION AND USE OF STAINLESS STEEL NiDI Distributed by NICKEL DEVELOPMENT INSTITUTE courtesy of AMERICAN IRON AND STEEL INSTITUTE AND SPECIALTY STEEL INSTITUTE OF NORTH AMERICA.”
- [28] M. F. McGuire, “Austenitic Stainless Steels,” *Stainl. Steels Des. Eng.*, no. 2008, pp. 69–90, 2019, doi: 10.31399/asm.tb.ssde.t52310069.
- [29] “STAINLESS STEEL.”
- [30] K. Weman, “The weldability of steel,” in *Welding Processes Handbook*, Elsevier, 2012, pp. 191–206.
- [31] R. Ganesan, “Improving the quality of high alloy CA6NM stainless steel castings,” 2015.
- [32] A. K. Chauhan, D. B. Goel, and S. Prakash, “Solid particle erosion behaviour of 13Cr-4Ni and 21Cr-4Ni-N steels,” *J. Alloys Compd.*, vol. 467, no. 1–2, pp. 459–464, 2009, doi: 10.1016/j.jallcom.2007.12.053.
- [33] B. A. Tabatabae, F. Ashrafizadeh, and A. M. Hassanli, “Influence of retained austenite on the mechanical properties of low carbon martensitic stainless steel castings,” *ISIJ Int.*, vol. 51, no. 3, pp. 471–475, 2011, doi: 10.2355/isijinternational.51.471.
- [34] H. Bhadeshia and R. Honeycombe, “Formation of Martensite,” *Steels Microstruct. Prop.*, vol. 011, pp. 135–177, 2017, doi: 10.1016/b978-0-08-100270-4.00005-6.
- [35] R. De Paula Silva, M. I. S. T. Faria, L. F. C. B. De Almeida, C. A. Nunes, D. Vieira, and W. Borges, “Microstructure and mechanical properties of ASTM A743 CA6NM steel welded by FCAW process,” *Mater. Res.*, vol. 20, no. 6, pp. 1622–1629, 2017, doi: 10.1590/1980-5373-MR-2017-0468.
- [36] F. Mirakhorli, X. Cao, X. T. Pham, P. Wanjara, and J. L. Fihey, “Phase structures and morphologies of tempered CA6NM stainless steel welded by hybrid laser-arc process,” *Mater. Charact.*, vol. 123, pp. 264–274, 2017, doi: 10.1016/j.matchar.2016.10.029.
- [37] Lucideon, “AI 19607 Report - International Nuclear Services,” 2019, doi: 10.1016/b978-0-12-802924-4.09985-0.

- [38] George E. Dieter, *Mechanical Metallurgy (Third Edition)*. McGraw-Hill Education, 1986.
- [39] J. Wu, “Material Interface of Pantograph and Contact Line,” in *Pantograph and Contact Line System*, Elsevier, 2018, pp. 165–191.
- [40] K. Komori, “Macroscopic ductile fracture criteria,” in *Ductile Fracture in Metal Forming*, Elsevier, 2020, pp. 49–94.
- [41] L. Driemeier, M. Brünig, G. Micheli, and M. Alves, “Experiments on stress-triaxiality dependence of material behavior of aluminum alloys,” *Mech. Mater.*, vol. 42, no. 2, pp. 207–217, Feb. 2010, doi: 10.1016/j.mechmat.2009.11.012.
- [42] A. K. Dubey, “Stress and Strain,” *Springer Geol.*, no. 2009, pp. 3–15, 2014, doi: 10.1007/978-3-319-05588-6_1.
- [43] T. A. Dow and R. O. Scattergood, “Mesoscale and Microscale Manufacturing Processes: Challenges for Materials, Fabrication and Metrology.”
- [44] G. M. Gladysz and K. K. Chawla, “Applications,” in *Voids in Materials*, Elsevier, 2015, pp. 131–156.
- [45] M. Saby, P. O. Bouchard, and M. Bernacki, “Void closure criteria for hot metal forming: A review,” *Journal of Manufacturing Processes*, vol. 19. Elsevier Ltd, pp. 239–250, Aug. 09, 2015, doi: 10.1016/j.jmapro.2014.05.006.
- [46] G. Banaszek and A. Stefanik, “Theoretical and laboratory modelling of the closure of metallurgical defects during forming of a forging,” *J. Mater. Process. Technol.*, vol. 177, no. 1–3, pp. 238–242, Jul. 2006, doi: 10.1016/j.jmatprotec.2006.04.023.
- [47] U. Ståhlberg, H. Keife, M. Lundberg, and A. Melander, “A study of void closure during plastic deformation,” *J. Mech. Work. Technol.*, vol. 4, no. 1, pp. 51–63, 1980, doi: 10.1016/0378-3804(80)90005-4.
- [48] F. Scheyvaerts, T. Pardoën, and P. R. Onck, “A new model for void coalescence by internal necking,” *Int. J. Damage Mech.*, vol. 19, no. 1, pp. 95–126, Jan. 2010, doi: 10.1177/1056789508101918.
- [49] W. M. Garrison, N. Moody, W. M. Garrison Jr, and N. R. Moody, “Ductile fracture,” *Artic. J. Phys. Chem. Solids*, vol. 48, pp. 103–1074, 1976, doi: 10.1016/0022-3697(87)90118-1.
- [50] S. Gatea, H. Ou, B. Lu, and G. McCartney, “Modelling of ductile fracture in single point incremental forming using a modified GTN model,” *Eng. Fract. Mech.*, vol. 186, pp. 59–79, Dec. 2017, doi: 10.1016/j.engfracmech.2017.09.021.
- [51] D. Mohr and S. J. Marcadet, “Micromechanically-motivated phenomenological

- Hosford-Coulomb model for predicting ductile fracture initiation at low stress triaxialities,” *Int. J. Solids Struct.*, vol. 67–68, pp. 40–55, Aug. 2015, doi: 10.1016/j.ijsolstr.2015.02.024.
- [52] C. Tekoğlu, J. W. Hutchinson, and T. Pardoen, “On localization and void coalescence as a precursor to ductile fracture,” *Philos. Trans. R. Soc. A Math. Phys. Eng. Sci.*, vol. 373, no. 2038, Mar. 2015, doi: 10.1098/rsta.2014.0121.
- [53] S. Kweon, “Damage at negative triaxiality,” *Eur. J. Mech. A/Solids*, vol. 31, no. 1, pp. 203–212, Jan. 2012, doi: 10.1016/j.euromechsol.2011.02.005.
- [54] M. Zapara, N. Tutyshkin, and W. H. Müller, “Growth and closure of voids in metals at negative stress triaxialities,” *Key Eng. Mater.*, vol. 554–557, no. June 2013, pp. 1125–1132, 2013, doi: 10.4028/www.scientific.net/KEM.554-557.1125.
- [55] A. M. Freudenthal, *The Inelastic Behavior of Engineering Materials and Structures*. John Wiley & Sons In, 1950.
- [56] S. Baltic, J. Magnien, H. P. Gänser, T. Antretter, and R. Hammer, “Coupled damage variable based on fracture locus: Modelling and calibration,” *Int. J. Plast.*, vol. 126, p. 102623, Mar. 2020, doi: 10.1016/j.ijplas.2019.11.002.
- [57] P. W. Bridgman, *Studies in large plastic flow and fracture with special emphasis on the effects of hydrostatic pressure*. New York: McGraw-Hill, 1952.
- [58] Y. Bai, X. Teng, and T. Wierzbicki, “On the application of stress triaxiality formula for plane strain fracture testing,” *J. Eng. Mater. Technol. Trans. ASME*, vol. 131, no. 2, pp. 0210021–02100210, 2009, doi: 10.1115/1.3078390.
- [59] Joseph Datsko, *Material Properties and Manufacturing Processes*. John Wiley & Sons In, 1966.
- [60] F. A. McClintock, “A criterion for ductile fracture by the growth of holes,” *J. Appl. Mech. Trans. ASME*, vol. 35, no. 2, pp. 363–371, 1968, doi: 10.1115/1.3601204.
- [61] J. R. Rice and D. M. Tracey, “On the ductile enlargement of voids in triaxial stress fields*,” *J. Mech. Phys. Solids*, 1969, doi: 10.1016/0022-5096(69)90033-7.
- [62] J. W. Hancock and A. C. Mackenzie, “On the mechanisms of ductile failure in high-strength steels subjected to multi-axial stress-states,” *J. Mech. Phys. Solids*, 1976, doi: 10.1016/0022-5096(76)90024-7.
- [63] V. Tvergaard and A. Needleman, “ANALYSIS OF THE CUP-CONE FRACTURE IN A ROUND TENSILE BAR,” 1984.
- [64] V. Tvergaard, “Influence of voids on shear band instabilities under plane strain conditions,” *Int. J. Fract.*, vol. 17, no. 4, pp. 389–407, 1981, doi: 10.1007/BF00036191.

- [65] V. Tvergaard, "On localization in ductile materials containing spherical voids," *Int. J. Fract.*, vol. 18, no. 4, pp. 237–252, 1982, doi: 10.1007/BF00015686.
- [66] A. Kami, B. M. Dariani, A. Sadough Vanini, D. S. Comsa, and D. Banabic, "Numerical determination of the forming limit curves of anisotropic sheet metals using GTN damage model," *J. Mater. Process. Technol.*, vol. 216, pp. 472–483, 2015, doi: 10.1016/j.jmatprotec.2014.10.017.
- [67] M. Wilkins, R. Streit, and J. Reaugh, "Cumulative-strain-damage model of ductile fracture: simulation and prediction of engineering fracture tests," 1980, doi: 10.2172/6628920.
- [68] M. OYANE, "Criteria of Ductile Fracture Strain," *Bull. JSME*, vol. 15, no. 90, pp. 1507–1513, 1972, doi: 10.1299/jsme1958.15.1507.
- [69] J. W. Hancock and D. K. Brown, "On the role of strain and stress state in ductile failure," *J. Mech. Phys. Solids*, vol. 31, no. 1, pp. 1–24, 1983, doi: 10.1016/0022-5096(83)90017-0.
- [70] G. R. Johnson and W. H. Cook, "Fracture characteristics of three metals subjected to various strains, strain rates, temperatures and pressures," *Eng. Fract. Mech.*, vol. 21, no. 1, pp. 31–48, 1985, doi: 10.1016/0013-7944(85)90052-9.
- [71] L. M. Kachanov and D. Krajcinovic, *Introduction to Continuum Damage Mechanics*, vol. 54, no. 2. Springer Netherlands, 1987.
- [72] Xue Liang, "Ductile Fracture Modeling - Theory, Experimental Investigation and Numerical Verification," *PhD Thesis*, no. January 2009, p. 251, 2007.
- [73] J. L. Chaboche, "Continuum Damage Mechanics: Part I - General Concepts.," *J. Appl. Mech. Trans. ASME*, vol. 55, no. 1, pp. 59–64, 1988, [Online]. Available: <http://www.scopus.com/inward/record.url?eid=2-s2.0-0023978287&partnerID=tZOtx3y1>.
- [74] J. Lemaitre, "A Continuous Damage Mechanics Model for Ductile Fracture," *J. Eng. Mater. Technol.*, vol. 107, no. 1, pp. 83–89, Jan. 1985, doi: 10.1115/1.3225775.
- [75] A. S. Kao, W. A. Spitzig, O. Richmond, and H. A. Kuhn, "Tensile fracture and fractographic analysis of 1045 spheroidized steel under hydrostatic pressure," *J. Mater. Res.*, vol. 5, no. 1, pp. 83–91, 1990, doi: 10.1557/JMR.1990.0089.
- [76] F. D. Fischer, O. Kolednik, G. X. Shan, and F. G. Rammerstorfer, "A note on calibration of ductile failure damage indicators," *Int. J. Fract.*, vol. 73, no. 4, pp. 345–357, 1995, doi: 10.1007/BF00027274.
- [77] A. M. Beese, M. Luo, Y. Li, Y. Bai, and T. Wierzbicki, "Partially coupled anisotropic

- fracture model for aluminum sheets,” *Eng. Fract. Mech.*, vol. 77, no. 7, pp. 1128–1152, May 2010, doi: 10.1016/j.engfracmech.2010.02.024.
- [78] M. S. Mirza, D. C. Barton, and P. Church, “The effect of stress triaxiality and strain-rate on the fracture characteristics of ductile metals,” *J. Mater. Sci.*, vol. 31, no. 2, pp. 453–461, 1996, doi: 10.1007/BF01139164.
- [79] Yingbin Bao, “Prediction of Ductile Crack Formation in Uncracked Bodies,” 2003.
- [80] T. Borvik, O. S. Hopperstad, T. Berstad, and M. Langseth, “Perforation of 12mm thick steel plates by 20mm diameter projectiles with flat, hemispherical and conical noses - Part II: Numerical simulations,” *Int. J. Impact Eng.*, vol. 27, no. 1, pp. 37–64, 2001, doi: 10.1016/S0734-743X(01)00035-5.
- [81] L. Xue, “Damage accumulation and fracture initiation in uncracked ductile solids subject to triaxial loading,” *Int. J. Solids Struct.*, vol. 44, no. 16, pp. 5163–5181, Aug. 2007, doi: 10.1016/j.ijsolstr.2006.12.026.
- [82] L. Xue and T. Wierzbicki, “Ductile fracture initiation and propagation modeling using damage plasticity theory,” *Eng. Fract. Mech.*, vol. 75, no. 11, pp. 3276–3293, 2008, doi: 10.1016/j.engfracmech.2007.08.012.
- [83] D. Mohr and S. Henn, “Calibration of stress-triaxiality dependent crack formation criteria: A new hybrid experimental-numerical method,” *Exp. Mech.*, vol. 47, no. 6, pp. 805–820, 2007, doi: 10.1007/s11340-007-9039-7.
- [84] Y. Bai and T. Wierzbicki, “A new model of metal plasticity and fracture with pressure and Lode dependence,” *Int. J. Plast.*, vol. 24, no. 6, pp. 1071–1096, Jun. 2008, doi: 10.1016/j.ijplas.2007.09.004.
- [85] K. Nahshon and J. W. Hutchinson, “Modification of the Gurson Model for shear failure,” *Eur. J. Mech. A/Solids*, vol. 27, no. 1, pp. 1–17, Jan. 2008, doi: 10.1016/j.euromechsol.2007.08.002.
- [86] L. Malcher, F. M. Andrade Pires, and J. M. A. César De Sá, “An assessment of isotropic constitutive models for ductile fracture under high and low stress triaxiality,” *Int. J. Plast.*, vol. 30–31, pp. 81–115, 2012, doi: 10.1016/j.ijplas.2011.10.005.
- [87] T. B. Stoughton and J. W. Yoon, “A new approach for failure criterion for sheet metals,” *Int. J. Plast.*, vol. 27, no. 3, pp. 440–459, 2011, doi: 10.1016/j.ijplas.2010.07.004.
- [88] T. Wierzbicki, Y. Bao, Y. W. Lee, and Y. Bai, “Calibration and evaluation of seven fracture models,” *Int. J. Mech. Sci.*, vol. 47, no. 4-5 SPEC. ISS., pp. 719–743, Apr. 2005, doi: 10.1016/j.ijmecsci.2005.03.003.
- [89] A. S. Khan and H. Liu, “A new approach for ductile fracture prediction on Al 2024-

- T351 alloy,” *Int. J. Plast.*, vol. 35, pp. 1–12, Aug. 2012, doi: 10.1016/j.ijplas.2012.01.003.
- [90] Y. Bao and T. Wierzbicki, “On the cut-off value of negative triaxiality for fracture,” *Eng. Fract. Mech.*, vol. 72, no. 7, pp. 1049–1069, May 2005, doi: 10.1016/j.engfracmech.2004.07.011.
- [91] M. Brünig, S. Gerke, and M. Schmidt, “Damage and failure at negative stress triaxialities: Experiments, modeling and numerical simulations,” *Int. J. Plast.*, vol. 102, no. December 2017, pp. 70–82, 2018, doi: 10.1016/j.ijplas.2017.12.003.
- [92] Z. Li, X. Yang, and A. Tang, “A Fracture Criterion for Prediction of Fracture Initiation of Metal Materials at Various Stress States for Nuclear Waste Storage,” *Sci. Technol. Nucl. Install.*, vol. 2019, 2019, doi: 10.1155/2019/3591925.
- [93] S. H. Zhang, X. R. Jiang, C. C. Xiang, L. Deng, and Y. X. Li, “Proposal and application of a new yield criterion for metal plastic deformation,” *Arch. Appl. Mech.*, vol. 90, no. 8, pp. 1705–1722, Aug. 2020, doi: 10.1007/s00419-020-01691-6.
- [94] S. J. Park, K. Lee, B. C. Cerik, and J. Choung, “Ductile fracture prediction of EH36 grade steel based on Hosford–Coulomb model,” *Ships Offshore Struct.*, vol. 14, no. sup1, pp. 219–230, Oct. 2019, doi: 10.1080/17445302.2019.1565300.
- [95] M. Dunand and D. Mohr, “Hybrid experimental-numerical analysis of basic ductile fracture experiments for sheet metals,” *Int. J. Solids Struct.*, vol. 47, no. 9, pp. 1130–1143, May 2010, doi: 10.1016/j.ijsolstr.2009.12.011.
- [96] H. Ghadbeigi, C. Pinna, and S. Celotto, “Failure mechanisms in DP600 steel: Initiation, evolution and fracture,” *Mater. Sci. Eng. A*, vol. 588, pp. 420–431, Dec. 2013, doi: 10.1016/j.msea.2013.09.048.
- [97] C. K. Oh, Y. J. Kim, J. H. Baek, Y. P. Kim, and W. S. Kim, “Ductile failure analysis of API X65 pipes with notch-type defects using a local fracture criterion,” *Int. J. Press. Vessel. Pip.*, vol. 84, no. 8, pp. 512–525, Aug. 2007, doi: 10.1016/j.ijpvp.2007.03.002.
- [98] L. E. Malvern, *Introduction to the Mechanics of a Continuous Medium*. 1969.
- [99] D. Mohr and E. Zurich, “Basic Notions of Fracture Mechanics - Ductile Fracture,” 2015.
- [100] Dassault Systèmes, *Abaqus Analysis User’s Guide*. 2006.
- [101] C. F. Guzmán, “About the Lode angle influence in ductile fracture,” pp. 1–18, 2013, doi: 10.13140/RG.2.2.27178.00966.
- [102] Y. Bai, “Effect of loading history in necking and fracture,” 2008. [Online]. Available: <https://www.researchgate.net/publication/38003378>.
- [103] I. Peshekhodov, M. Dykiert, M. Vucetic, and B.-A. Behrens, “Evaluation of common

- tests for fracture characterisation of advanced high-strength sheet steels with the help of the FEA,” doi: 10.1088/1757-899X/159/1/012014.
- [104] Y. C. Jang and Y. Lee, “A method to construct the fracture locus in the range of high stress triaxiality when only a round tensile specimen is available,” *J. Mech. Sci. Technol.*, vol. 33, no. 3, pp. 1195–1201, Mar. 2019, doi: 10.1007/s12206-019-0219-z.
- [105] Y. Bao, “Dependence of ductile crack formation in tensile tests on stress triaxiality, stress and strain ratios,” *Eng. Fract. Mech.*, vol. 72, no. 4, pp. 505–522, Mar. 2005, doi: 10.1016/j.engfracmech.2004.04.012.
- [106] C. K. Oh, Y. J. Kim, J. H. Baek, and W. S. Kim, “Development of stress-modified fracture strain for ductile failure of API X65 steel,” *Int. J. Fract.*, vol. 143, no. 2, pp. 119–133, Jan. 2007, doi: 10.1007/s10704-006-9036-3.
- [107] M. Dunand and D. Mohr, “Optimized butterfly specimen for the fracture testing of sheet materials under combined normal and shear loading,” *Eng. Fract. Mech.*, vol. 78, no. 17, pp. 2919–2934, 2011, doi: 10.1016/j.engfracmech.2011.08.008.
- [108] C. Glenn and Maclean, “Fracture and Plasticity Characterization of DH-36 Navy Steel,” 2007.
- [109] N. Saba, M. Jawaid, and M. T. H. Sultan, *I - An overview of mechanical and physical testing of composite materials*. Elsevier Ltd, 2019.
- [110] K. Komori, “Macroscopic ductile fracture phenomena,” in *Ductile Fracture in Metal Forming*, Elsevier, 2020, pp. 1–48.
- [111] R. Kiran and K. Khandelwal, “Experimental studies and models for ductile fracture in ASTM A992 steels at high triaxiality,” *J. Struct. Eng. (United States)*, vol. 140, no. 2, Feb. 2014, doi: 10.1061/(ASCE)ST.1943-541X.0000828.
- [112] Y. Bao, “Dependence of fracture ductility on thickness,” *Thin-Walled Struct.*, vol. 42, no. 8, pp. 1211–1230, 2004, doi: 10.1016/j.tws.2004.03.011.
- [113] L. Qian, X. Wang, C. Sun, and A. Dai, “Correlation of macroscopic fracture behavior with microscopic fracture mechanism for AHSS sheet,” *Materials (Basel)*, vol. 16, no. 6, Mar. 2019, doi: 10.3390/ma12060900.
- [114] M. Španiel, A. Prantl, J. Džugan, J. Ružička, M. Moravec, and J. Kuželka, “Calibration of fracture locus in scope of uncoupled elastic-plastic-ductile fracture material models,” *Adv. Eng. Softw.*, vol. 72, pp. 95–108, 2014, doi: 10.1016/j.advengsoft.2013.05.007.
- [115] M. D. Dirk Mohr, “Experimental Investigation on the Plasticity of Hexagonal Aluminum Honeycomb Under Multiaxial Loading,” *J. Appl. Mech.*, vol. 71, pp. 375–385, 2004.

- [116] H. Mae, X. Teng, Y. Bai, and T. Wierzbicki, “Comparison of ductile fracture properties of aluminum castings: Sand mold vs. metal mold,” *Int. J. Solids Struct.*, vol. 45, no. 5, pp. 1430–1444, 2008, doi: 10.1016/j.ijsolstr.2007.10.016.
- [117] D. Mohr and R. Treitler, “Onset of fracture in high pressure die casting aluminum alloys,” *Eng. Fract. Mech.*, vol. 75, no. 1, pp. 97–116, 2008, doi: 10.1016/j.engfracmech.2007.01.029.
- [118] S. Dwivedi, R. S. Rana, A. Rana, S. Rajpurohit, and R. Purohit, “Investigation of Damage in Small Deformation in Hot Rolling Process Using FEM,” Elsevier Ltd, Jan. 2017. doi: 10.1016/j.matpr.2017.02.085.
- [119] H. Kudo and K. Aoi, “Effect of Compression Test Condition Upon Fracturing of a Medium Carbon Steel – Study on Cold – Forgeability Test; Part II,” *J. Japan Soc. Tech. Plast.*, vol. 8, pp. 17–72, 1967.
- [120] H. Li, M. W. Fu, J. Lu, and H. Yang, “Ductile fracture: Experiments and computations,” *Int. J. Plast.*, vol. 27, no. 2, pp. 147–180, 2011, doi: 10.1016/j.ijplas.2010.04.001.
- [121] J. Landre, A. Pertence, P. R. Cetlin, J. M. C. Rodrigues, and P. A. F. Martins, “On the utilisation of ductile fracture criteria in cold forging,” *Finite Elem. Anal. Des.*, vol. 39, no. 3, pp. 175–186, Jan. 2003, doi: 10.1016/S0168-874X(02)00065-3.
- [122] Instron, “What is Compression Testing? - Instron.” <https://www.instron.us/en-us/our-company/library/test-types/compression-test> (accessed Dec. 09, 2020).
- [123] H. W. S. Sutton, Michael A, Jean-José Orteu, *Image Correlation for Shape, Motion and Deformation Measurements*, no. 2009. Boston, MA: Springer US, 2009.
- [124] P. Hariharan, “Interferometry,” in *Optical Interferometry*, Elsevier, 2003, pp. 1–8.
- [125] W. H. Peters and W. F. Ranson, “Digital Imaging Techniques In Experimental Stress Analysis,” *Opt. Eng.*, vol. 21, no. 3, Jun. 1982, doi: 10.1117/12.7972925.
- [126] M. Sutton, C. Mingqi, W. Peters, Y. Chao, and S. McNeill, “Application of an optimized digital correlation method to planar deformation analysis,” *Image Vis. Comput.*, vol. 4, no. 3, pp. 143–150, 1986, doi: 10.1016/0262-8856(86)90057-0.
- [127] M. A. Sutton and J. Yan, “Computer vision for shape and deformation measurements: Recent developments and applications,” *SAE Tech. Pap.*, vol. 115, pp. 495–500, 2006, doi: 10.4271/2006-01-0526.
- [128] D. Mohr and M. Oswald, “A new experimental technique for the multi-axial testing of advanced high strength steel sheets,” *Exp. Mech.*, vol. 48, no. 1, pp. 65–77, 2008, doi: 10.1007/s11340-007-9053-9.
- [129] J. D. Littell *et al.*, “Photogrammetry Measurements During a Tanking Test on the Space

- Shuttle External Tank, ET-137,” 2013. [Online]. Available: www.nasa.gov.
- [130] Trillion, “Trillion Automotive.” <https://trillion.com/automotive/> (accessed Apr. 15, 2020).
- [131] K. Rankin, M. Browne, and A. Dickinson, “Digital Image Correlation for Strain Analysis of Whole Bones and Implants,” in *Experimental Methods in Orthopaedic Biomechanics*, Elsevier Inc., 2017, pp. 65–83.
- [132] C. Nonis *et al.*, “Structural health monitoring of bridges using digital image correlation,” vol. 869507, no. April 2013, 2020, doi: 10.1117/12.2009647.
- [133] N. W. Gardner, M. W. Hilburger, W. T. Haynie, M. C. Lindell, and W. A. Waters, “Digital image correlation data processing and analysis techniques to enhance test data assessment and improve structural simulations,” *AIAA/ASCE/AHS/ASC Struct. Struct. Dyn. Mater. Conf. 2018*, no. 210049, pp. 1–16, 2018, doi: 10.2514/6.2018-1698.
- [134] N. McCormick and J. Lord, “Digital image correlation,” *Mater. Today*, vol. 13, no. 12, pp. 52–54, 2010, doi: 10.1016/S1369-7021(10)70235-2.
- [135] J. Peng, Y. Wang, Q. Dai, X. Liu, L. Liu, and Z. Zhang, “Effect of stress triaxiality on plastic damage evolution and failure mode for 316L notched specimen,” *Metals (Basel)*, vol. 9, no. 10, Oct. 2019, doi: 10.3390/met9101067.
- [136] J. Papisidero, V. Doquet, and D. Mohr, “Ductile fracture of aluminum 2024-T351 under proportional and non-proportional multi-axial loading: Bao-Wierzbicki results revisited,” *Int. J. Solids Struct.*, vol. 69–70, pp. 459–474, 2015, doi: 10.1016/j.ijsolstr.2015.05.006.
- [137] K. Wang, “Calibration Of The Johnson-Cook Failure Parameters As The Chip Separation Criterion In The Modelling Of The Orthogonal Metal Cutting Process,” 2016.
- [138] D. Gerbig, A. Bower, V. Savic, and L. G. Hector, “Coupling digital image correlation and finite element analysis to determine constitutive parameters in necking tensile specimens,” *Int. J. Solids Struct.*, vol. 97_98, pp. 496–509, Oct. 2016, doi: 10.1016/j.ijsolstr.2016.06.038.
- [139] M. Palanca, G. Tozzi, and L. Cristofolini, “The use of digital image correlation in the biomechanical area: A review,” *International Biomechanics*, vol. 3, no. 1. Taylor and Francis Ltd., pp. 1–21, 2016, doi: 10.1080/23335432.2015.1117395.
- [140] H. Quach, J. J. Kim, D. T. Nguyen, and Y. S. Kim, “Uncoupled ductile fracture criterion considering secondary void band behaviors for failure prediction in sheet metal forming,” *Int. J. Mech. Sci.*, vol. 169, Mar. 2020, doi: 10.1016/j.ijmecsci.2019.105297.

- [141] S. Yoneyama, “Basic principle of digital image correlation for in-plane displacement and strain measurement,” *Adv. Compos. Mater.*, vol. 25, no. 2, pp. 105–123, Mar. 2016, doi: 10.1080/09243046.2015.1129681.
- [142] H. A. Bruck, S. R. McNeill, M. A. Sutton, and W. H. Peters, “Digital image correlation using Newton-Raphson method of partial differential correction,” *Exp. Mech.*, vol. 29, no. 3, pp. 261–267, Sep. 1989, doi: 10.1007/BF02321405.
- [143] Daniel Shiffman, “Learning Processing 1st Edition,” 2008.
- [144] Will LePage, “DIC fundamentals.” <https://digitalimagecorrelation.org/> (accessed Jul. 05, 2021).
- [145] W. Tong, “An evaluation of digital image correlation criteria for strain mapping applications,” *Strain*, vol. 41, no. 4, pp. 167–175, 2005, doi: 10.1111/j.1475-1305.2005.00227.x.
- [146] B. Pan, H. Xie, and Z. Wang, “Equivalence of digital image correlation criteria for pattern matching,” *Appl. Opt.*, vol. 49, no. 28, pp. 5501–5509, 2010, doi: 10.1364/AO.49.005501.
- [147] B. Pan, “Digital image correlation for surface deformation measurement: Historical developments, recent advances and future goals,” *Meas. Sci. Technol.*, vol. 29, no. 8, 2018, doi: 10.1088/1361-6501/aac55b.
- [148] B. Pan, K. Qian, H. Xie, and A. Asundi, “Two-dimensional digital image correlation for in-plane displacement and strain measurement: A review,” *Meas. Sci. Technol.*, vol. 20, no. 6, 2009, doi: 10.1088/0957-0233/20/6/062001.
- [149] S. Yuan, *Digital Image Correlation and Edge Detection: Applications in Materials Testing*. 2014.
- [150] B. Pan, H. M. Xie, B. Q. Xu, and F. L. Dai, “Performance of sub-pixel registration algorithms in digital image correlation,” *Meas. Sci. Technol.*, vol. 17, no. 6, pp. 1615–1621, 2006, doi: 10.1088/0957-0233/17/6/045.
- [151] B. Pan, Z. Wang, and H. Xie, “Generalized spatial-gradient-based digital image correlation for displacement and shape measurement with subpixel accuracy,” *J. Strain Anal. Eng. Des.*, vol. 44, no. 8, pp. 659–669, 2009, doi: 10.1243/03093247JSA546.
- [152] R. Bigger *et al.*, “A Good Practices Guide for Digital Image Correlation,” Oct. 2018. doi: 10.32720/idics/gpg.ed1.
- [153] P. Reu, “Hidden Components of DIC: Calibration and Shape Function-Part 1,” 2012.
- [154] F. Trebuña, R. Huňady, M. Hagara, and I. Virgala, “High-speed Digital Image Correlation as a Tool for 3D Motion Analysis of Mechanical Systems,” vol. 3, no. 6, pp.

- 195–200, 2015, doi: 10.12691/ajme-3-6-8.
- [155] P. Mazzoleni, F. Matta, E. Zappa, M. A. Sutton, and A. Cigada, “Gaussian pre-filtering for uncertainty minimization in digital image correlation using numerically-designed speckle patterns,” *Opt. Lasers Eng.*, vol. 66, pp. 19–33, 2015, doi: 10.1016/j.optlaseng.2014.08.004.
- [156] P. Reu, “Stereo-rig design: Lens selection - Part 3,” *Exp. Tech.*, vol. 37, no. 1, pp. 1–3, 2013, doi: 10.1111/ext.12000.
- [157] Y. Wang, S. C. Garcea, and P. J. Withers, “7.6 Computed Tomography of Composites,” doi: 10.1016/B978-0-12-803581-8.10250-4.
- [158] L. S. Athanasiou, D. I. Fotiadis, and L. K. Michalis, “Propagation of Segmentation and Imaging System Errors,” in *Atherosclerotic Plaque Characterization Methods Based on Coronary Imaging*, Elsevier, 2017, pp. 151–166.
- [159] P. Reu, “Stereo-rig Design : Stereo-Angle Selection — Part 4,” vol. 37, pp. 1–2, 2013.
- [160] P. Zhou, “Subpixel displacement and deformation gradient measurement using digital image/speckle correlation (DISC),” *Opt. Eng.*, vol. 40, no. 8, p. 1613, Aug. 2001, doi: 10.1117/1.1387992.
- [161] G. Stoilov, V. Kavardzhikov, and D. Pashkouleva, “A Comparative Study of Random Patterns for Digital Image Correlation,” *J. Theor. Appl. Mech.*, vol. 42, no. 2, pp. 55–66, Jun. 2012, doi: 10.2478/v10254-012-0008-x.
- [162] P. Reu, “Speckles and their relationship to the digital camera,” *Exp. Tech.*, vol. 38, no. 4, pp. 1–2, 2014, doi: 10.1111/ext.12105.
- [163] P. Reu, “All about speckles: Aliasing,” *Exp. Tech.*, vol. 38, no. 5, pp. 1–3, 2014, doi: 10.1111/ext.12111.
- [164] P. Reu, “All about speckles: Speckle Size Measurement,” *Exp. Tech.*, vol. 38, no. 6, pp. 1–2, Nov. 2014, doi: 10.1111/ext.12110.
- [165] P. L. Reu, W. Sweatt, T. Miller, and D. Fleming, “Camera System Resolution and its Influence on Digital Image Correlation,” *Exp. Mech.*, vol. 55, no. 1, pp. 9–25, Jan. 2015, doi: 10.1007/s11340-014-9886-y.
- [166] Andor, “Essential overview of ccd spatial resolution,” *Oxford Instrum. Gr.*, pp. 0–2, 2020, [Online]. Available: <https://andor.oxinst.com/learning/view/article/ccd-spatial-resolution>.
- [167] Y. H. Wang *et al.*, “Whole field sheet-metal tensile test using digital image correlation,” *Exp. Tech.*, vol. 34, no. 2, pp. 54–59, Mar. 2010, doi: 10.1111/j.1747-1567.2009.00483.x.

- [168] B. Pan, H. Xie, Z. Wang, K. Qian, and Z. Wang, "Study on subset size selection in digital image correlation for speckle patterns," *Opt. Express*, vol. 16, no. 10, p. 7037, 2008, doi: 10.1364/oe.16.007037.
- [169] P. Reu, "All about speckles: Speckle density," *Exp. Tech.*, vol. 39, no. 3, pp. 1–2, 2015, doi: 10.1111/ext.12161.
- [170] P. Reu, "All about Speckles: Edge Sharpness," 2015. doi: 10.1111/ext.12139.
- [171] Y. L. Dong and B. Pan, "A Review of Speckle Pattern Fabrication and Assessment for Digital Image Correlation," *Exp. Mech.*, vol. 57, no. 8, pp. 1161–1181, Oct. 2017, doi: 10.1007/s11340-017-0283-1.
- [172] F. M. Sánchez-Arévalo and G. Pulos, "Use of digital image correlation to determine the mechanical behavior of materials," *Mater. Charact.*, vol. 59, no. 11, pp. 1572–1579, 2008, doi: 10.1016/j.matchar.2008.02.002.
- [173] M. Ashrafi and M. E. Tuttle, "Measurement of Strain Gradients Using Digital Image Correlation by Applying Printed-Speckle Patterns," *Exp. Tech.*, p. n/a-n/a, Feb. 2015, doi: 10.1111/ext.12145.
- [174] P. Reu, "Points on Paint," *Exp. Tech.*, vol. 39, no. 4, pp. 1–2, 2015, doi: 10.1111/ext.12147.
- [175] P. Reu, "Stereo-rig design: Creating the STEREO-RIG LAYOUT - PART 1," *Exp. Tech.*, vol. 36, no. 5, pp. 3–4, 2012, doi: 10.1111/j.1747-1567.2012.00871.x.
- [176] R. Huňady, M. Hagara, and M. Kalina, "The aspects of strain fields' measurement performed on small surfaces using digital image correlation method," *EAN 2014 - 52nd Int. Conf. Exp. Stress Anal.*, no. June, 2014.
- [177] VIKTOR ELIZAROV, "The Exposure Triangle: Making Sense of Aperture, Shutter Speed, and ISO." <https://petapixel.com/2017/03/25/exposure-triangle-making-sense-aperture-shutter-speed-iso/>.
- [178] D. Measurements, "Chapter 7 Stereo-vision System Applications," no. 2009, 2021.
- [179] P. Reu, "Calibration: Stereo Calibration," *Exp. Tech.*, vol. 38, no. 1, pp. 1–2, 2014, doi: 10.1111/ext.12048.
- [180] P. Reu, "Calibration : Care and Feeding of a Stereo-rig," vol. 38, pp. 1–2, 2014.
- [181] D. Lecompte *et al.*, "Quality assessment of speckle patterns for digital image correlation," *Opt. Lasers Eng.*, vol. 44, no. 11, pp. 1132–1145, Nov. 2006, doi: 10.1016/j.optlaseng.2005.10.004.
- [182] M. Bornert *et al.*, "Assessment of digital image correlation measurement errors: Methodology and results," *Exp. Mech.*, vol. 49, no. 3, pp. 353–370, 2009, doi:

- 10.1007/s11340-008-9204-7.
- [183] H. Haddadi and S. Belhabib, “Use of rigid-body motion for the investigation and estimation of the measurement errors related to digital image correlation technique,” *Opt. Lasers Eng.*, vol. 46, no. 2, pp. 185–196, 2008, doi: 10.1016/j.optlaseng.2007.05.008.
- [184] P. Reu, “Calibration: A good calibration image,” *Exp. Tech.*, vol. 37, no. 6, pp. 1–3, 2013, doi: 10.1111/ext.12059.
- [185] M. Jerabek, Z. Major, and R. W. Lang, “Strain determination of polymeric materials using digital image correlation,” *Polym. Test.*, vol. 29, no. 3, pp. 407–416, 2010, doi: 10.1016/j.polymertesting.2010.01.005.
- [186] M. A. Sutton, J. H. Yan, V. Tiwari, H. W. Schreier, and J. J. Orteu, “The effect of out-of-plane motion on 2D and 3D digital image correlation measurements,” *Opt. Lasers Eng.*, vol. 46, no. 10, pp. 746–757, 2008, doi: 10.1016/j.optlaseng.2008.05.005.
- [187] O. Angel, G. Rothwell, R. English, J. Ren, and A. Cummings, “Effect of post processing of digital image correlation on obtaining accurate true stress-strain data for AISI 304L,” *Nucl. Eng. Technol.*, no. xxxx, 2022, doi: 10.1016/j.net.2022.03.038.
- [188] K. Zhao, L. Wang, Y. Chang, and J. Yan, “Identification of post-necking stress-strain curve for sheet metals by inverse method,” *Mech. Mater.*, vol. 92, pp. 107–118, Jan. 2016, doi: 10.1016/j.mechmat.2015.09.004.
- [189] M. S. Joun, J. G. Eom, and M. C. Lee, “A new method for acquiring true stress-strain curves over a large range of strains using a tensile test and finite element method,” *Mech. Mater.*, vol. 40, no. 7, pp. 586–593, Jul. 2008, doi: 10.1016/j.mechmat.2007.11.006.
- [190] L. Wang and W. Tong, “Identification of post-necking strain hardening behavior of thin sheet metals from image-based surface strain data in uniaxial tension tests,” *Int. J. Solids Struct.*, vol. 75–76, pp. 12–31, Dec. 2015, doi: 10.1016/j.ijsolstr.2015.04.038.
- [191] M. Kamaya and M. Kawakubo, “A procedure for determining the true stress-strain curve over a large range of strains using digital image correlation and finite element analysis,” doi: 10.1016/j.mechmat.2011.02.007.
- [192] J. Li, G. Yang, T. Siebert, M. F. Shi, and L. Yang, “A method of the direct measurement of the true stress–strain curve over a large strain range using multi-camera digital image correlation,” *Opt. Lasers Eng.*, vol. 107, pp. 194–201, Aug. 2018, doi: 10.1016/j.optlaseng.2018.03.029.
- [193] P. D. Versaillot *et al.*, “Experimental study on the evolution of necking zones of metallic materials,” *Int. J. Mech. Sci.*, vol. 189, p. 106002, Jan. 2021, doi:

- 10.1016/j.ijmecsci.2020.106002.
- [194] F. Zhu, P. Bai, J. Zhang, D. Lei, and X. He, “Measurement of true stress-strain curves and evolution of plastic zone of low carbon steel under uniaxial tension using digital image correlation,” *Opt. Lasers Eng.*, vol. 65, pp. 81–88, Feb. 2015, doi: 10.1016/j.optlaseng.2014.06.013.
- [195] H. C. Ho, K. F. Chung, X. Liu, M. Xiao, and D. A. Nethercot, “Modelling tensile tests on high strength S690 steel materials undergoing large deformations,” *Eng. Struct.*, vol. 192, no. November 2018, pp. 305–322, 2019, doi: 10.1016/j.engstruct.2019.04.057.
- [196] S. Yaofeng and J. H. L. Pang, “Study of optimal subset size in digital image correlation of speckle pattern images,” *Opt. Lasers Eng.*, vol. 45, no. 9, pp. 967–974, 2007, doi: 10.1016/j.optlaseng.2007.01.012.
- [197] J. Baldoni, G. Lionello, F. Zama, and L. Cristofolini, “Comparison of different filtering strategies to reduce noise in strain measurement with digital image correlation,” *J. Strain Anal. Eng. Des.*, vol. 51, no. 6, pp. 416–430, 2016, doi: 10.1177/0309324716646690.
- [198] R. K. Blandford, D. K. Morton, S. D. Snow, and T. E. Rahl, “Tensile Stress-Strain Results for 304L and 316L Stainless Steel Plate at Temperature 2007 ASME Pressure Vessels and Piping Division Conference TENSILE STRESS-STRAIN RESULTS FOR 304L AND 316L STAINLESS STEEL 1 PLATE AT TEMPERATURE,” 2007.
- [199] British Standards Institution, “BSI Standards Publication Testing hardened concrete,” no. April, p. 18, 2019.
- [200] B. Hutchinson, “Critical assessment 16: Anisotropy in metals,” *Mater. Sci. Technol. (United Kingdom)*, vol. 31, no. 12, pp. 1393–1401, 2015, doi: 10.1179/1743284715Y.0000000118.
- [201] R. Wouters and L. Froyen, “Scanning electron microscope fractography in failure analysis of steels,” *Mater. Charact.*, vol. 36, no. 4–5, pp. 357–364, 1996, doi: 10.1016/s1044-5803(96)00070-8.
- [202] A. C. Mackenzie, J. W. Hancock, and D. K. Brown, “On the influence of state of stress on ductile failure initiation in high strength steels,” *Eng. Fract. Mech.*, vol. 9, no. 1, 1977, doi: 10.1016/0013-7944(77)90062-5.
- [203] C. C. Roth and D. Mohr, “Determining the strain to fracture for simple shear for a wide range of sheet metals,” *Int. J. Mech. Sci.*, vol. 149, no. July, pp. 224–240, 2018, doi: 10.1016/j.ijmecsci.2018.10.007.
- [204] T. Container and S. Committee, “Transport of Radioactive Material Code of Practice,” *Transport*, no. December, p. 140, 2002.

- [205] S. Qu *et al.*, “Tensile and compressive properties of AISI 304L stainless steel subjected to equal channel angular pressing,” *Mater. Sci. Eng. A*, vol. 475, no. 1–2, pp. 207–216, 2008, doi: 10.1016/j.msea.2007.04.111.
- [206] S. Rout, Matruprasad & Biswas, Somjeet & Ranjan, Ravi & Pal, Surjya & Singh, “Deformation Behavior and Evolution of Microstructure and Texture During Hot Compression of AISI 304LN Stainless Steel,” *Metall. Mater. Trans. A*, vol. 49, pp. 864–880, 2018.
- [207] ASTM, “E3-11 Standard Guide for Preparation of Metallographic Specimens 1,” *ASTM Copyright.*, vol. i, no. Reapproved, pp. 1–12, 2011, doi: 10.1520/E0003-11.2.
- [208] T. Wierzbicki, “Email Correspondence,” 2021.
- [209] H. Davis, *Creative Composition. Digital Photography Tips & Techniques*. 2010.
- [210] A. Rowlands, *Exposure strategy*. 2017.
- [211] H. J. Kamps, *Macro Photography Photo Workshop*. John Wiley & Sons In, 2011.

Appendix

Appendix A - Fracture Locus for a Range of Materials

Specimen Description	Material	Testing Data from	Year	Stress Triaxiality	Equivalent strain to fracture
1.Bi-axial Compression	AL2024-T351	Khan, Lui	2012	-0.4960	0.3490
2.Cylinder D/H =0.5		Y Bao, T. Wierzbicki	2003	-0.2780	0.4505
3.Round Notched, Compression				-0.2476	0.6217
4.Cylinder D/H=0.8				-0.2339	0.3800
5. Cylinder D/H=1				-0.2326	0.3563
6. Cylinder D/H=1.5				-0.2235	0.3410
7. Pure Shear, Flat Plate				0.0124	0.2107
8.Shear and Tension, Flat Plate				0.1173	0.2613
9.D9-Test (Smooth and Notched Round Bar)	1045 Steel	Yuanli Bai, Xiaoqing Teng, Tomasz Wierzbicki	2009	0.3333	0.4242
10.D9-Test A (Smooth and Notched Round Bar)				0.3333	0.4269
11.Plate with a Circular Hole	AL2024-T351	Y Bao, T. Wierzbicki	2003	0.3431	0.3099
12.Round, Pipe				0.3557	0.3255
13.Solid Square Bar				0.3687	0.3551
14.Dog-bone				0.3750	0.4798
15.Dog-bone	TRIP690 Steel	Y Bai, T. Wierzbicki	2009	0.3790	0.7510
16.Smooth Round Bar	AL2024-T351	Y Bai, T. Wierzbicki	2003	0.4041	0.4687
17.Flat Specimen with Cutouts	TRIP690 Steel	Y Bai, T. Wierzbicki	2009	0.4720	0.3940
18.D9-Simulation (Smooth and Notched Round Bar)	1045 Steel		2009 2009	0.5044	0.4892

19.R10.5-test B (Smooth and Notched Round Bar)		Yuanli Bai, Xiaoqing Teng, Tomasz Wierzbicki	2009	0.5513	0.2542
20.R10.5-test A (Smooth and Notched Round Bar)				0.5513	0.2589
21.Butterfly Specimen, Tension	TRIP690 Steel	Y Bai, T. Wierzbicki	2009	0.5770	0.4600
22.Flat Grooved	AL2024-T351	Y Bao, T. Wierzbicki	2003	0.6030	0.2100
23.R12.7-test C	1045 Steel	Yuanli Bai, Xiaoqing Teng, Tomasz Wierzbicki	2009	0.6061	0.1137
24.R12.7-test B			2009	0.6105	0.1321
25.R12.7-test A			2009	0.6136	0.1441
26.Round large, notched bar	AL2024-T351	Y Bao, T. Wierzbicki	2003	0.6264	0.2830
27.Equi-biaxial Tension, Disk Specimen	TRIP690 Steel	Y Bai, T. Wierzbicki	2009	0.6670	0.9500
28.R12.7-test A simulation	1045 Steel	Yuanli Bai, Xiaoqing Teng, Tomasz Wierzbicki	2009	0.6705	0.2184
29.R3.97-test B	1045 Steel	Yuanli Bai, Xiaoqing Teng, Tomasz Wierzbicki	2009	0.6842	0.1101
30.R3.97-test A	1045 Steel	Yuanli Bai, Xiaoqing Teng, Tomasz Wierzbicki	2009	0.6849	0.1101
31.R3.97-test A simulation	1045 Steel	Yuanli Bai, Xiaoqing Teng, Tomasz Wierzbicki	2009	0.7799	0.1765
32.R10.5-simulation (Smooth and Notched Round Bar)	1045 Steel	Yuanli Bai, Xiaoqing Teng, Tomasz Wierzbicki	2009	0.8130	0.2312
33.R1.59-test A	1045 Steel	Yuanli Bai, Xiaoqing Teng, Tomasz Wierzbicki	2009	0.8365	0.0669

34.R1.59-test B	1045 Steel	Yuanli Bai, Xiaoqing Teng, Tomasz Wierzbicki	2009	0.8523	0.0768
35.Round Small Notched Bar	AL2024-T351	Y Bao, T. Wierzbicki	2003	0.9274	0.1665
36.R1.59-test B simulation	1045 Steel	Yuanli Bai, Xiaoqing Teng, Tomasz Wierzbicki	2009	1.0237	0.1005

Appendix B - Design of DIC Measurement

Measurement Requirements		
Name:	Definition:	Equations:
Quantity of Interest (QOI)	The results required during testing this could be displacement, strain etc.	
Region of Interest (ROI)	This is the selected region of the specimen in which any motion or deformation is expected. This may be specific part of the whole specimen.	
Stereo Angle (α)	The angle between the two camera axes and the baseline. Baseline is the known distance between optical centres of the cameras [159].	$\alpha = 2 \sin^{-1}\left(\frac{Baseline}{2D}\right)$
Field of View (FOV/L_{FOV})	Region of space which is shown when projected through a lens system onto a camera detector. In order to determine the necessary FOV, the ROI should almost fill the FOV.	$L_{FOV} = L_{CS} \left(\frac{L_{SOD} - L_{FL}}{L_{FL}} \right)$
Depth-of-Field (DOF)	Is defined as the distance behind and in front of the subject that is in focus. Lens selection and aperture directly affects the DOF [209]. The DOF is needed to ensure that the ROI remains in focus for the duration of the test, whilst taking into account out of plane motion and the stereo angle.	
Stand-off Distance (D) (SOD/L_{SOD})	The distance between the aperture of the lens and the specimen.	$L_{SOD} = L_{FL} \left(\frac{L_{FOV}}{L_{CS}} + 1 \right)$

Noise floor	Defined as the signal noise due to the electronic readout circuitry. Noise will be present regardless of any light intensity exposure [210].
Frame Rate	The cameras capture individual frames for a video, the amount of frames that the camera captures per second is known as the frame rate, which is measured in fps.
Exposure Time	Also known as shutter speed, is the length of time in which the camera shutter is open, exposing light onto the camera sensor.

Other measurements of interest The mechanical test must be synchronised with the DIC images for parameters such as, force and strain gauges. Also, data acquisitions must be triggered at the start of the testing [152].

Equipment Selection

Camera and Lens FOV, lens and camera selection all directly affect one another. Cameras are optical devices used to capture and record images. Lens are tools utilised to bring the light to a fixed focal point. Camera lenses are constructed from a series of glass plates that are convex or concave. Lens are defined by three characteristics: focal length, aperture and resolution.

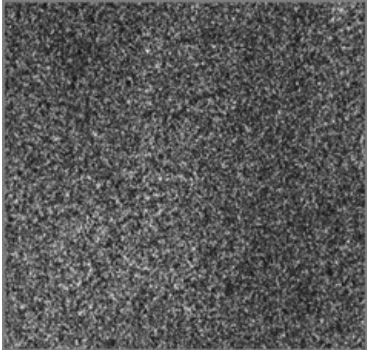
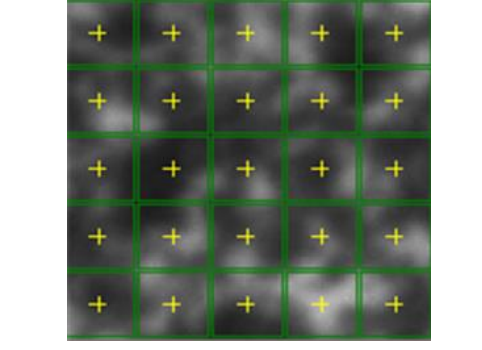
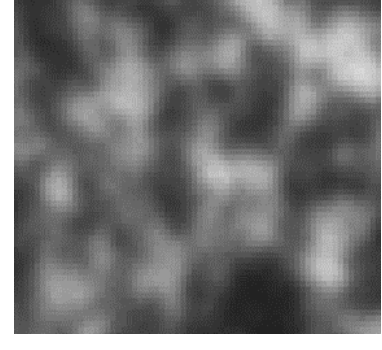
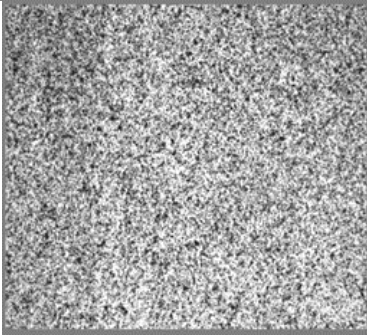
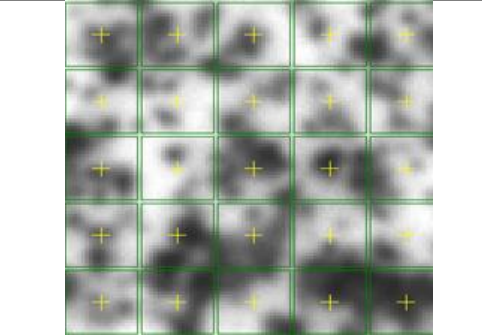
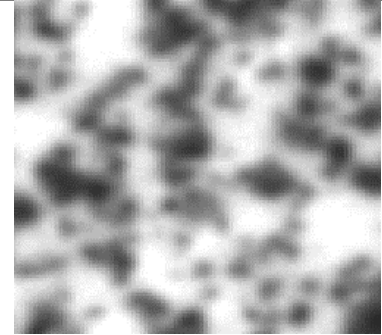
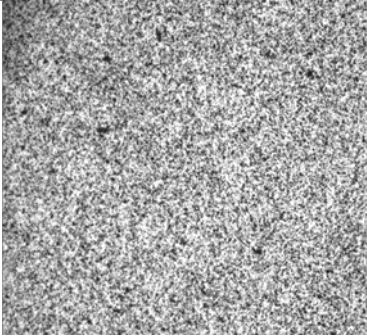
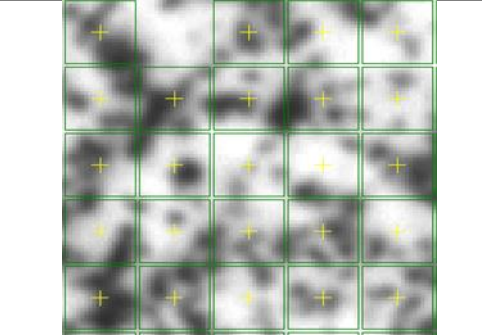
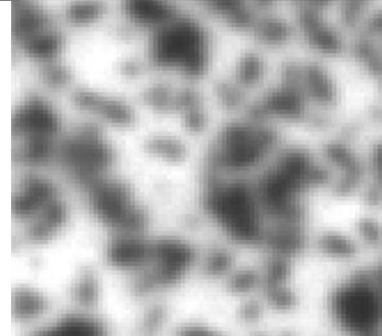
Lens Resolution: is the necessary resolving power of the lens which can be related to the pixel size of the selected camera [156].

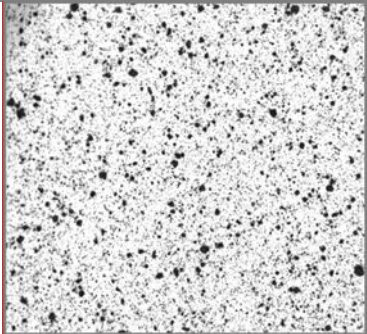
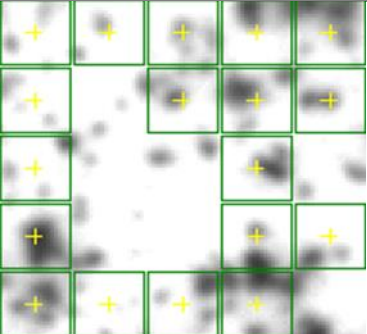
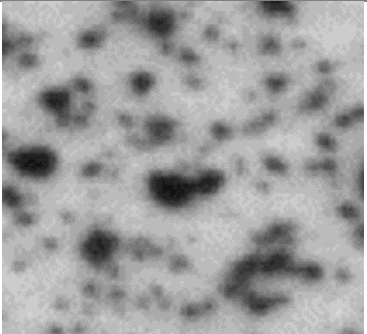
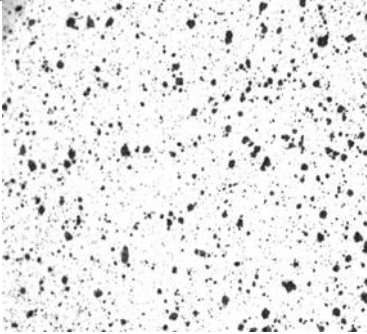
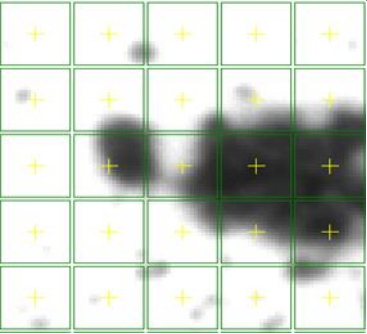
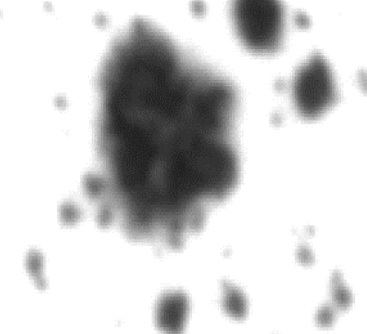
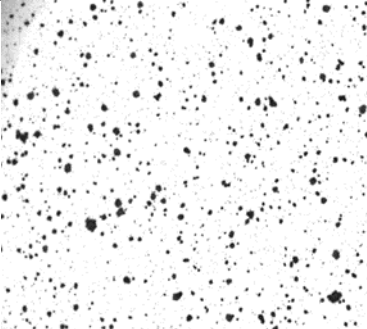
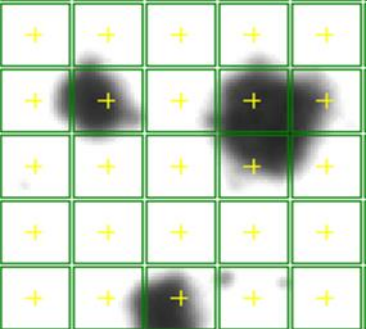
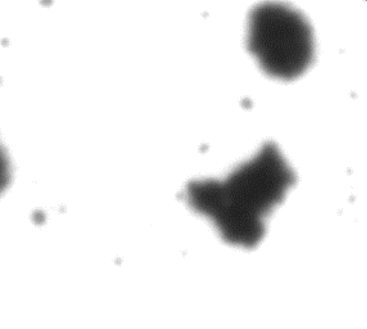
$$Res = \frac{1}{2 * Pixel\ size\ (mm)}$$

	<p>Camera chip size (L_{CS}): is also known as a chip sensor, it is the section of a camera that's sensitive to light and it is able to record an image when active.</p>
	<p>Focal Length (L_{FL}): measure of the magnification power of the lens. <i>Example: The larger the focal length the bigger the magnification</i> [156].</p>
	<p>Aperture: works as the iris within the lens, which can be used to determine the amount of light that reaches the detector [156].</p>
Extension Tubes	<p>Tubing that can be fitted to the camera and to the lens. They can act as a lens with different sizes providing different magnifications [211].</p>
Lighting	<p>Additional lighting may be needed for good contrast for a given aperture and exposure time. This must be evenly distributed onto the specimen to obtain data.</p>
Specimen Pattern	<p>In order for the DIC algorithms to work they require a pattern, consisting of random speckles.</p>
Calibration Target	<p>A calibration target contains known points or corners that are located as special targets. The pattern on the calibration board may be taken as an image, at the specimen location with different tilting directions in order to triangulate a stereo rig set up [167].</p>

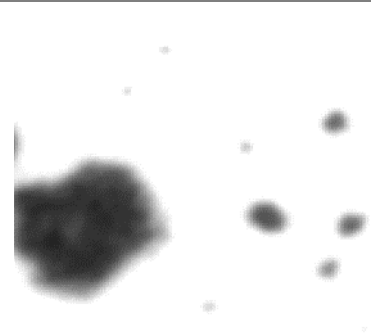
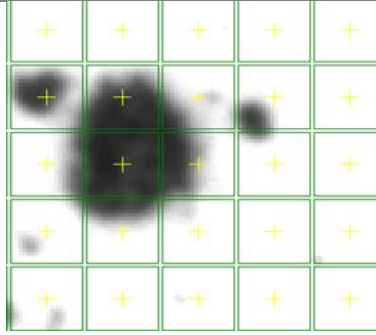
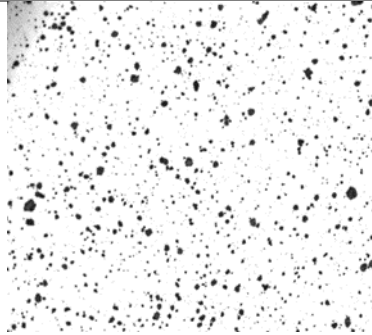
Appendix C – Speckle Pattern Test

In this study speckle pattern was applied using spray paints. To demonstrate finding the optimum speckle pattern 9 different speckles were produced using spray paints, as shown in the setup in Figure 3.21. The set up used the following: 50 mm lens + 20mm Extension Tubes, $D = 0.3$ m, $FOV = 0.02$ m. The different speckle patterns shown in the Table below have a range of contrast, size and speckle edge and density. The DIC system was correlated in order to show the matched subsets of a pattern. The subset size for this comparison was kept at 21x21 throughout.

No.	Speckle Pattern	Grid of Matched Subsets	Pattern showing Pixels	Comments
1				<p>Speckle size too large.</p> <p>Speckle edge and density is optimum.</p>
2				<p>Speckle size is slightly bigger than ideal.</p> <p>Sharper speckle edge and pattern is evenly distributed.</p>
3				<p>Slightly less contrast to speckle pattern number 2.</p> <p>Speckle size is slightly bigger than ideal.</p> <p>Sharper speckle edge.</p>

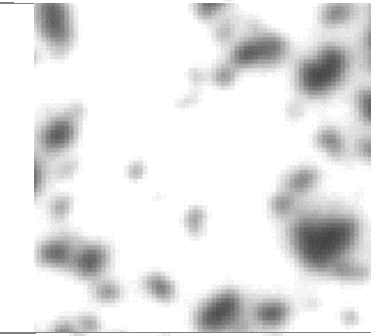
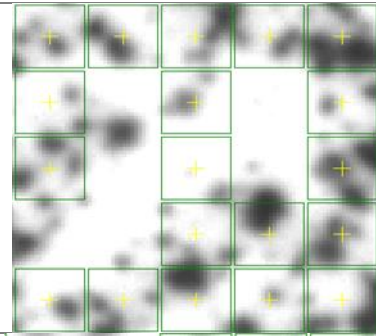
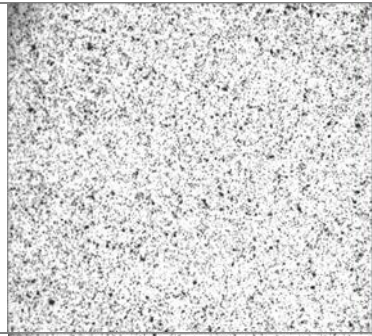
4				<p>The pattern was missing a lot of data points where the grey levels were 255.</p>
5				<p>Not enough speckles. Therefore, the subsets did not evaluate for this pattern.</p> <p>Speckle size is large</p>
6				<p>The subsets did not evaluate for this pattern.</p> <p>Similar speckle properties to speckle number 5, but with less density.</p>

7



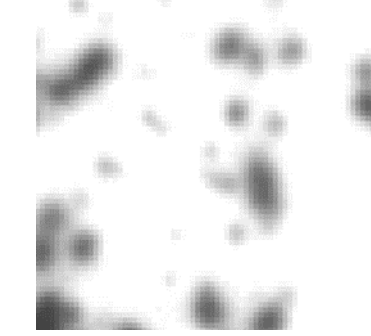
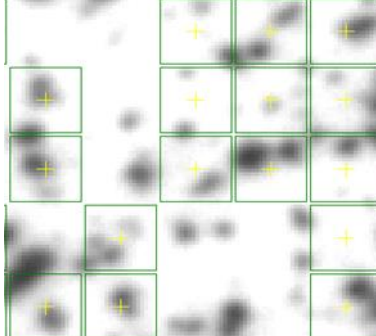
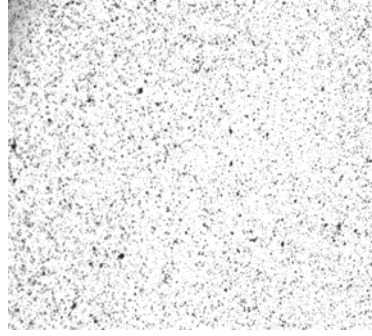
Same properties as pattern number 6

8



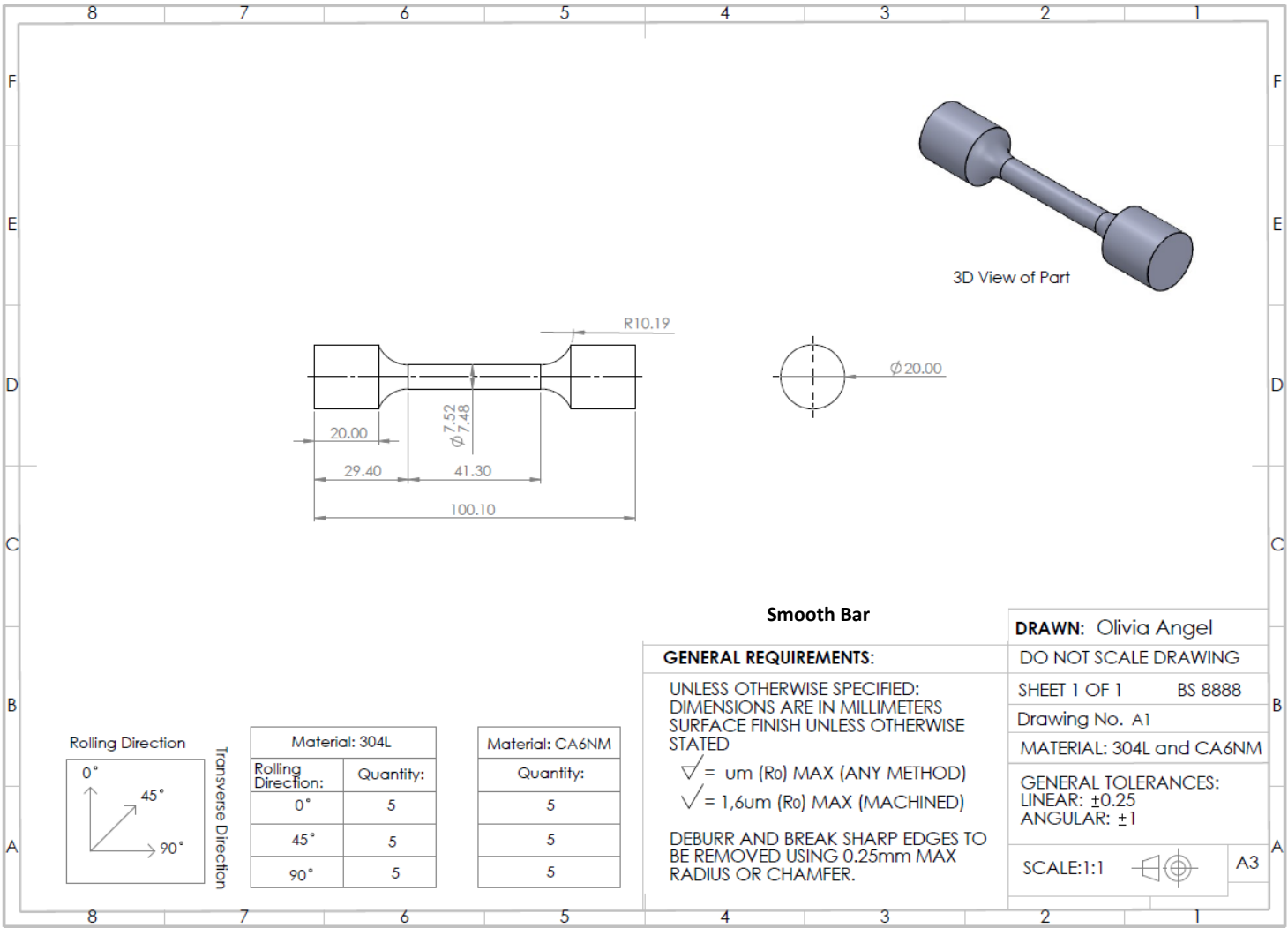
Uneven Speckle size and patterns density is too low, leading to areas unable to be matched.

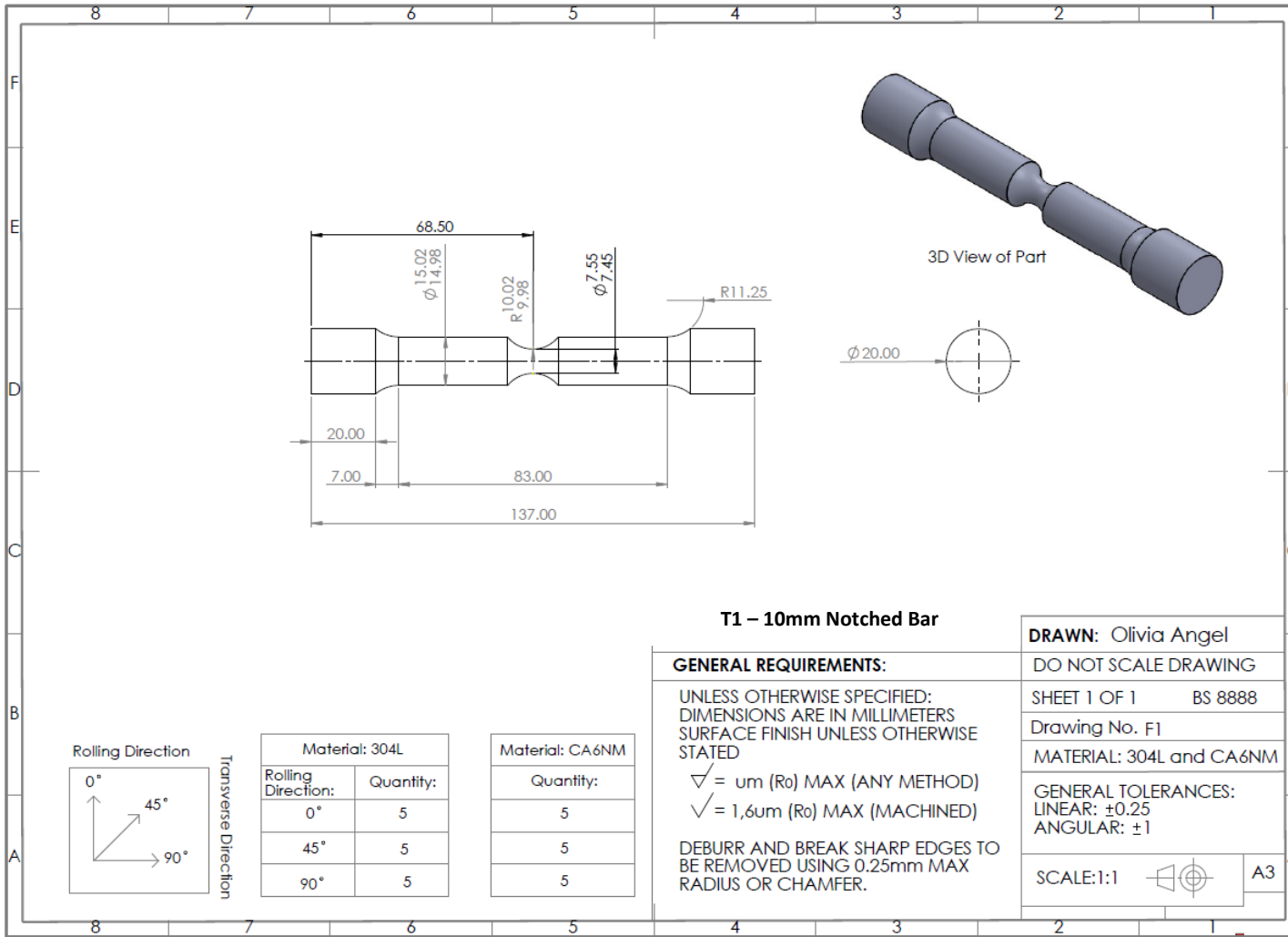
9

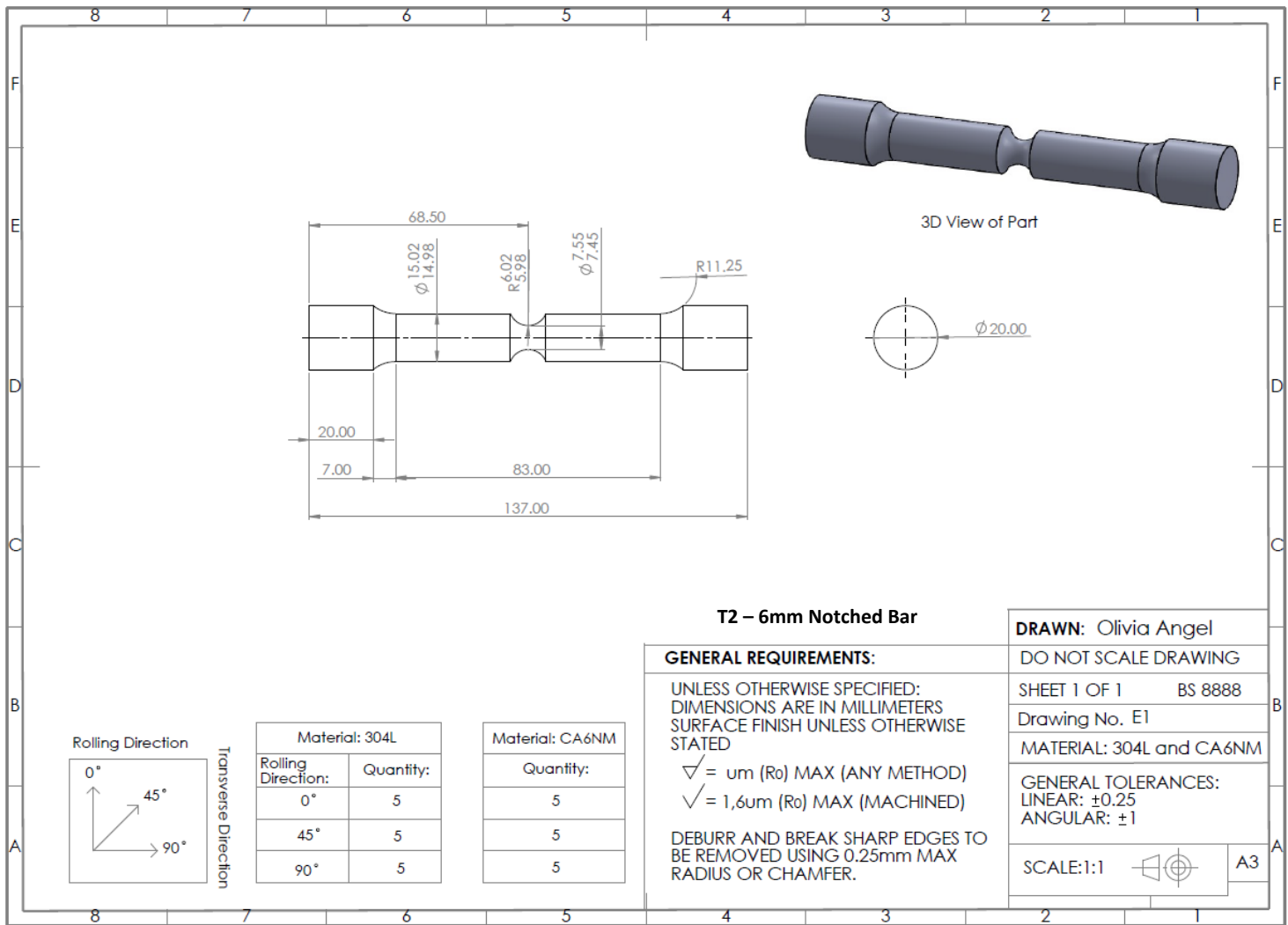


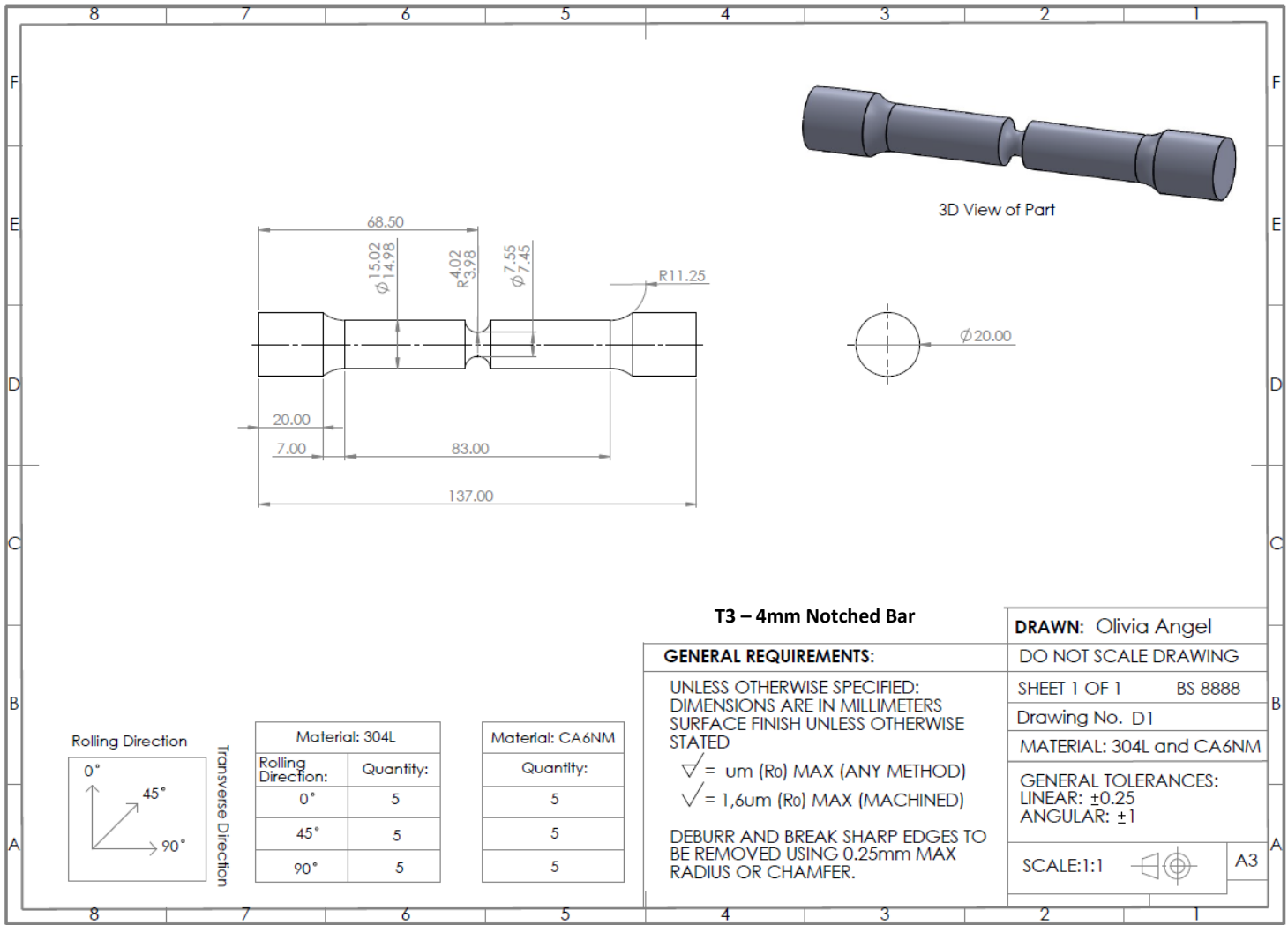
Did evaluate however, the majority of the pattern was missing. This was caused by the contrast and density.

Appendix D – Engineering Drawings

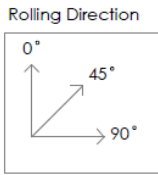








T3 – 4mm Notched Bar



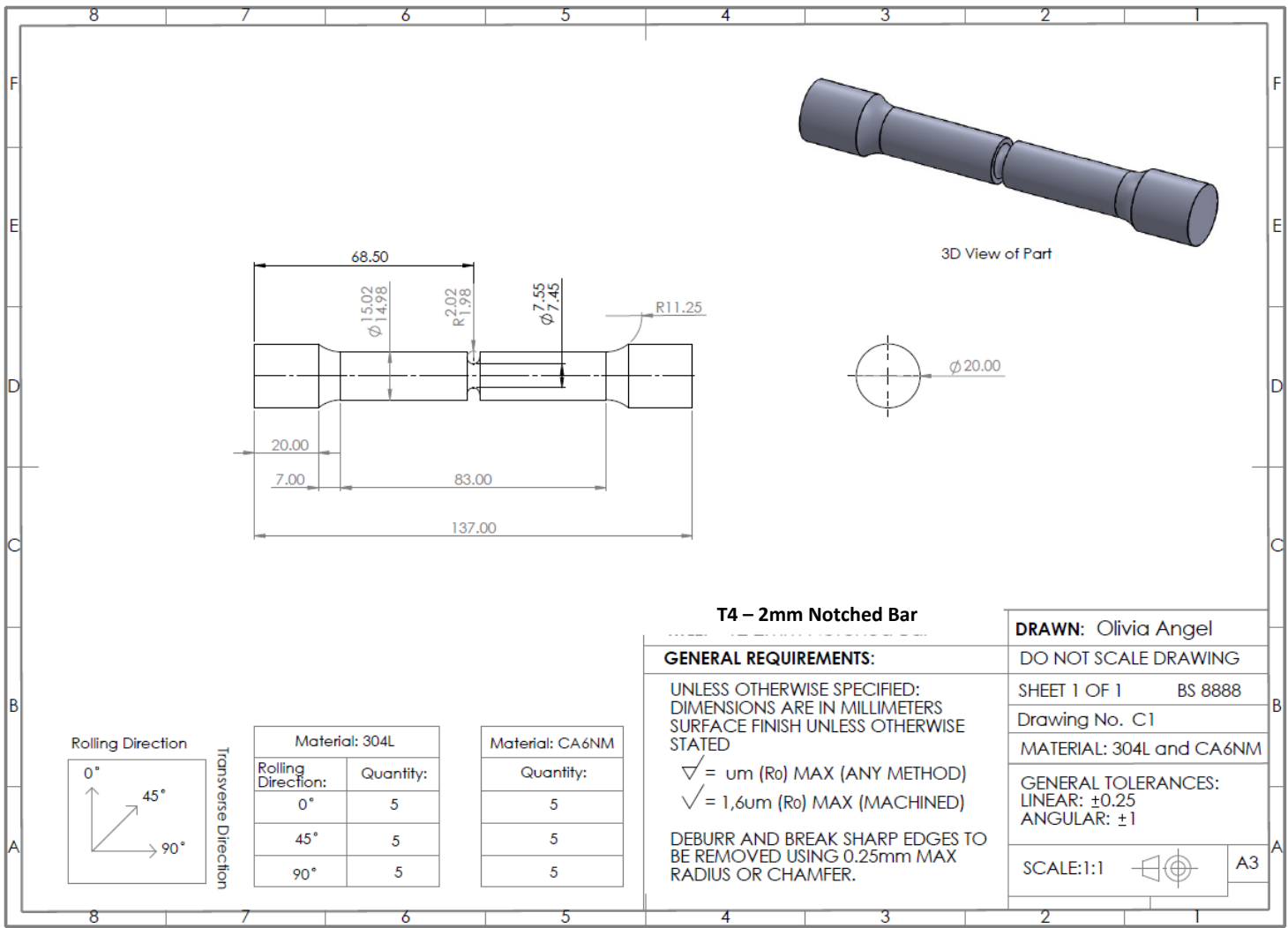
Material: 304L		Material: CA6NM	
Rolling Direction:	Quantity:	Quantity:	
0°	5	5	
45°	5	5	
90°	5	5	

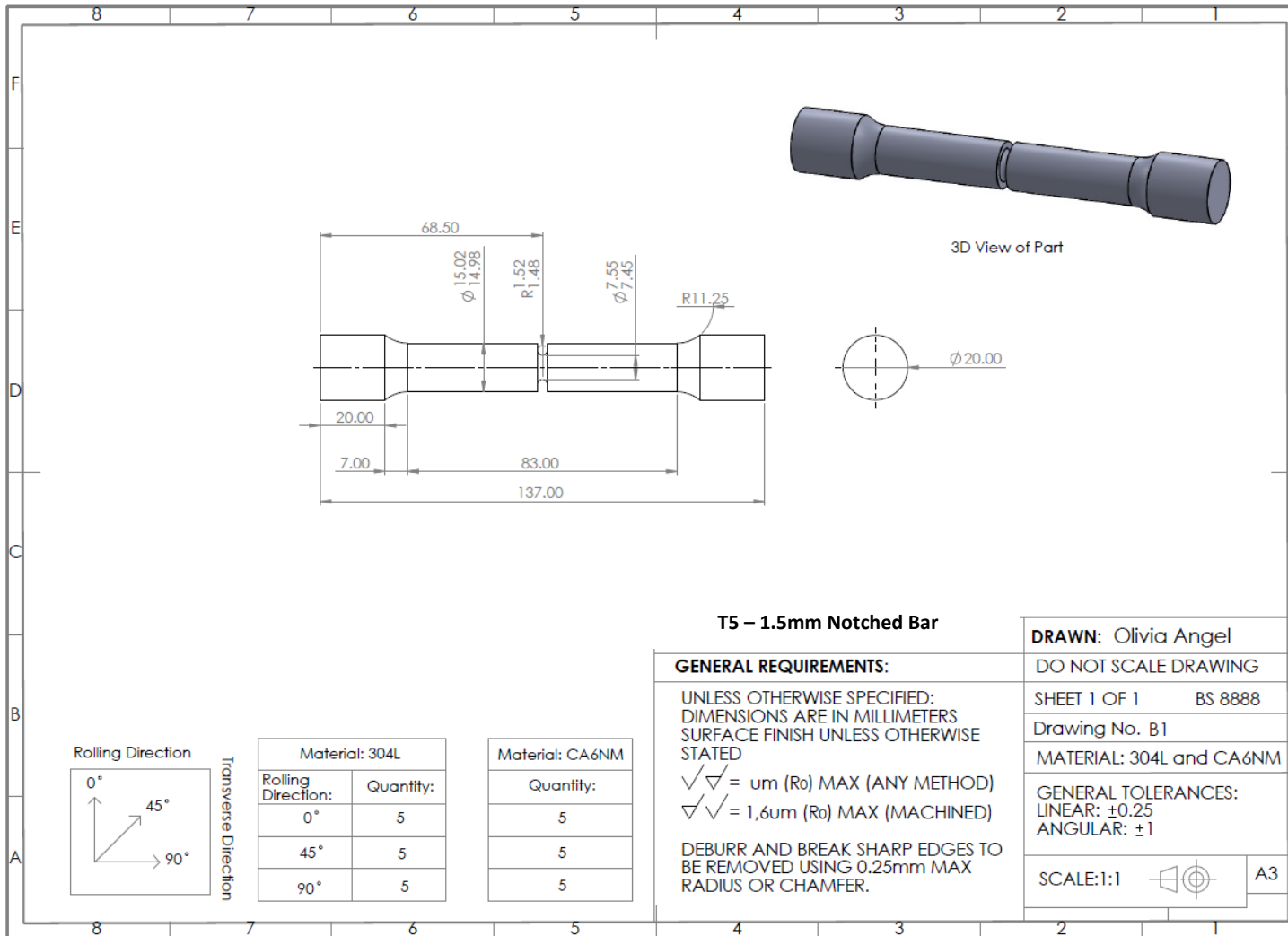
GENERAL REQUIREMENTS:
 UNLESS OTHERWISE SPECIFIED:
 DIMENSIONS ARE IN MILLIMETERS
 SURFACE FINISH UNLESS OTHERWISE STATED

✓ = μm (Ro) MAX (ANY METHOD)
 ✓ = 1,6 μm (Ro) MAX (MACHINED)

DEBURR AND BREAK SHARP EDGES TO BE REMOVED USING 0.25mm MAX RADIUS OR CHAMFER.

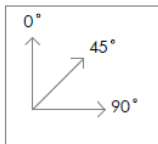
DRAWN: Olivia Angel
DO NOT SCALE DRAWING
SHEET 1 OF 1 BS 8888
Drawing No. D1
MATERIAL: 304L and CA6NM
GENERAL TOLERANCES: LINEAR: ± 0.25 ANGULAR: ± 1
SCALE: 1:1 A3





T5 – 1.5mm Notched Bar

Rolling Direction



Transverse Direction

Material: 304L	
Rolling Direction:	Quantity:
0°	5
45°	5
90°	5

Material: CA6NM	
Quantity:	
5	
5	
5	

GENERAL REQUIREMENTS:

UNLESS OTHERWISE SPECIFIED:
DIMENSIONS ARE IN MILLIMETERS
SURFACE FINISH UNLESS OTHERWISE STATED

- ✓✓ = um (Ro) MAX (ANY METHOD)
- ✓✓ = 1,6um (Ro) MAX (MACHINED)

DEBURR AND BREAK SHARP EDGES TO BE REMOVED USING 0.25mm MAX RADIUS OR CHAMFER.

DRAWN: Olivia Angel

DO NOT SCALE DRAWING

SHEET 1 OF 1 BS 8888

Drawing No. B1

MATERIAL: 304L and CA6NM

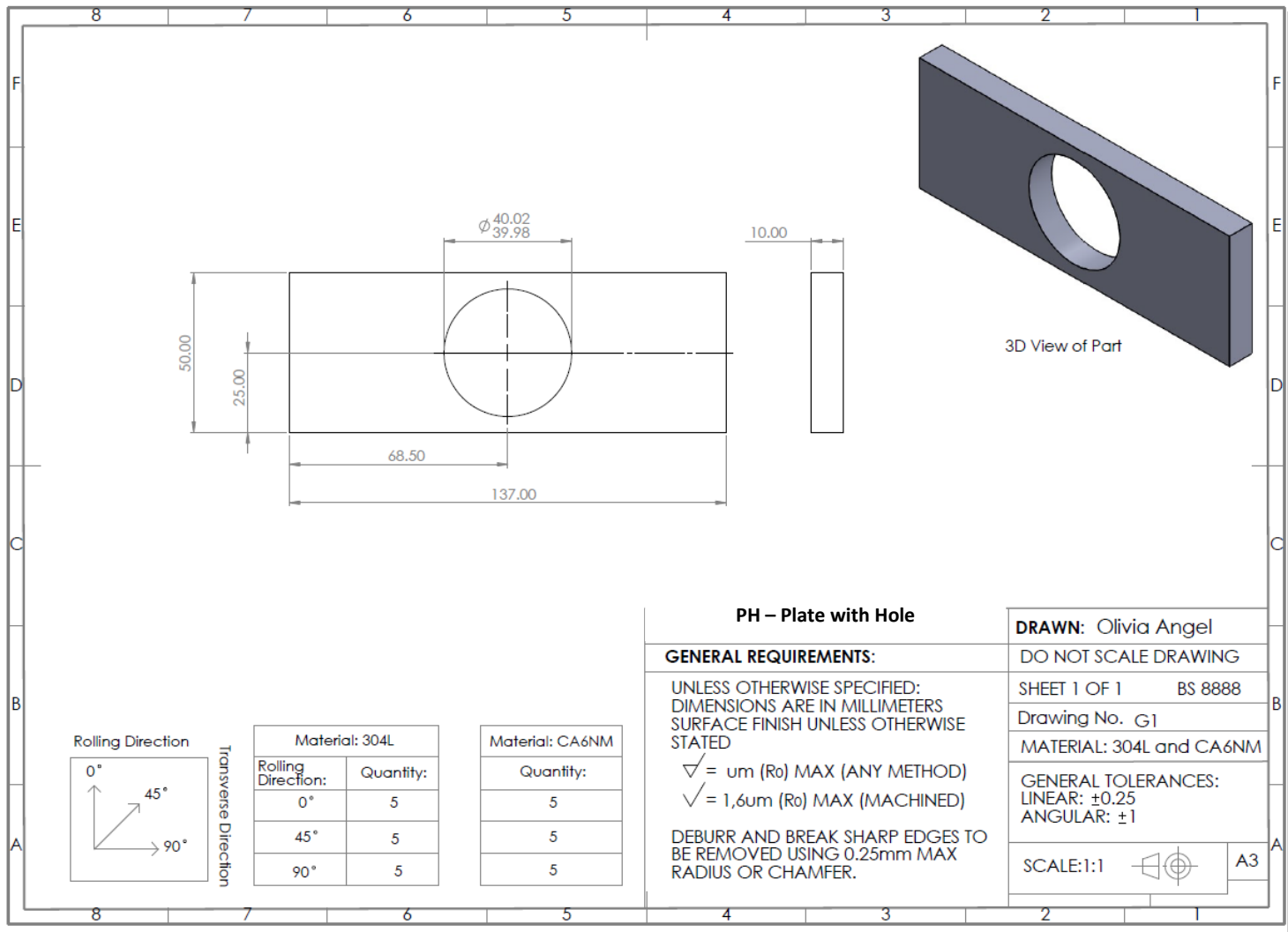
GENERAL TOLERANCES:

LINEAR: ±0.25
ANGULAR: ±1

SCALE: 1:1



A3



PH – Plate with Hole

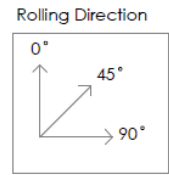
GENERAL REQUIREMENTS:

UNLESS OTHERWISE SPECIFIED:
 DIMENSIONS ARE IN MILLIMETERS
 SURFACE FINISH UNLESS OTHERWISE
 STATED

- √ = μm (Ro) MAX (ANY METHOD)
- √ = 1,6 μm (Ro) MAX (MACHINED)

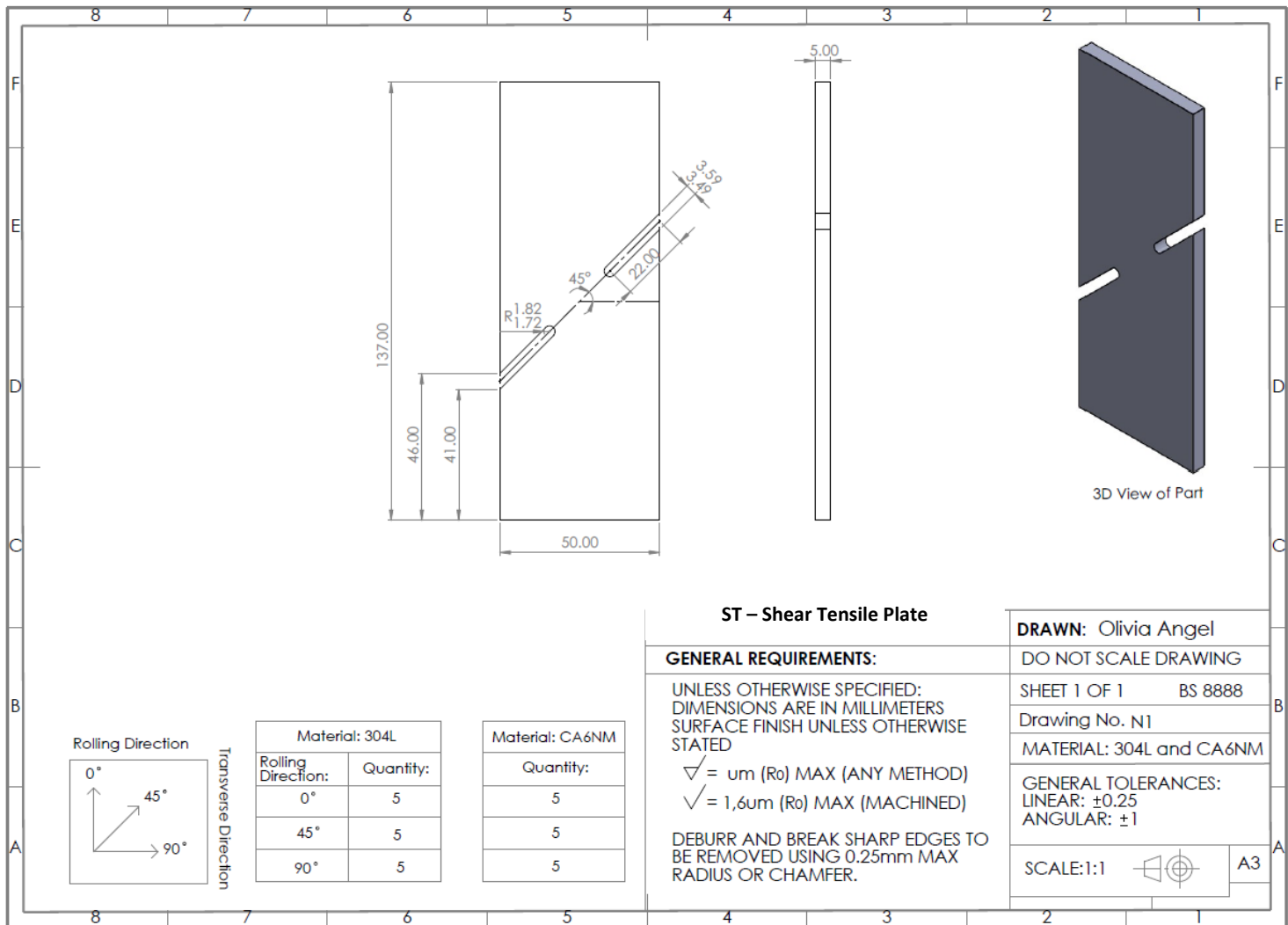
DEBURR AND BREAK SHARP EDGES TO
 BE REMOVED USING 0.25mm MAX
 RADIUS OR CHAMFER.

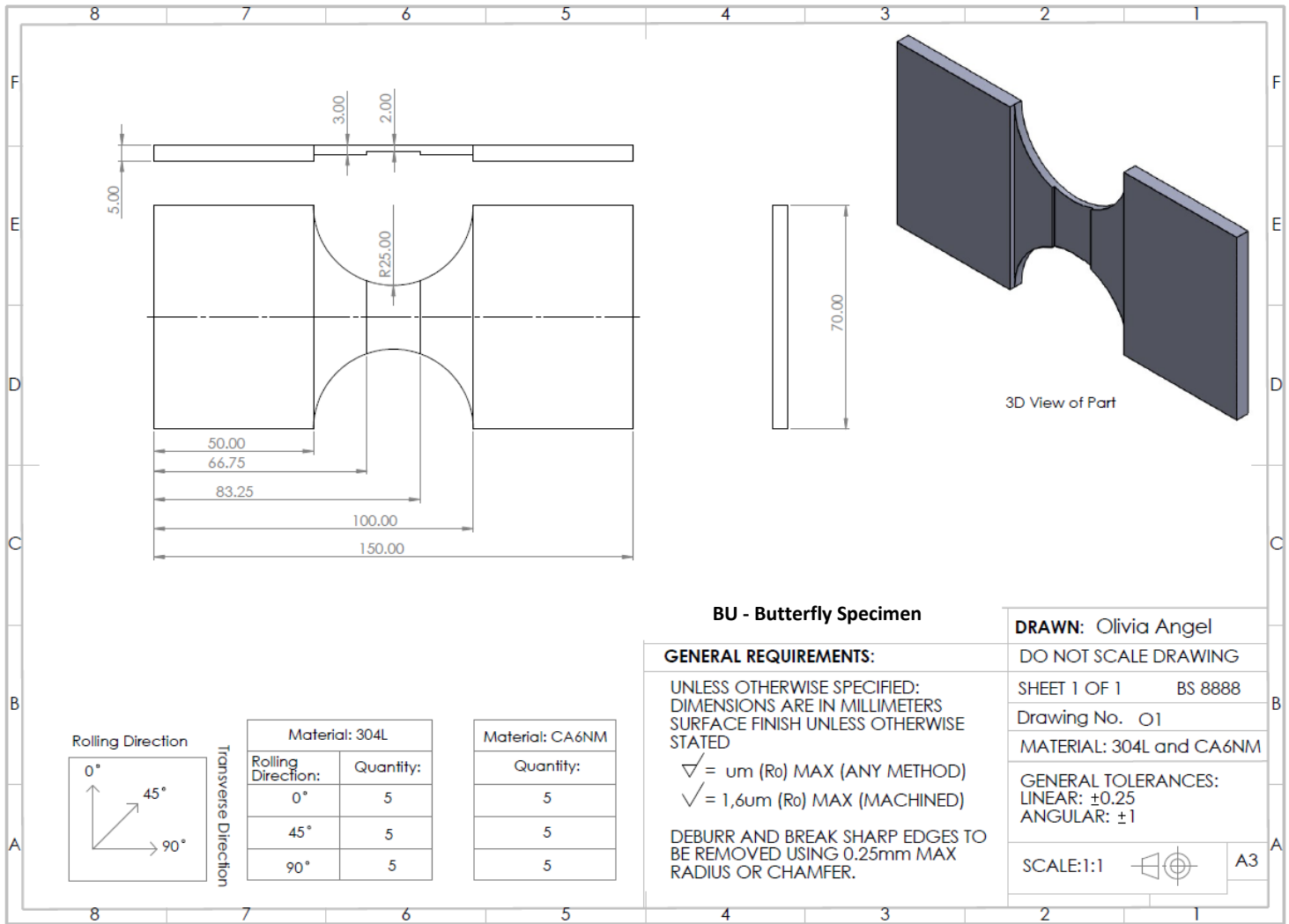
DRAWN: Olivia Angel
DO NOT SCALE DRAWING
SHEET 1 OF 1 BS 8888
Drawing No. G1
MATERIAL: 304L and CA6NM
GENERAL TOLERANCES: LINEAR: ± 0.25 ANGULAR: ± 1
SCALE: 1:1 A3

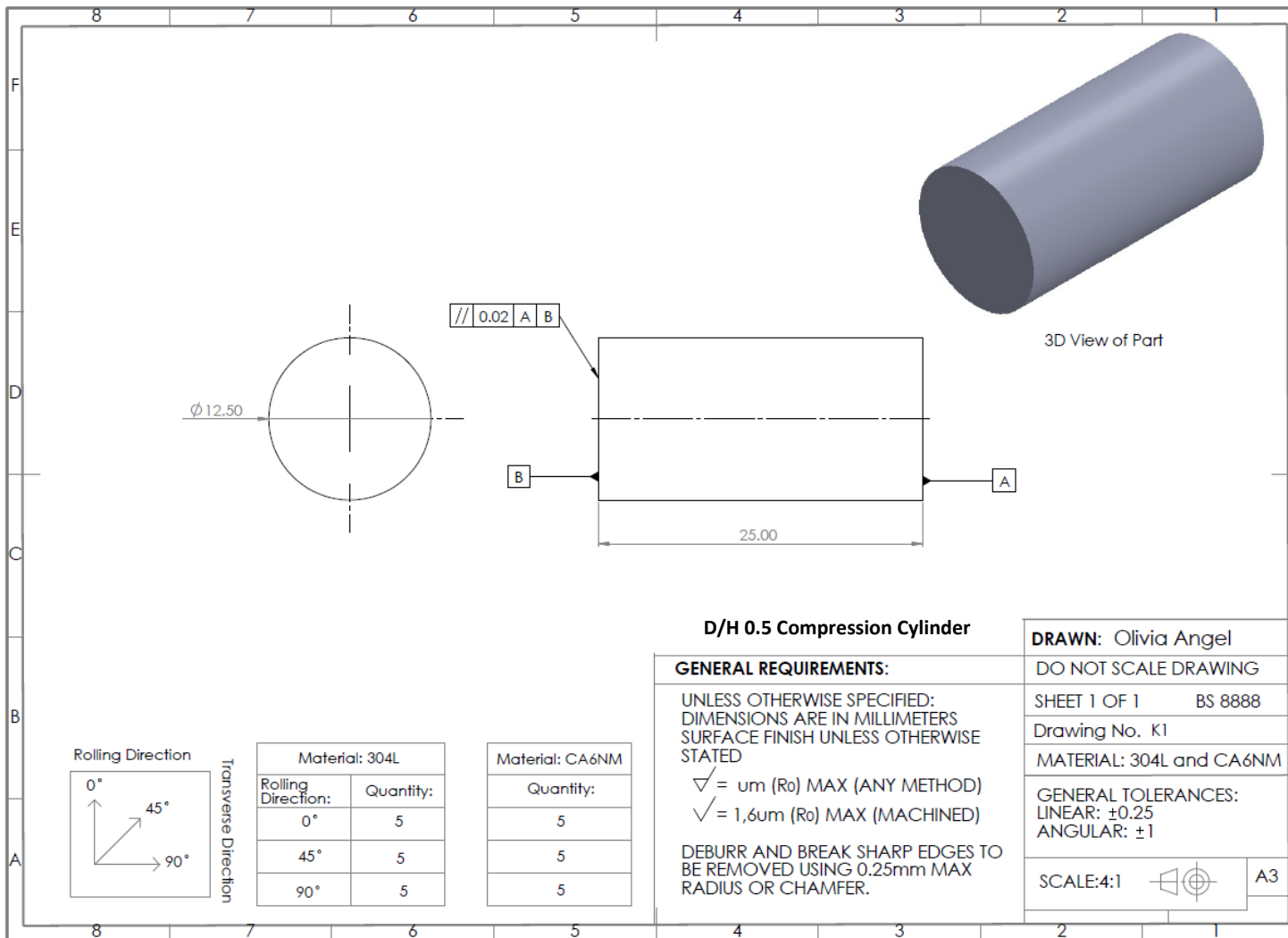


Material: 304L	
Rolling Direction:	Quantity:
0°	5
45°	5
90°	5


Material: CA6NM	
Quantity:	
5	
5	
5	



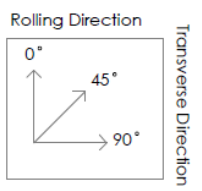




D/H 0.5 Compression Cylinder

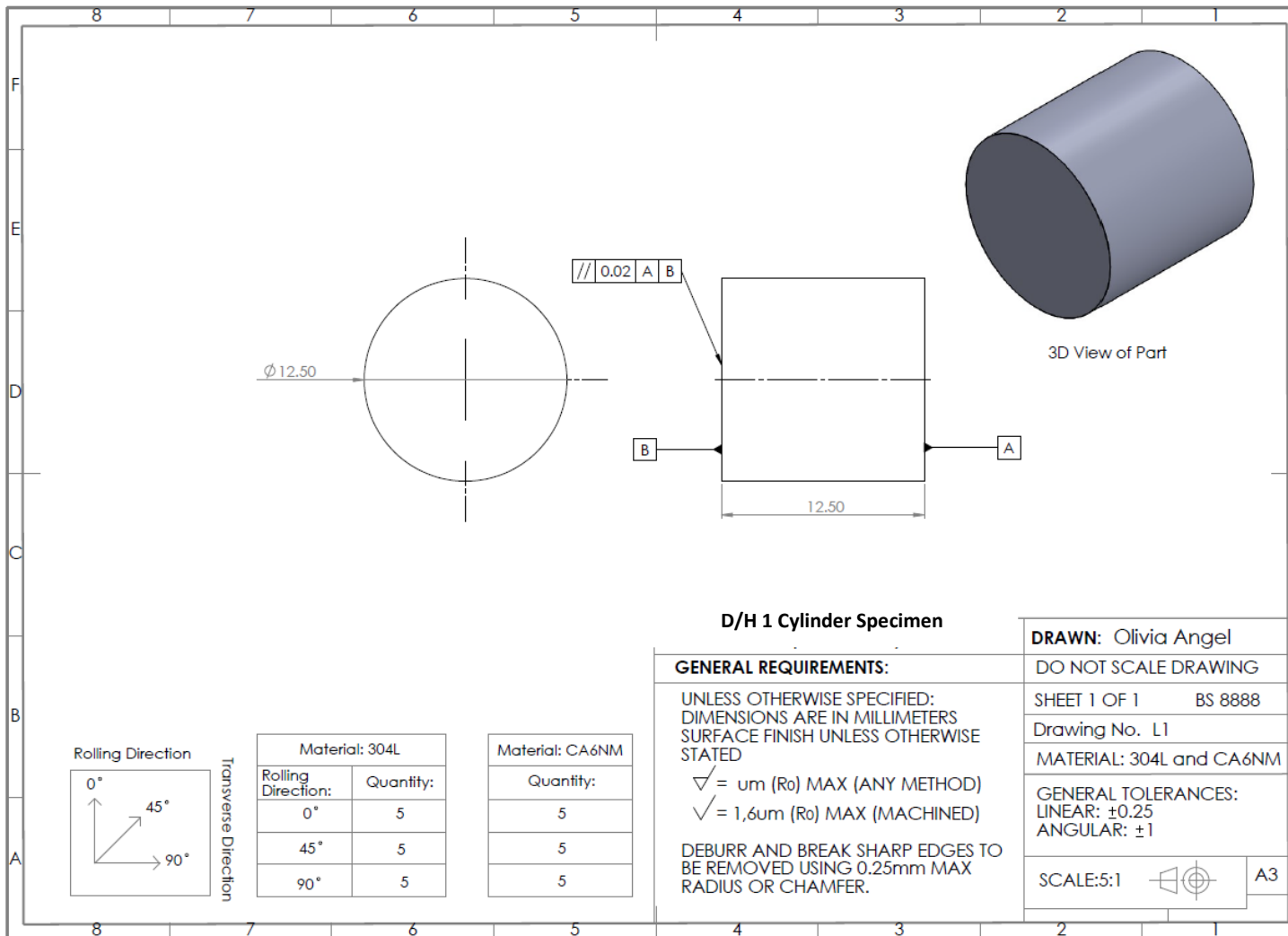
DRAWN: Olivia Angel
DO NOT SCALE DRAWING
SHEET 1 OF 1 BS 8888
Drawing No. K1
MATERIAL: 304L and CA6NM
GENERAL TOLERANCES: LINEAR: ±0.25 ANGULAR: ±1
SCALE:4:1  A3

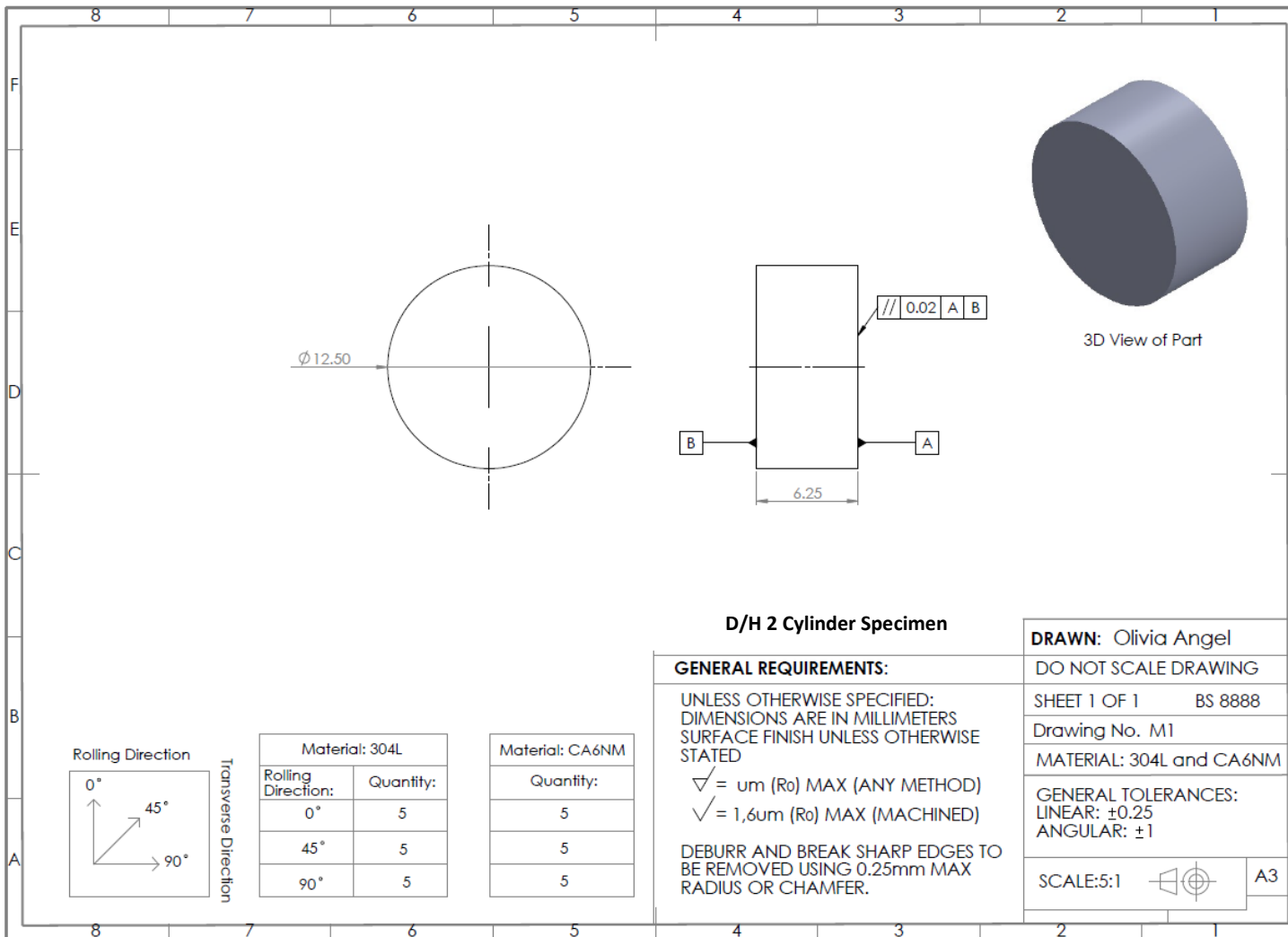
GENERAL REQUIREMENTS:
 UNLESS OTHERWISE SPECIFIED:
 DIMENSIONS ARE IN MILLIMETERS
 SURFACE FINISH UNLESS OTHERWISE STATED
 ✓ = um (Ro) MAX (ANY METHOD)
 ✓ = 1,6um (Ro) MAX (MACHINED)
 DEBURR AND BREAK SHARP EDGES TO BE REMOVED USING 0.25mm MAX RADIUS OR CHAMFER.

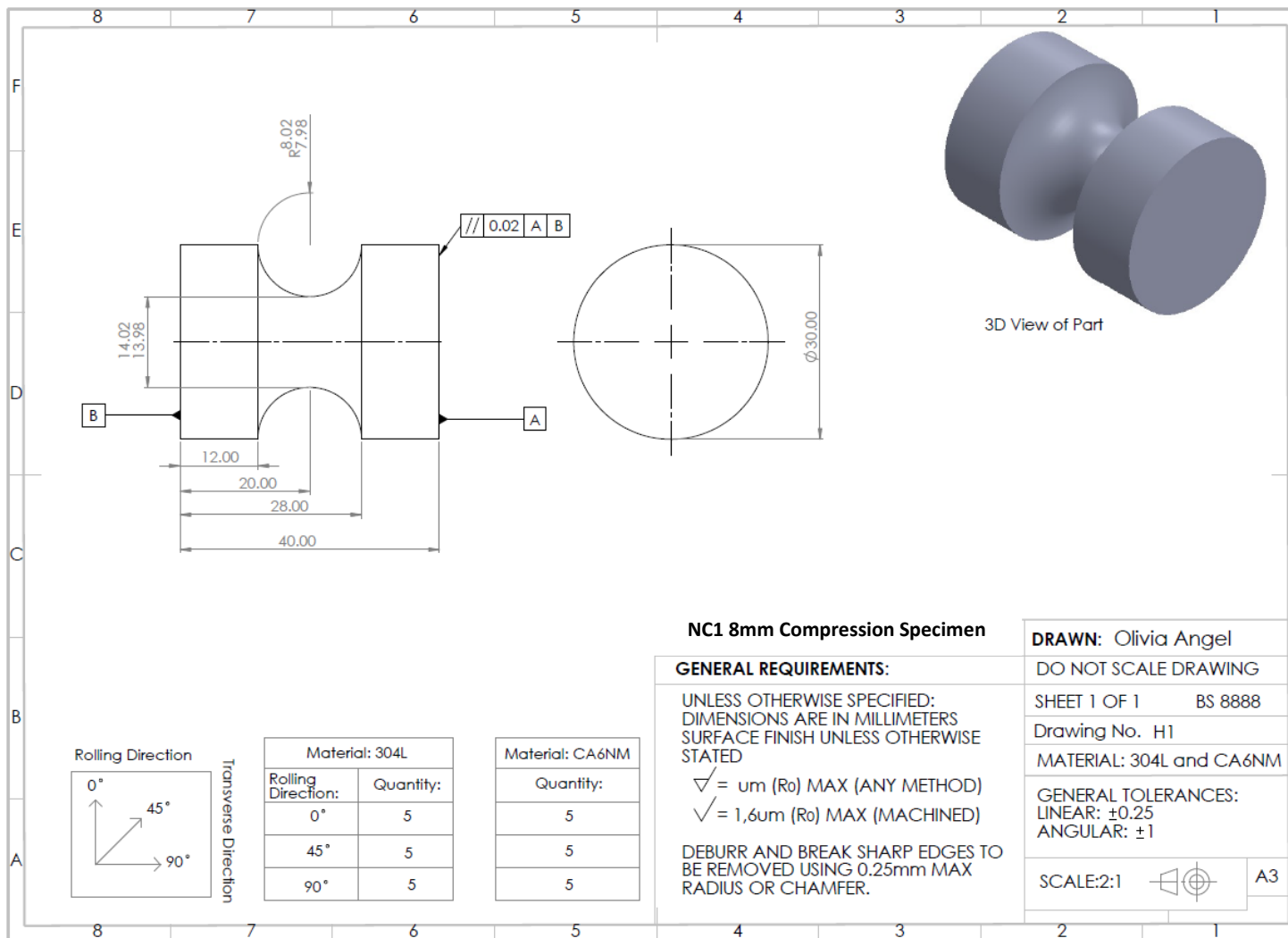


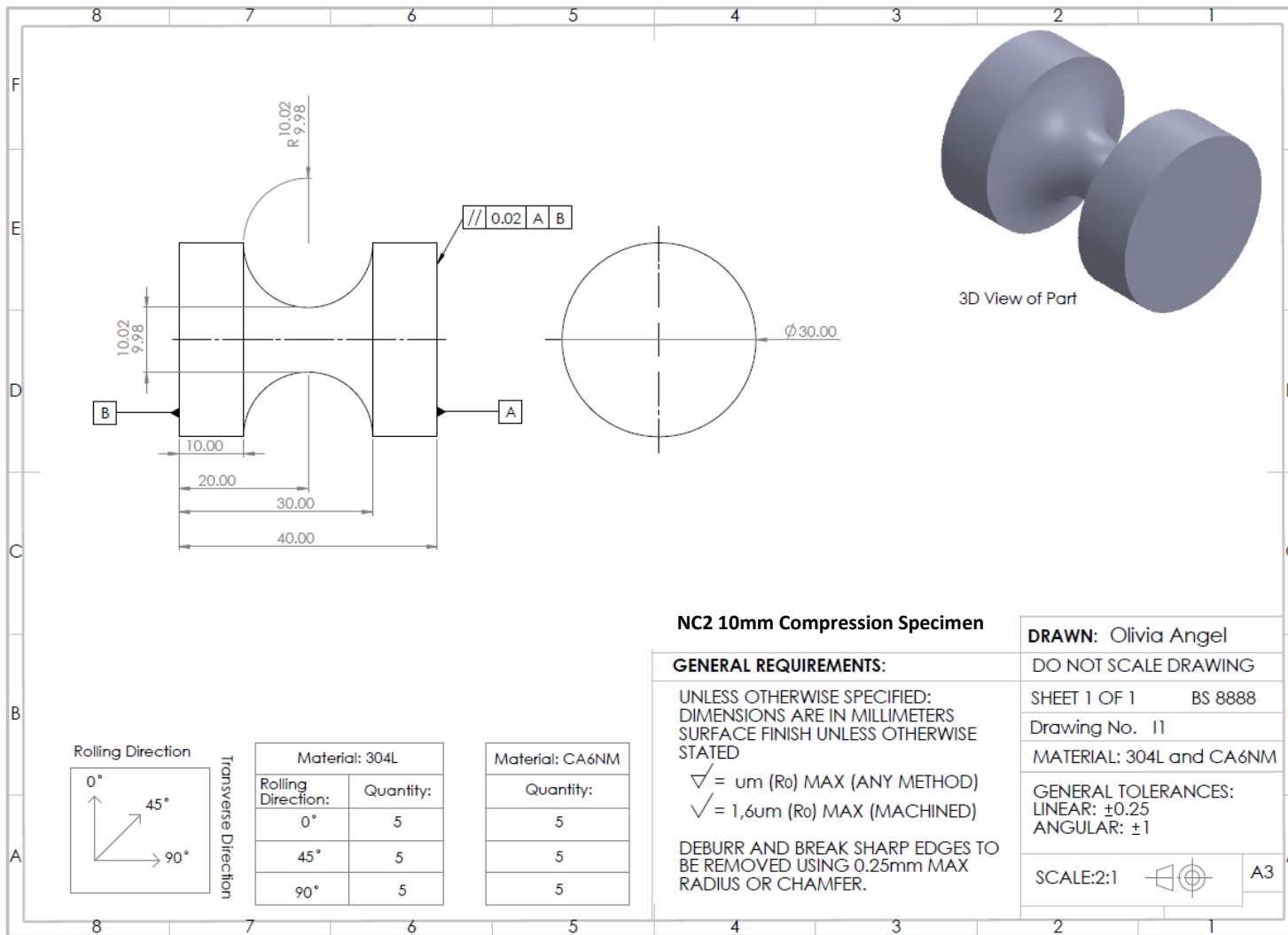
Material: 304L	
Rolling Direction:	Quantity:
0°	5
45°	5
90°	5

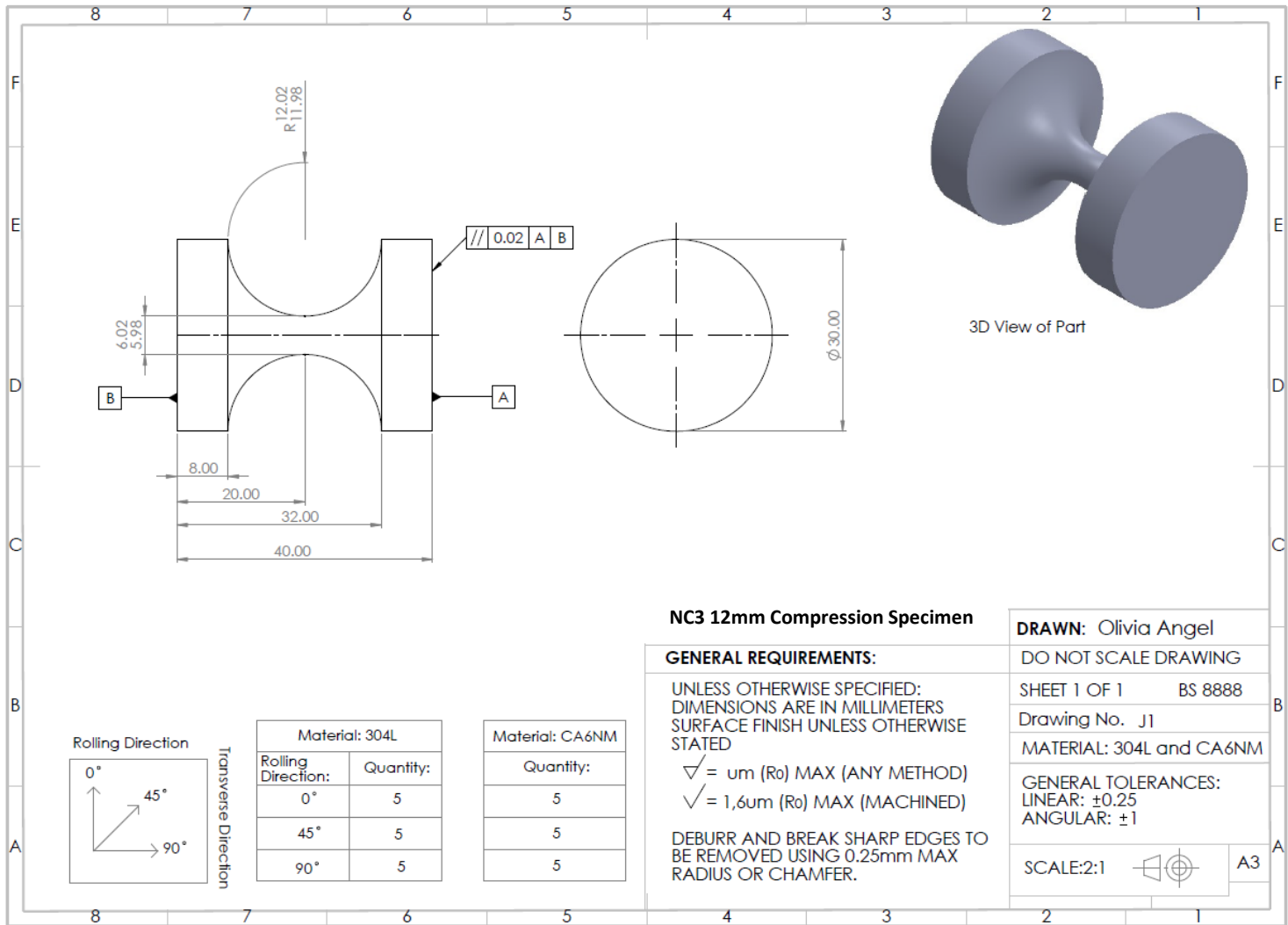
Material: CA6NM	
Quantity:	
5	
5	
5	











Appendix E - Manufacture Conformity and Inspection Report



DM Engineering Ltd

Cert N°: J21-261 - CoC-01

CERTIFICATE OF CONFORMITY

Client: INS

Client Order N°: Contract No IN002486 – Phase 2, 3, 4 & 5

DME Job N°: J21-261

Description of Supplies	Part N°	Qty	Drawing N°	Material Cast/Heat No
Smooth Bar	N/A	5	A1	304L Round Bar 2020/019257
Smooth Bar	N/A	5	A1	304L 25mm Plate 503474-404623:0
Smooth Bar	N/A	8	A1	CA6NM Free Issue
C1 Compression Specimen 8mm	N/A	5	H1	304L 35mm Plate 503311-401835:0
C2 Compression Specimen 10mm	N/A	5	I1	304L 35mm Plate 503311-401835:0
C3 Compression Specimen 12mm	N/A	5	J1	304L 35mm Plate 503311-401835:0
D/H 0.5 Compression Cylinder	N/A	5	K1	304L 15mm Plate 316222

ISSUE 01



DM Engineering Ltd

D/H 1 Compression Cylinder	N/A	5	L1	304L 15mm Plate 316222
D/H 2 Compression Cylinder	N/A	5	M1	304L 15mm Plate 316222
C1 Compression Specimen 8mm	N/A	5	H1	CA6NM Free Issue
C2 Compression Specimen 10mm	N/A	5	I1	CA6NM Free Issue
C3 Compression Specimen 12mm	N/A	5	J1	CA6NM Free Issue
D/H 0.5 Compression Cylinder	N/A	5	K1	CA6NM Free Issue
D/H 1 Compression Cylinder	N/A	5	L1	CA6NM Free Issue
D/H 2 Compression Cylinder	N/A	5	M1	CA6NM Free Issue
S1 Shear Plate	N/A	8	N1	CA6NM Free Issue
S1 Shear Plate	N/A	5	N1	304L 5mm Plate 938129

ISSUE 01



DM Engineering Ltd

Butterfly U-Notch Specimen	N/A	20	O1	304L 5mm Plate 938129
Butterfly U-Notch Specimen	N/A	20	O1	CA6NM Free Issue

Agreed Technical Queries/Concessions/Product Permit: N/A

Material / Consumable Certificates,

Enclosed
N/A

Remarks:

Certified that the supplies/services detailed heron have been inspected and tested in accordance with the conditions and requirements of the contract or purchase order, and unless otherwise noted above, conform in all respects to the relevant specifications & drawings.

Signed:  Name: Darren Martin Position: Managing Director

For and on the behalf of: DM Engineering Ltd

Date: 10-10-21

ISSUE 01



Manufacture Inspection Report

Page 1 of 2

Client: INS	Project: Stainless Steel and CA6NM Test Samples	Report No: J21-261-MIR-01
Client Contract No / PO: IN002486	DM Engineering Job No: J21-261	Location: DME Workshop

Date of inspection:	Method: Visual, Dimensional
Inspection Procedure DME 09 – Calibrated Equipment and Inspection	Extent of inspection: Dimensional Inspection of all Phase 2,3,4 & 5 items
Acceptance Criteria: Dimensions within tolerance indicated on drawings.	Stage of inspection: Post Machining
Test surface condition: Machined Finish	Minimum lighting and temperature level achieved: Yes

Inspection					
Item:	Quantity:	Drawing:	Material Grade:	Accept/Reject (A / R)	
Smooth Notched Bar	5	A1	304L	A	Insert lines as require
Smooth Notched Bar	5	A1	304L	A	
Smooth Notched Bar	8	A1	CA6NM	A	
C1 Compression Specimen 8mm	5	H1	304L	A	
C2 Compression Specimen 10mm	5	I1	304L	A	
C3 Compression Specimen 12mm	5	J1	304L	A	
D/H 0.5 Compression Cylinder	5	K1	304L	A	
D/H 1 Compression Cylinder	5	L1	304L	A	
D/H 2 Compression Cylinder	5	M1	304L	A	
C1 Compression Specimen 8mm	5	H1	CA6NM Free Issue	A	


Issue 1



Manufacture Inspection Report

Page 2 of 2

Client: INS	Project: Stainless Steel and CA6NM Test Samples	Report No: J21-261-MIR-01
Client Contract No / PO: IN002486	DM Engineering Job No: J21-261	Location: DME Workshop

C2 Compression Specimen 10mm	5	I1	CA6NM Free Issue	A	
C3 Compression Specimen 12mm	5	J1	CA6NM Free Issue	A	
D/H 0.5 Compression Cylinder	5	K1	CA6NM Free Issue	A	
D/H 1 Compression Cylinder	5	L1	CA6NM Free Issue	A	
D/H 2 Compression Cylinder	5	M1	CA6NM Free Issue	A	
S1 Shear Plate	8	N1	CA6NM Free Issue	A	
S1 Shear Plate	5	N1	CA6NM Free Issue	A	
Butterfly U-Notch Specimen	20	O1	304L	A	
Butterfly U-Notch Specimen	20	O1	CA6NM Free Issue	A	
Test restrictions / Comments: None			Test / Measure Equipment Used: 0-25 outside micrometer – DM 01 25-50 outside micrometer – DM 02 0-150 digital vernier calipers – DM15 Vernier protractor – DM 36 0-25 point micrometer – DM 27 Slip Gauges – DM 39		
Inspected by:	Darren Martin		Sign / Date: 		

Issue 1

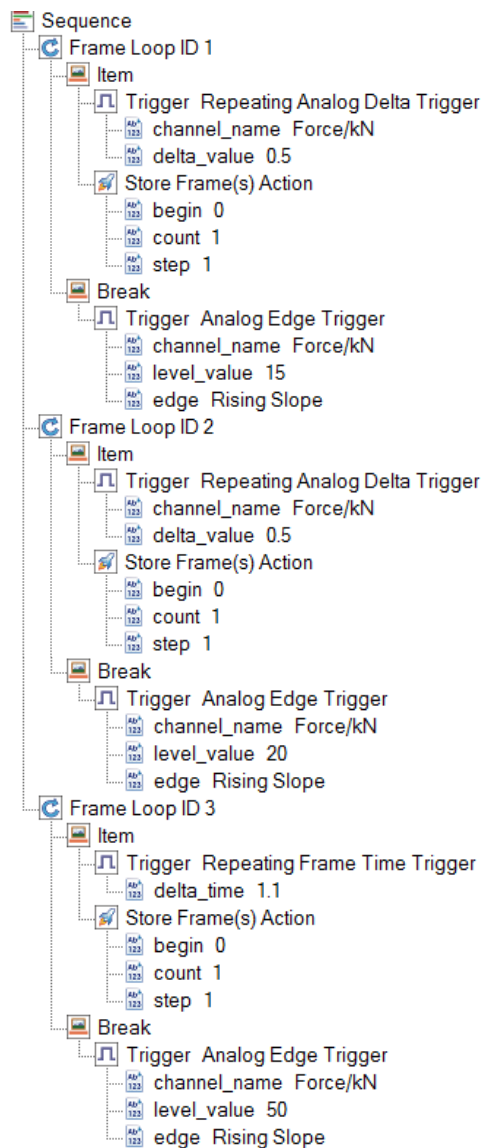
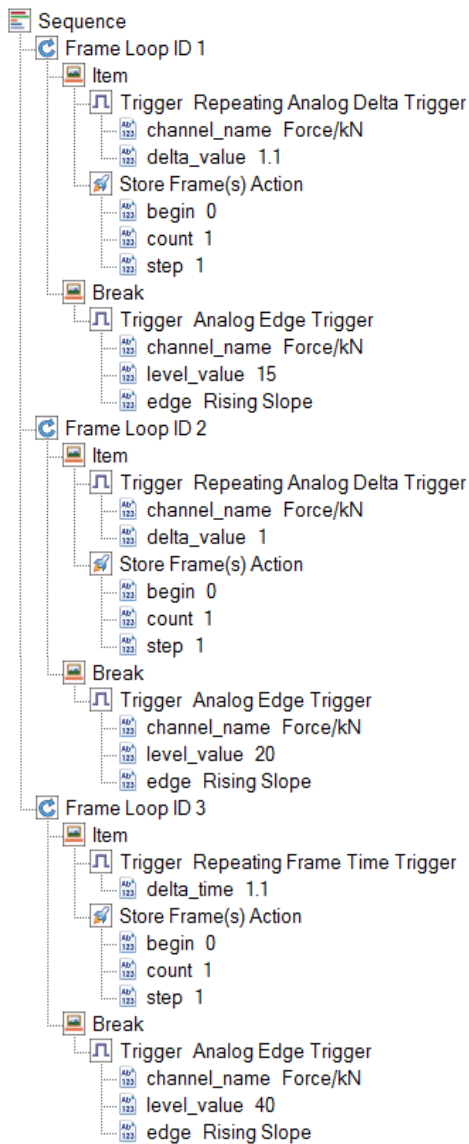
Appendix F – Summary of DIC Measurements

Geometry:	SB	T1-T5/ PH	ST	C1-C3 / DH 0.5 -DH 2	BU
Stereo Angle	15 deg	13 deg	27 deg	25 deg	14 deg
Stand-off Distance	500 mm	550 mm	250 mm	230 mm	500 mm
Field of View	70 mm x 70 mm	80 mm x 80 mm	120 mm x 120 mm	60 mm x 60 mm	80 mm x 80mm
Exposure Time	70 ms	65 ms	70 ms	8 ms	70 ms
Lens / Extension Tubes	50 mm + 5mm	50mm + 5mm	16 mm	50 mm + 10mm	50 mm + 5mm
Aperture	F16	F16	F8	F16	F8
Calibration Target	GL-06-WMB 9X9	GL-06-WMB 9X9	GL-06-WMB 9X9	GI-02-WMB-9X9	GL-06-WMB 9X9
Baseline	140 mm	140 mm	140 mm	120 mm	140 mm
Facet Size	25	25	25	45	25
Grid Size	17	17	17	37	17

Appendix G – Recording Procedures for DIC

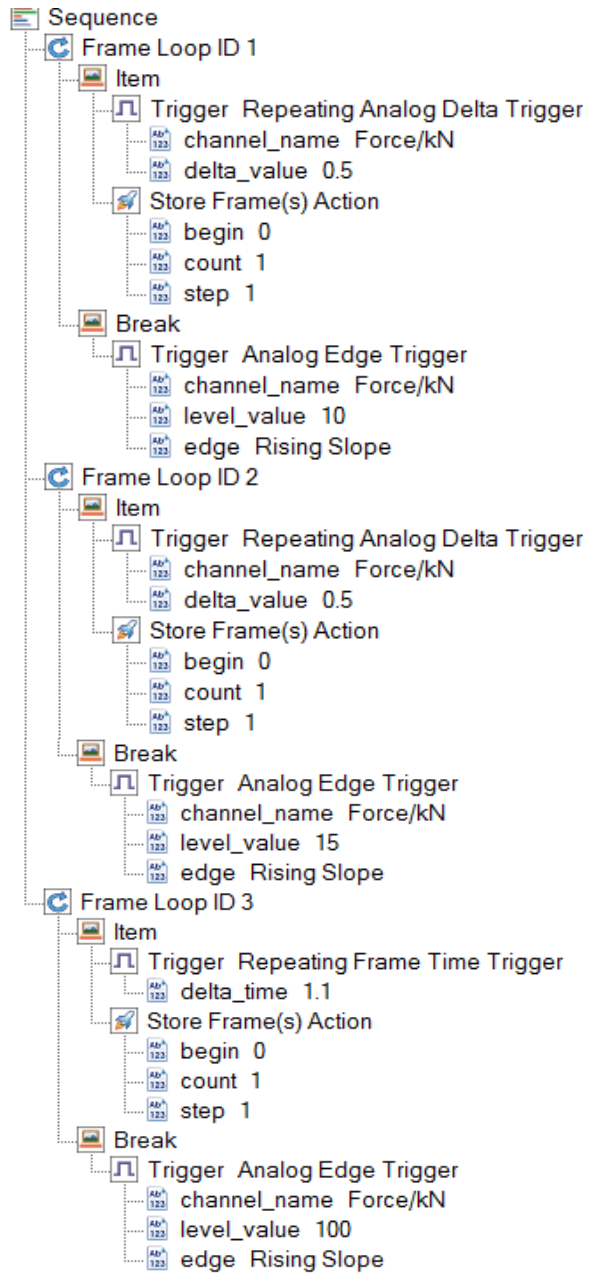
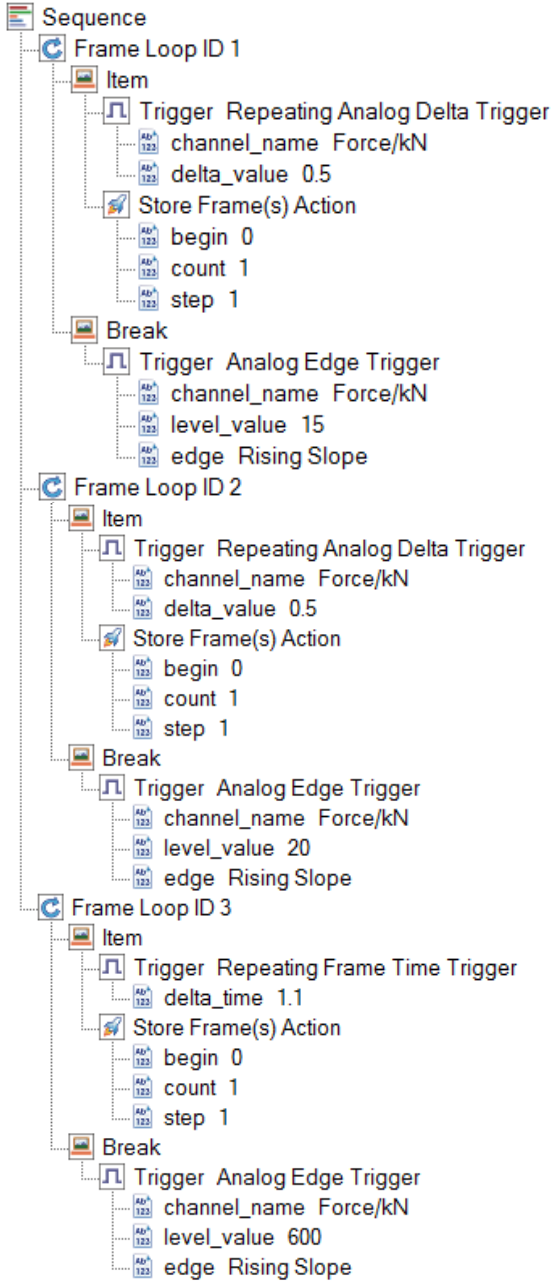
SB

T1-T5

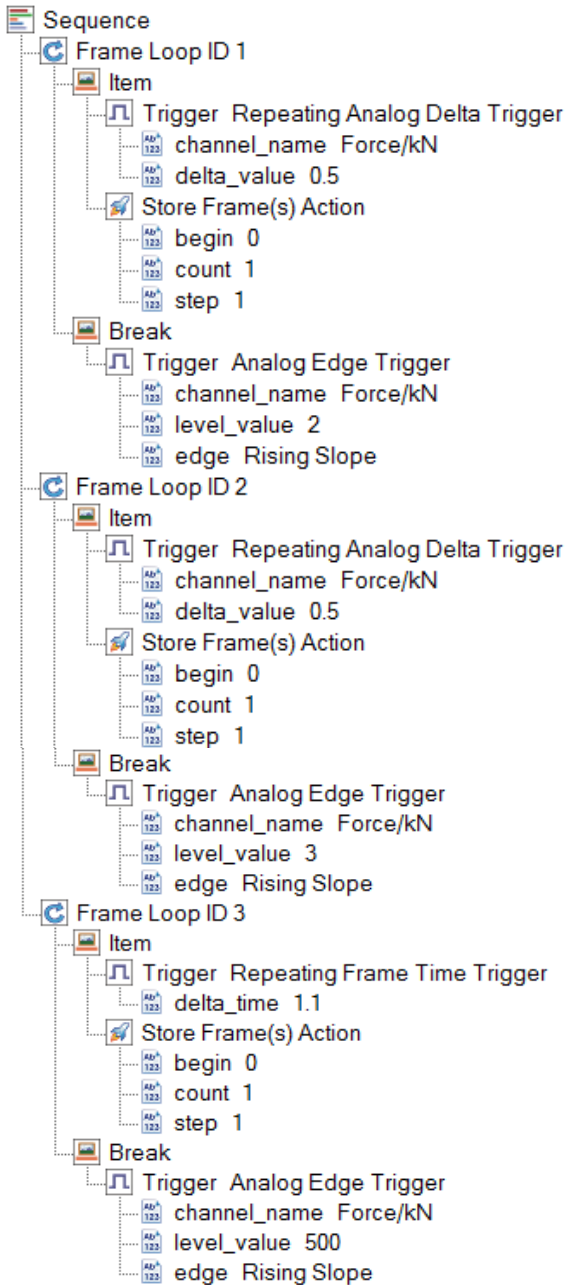


C1-C3 / DH 0.5 -DH 2

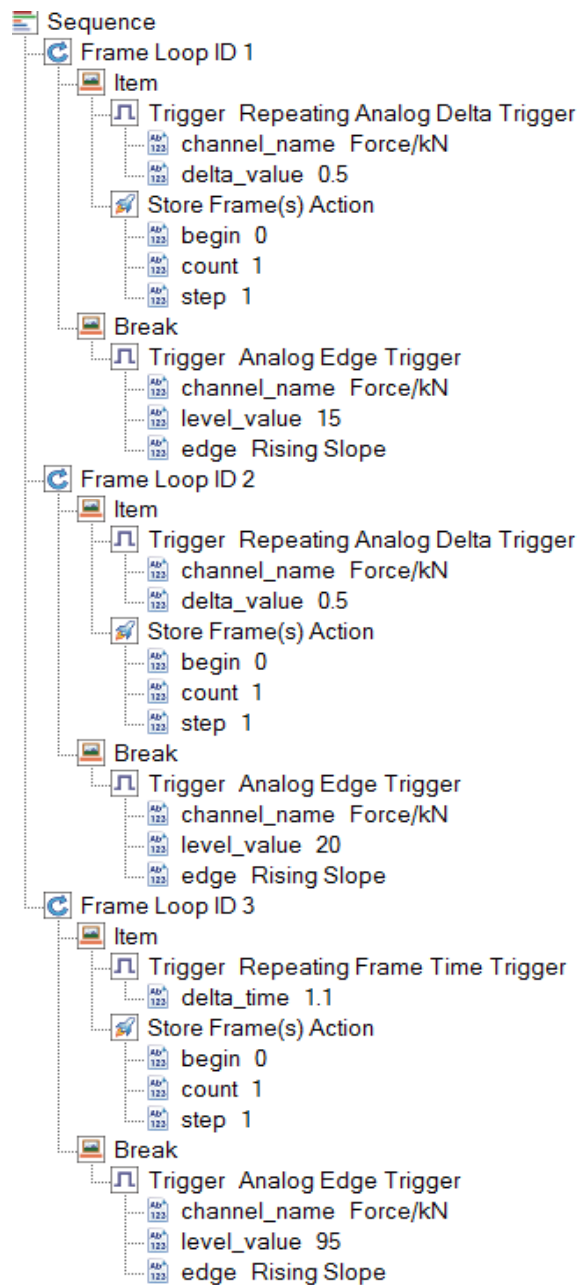
ST



BU



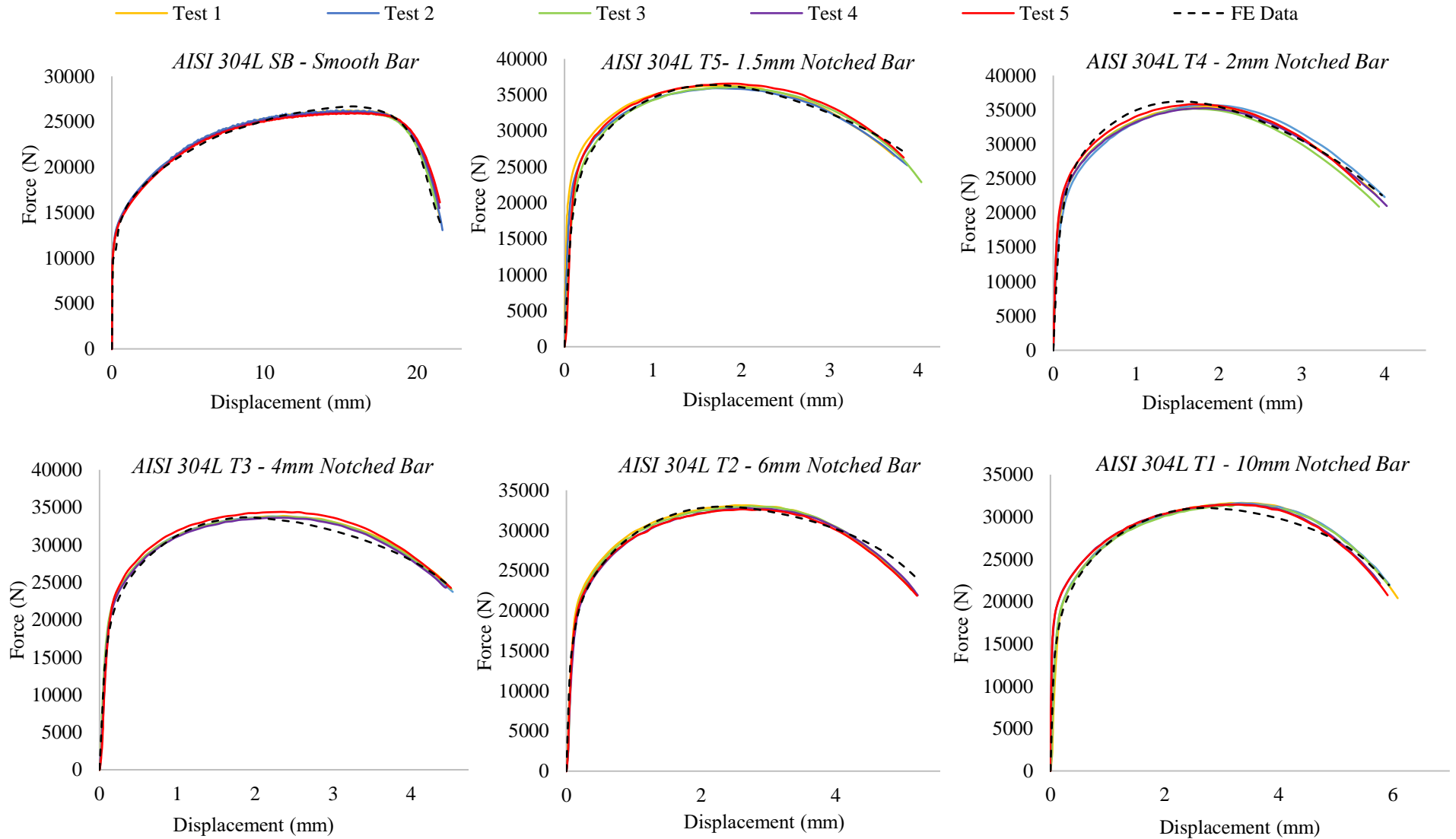
PH

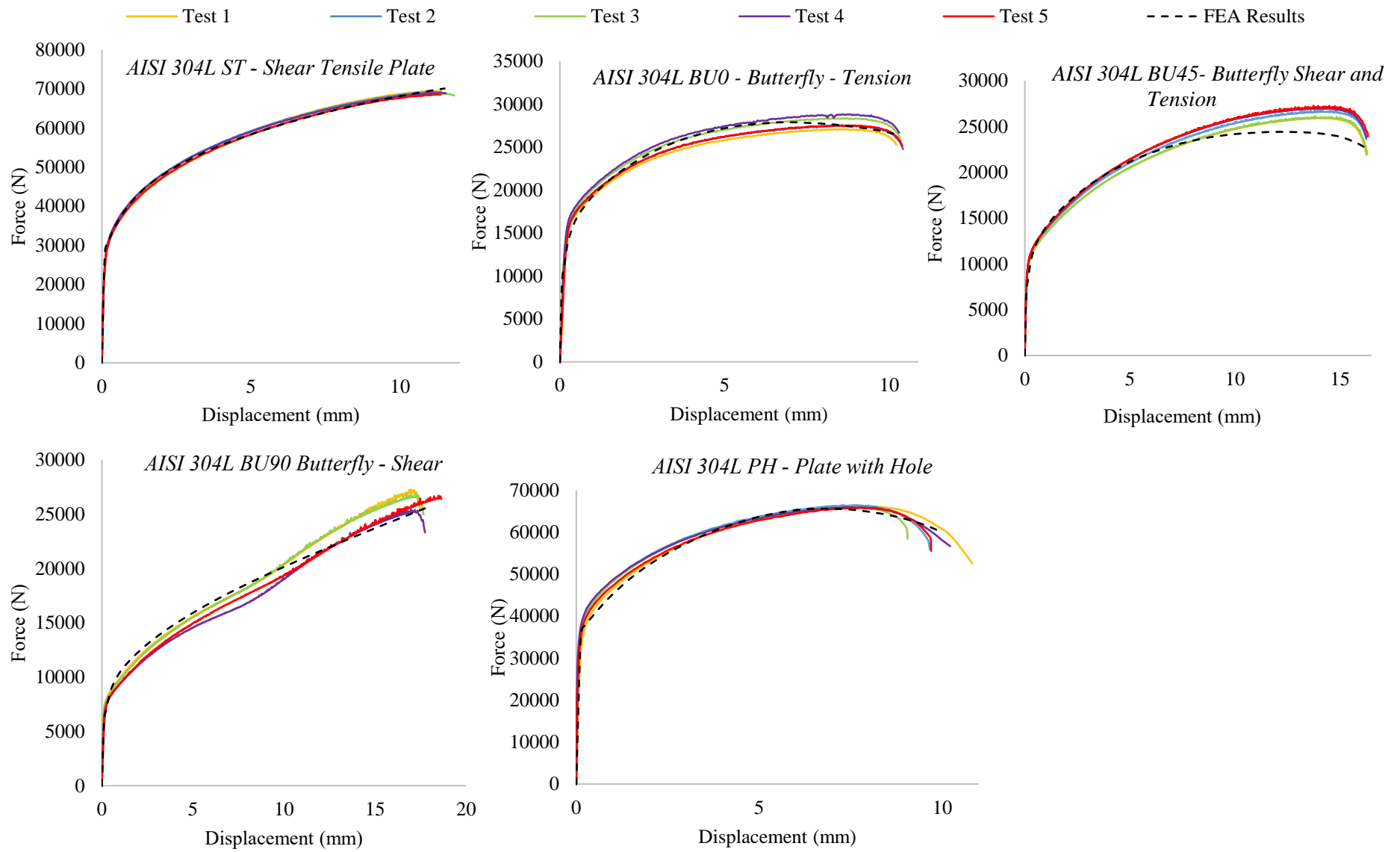


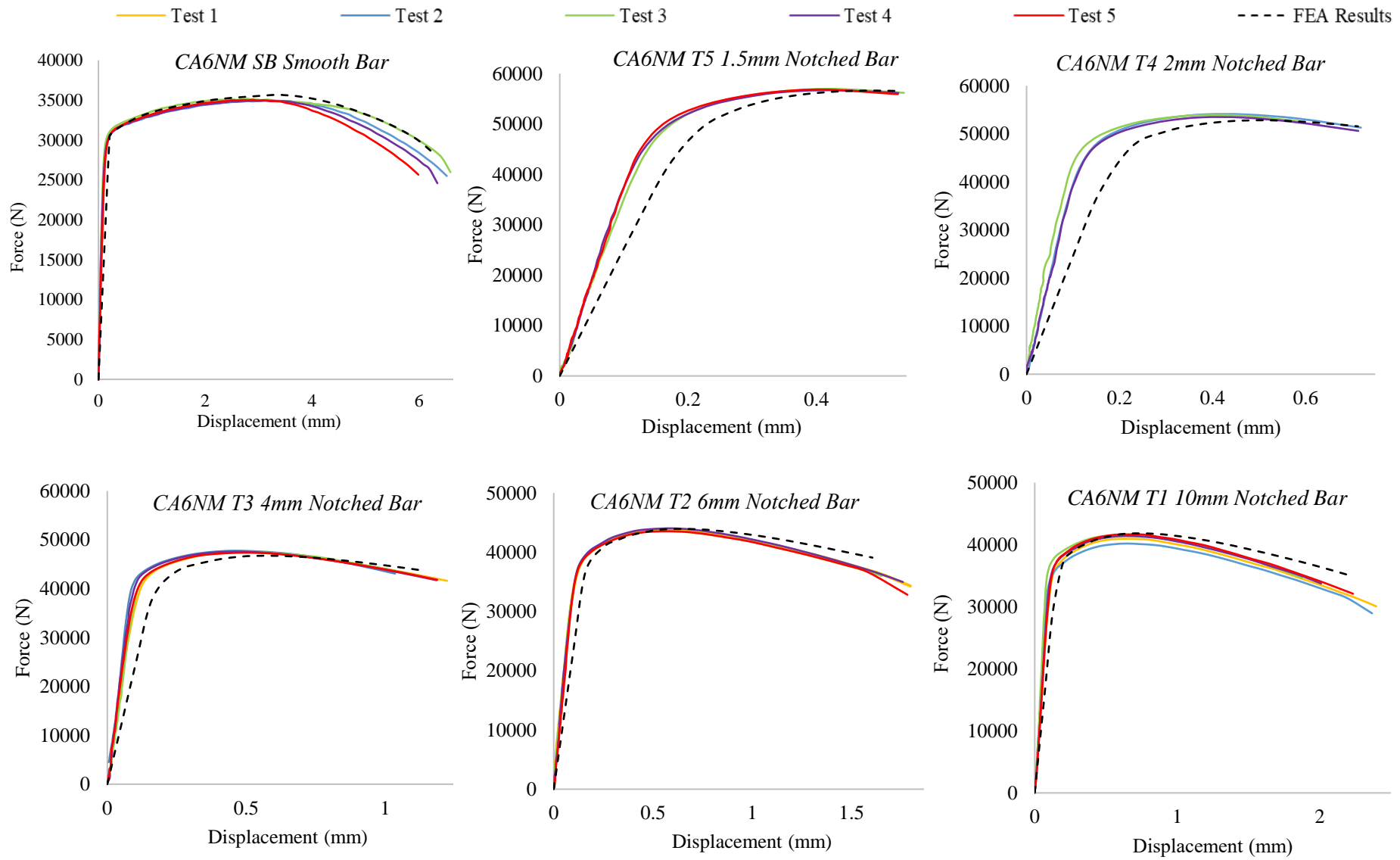
Appendix H – Yield Stress and Plastic Strain

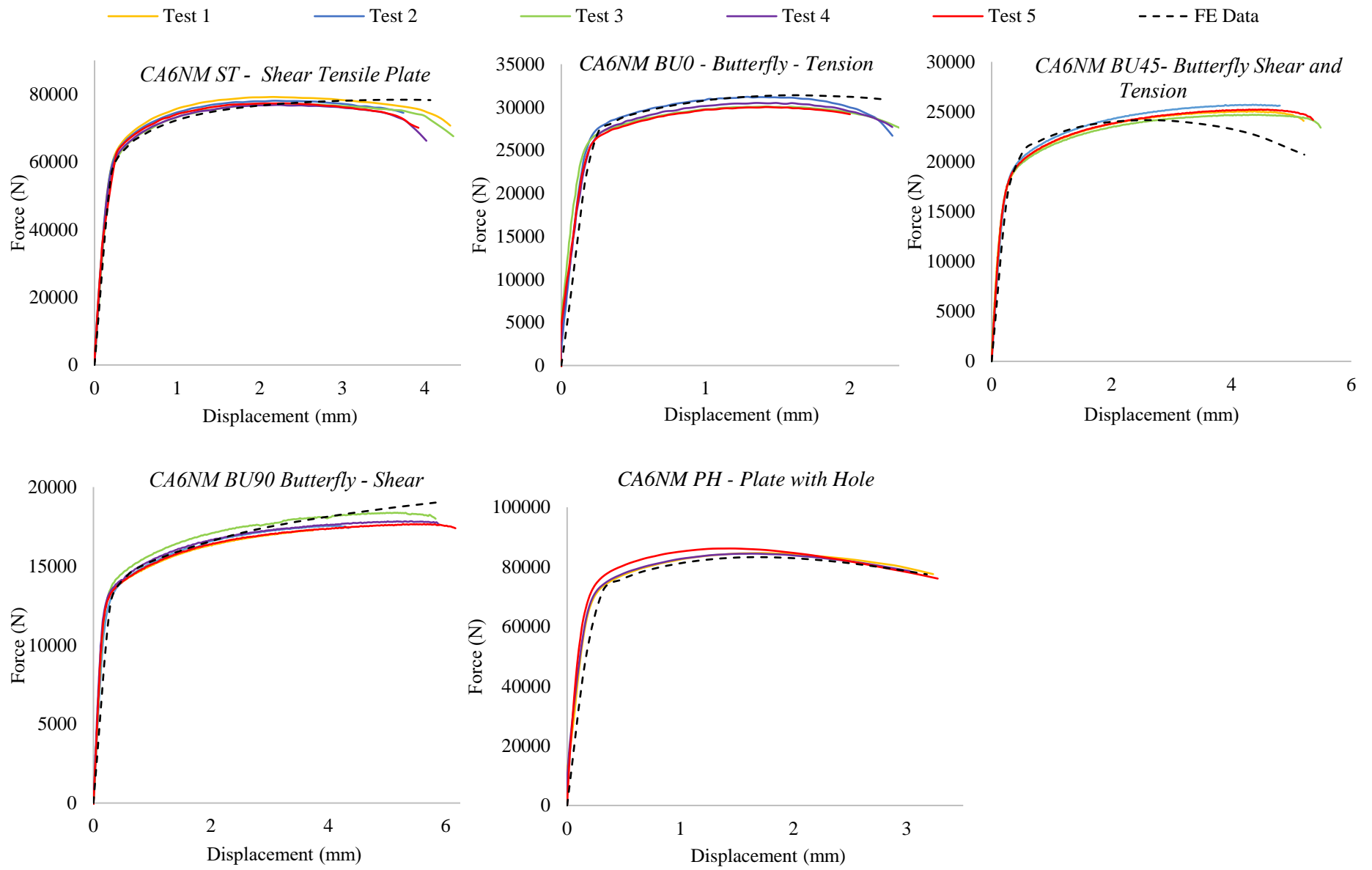
AISI 304L		CA6NM	
Yield Stress (MPa)	Plastic Strain	Yield Stress (MPa)	Plastic Strain
215.59	0.000	685.52	0.000
290.07	0.010	728.72	0.012
483.06	0.080	759.88	0.022
556.50	0.120	781.19	0.032
590.89	0.140	800.33	0.042
622.92	0.162	805.35	0.044
653.53	0.183	822.54	0.054
682.15	0.205	837.69	0.064
708.99	0.225	853.59	0.073
734.56	0.245	866.80	0.083
759.18	0.266	860.15	0.078
783.12	0.288	857.03	0.076
806.37	0.309	866.80	0.083
828.84	0.331	880.20	0.094
851.52	0.354	893.05	0.109
874.43	0.377	906.87	0.125
897.88	0.403	921.76	0.144
922.68	0.432	940.99	0.172
950.04	0.465	946.50	0.182
983.21	0.505	972.31	0.227
1032.92	0.562	1003.50	0.289
1126.23	0.672	1036.85	0.364
1286.69	0.865	1078.74	0.453
1501.56	1.205	1124.04	0.560
1579.15	1.458	1160.71	0.672

Appendix I – High and Low Stress Triaxiality Force Displacement Curves









Appendix J – Python Scripts

Appendix J-1 - Script to obtain the Lode angle parameter in Abaqus for each frame

```
1  import math
2  import numpy as np
3  import odbAccess
4  import os
5  import shutil
6  import time
7  import datetime
8  from abaqus import *
9  from abaqusConstants import *
10 from numpy.lib.recfunctions import append_fields
11 from operator import itemgetter
12
13 def getODB(ODBNum=None):
14
15     ###Gets ODB object by number in current session. Does not need a number
16     if only odb is open.
17
18     if ODBNum is None:
19         odbs = session.odbs.items()
20         if len(odbs) == 1:
21             odb = session.odbs.items()[0][1]
22         else:
23             print "Only 1 ODB file can be open for getODB() to work without
24 an integer input"
25             odb = None
26     else:
27         odb = session.odbs.items()[ODBNum][1]
28     return odb
29
30 def addLodeField(myODB, elementType=None, instanceName=None):
31
32     ###Calculate normalized third invariant and normalized lode angle
33
34     steps = myODB.steps
35     ii = steps.keys()
36     for i in ii:
37         myStep = steps[i]
38         # Iterate over frames for given step
39         frames = myStep.frames
40         n_f = len(frames)
41         for j in xrange(n_f):
42             frame=frames[j]
43             t_f_start = time.time()
44             if 'NormInv3' in frame.fieldOutputs.keys():
45                 continue
46             if 'Lode' in frame.fieldOutputs.keys():
47                 continue
48             S_all = frame.fieldOutputs['S'] # Stress Field Output Object
49             # Get subsets of field output object if specified
50             if instanceName is not None:
51                 instance = myODB.rootAssembly.instances[instanceName]
```

```

52         S_all = S_all.getSubset(INTEGRATION_POINT,
53 region=instance)
54         if elementType is not None:
55             S_all = S_all.getSubset(INTEGRATION_POINT,
56 elementType=elementType)
57         mises = S_all.getScalarField(invariant=MISES)
58         inv3 = S_all.getScalarField(invariant=INV3)
59         # eps ensures (mises + eps) > abs(inv3) for acos calculation
60         # eps prevents division by 0
61         # eps determined empirically with units of psi
62         eps = 0.1
63         normInv3 = power(inv3/(mises + eps), 3)
64         lode = 1.-2./math.pi*acos(normInv3)
65         normInv3Field = frame.FieldOutput(name='NormInv3',
66 description='Normalized Third Invariant of Deviatoric
67 Stress Tensor',
68         field=normInv3)
69         lodeField = frame.FieldOutput(name='Lode',
70 description='Normalized Lode Angle',
71         field=lode)
72         print('Processed frame '+ str(j) + ' / ' + str(n_f - 1) + '
73 in ' +
74         myStep.name + ' step.')
75
76
77 #####End of definitions
78
79 # Backup ODB, close, and open backup with write permissions
80 myODB = getODB()
81 path1 = myODB.path
82 path2 = path1[:-4] + '_lode.odb'
83 shutil.copy(path1, path2)
84 myODB.close()
85 myODB = odbAccess.openOdb(path=path2)
86
87 # Add New Field Outputs for normalized Lode angle and normalized third
88 invariant
89 addLodeField(myODB, elementType=None, instanceName=None)
90
91 # Save, close, and reopen ODB to get fields to display properly
92 myODB.save()
93 myODB.close()
94 myODB = odbAccess.openOdb(path=path2, readOnly=True)
95
96 # Change viewport to show normalized Lode angle
97 session.viewports['Viewport: 1'].setValues(displayedObject=myODB)
98 session.viewports['Viewport:
99 1'].odbDisplay.display.setValues(plotState=(CONTOURS_ON_DEF, ))
100 session.viewports['Viewport: 1'].odbDisplay.setFrame(step=0, frame=0 )
101 session.viewports['Viewport: 1'].odbDisplay.contourOptions.setValues(
102     maxAutoCompute=OFF, minAutoCompute=OFF)
103 session.viewports['Viewport:
104 1'].odbDisplay.contourOptions.setValues(maxValue=1.0001,
105     minValue=-1.0001)
106 session.viewports['Viewport: 1'].view.setValues(session.views['Iso'])
107 session.viewports['Viewport:
108 1'].odbDisplay.setPrimaryVariable(variableLabel='Lode',
109     outputPosition=INTEGRATION_POINT)
110 session.viewports['Viewport: 1'].view.setProjection(projection=PARALLEL)

```

Appendix J-2 - Script to obtain the PEEQ of selected nodes/elements for the last frame

```
1  from abaqusConstants import *
2  from caeModules import *
3  from driverUtils import executeOnCaeStartup
4  from odbAccess import *
5  from odbMaterial import *
6  from odbSection import *
7  import numpy as np
8  import time
9  import math
10
11  ### Setting the numpy print display size for maximum size and also up to 10
12  decimal places ###
13  np.set_printoptions(suppress=True)
14  np.set_printoptions(threshold=sys.maxsize)
15  np.set_printoptions(precision=10)
16
17
18  def Extract_PEEQ(pickedElementsPEEQ):
19
20      global Numberofframes
21      global PEEQ_Array
22      global PEEQData
23      global Elements_For_Processing
24      global EVOLData
25      global EVOL_Array
26      global EVOL_Sum
27      global PEEQ_FinalValue
28
29      ### Opens the odb file ###
30      odb= session.openOdb('Job-1_lode.odb')
31      steptoread='Step-1'
32      Numberofframes=len(odb.steps[steptoread].frames)
33
34      print 'Opened odb File'
35
36          Elements_For_Processing = []
37      for x in pickedElementsPEEQ:
38          Elements_For_Processing.append(x.label)
39
40      print Elements_For_Processing
41
42      ### Creating Array for PEEQ
43      PEEQ_Array = np.zeros([0,2])
44
45      ### Get PEEQ data and save to csv
46          PEEQElementLabels = odb.steps[steptoread].frames[-
47 1].fieldOutputs['PEEQ'].bulkDataBlocks[0].elementLabels
48      PEEQData = odb.steps[steptoread].frames[-
49 1].fieldOutputs['PEEQ'].bulkDataBlocks[0].data
50      print PEEQElementLabels
51
52          for x, y in zip(PEEQElementLabels,PEEQData):
53              if x in Elements_For_Processing:
54      PEEQ_Array = np.append(PEEQ_Array, [[int(x), y[0]]], axis=0
55      np.savetxt('PEEQ_Array.csv',PEEQ_Array, fmt='%10.50f' , delimiter=',')
```

Appendix J-3 - Script to obtain the average Stress Triaxiality and Lode angle parameter for selected nodes/elements

```
1 from abaqus import *
2 from abaqusConstants import *
3 from caeModules import *
4 from driverUtils import executeOnCaeStartup
5 from odbAccess import *
6 from odbMaterial import *
7 from odbSection import *
8 import numpy as np
9 import time
10 import math
11
12 ### Setting the numpy print display size for maximum size and also up to 10
13 decimal places ###
14 np.set_printoptions(suppress=True)
15 np.set_printoptions(threshold=sys.maxsize)
16 np.set_printoptions(precision=10)
17
18 def Extract_TriAx_and_Lode(pickedElements):
19
20     ### Global Definitions
21     global Numberofframes
22     global List_of_Nodes
23     global TRIAX_Avg
24     global Lode_Avg
25     global TRIAX_Avg_Final
26     global Lode_AVG_Final
27     global Elements_For_Processing
28     global EVOLData
29     global EVOL_Array
30     global EVOL_Sum
31
32     ### Opens the odb file ###
33     odb= session.openOdb('Job-1_lode.odb')
34     steptoread='Step-1'
35     Numberofframes=len(odb.steps[steptoread].frames)
36
37     print 'Opened odb File'
38
39     ##### This is for the selected elements (Will need to change this based
40 on the model) ###
41
42     Elements_For_Processing = []
43     for x in pickedElements:
44         Elements_For_Processing.append(x.label)
45
46     ### Sets up the arrays for the Raw Data ###
47     TRIAX_Avg= np.zeros([0,3])
48     Lode_Avg= np.zeros([0,3])
49
50     ### Loop through the data from abaqus, and only save the data (both
51 TRIAX and Lode) together which is included in the pickedElements ###
52     for i in xrange(Numberofframes):
53         TRIAXNodeLabels =
54 odb.steps[steptoread].frames[i].fieldOutputs['TRIAX'].bulkDataBlocks[0].ele
55 mentLabels
```

```

56         TRIAXData         =
57 odb.steps[steptoread].frames[i].fieldOutputs['TRIAX'].bulkDataBlocks[0].dat
58 a
59
60         LodeNodeLabels    =
61 odb.steps[steptoread].frames[i].fieldOutputs['Lode'].bulkDataBlocks[0].elem
62 entLabels
63         LodeData          =
64 odb.steps[steptoread].frames[i].fieldOutputs['Lode'].bulkDataBlocks[0].data
65
66         for x, y, z in zip(TRIAXNodeLabels,TRIAXData,LodeData):
67             if x in Elements_For_Processing:
68                 TRIAX_Avg    = np.append(TRIAX_Avg, [[int(i), int(x),
69 y[0]]], axis=0)
70                 Lode_Avg    = np.append(Lode_Avg, [[int(i), int(x),
71 z[0]]], axis=0)
72
73             print ('Number of Frames completed: ') + str(i)
74
75             ### Saves the raw data in to csv files. TRIAX_Avg and Lode_Avg ###
76             np.savetxt('TRIAX_Avg.csv',TRIAX_Avg, fmt='%10.50f' , delimiter=',')
77             np.savetxt('Lode_Avg.csv',Lode_Avg, fmt='%10.50f' , delimiter=',')
78
79             ###Sets up the array for Final Average Daata ###
80             TRIAX_Avg_Final= np.zeros([0,2])
81             Lode_AVG_Final= np.zeros([0,2])
82
83             ### Loop through the raw data and temporarily save the TRIAX/Lode into
84             a temp array for all frames and sum the total. Then Average it over the
85             number of frames in the model ###
86             for x in Elements_For_Processing:
87                 temparrayTRIAX=[]
88                 temparrayLode=[]
89                 for y,z in zip(TRIAX_Avg,Lode_Avg):
90                     if x == y[1] and y[2] != 0:
91                         temparrayTRIAX.append(y[2])
92                         temparrayLode.append(z[2])
93
94             TRIAX_AVG_Sum    = sum(temparrayTRIAX)/len(temparrayTRIAX)
95             Lode_AVG_Sum    = sum(temparrayLode)/len(temparrayLode)
96
97             TRIAX_Avg_Final = np.append(TRIAX_Avg_Final, [[x,TRIAX_AVG_Sum]],
98 axis=0)
99             Lode_AVG_Final  = np.append(Lode_AVG_Final, [[x,Lode_AVG_Sum]],
100 axis=0)
101
102             ### Saves the TRIAX and Lode averages over the number of frames in
103             arrays, TRIAX_AVG_Final and Lode_AVG_Final ###
104             np.savetxt('TRIAX_Avg_Final.csv',TRIAX_Avg_Final, fmt='%10.50f' ,
105 delimiter=',')
106             np.savetxt('Lode_AVG_Final.csv',Lode_AVG_Final, fmt='%10.50f' ,
107 delimiter=',')

```

Appendix J-4 - Additional Script to obtain Element volume for selected elements for the last frame -

```
### Get EVOL for the last frame for the selected elements

### Creating Array for EVOL
EVOL_Array = np.zeros([0,2])

### Get EVOL data and save to csv

EVOLElementLabels = odb.steps[steptoread].frames[-
1].fieldOutputs['EVOL'].bulkDataBlocks[0].elementLabels
EVOLData = odb.steps[steptoread].frames[-
1].fieldOutputs['EVOL'].bulkDataBlocks[0].data

for x, y in zip(EVOLElementLabels, EVOLData):
    if x in Elements_For_Processing:
        EVOL_Array = np.append(EVOL_Array, [[int(x), y[0]]], axis=0)

np.savetxt('EVOL_Array.csv', EVOL_Array, fmt='%10.50f', delimiter=',')

print(EVOL_Array)

### Get sum EVOL data and print

EVOL_Sum = EVOL_Array.sum(axis=0)

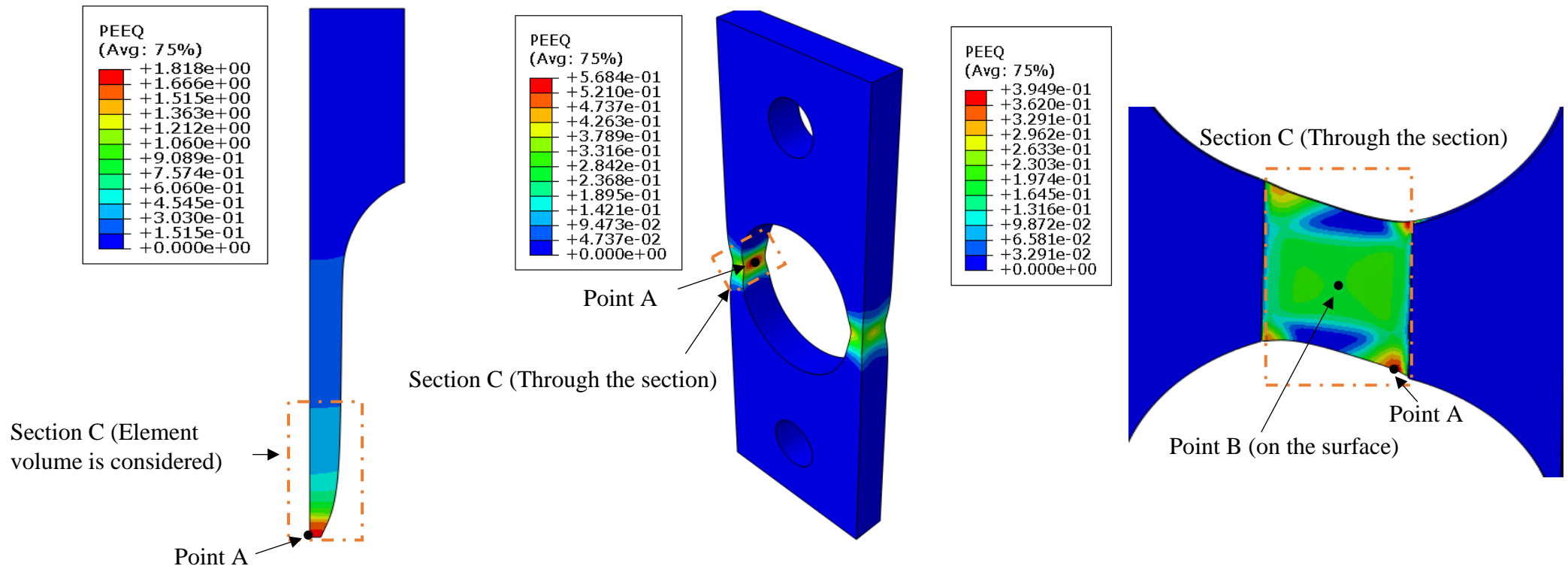
print(EVOL_Sum)
```


Appendix K – High Stress Triaxiality Range of Locations

Method 1: This was based on the critical failure point being taken at the maximum plastic equivalent strain, by point A.

Method 2: Following Method 1, the critical failure point was taken at the maximum plastic equivalent strain, however, for the shear specimens (this included ST/BU45/BU90) the critical failure point was taken at the centre of the specimen, on the outer surface, as shown by point B.

Method 3: A spatial averaging method was used, where the failure process zone was averaged for equivalent fracture strain, average stress triaxiality and the average Lode angle parameter, as shown in section C.



Appendix L – Negative Stress Triaxiality Force Displacement Curves

